Cerebrovascular reactivity mapping and its impact on BOLD fMRI of task induced activity and rest

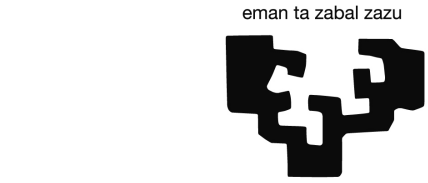

Universidad del País Vasco
Euskal Herriko Unibertsitatea

Doctoral dissertation by:
Stefano Moia

Supervised by:
Dr. César Caballero-Gaudes and Dr. Maite Termenon

2021

This work was supported by the European Union's Horizon 2020 research and innovation program (Marie Skłodowska-Curie grant agreement No. 713673) and a fellowship from "La Caixa" Foundation (ID 100010434, fellowship code LCF/BQ/IN17/11620063), and was developed at the Basque Center on Cognition, Brain and Language.

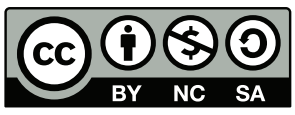

© Stefano Moia, 2021
Basque Center on Cognition, Brain and Language
Paseo Mikeletegi 69
Donostia, Spain
September 2021

To the person that took me for a pillow that one time,
and five years later is still willing to do so every night.

Acknowledgments

This couple of hundreds of pages, most of which are figures and bibliography, show only a little part of the long journey that the last four years have been, of the long days, the long nights (who needs to sleep anyway?), the happy moments, the frustration, and the great achievements that have made up this predoctoral period. Four years that never would have even started without a great scholarship (for that, gratitude goes to the *Obra Social la Caixa*), but for sure would have never continued without the extraordinary people I had around.

Starting with my supervisors, both here in Donostia and on the other side of *the big pond*. A huge thanks goes to César Caballero-Gaudes, Maite Termenon, and Molly Bright: without the three of you I wouldn't have discovered an incredible topic of research, that I had no idea existed before, I had trouble getting used to, and that now I don't want to leave any more! Thank you for your great support, all of the time that you dedicated to me and my work, and for giving me the freedom to explore different aspects of this job and projects related (and not so related) to it.

César, thank you for your kindness and your respect. I know I haven't made it easy for you, but you taught me a great deal, and you kept guiding me this far with a whole lot of patience and support - I won't forget that. I also won't forget your *tarta de queso*, but that's another story... I know the work is not over (is it ever?), but let's enjoy this milestone for a little!

Maite, thank you for your help and your presence, at each (very) long meeting and outside of these. Thank you for helping me out a whole lot (because yes, you did!), for keeping all of us on track and for smoothing things when they needed to be smoothed. Without you this journey would have been much harder!

Molly, thank you for making me discover a great city, for inviting me to work in a fantastic environment, and for teaching me a different approach to this job. It has always been incredibly interesting to talk together and discuss new and exciting ideas, and I hope I'll have more opportunities to keep learning from you in the future!

Thanks also to my *brothers in work*, a.k.a. the PhDs of the *SPiNlab* group, and to the

members of the *Brightlab -ANVIL* group!

Another whole lot of gratitude goes to all of the admins of the BCBL, the IT crew, and the lab assistants. Thank you all for making this work a whole lot easier, for helping me keep track of the bureaucracy, for helping me with the tasks in the lab, and with my crazy computer-related requests.

A special acknowledgement goes to the *physiopy* community, to the *tedana* community, and to the *Brainhack Donostia* organisation teams. You all taught me another whole deal of things, and helped me to develop and enhance a set of skills that I couldn't have been able to address otherwise. You also helped me putting things in perspective, and think again about some of my priorities in science and in a work environment!

Many thanks to the *freaks table* and the *zucchero liquido* group, for the laughs, the jokes, the games, and the help. I'm really glad to be able to call you all friends. Thank you also to the Italians of the BCBL: our coffees alone were always a very good reason to come to work, and to not forget my native language! I'm still waiting for the *Friday's teachings of trash culture*, so don't think I'll forget about that!

Another special thanks to Alberto: thank you for bearing with my mess, both at home and in my train of thoughts, for sharing the happy moments and the troubles of these last few years, and for taking good care of me!

Finally, a huge thanks to my family, to my mom, my grandmother, my uncle, my cousin, and to all of their beloveds, that kept supporting me in these years, as you always did. Thank you for helping me get on my feet when I needed it, for letting me be here doing what I do, and for bearing with having me far away from the nest. Having you there, not just for me but also for each other, has always been and is a great source of comfort and serenity.

Last, but definitely not least, thank you Merel. Thank you for cheering me up when I need it (which happens a lot), for keeping up with those moments in which I'm in my head more than anywhere else, and for sharing with me this last five years. I couldn't ask for a better person to have at my side, and for that, if it wasn't clear, this work is dedicated to you.

Abstract

Cerebrovascular reactivity (CVR) is a physiological response of the cerebral vessels to vasodilatory or vasoconstrictive stimuli. CVR estimations can be obtained by evoking a vasodilatory response during functional Magnetic Resonance Imaging (fMRI) with simultaneous recording of the pressure of expired CO_2 fluctuations during a breath-hold (BH) task. Another approach for assessing CVR consists in measuring the fluctuations of the BOLD signal during Resting State (RS). Interestingly, RS fluctuations have also been studied in relation with task Induced Activations (tIA), thus leading to hypothesise a relationship between CVR and tIA. Hence, the aim of this work is to understand if BH-induced CVR mapping holds a relationship with RS fluctuations and tIA.

With that goal in mind, a ten subjects, ten sessions multi-echo fMRI dataset with concurrent physiological fluctuations recording was collected for this thesis. Each session was composed by four RS, a Simon, a Motor, a Pinel functional localiser, and a BH task. The resulting estimated CVR, RS fluctuations and tIA maps showed high sensitivity and generally excellent reproducibility.

To benefit from this dense mapping dataset, various methods have also been investigated with the goal of improving BH-induced CVR estimation. On the one hand, there is a regional specific temporal offset between recorded CO_2 pressure and local BOLD response, due to both measurement and physiological delays, that presents local variations. Moreover, during BH movement and breathing-related artefacts caused by the task can substantially hinder CVR estimates due to their high temporal collinearity with noise. Hence, a framework based on a lagged-GLM approach for taking into account the haemodynamic lag of CVR and simultaneously remove the effect of collinear motion, as well as the performance of multiple denoising analysis strategies applied on ME-fMRI BOLD data, are discussed in this work. The chosen approach provided robust, lag-optimised maps of haemodynamic delay and higher CVR amplitudes than non-optimised CVR estimations, with consistent regional variation across subjects, and improved contrast-to-noise ratio compared to methods where motion regression was ignored or performed sequentially.

On the other hand, a conservative independent component analysis denoising model applied on the optimally-combined ME-fMRI signal offered the largest reduction of motion-related effects while yielding reliable CVR amplitude and lag estimates, although a conventional regression model applied on the optimally-combined data resulted in similar estimates.

To insert CVR estimation in a broader physiological context, this thesis also investigates the effect of blood pressure on CVR mapping by taking advantage of the multiple precise measurements collected in each subject. It was found that Mean Arterial (MAP) and Pulse Pressure (PP) had spatially independent significant regional impacts on CVR estimation, as did the sex of the subject.

Finally, the impact of CVR on RS fluctuations and tIA was assessed using a set of Linear Mixed Effect models to take into account the impact of multiple sessions. Although focalised regions of significant relationship between CVR, RS fluctuations and tIA were found, a general failure to generalise previous results was assessed, indicating that these relationship, if existing, exhibit a more complex and variable nature than previously described.

Resumen

La reactividad cerebrovascular (Cerebrovascular Reactivity, CVR) es una respuesta fisiológica de los vasos sanguíneos cerebrales a estímulos vasodilativos o vasoconstrictores debido a un cambio en el pH de su contenido. Tal cambio es normalmente inducido por aumentos y disminuciones de ciertos gases, principalmente CO_2 (Liu, De Vis & Lu, 2018). En los últimos años, la resonancia magnética funcional (functional Magnetic Resonance Imaging, fMRI) basada en el contraste dependiente del nivel de oxigenación sanguínea (Blood Oxygen Level Dependent, BOLD) ha demostrado su eficacia para evaluar la CVR de forma no invasiva y robusta, permitiendo una estimación de CVR con alta resolución espacial.

Las mediciones de CVR se pueden obtener registrando las fluctuaciones de la presión de CO_2 al final de la espiración (conocido como Pressure of end-tidal CO_2 ó $P_{ET}CO_2$) durante una tarea con un desafío respiratorio, por ejemplo con apneas voluntarias (Breath-Hold, BH). El paradigma recomendado de BH consiste en varios bloques consecutivos, cada uno de ellos incluyendo al inicio varios ciclos de respiración guiada (inspiración y espiración) con una periodicidad determinada y terminando en espiración, seguida por 15-20 segundos de apnea terminados por una exhalación, y un período final de recuperación con respiración natural (Ratnatunga & Adiseshiah, 1990). Con este paradigma, la variabilidad de la línea de base CO_2 se minimiza y la forma de respuesta $P_{ET}CO_2$ es simple y cerca a su límite (Pinto, Bright, Bulte & Figueiredo, 2021). Los paradigmas de BH se pueden implementar con éxito en estudios con niños pequeños, personas mayores y otros grupos de sujetos menos cooperativos (Handwerker, Gazzaley, Inglis & D'Esposito, 2007; Kannurpatti, Motes, Rypma & Biswal, 2010; Raut, Nair, Sattin & Prabhakaran, 2016; Riecker y col., 2003; Thomas, Logan, Donner & Shroff, 2013; Thomason, Burrows, Gabrieli & Glover, 2005), y ofrecen mediciones robustas de CVR incluso cuando los sujetos no son capaces de realizar la apnea, es decir mantener la respiración, durante el tiempo indicado (Bright & Murphy, 2013a). Además, estas medidas producen resultados fiables a corto y largo plazo (Peng, Yang, Chen & Shih, 2019), tanto en términos de fiabilidad espacial, es decir comparando la variabilidad de las medidas de CVR a nivel de voxel en varias sesiones, como de fiabilidad general en el valor medio de CVR entre sesiones a nivel de sujetos individuales (Lipp, Murphy, Caseras & Wise, 2015; Magon y col., 2009)).

También se ha demostrado que la estimación de CVR a través de las fluctuaciones de $P_{ET}CO_2$ es similar a la medición de las fluctuaciones de la señal durante un estado de reposo (Resting State, RS) en sujetos sanos (De Vis, Bhogal, Hendrikse, Petersen & Siero, 2018). Esta similitud se ha observado en métricas como la amplitud de las fluctuaciones en estado de reposo (RSFA) definida como la desviación estándar de una banda de frecuencia específica de la señal BOLD (Kannurpatti & Biswal, 2008; Kannurpatti, Motes, Biswal & Rypma, 2014; Wang y col., 2019), o la amplitud (ó potencia) de las fluctuaciones de baja frecuencia (ALFF), y su fracción con la potencia del espectro completo (fALFF) (De Vis y col., 2018; Golestani, Wei & Chen, 2016). Curiosamente, tales medidas también se han utilizado previamente para reportar una posible relación entre las fluctuaciones intrínsecas del cerebro en RS con la

actividad hemodinámica inducida por la actividad neuronal durante la relización de una tarea (task Induced Activity, tIA), por ejemplo en paradigmas de memoria de trabajo (Zou y col., 2013) y paradigmas de función ejecutiva como la tarea de Flanker (Mennes y col., 2011). Por otra parte, las fluctuaciones de RS se han utilizado para reescalar y normalizar la amplitud de tIA a nivel de estudios de grupo con el fin de tener en cuenta las diferencias a nivel vascular entre diferentes sujetos (Kazan y col., 2016). Estos hallazgos, así como el impacto que las señales fisiológicas pueden tener sobre la conectividad funcional y las fluctuaciones de RS, podrían indicar que las fluctuaciones fisiológicas y la CVR constituyen la base, o modelan de alguna manera, la relación entre RS y tIA, indicando que al menos parte de lo que se ha atribuido a las fluctuaciones intrínsecas del cerebro podría explicarse realmente por factores fisiológicos y vasculares estables, como la CVR.

Esta tesis está dedicada a explorar dicho impacto y generalizar resultados presentados recientemente en la literatura, en particular el trabajo de Golestani y col. (2016), Mennes y col. (2011), aprovechando nuevos diseños experimentales que enfatizan el hecho de realizar múltiples mediciones en el mismo sujeto (conocido como Dense Mapping, DM), y utilizando secuencias avanzadas de fMRI que permiten reducir el nivel de ruido de la señal y mejorar la sensibilidad al contraste BOLD, como Multi-Echo (ME) fMRI.

Capítulo 2: Experimento y datos EuskalIBUR

Con el fin de estudiar las relaciones entre la CVR, las fluctuaciones de RS y la tIA, para esta tesis se diseño un experimento de DM, denominado EuskalIBUR, en el cual se recopiló un conjunto de datos de neuroimagen, fisiológicos y variables de conducta y estado en 10 sujetos que participaron en 10 sesiones de MRI. Cada sesión estuvo compuesta por 4 registros de fMRI mientras los participantes realizaban la tarea de función ejecutiva de Simon (Simon & Rudell, 1967), una tarea motora (Buckner, Krienen, Castellanos, Diaz & Yeo, 2011) y un localizador de diferentes abilidades cognitivas (lectura, procesamiento matemático) y sensoriales (audición, visual, motor) (Pinel y col., 2007) que fueron intercaladas entre 4 adquisiciones de fMRI en RS, y finalmente una tarea de BH. Durante las adquisiciones funcionales se registraron señales fisiológicas de pulso cardíaco, esfuerzo de respiración y CO_2. Así mismo, cada sesión incluyo la adquisición de imágenes anatómicas ponderadas en T1 (MP2RAGE) y T2 (Turbo Spin Echo). Además, antes de empezar cada sesión de MRI se recogieron datos del estado de salud y conducta (presión sanguínea, horas de sueño, hidratación, consumo de alcohol y cafeina, etc, ver Appendix A).

Los experimentos DM presentan muchas ventajas en comparación con la adquisición de datos tradicional basada en grupos. Entre otras, se simplifican los tiempos de reclutamiento y acceso al escáner (Gordon y col., 2017), resuelven el problema de los grupos experimentales de tamaño insuficiente (Naselaris, Allen & Kay, 2021; Poldrack, 2021), permiten una mejor estimación de la estabilidad de la activación neuronal y la conectividad, dinámica, e interacciones funcionales (Gordon y col., 2018; Gratton y col., 2018; Laumann y col., 2015; Lynch y col., 2020), y cómo esta estabilidad se relaciona con el comportamiento (Seitzman y col., 2019). Además, este diseño de experimentos pueden abrir la posibilidad de estudiar variaciones en fluctuaciones cerebrales a lo largo del tiempo (Shine, Koyejo & Poldrack, 2016), por ejemplo debido a la recon-

figuración funcional (Salehi, Karbasi, Barron, Scheinost & Constable, 2020), plasticidad cerebral (Newbold & Dosenbach, 2021; Newbold y col., 2020), sorpresa y novedad (Betzel, Satterthwaite, Gold & Bassett, 2017), o el efecto del sistema endocrino durante el ciclo menstrual (Arélin y col., 2015; Barth y col., 2016; Pritschet y col., 2020; Pritschet, Taylor, Santander & Jacobs, 2021).

Además, los datos de fMRI en EuskalIBUR se obtuvieron usando secuencias multi-eco (ME) BOLD que muestrean la señal fMRI ponderada en el parámetro T_2^* en múltiples tiempos de eco (TE) sucesivos. Esta técnica permite mejorar el contraste BOLD, por ejemplo mediante el uso de una combinación ponderada de los múltiples volúmenes de eco (Poser, Versluis, Hoogduin & Norris, 2006; Posse y col., 1999). La combinación óptima de múltiples volúmenes de eco también puede mejorar la sensibilidad, la especificidad, la repetibilidad y la confiabilidad del mapeo CVR (Cohen y col., 2021; Cohen & Wang, 2019).

Tras el preprocesamiento de los datos funcionales y anatómicos, basado en AFNI, FSL, y ANTs, se calcularon metricas de evaluación de las fluctuaciones de RS utilizando las adquisiciones de RS, y la tIA fue estimada en las adquisiciones en tarea utilizando modelos de regresión lineal (General Linear Models, GLM). Una vez calculados los mapas a nivel de sujeto y sesión, el análisis estadístico a nivel de grupo se realizó mediante el calculó del coeficiente de correlación intraclase (ICC) para cada contraste de tarea y las métricas de fluctuación RS. También se calculó un análisis de grupo basados en modelos mixtos de varianza en el sujeto y a nivel de grupo para todos los contrastes de tareas.

Las mapas de CVR, de fluctuaciones de RS, y de tIA mostraron alta sensibilidad para todas las tareas y las runs, a nivel del sujeto como del grupo, y en la mayoría de los casos, una reproducibilidad excelente.

Capítulo 3: Estimación de CVR con optimización temporal

En el modelado y estimación de la CVR usando fMRI hay que tener en cuenta que existe un retardo temporal que varía entre regiones del cerebro entre la $P_{ET}CO_2$ y la respuesta local de la señal BOLD. Este retardo se debe tanto a un retardo en la medida debido a la transmisión y registro de los gases, como a un retardo fisilógico asociado a la respuesta vasodilatadora de CVR y la propagación de gases en el sistema respiratorio. Si no se tiene en cuenta este retardo en el modelo y su variabilidad no se considera de forma adecuada, la estimación de CVR a nivel de voxel podría ser imprecisa (por ejemplo, ver (Blockley, Harkin & Bulte, 2017; Donahue y col., 2016; Sousa, Vilela & Figueiredo, 2014)). Por otra parte, durante la tarea de BH, el movimiento y los artefactos relacionados a la respiración causados por la tarea pueden deteriorar las estimaciones de CVR sustancialmente (Bright, Bulte, Jezzard & Duyn, 2009), debido a la alta colinearidad temporal con el efecto de interés, es decir la respuesta de CVR (Lindquist, Geuter, Wager & Caffo, 2019). Por este motivo, en este capitulo se estudia el modelo más apropiado basado en un enfoque de lagged-GLM que tenga en cuenta el retardo hemodinámico de la CVR y considere al mismo tiempo los efectos de artefactos y señales de ruido colinea.

Este modelo se evaluó primero en un pequeño subconjunto de los datos EuskalIBUR comparandolo frente a una estimación de CVR sin considerar el retardo hemodinámico, así como frente a modelos en los que la regresión de los artefactos de movimiento y señales de baja frecuencia se realiza anteriormente

al modelo de regresión de CVR. Es decir, el modelo de regresión de la señal de fMRI se realiza secuencialmente y no de forma simultánea como sería más apropiado desde un punto de vista analítico y estádistico. Los resultados obtenidos demuestran que unmodelo de regresión simultáneo y optimizado para el retraso obtiene mapas de CVR con una amplitud más alta que las estimaciones de CVR no optimizadas. Estos mapas mostraron también una variación regional consistente en todos los sujetos, y un ratio de contraste y ruido mejor que en los mapas obtenidos con los otros modelos, demostrando la relevancia de los modelos lagged-GLM en la estimación de CVR.

Capítulo 4: Mejora de la estimación de CVR con secuencias ME-fMRI

Para abordar el problema de eliminar el efecto del movimiento y otros artefactos de forma efectiva, y al mismo tiempo conservar la mayor parte de la respuesta de CVR, se evaluó el rendimiento de varias estrategias de preprocesado y análisis que consideran las características de los datos de ME-fMRI BOLD. En particular, como la señal relacionada con el efecto BOLD se puede expresar en función del TE, mientras que las variaciones del señal relacionados con el ruido en la magnetización son independientes del TE, se puede aprovechar de la información disponible en los ecos múltiples con el propósito de mejorar la limpieza de la señal de fMRI. Por ejemplo, es posible clasificar el resultado de un análisis multivariado de componentes independientes (Independent Component Analysis, ICA) en fuentes de señal BOLD o ruido y artefactos (ME-ICA, Kundu y col., 2013; Kundu, Inati, Evans, Luh & Bandettini, 2012; Kundu y col., 2017). ME-ICA permite mejorar el mapeo de la activación inducida por tareas (Amemiya, Yamashita, Takao & Abe, 2019; DuPre, Luh & Spreng, 2016; Evans, Kundu, Horovitz & Bandettini, 2015; Gonzalez-Castillo y col., 2016; Lombardo y col., 2016), y la reducción de ruido y artefactos en datos de fMRI en estado de reposo (Dipasquale y col., 2017; Lynch y col., 2020), logrando una representación de la conectividad funcional más eficiente y fiable en sujetos individuales (Lynch y col., 2020) y en regiones cerebrales donde las adquisiciones tradicionales con un solo eco ofrecen una relación señal-ruido reducida, como en el cerebro basal (Markello, Spreng, Luh, Anderson & De Rosa, 2018).

Sin embargo, cómo usar la información de clasificación de las componentes de la señal de fMRI proporcionada por ME-ICA para mejorar la limpieza de los datos de CVR no es trivial y requiere una investigación detallada para determinar cuál es el equilibrio correcto entre una eliminación adecuada de los artefactos (movimiento, respiración, susceptibilidad) y la preservación de la señal de CVR de interés. Realizar este estudio es fundamental teniendo en cuenta especialmente la colinearidad entre los regresores del modelo que caracteriza las tareas de BH. Por lo tanto, este capítulo estudia multiples modelos de análisis lagged-GLM: desde modelos de regresión convencionales en los que la matriz de diseño incluye la respuesta BOLD de interés, resultante de la convolución de la señal $P_{ET}CO_2$ con la respuesta hemodinámica, y covariables de no interés definidos a partir de los parámetros de movimiento y señales de baja frecuencia que se aplica en los datos de eco único u combinados de forma óptima (OC), hasta modelos más complejos que además incluyen regresores obtenidos de ME-ICA con diferentes grados de ortogonalización para preservar el efecto de interés, es

decir la CVR. En este caso, se evaluaron tres tipos de análisis: 1) un modelo lagged-GLM agresivo en el que las señales temporales de los componentes de ICA clasificados como ruido se añadieron directamente como regresores de no interés en la matriz de diseño; 2) un modelo lagged-GLM moderado, en el que las señales de ICA de ruido fueron previamente ortogonalizadas con respecto al regresor de interés de CVR, y 3) un modelo lagged-GLM conservador, en el que las señales de ICA de ruido también fueron ortogonalizadas tanto con respecto a la señal de CVR como con los otros componentes de ICA clasificados como señal BOLD y por tanto hipotéticamente asociada con la actividad neuronal o de CVR.

La evaluación y comparación de estos modelos de análisis se realizó en función de su capacidad para hacer que los cambios de intensidad de la señal BOLD sean independientes del movimiento, así como su fiabilidad y reproducibilidad de los mapas de CVR y retardo hemodinámico en términos del coeficiente de correlación intraclase (ICC) a nivel de voxel. Los resultados revelaron que un modelo de análisis de componentes independiente conservador aplicado en la señal de ME-fMRI combinada de manera óptima ofrece la mayor reducción de los efectos relacionados con el movimiento en la señal, y contemporáneamente produce estimaciones mas reproducibles de amplitud CVR y lag. Así mismo, se observó que un modelo de regresión convencional aplicado en los datos combinados de manera óptima ofrece estimaciones de CVR y retardo similares sin la necesidad de realizar el preprocesado y clasificación de ME-ICA.

Capítulo 5: CVR y presión arterial

Para enfocar la relevancia de la CVR dentro de un contexto mas amplio de la fisiología del cerebro y del cuerpo humano, en esta tesis se ha estudiado el efecto de otros factores fisiológicos y de las características individuales de los sujetos sobre el mapeo de CVR.

Previos estudios han mostrado que cambios en la presión arterial podrían producir cambios en el nivel basal de CO_2, y viceversa, y ambas alteraciones podrían influir en la resistencia cerebrovascular Aaslid, Lindegaard, Sorteberg y Nornes (1989). Sin embargo, estudios recientes no han podido replicar tales observaciones (Thrall y col., 2021). Es probable que como cambios en la presión arterial y en el nivel de CO_2 dan origen a mecanismos de vasodilatación, independientemente que estén relacionados con la autoregulación cerebral o la CVR (Carr, Caldwell & Ainslie, 2021), la presión arterial podría actuar como un factor de ruido en la estimación de CVR (Hetzel, Braune, Guschlbauer & Dohms, 1999; Pericot Nierga, Molina Cateriano, Álvarez Sabín & Codina Puiggrós, 2000; Regan, Fisher & Duffin, 2014). Además, se ha observado que cambios en la presión arterial media (Mean Arterial Pressure, MAP) durante la hipercapnia no están correlacionados con incrementos en el nivel de CO_2 al final de la espiración ($_{ET}CO_2$) (Smielewski, Kirkpatrick, Minhas, Pickard & Czosnyka, 1995). También se ha demonstrado que un estado anormal de la presión arterial puede alterar la respuesta cerebral a las variaciones del nivel de CO_2 en la sangre. Por ejemplo, Artru y Colley (1984) demostró la ausencia de CVR durante la hipocapnia en casos de un hipotensión inducida en perros. Una reactividad anormal a los cambios en CO_2 también se ha reportado en pacientes con hipertensión (Dumville, Panerai, Lennard, Naylor & Evans, 1998; Ficzere y col., 1997; Leoni y col., 2011; Li y col., 2021; Settakis, Páll y col., 2003), con

vínculos a un empeoramiento en las funciones ejecutivas (Hajjar, Marmerelis, Shin & Chui, 2014). En resumen, la influencia de la presión arterial como un factor en la estimación de CVR todavía necesita mas estudios.

Las características de DM del experimento EuskalIBUR y los datos recogidos permiten arrojar nuevos evidencias sobre la posible relación la presión y la CVR. En este estudio se estimó la presión arterial promedio (MAP) y la presión de pulso (PP) a partir de las mediciones de presión arterial y el pulso cardíaco realizadas en cada sujeto antes de cada sesión de MRI. Luego, se planteó un modelo lineal de efectos mixtos (Linear Mixed Effects, LME) para estimar la relación entre las medidas de CVR y el retardo hemodinámico con la MAP, PP, o pulso cardíaco, así como posibles interacciones de estas variables con el sexo del sujeto. Este análisis se realizó tanto a nivel de voxel como considerando en el valor medio de CVR y retardo en la materia gris (Grey Matter, GM).

Teniendo en cuenta los valores medios de GM, solo se encontró un efecto leve y negativo del pulso cardíaco sobre el retardo, lo que indica que un aumento en el pulso cardíaco produce retardos mas cortos de CVR. Los análisis a nivel de voxel demostraron que MAP y PP presenta una relación significativa con CVR en multiples regiones cerebrales, tanto a nivel cortical como subcortical, al igual que el sexo del sujeto. No se observó ninguna interacción entre estas variables. Curiosamente, el impacto del MAP y PP sobre la amplitud de CVR muestran distribuciones espaciales independientes, lo que indica que ambas mediciones presentan información importante y distinta que se debe tener en cuenta en la evalución de la CVR.

Capítulo 6: CVR, RS, y tIA

Finalmente, el impacto de la CVR en las fluctuaciones de RS y TIA se evaluó utilizando un conjunto de modelos LME para tener en cuenta el impacto de múltiples sesiones, tanto a nivel de valor medio en la GM como voxelwise. El enfoque particular de este estudio fue replicar y generalizar los resultados de Mennes y col. (2011), que vinculó las fluctuaciones de RS a tIA, y de Golestani y col. (2016), que vinculó las fluctuaciones de RS, y ALFF en particular, a la CVR. En estos estudios no se considera la varianza intra-sujeto pues sólo se obtuvieron una única medida de CVR, tIA or RS en cada sujeto, mientras que el experimento EuskalIBUR permite tener en cuenta ambas terminos de varianza intra-sujeto y entre-sujeto.

En el caso del estudio presentado Golestani y col. (2016) se calcularon los valores medios de ALFF, RSFA y fALFF considerando la GM, y se utilizó un modelo LME para estimar la relación entre estas métricas de RS y CVR. El mismo modelo de LME también se implementó a nivel de voxel. En el caso del estudio de Mennes y col. (2011), se implmentó un modelo LME similar para evaluar la relación entre las fluctuaciones de tIA y las medidas de RS, y entre tIA y CVR, a nivel de voxel.

Si bien se encontraron regiones focalizadas de relación significativa entre CVR, fluctuaciones de RS y tIA, en general los resultados obtenidos demuestran la falta de generalización de los resultados anteriores, indica que esta relación, si existe, tiene una naturaleza mucho más compleja y variable de lo descrito anteriormente.

Contents

R

Table of Acronyms

Acronym	Meaning
ALFF	Amplitude of Low Frequency Fluctuations
AP	Anterior-Posterior (direction)
ARMA	Autoregressive Moving Average
ASL	Arterial Spin Labelling
BH	Breath-Hold
BIDS	Brain Imaging Data Structure
BOLD	Blood Oxygen Level Dependent (signal)
CDB	Cued Deep Breathing
CI	Confidence Interval
CMRR	Center for Magnetic Resonance Research (Minnesota)
CNR	Contrast to Noise Ratio
CSF	Cerebrospinal Fluid
CVR	Cerebrovascular Reactivity
DM	Dense Mapping
DMN	Default Mode Network
DoF	Degrees of Freedom
DP	Diastolic Pressure
DVARS	Root of the spatial mean square of the first derivative of the signal
EPI	Echo Planar Images
fALLF	fractional ALFF
FD	Framewise Displacement
FDR	False Discovery Rate (correction)
fMRI	functional Magnetic Resonance Imaging
fNIRS	functional Near Infrared Spectroscopy
FoV	Field of View
FWHM	Full Width Half Maximum
GLM	General Linear Model
GM	Grey Matter
HR	Heart Rate
HRF	Haemodynamic Response Function
IC	Independent Component
ICA	Independent Component Analysis
ICC	Intraclass Correlation Coefficient
ISI	Interstimulus Interval
LBNP	Lower Body Negative Pressure
LME	Linear Mixed Effect (model)
MAP	Mean Arterial Pressure
ME	Multi-Echo
ME-AGG	Multi-Echo Aggressive (approach)
ME-CON	Multi-Echo Conservative (approach)
MEMA	Mixed Effects Meta Analysis
MNI	Montreal Neurological Institute
ME-MOD	Multi-Echo Moderate (approach)
SE-MPR	Single-Echo Motion Polynomials Regression (approach)
OC-MPR	Optimally Combined Motion Polynomial Regression (approach)

Acronym	Meaning
MR	Magnetic Resonance
MRI	Magnetic Resonance Imaging
NMR	Nuclear Magnetic Resonance
NN	Nearest Neighbours
OC	Optimally Combined
PA	Posterior-Anterior (direction)
PETCO2	Pressure of End-Tidal CO2
PP	Pulse Pressure
PPG	Photoplethysmogram
SE-PRE	Single-Echo pre-motion realignment
ReML	Restricted Maximum Likelihood
ROI	Region of Interest
RS	Resting State
RSFA	Resting State Fluctuation Amplitude
RVT	Respiration Volume per Time
SE	Single-Echo
SP	Systolic Pressure
SPC	Signal Percentage Change
TA	Acquisition Time
TCD	Transcranial Doppler
TE	Echo Time
tIA	task Induced Activation
TR	Repetition Time
tSNR	temporal Signal to Noise Ratio
WM	White Matter

1. Introduction

1.1 Brief history of Magnetic Resonance Imaging

In recent years, Magnetic Resonance Imaging (MRI) has become a cornerstone of neuroscience research and clinical practice. MRI is based on the principles of Nuclear Magnetic Resonance (NMR), a phenomenon described for the first time between the end of the 1930s and the beginning of the 1940s (Bloch, 1946; Gorter & Broer, 1942; Purcell, Torrey & Pound, 1945; Rabi, 1937). NMR consists in an electromagnetic signal that nuclei in a strong magnetic field emits when a weaker, oscillating magnetic field perturbs them with a specific frequency, the so called *Larmor frequency*. The Larmor frequency is the angular frequency with which the spin of the nuclei precesses around the strong magnetic field. It depends on the strength of such field and on the magnetic properties of the nuclei itself, and as such it is intrinsic to the nuclei. When the weaker magnetic field matches the Larmor frequency, the nuclei resonate, and emit energy in the form of an electromagnetic signal that can be recorded by a receiving coil in the nearby space.

In the late 1970s Damadian (1971), Lauterbur (1973), and Mansfield and Grannell (1973) independently demonstrated how to use NMR to image (living) objects. While Lauterbur introduced the mathematical principles to obtain a 2D back-projection of recorded NMR signal (Lauterbur, 1973), Mansfield showed how to use a linear field gradient to localise different "slices" of material (i.e. slice selection) and also introduced the principles of the Echo Planar Imaging (EPI) sequence (Mansfield & Grannell, 1973). At the same time, Damadian demonstrated that pathological tissues in the human body produced a different signal from healthy tissue (Damadian, 1971) and built a scanner to image the human body. Shortly after, Clow and Young produced the first brain image (cf. McRobbie, Moore, Graves & Prince, 2017).

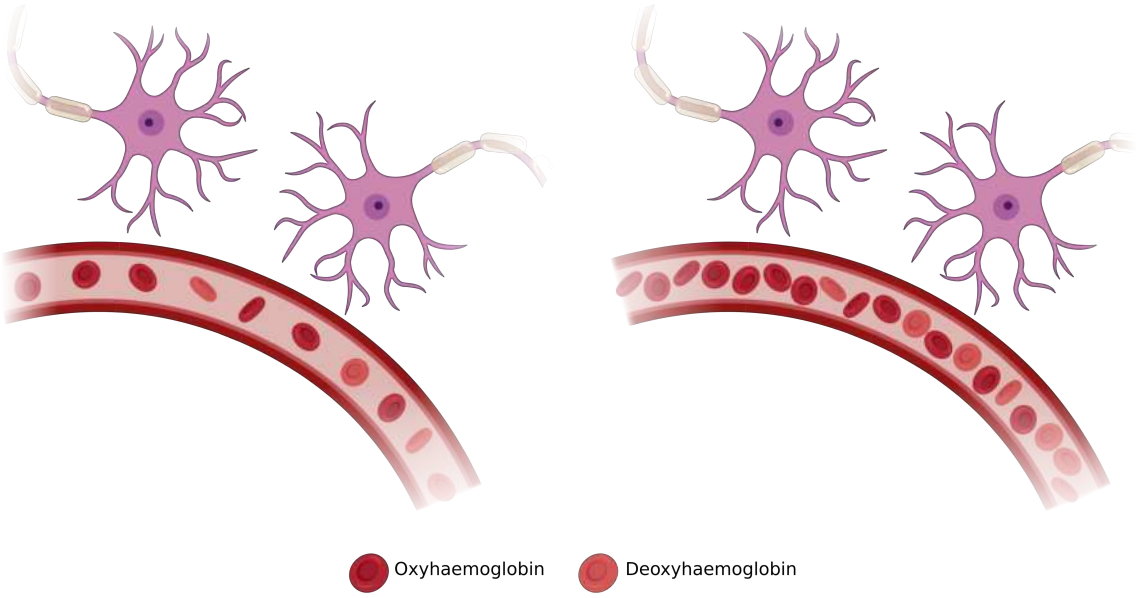

Figure 1.1: Schema of BOLD effect. During neuronal activity, HbO increases and perturbs the magnetic field.

1.2 Functional Magnetic Resonance Imaging and Blood Oxygen Level Dependent signal: task Induced Activity and Resting State

It took about fifteen years more for the birth of *functional* MRI (fMRI). In 1990 and 1992 Ogawa and colleagues showed that haemoglobin bonded with oxygen (oxyhaemoglobin, HbO) had a different signal compared to unbounded haemoglobin (deoxyhaemoglobin) due to their magnetic properties (diamagnetic and paramagnetic, respectively), and that this difference could be used as an intrinsic, non-invasive contrast mechanism to image brain function (see Figure 1.1). This contrast mechanism was termed as the Blood Oxygen Level Dependent (BOLD) effect, and used to map cerebral responses to watching a flickering chequerboard (Ogawa & Lee, 1990; Ogawa et al., 1992). Together with the images of Belliveau et al. (1991), these were the first task-induced activity (tIA) fMRI experiments, and the first confirmations that blood could be used to indicate a correlation between behaviour (or cognition) and brain activity after the theorisations of Mosso (1883). Three years later, Biswal, Yetkin, Haughton and Hyde (1995) showed that patterns similar to the ones observed in tIA-fMRI studies could be seen in the brain at rest: correlated fluctuation in the BOLD signal were found in auditory, visual, and somatomotor areas in subjects laying down in the scanner, in a "Resting State" (RS). Still today, tIA- and RS-fMRI are the most adopted designs and frameworks to investigate brain properties with BOLD fMRI.

It is important to note that the BOLD signal is not a direct observation of neural events associated to behaviour, sensory stimuli, and other cognitive tasks. In fact, the BOLD signal measures changes in haemoglobin that are the physiological response to neural activity, i.e. the neuro-vascular coupling (Hillman, 2014), rather than measuring the microcurrents generated by action potentials or their related chemical shifts (e.g. sodium/potassium or calcium). The reason behind this interpretation is mainly related to the action of astrocytes and perycites and their impact on the blood vessels (Hillman, 2014; Parri & Crunelli, 2003). In practice, when there is a synaptic event, the astrocyte around the synapses sense such activity and stimulate the walls of the microvessels for them to vasodilate (Zonta et al., 2003). In this way, there is a local surge of HbO meant to support the sustained metabolic

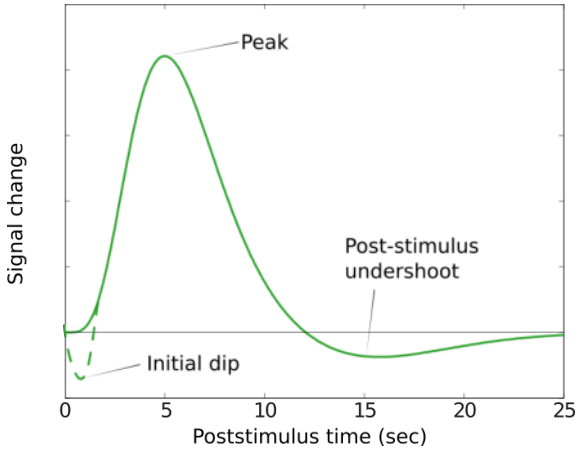

Figure 1.2: The canonical HRF. The function starts with an almost undetectable negative trough, the initial undershoot, corresponding to a moment of oxygen consumption. At around 5-6 seconds, it switches polarity and reach a strong positive peak, modelling the vasodilation and subsequent surge in HbO. After about 10-15 seconds, it switches again polarity for a prolonged period of time (the post-stimulus undershoot, about 10 seconds) before returning to homoeostasis.

activity of active neurons. If the activity ceases, the level of HbO slowly decreases, reaching a lack of local HbO, otherwise it stabilises for the duration of the continuous activity before such decrease. This process is known as the haemodynamic response, and although it varies within the brain and with aging (Arichi et al., 2012; Poppe, Willers Moore & Arichi, 2021), it is canonically modelled mathematically as a double-gamma function (Haemodynamic Response Function, HRF, see Figure 1.2).

The HRF plays an important role in detecting activations in tIA-fMRI. Indeed, the design of the tasks is typically convolved with the HRF, and the result is used as a regressor in a General Linear Model (GLM) in order to fit it with the recorded BOLD signal (Friston, Holmes et al., 1995; Monti, 2011; Poline & Brett, 2012). As for the task design itself, there exist different types of experimental paradigms. Ogawa's original experiment was based on a block design (Ogawa et al., 1992), normally consisting in stimuli of an extended period of time (e.g. 10-15 seconds) alternated with periods of rest. Block designs elicit strong, easily identifiable responses with high signal to contrast ratio, thus more appropriate for localization purposes and detection of the BOLD response. In addition, they are less prone to multicollinearity of different task stimuli (Sacco, 2012, p. 141). However, block designs are not suited for some types of experiments (e.g. involving higher cognitive functions or rapid transition between cognitive processes) (McRobbie et al., 2017, pp. 320-321), and they can become collinear to motion (Birn, Bandettini, Cox & Shaker, 1999) and spurious fluctuations. Alternatively, an event-related design involves short, transient stimuli interspersed in variable periods of rest. Event related designs elicit responses that are less easy to detect and they are statistically less efficient (Sacco, 2012, p. 142). However, event-related designs are more appropriate to characterize the temporal pattern of the hemodynamic response, might be less affected by motion (Birn et al., 1999), and different stimuli can be randomised in order to reduce multicollinearity (Sacco, 2012, p. 142).

RS-fMRI data is commonly used to assess functional connectivity by measuring signal correlations from different areas. This can be achieved by simply correlating the mean signal of regions of interest (ROI), using the signal of a ROI as a predictor for the rest of the brain (seed correlation, see Biswal et al., 1995), observing the correlation of neighbouring

areas (Zang, Jiang, Lu, He & Tian, 2004) or decomposing the signal and its different sources with data-driven methods (Beckmann & Smith, 2004; Liu, Chang & Duyn, 2013; Liu & Duyn, 2013; Liu, Zhang, Chang & Duyn, 2018; Mckeown et al., 1998; Tagliazucchi, Balenzuela, Fraiman & Chialvo, 2011). For instance, with spatial Independent Component Analysis (ICA) it is possible to model various *functional networks*, i.e. different patterns of spontaneous connectivity, that are spatially similar to tIA (Buckner, Andrews-Hanna & Schacter, 2008; Fox et al., 2005) Alternatively, various types of clustering can be applied on a subset of temporal volumes, which selection is based on the extreme fluctuations of a ROI signal. This technique, called Co-Activation Pattern analysis, shows similar patterns to seed correlation analysis (Liu et al., 2013; Liu & Duyn, 2013; Liu, Zhang et al., 2018).

Otherwise, RS-fMRI can be also used to assess different properties of the signal at rest by observing the spectral characteristics of its fluctuations. Two broadly adopted measures for this scope are the (fractional) Amplitude of Low Frequency Fluctuations (f/ALFF, Zang et al., 2007; Zou et al., 2008) and the Resting State Physiological Fluctuation Amplitude (RSFA, Kannurpatti & Biswal, 2008). ALFF was initially proposed as the power of the low frequency band of the signal (0.01-0.08 Hz) (Zang et al., 2007), and successively formulated for fALLF as the ratio between the power of the low frequency band and that of the entire range in order to be less susceptible to physiological factors (Zou et al., 2008). Instead, RSFA has been proposed as the standard deviation of the signal in the same low frequency band.

Finally, a similar concept to GLM analysis can be applied to RS-fMRI. In this case, rather than convolving a hypothesized timecourse of neuronal activity based on the experimental design with the HRF and fit the result to the BOLD signal, the latter is deconvolved with the HRF, in order to recover the activity signal underlying the RS fluctuations (Caballero-Gaudes, Karahanoğlu, Lazeyras & Van De Ville, 2012; Caballero-Gaudes, Moia, Panwar, Bandettini & Gonzalez-Castillo, 2019; Caballero-Gaudes et al., 2011; Karahanoğlu, Caballero-Gaudes, Lazeyras & Van De Ville, 2013).

1.3 "Noise" in fMRI

1.3.1 Motion and other sources of artefacts

In addition to neuronal-related activity, the BOLD signal presents multiple sources of noise related to hardware-related artefacts and drifts, head motion, confounding physiological fluctuations (Bianciardi et al., 2009; Jorge, Figueiredo, van der Zwaag & Marques, 2013) as well as image distortions related to data acquisition that should be accounted for and corrected during fMRI data preprocessing. For instance, the images could present geometric distortions in the phase direction of the acquisition that can be removed by means of mapping field distorsions, either using field maps or using two images acquired in opposite phase-encoding directions, and then with a non-linear transformation of the fMRI volumes (e.g. TOPUP, Andersson, Skare & Ashburner, 2003; Glasser et al., 2018). Also, fMRI images are typically acquired slice by slice and the difference in their time of acquisition can be compensated via slice timimg correction (Parker & Razlighi, 2019), although this step can also introduce confounding effects in the data due to signal interpolation (Parker & Razlighi, 2019). More generally, realigning all fMRI volume to a reference image can deal with part of the artefacts introduced by head motion (Friston, Ashburner et al., 1995). However, this step does not remove the effect of motion completely (Caballero-Gaudes & Reynolds, 2017).

The most straight-forward way to deal with signal artefacts is to model them as regressors of non-interest along with the task regressors (in tIA-fMRI) or to project them

out of the fMRI data if there is no task paradigm (RS-fMRI). For instance, motion-related effects can be expressed as a set of the relative translations and rotation obtained during realignment, considering their first derivative and their squared transformation for up to 24 regressors for a better denoising (Friston, Holmes et al., 1995). Similarly, very low frequency trends due to scanner inestabilities can be modelled as a set of basis functions (e.g. Legendre polynomials, discrete cosine functions).

Furthermore, large deviations in the fMRI signal (e.g. spikes) caused by motion jerks and scanner noise can be removed through scrubbing or censoring (Power, Barnes, Snyder, Schlaggar & Petersen, 2012). This process consists in identifying those fMRI volumes characterised by abrupt changes in the BOLD signal and removing or interpolating them. The identification can be performed by using summary metrics of motion, like Framewise Displacement (Power et al., 2012), or by observing transient changes in the signal (DVARS, Power et al., 2012; Smyser et al., 2010). However, it is important to notice that, if correctly accounted for, scrubbing could reduce the degrees of freedom in statistical analysis (Mascali et al., 2021), leading to biases in second-level analysis between subjects that move too much and others, or introduce discontinuity in the signal itself, limiting the use of particular analyses dependent on signal continuity (e.g. ICA, see Caballero-Gaudes & Reynolds, 2017), and biasing the estimation of functional connectivity (Mascali et al., 2021). Moreover, interpolating the signal could introduce spurious changes in the signal.

Another common approach to remove not only motion, but also other sources of noise, is based on data decomposition techniques. For instance, ICA can be leveraged to model, identify and remove motion artefacts as well as other sources of noise (Behzadi, Restom, Liau & Liu, 2007; Griffanti et al., 2014; Muschelli et al., 2014; Pruim, Mennes, Buitelaar & Beckmann, 2015; Pruim, Mennes, Rooij et al., 2015; Salimi-Khorshidi et al., 2014). Ideally, the best candidate to identify noisy timeseries would be temporal ICA, i.e. a decomposition in which the independence is forced in the temporal domain (Glasser et al., 2018; Smith et al., 2012). However, such approach is not feasible in a normal fMRI context since it would require the samples in time to be much higher than the samples in space (Smith et al., 2012). Hence, spatial ICA is the most common application for fMRI decomposition, although this might lead to detect spurious components that contain both true BOLD signal and noise (Caballero-Gaudes & Reynolds, 2017). Alternatively, several fMRI sessions could be concatenated to apply temporal ICA, although this approach would lead to the impossibility of removing session-specific noise. The challenging factor in adopting ICA for denoising is the classification of the independent components. Although manual classification is still the approach with the best outcome (Griffanti et al., 2017), it is time consuming, it requires trained researchers, and the result is dependent on the observer. For this reason, different approaches for automatic classification of ICA components have been proposed in time, from full classifiers (FIX, Salimi-Khorshidi et al., 2014) to approaches specifically targeting motion artefacts (ICA-AROMA, Pruim, Mennes, Buitelaar & Beckmann, 2015; Pruim, Mennes, Rooij et al., 2015).

Alternatively, decomposing the signal of white matter (WM) and cerebrospinal fluid (CSF) into principal components and considering the first few (a technique called anatomical CompCor, see Behzadi et al., 2007) can help retrieving proxies of motion-related artefacts and physiological fluctuations (Behzadi et al., 2007; Muschelli et al., 2014). In fact, it has been shown that CompCor can be more effective in denoising motion artefacts than ICA based techniques and censoring (Mascali et al., 2021).

Noise in fMRI can also be reduced by using Multi-Echo (ME) acquisitions that sample the data at multiple successive echo times (TE). A weighted combination of the multiple echoes based on each voxel's T_2^* value (Posse et al., 1999) or temporal signal-to-noise

ratio (Poser et al., 2006) can smear out random noise and enhance the sensitivity to the BOLD contrast. In fact, compared with single-echo data, this optimal combination can improve the mapping of neuronal activity at 3 Tesla (Fernandez, Leuchs, Sämann, Czisch & Spoormaker, 2017) and 7T (Puckett et al., 2018), with results comparable to other preprocessing techniques requiring extra data such as RETROICOR (Atwi et al., 2018). Optimal combination of multiple echo volumes can also improve sensitivity, specificity, repeatability and reliability of fMRI mapping (Cohen et al., 2021; Cohen & Wang, 2019).

Furthermore, assuming a monoexponential decay, the voxelwise fMRI signal S acquired at a given echo time TE can be expressed in signal percentage change as:

$$\frac{S - \overline{S}}{\overline{S}} = \Delta\rho - TE \cdot \Delta R_2^\star + n, \tag{1.1}$$

where $\Delta\rho$ represents non-BOLD related changes in the net magnetisation, $\Delta R_2^\star$ represents BOLD-related susceptibility changes (and is the inverse of $\Delta T_2^\star$), and n denotes random noise (Kundu et al., 2013; Kundu et al., 2012). As the BOLD-related signal can be expressed as a function of the TE, whereas noise-related non-BOLD changes in the net magnetization are independent of TE, the information available in multiple echoes can be leveraged for the purpose of denoising. For example, in a dual-echo acquisition where the first TE is sufficiently short, the first echo signal mainly captures changes in $\Delta\rho$ rather than in $\Delta R_2^\star$. It is then possible to remove artefactual effects, through voxelwise regression, from the second echo signal acquired at a longer TE with appropriate BOLD contrast (Bright & Murphy, 2013b).

Collecting more echoes opens up the possibility to leverage ICA and automatically classifying independent components into BOLD-related (i.e. describing $\Delta R_2^\star$ fluctuations with a linear TE-dependency) or noise (i.e. independent of TE, related to non-BOLD fluctuations in the net magnetization $\Delta\rho$), an approach known as ME independent component analysis (ME-ICA, Kundu et al., 2013; Kundu et al., 2012; Kundu et al., 2017). Compared to single-echo data denoising, ME-ICA can improve the mapping of task-induced activation (DuPre et al., 2016; Gonzalez-Castillo et al., 2016; Lombardo et al., 2016), for example in challenging paradigms with slow-varying stimuli (Evans et al., 2015) or language mapping and laterality (Amemiya et al., 2019). It also outperforms single-echo ICA-based denoising of resting-state fMRI data (Dipasquale et al., 2017; Lynch et al., 2020), and provide more efficient and reliable functional connectivity mapping in individual subjects (Lynch et al., 2020) and in brain regions where traditional single-echo acquisitions offer reduced signal-to-noise ratio, such as the basal forebrain (Markello et al., 2018). Finally, ME-ICA also enhances the deconvolution of neuronal-related signal changes (Caballero-Gaudes et al., 2019).

1.3.2 Physiological noise

When BOLD fMRI is used as an intrinsic contrast and the interest is in the neural correlates, the neurovascular coupling should possibly be *uncoupled*. To this purpose, physiological signals become noise, and it is necessary to model them so that their associated variance in the fMRI signal is accounted for and minimized during preprocessing or data analyses (Caballero-Gaudes & Reynolds, 2017; Liu, 2016). The principal frequencies characterising physiological signals like cardiac pulse and respiration are in a different band compared to those of the neural-related BOLD signal: namely, the primary component of cardiac related fluctuations are around 1 Hz, while the respiratory related ones are around 0.3 Hz. Thus, if the temporal sampling is high enough, a simple band-pass filter could easily remove their confounding effects (Biswal et al., 1995; Chuang & Chen, 2001; Lowe, Mock &

Sorenson, 1998). The downside is that this approach will remove the BOLD-related signal frequencies in the same range as well, and it will not remove the impact of physiological frequencies in the same range as the BOLD signal (Caballero-Gaudes & Reynolds, 2017). This is especially true if the temporal sampling is low and the physiological signal is aliased in the BOLD-related frequency range. Moreover, physiological signal, and respiration in particular, has an impact on other sources of noise, like magnetic field perturbation (Raj, Anderson & Gore, 2001), and motion (Fair et al., 2020; Pais-Roldán, Biswal, Scheffler & Yu, 2018; Power, Lynch et al., 2019) that should be taken into account and removed (Gratton et al., 2020).

An easy way to remove such perturbations is to remove the average brain signal (also called global signal), since it is often considered as a proxy of the combined impact of different sources of noise, especially related to movement or physiological in nature. However, its removal is controversial, since it can heavily alter the interpretation of BOLD fMRI (Power, Plitt, Laumann & Martin, 2017). For this reason, Power et al. (2018) proposed to decompose fMRI data in low and high rank components, and to consider the first few low rank components timeseries as noise. This technique, called GODEC, showed improved denoising of fMRI data after ME-ICA (Power et al., 2018; Zhou & Tao, 2011).

As a slightly more advanced alternative, the average signal in the white matter (WM) and cerebrospinal fluid (CSF) can be used as a proxy of physiological noise, since no neural-related signal is present in these tissues, that are conversely dominated by cardiac pulsatility and respiration (Anderson et al., 2011; Jo, Saad, Simmons, Milbury & Cox, 2010), although more recently Attarpour, Ward and Chen (2021) showed that the average CSF does not represent cardiac fluctuations properly. However, decomposing the signal of these two tissues into principal component with CompCor can retrieve more accurate physiological proxies (Behzadi et al., 2007). Similarly, ICA based decomposition can be specifically set up to retrieve physiological-related signals, both in space (CORSICA, Perlbarg et al., 2007) and in time (PESTICA, Beall & Lowe, 2007).

An alternative to data-driven approaches consists in acquiring physiological signals such as cardiac pulse and respiration effort during the imaging session, opening up the possibility to adopt more model-based approaches to deal with physiological noise. For instance, it is possible to estimate the frequencies of the amplitude envelope of cardiac and respiratory signals, and then selectively filter them from fMRI data (Biswal, DeYoe & Hyde, 1996). Alternatively, it is possible to use the measured cardiac and respiratory signals to model their periodic fluctuation. Cardiac and respiratory phases can be estimated from signal recordings, then their Fourier expansion can be removed from the data in a slice-dependent manner at the beginning of the preprocessing (RETROICOR, Glover, Li & Ress, 2000). However, RETROICOR does not remove completely the effect of physiological signal from the data, especially regional low frequency effects that vary between brain regions (Birn, Diamond, Smith & Bandettini, 2006; Chang, Cunningham & Glover, 2009; Shmueli et al., 2007).

Noticeably, variations in the heart rate (HR, Shmueli et al., 2007) and the respiration volume per time (RVT, Birn et al., 2006) have been applied successfully to denoise BOLD signal from physiological fluctuations after RETROICOR, especially when convolved with a modelled response function, cardiac (Chang et al., 2009) or respiratory (Birn, Smith, Jones & Bandettini, 2008). Various alternatives to RVT to improve breathing-related denoising have been proposed, either to simplify their calculation, that is normally based on the peak detection in the respiratory signal, or to improve the detection of particular changes in the respiratory signal. For instance, Chang and Glover (2009) proposed to simply use the standard deviation of the respiratory signal, avoiding the peak detection. Power et al.

(2018) suggested to compute the standard deviation of the respiratory envelope in small windows to be more susceptible to breathing changes. More recently, Harrison et al. (2021) showed that applying an Hilbert transform to compute RVT improves the characterisations of breathing rhythms and the detection of deep breaths. Although the regions impacted by slow variations in cardiac rate and breathing patterns frequently overlap (Chang et al., 2009; Kassinopoulos & Mitsis, 2019), HR and RVT regressor can be used together for better performance (Chang et al., 2009).

Another physiological confound related to RVT consists in spontaneous CO_2 fluctuations, called *poikilocapnia*. These fluctuations, that have been corroborated with Transcranial Doppler ultrasound (TCD), are related to low frequency fluctuations in the BOLD signal, and if not accounted for they can induce a bias in the signal estimation in up to a fifth of the cortex (Wise, Ide, Poulin & Tracey, 2004). The pattern of biases induced by poikilocapnia has been found comparable to that of RVT (Chang & Glover, 2009), although accounting for the latter is not sufficient to explain all the variability induced by the former (Golestani, Chang, Kwinta, Khatamian & Jean Chen, 2015). However, the fact that BOLD signal is susceptible to CO_2 fluctuations can be conversely seen as an advantage, and used to image cerebral physiology.

1.4 Cerebrovascular Reactivity Mapping

The fact that BOLD signal is substantially a physiological measurement, susceptible to changes in blood vessels, opens up the possibility of using it to image vascular mechanisms. One of such mechanisms is the ability to react to vasoactive stimuli, the so called Cerebrovascular Reactivity (CVR). In practice, when there is a decompensation of certain elements in the blood stream, such as CO_2, the pH changes. This will activate chemical receptors in the walls of the vessels that will in turn relax or constrict the vascular smooth muscles. Such change will adapt the internal calibre of the vessel, changing cerebral blood flow to maintain the homoeostasis of O_2. For instance, a high level of CO_2, called hypercapnia, will results in a decrease in pH due to the dissociation of CO_2 and H_2O into protons and ions of bicarbonate (H^+ and HCO_3^-), becoming a vasodilatory stimulus. The vascular muscles will relax as a response, increasing cerebral blood flow to provide sufficient O_2 to the surrounding tissues (Liu, De Vis & Lu, 2018) (see Figure 1.3). This increase in HbO results in a global increase in the BOLD signal as well.

This mechanism can be leveraged to measure CVR in experimental and clinical settings. In fact, the potential of BOLD-fMRI based CVR estimation as a diagnostic measure has been ascertained in different diseases, spanning from vascular diseases (e.g. Hartkamp, Bokkers, van Osch, de Borst & Hendrikse, 2017; Markus & Cullinane, 2001; Webster et al., 1995; Ziyeh et al., 2005), to stroke and aphasia (e.g. Krainik, Hund-Georgiadis, Zysset & Von Cramon, 2005; Van Oers et al., 2018), brain tumours (e.g. Fierstra et al., 2018; Zacà, Jovicich, Nadar, Voyvodic & Pillai, 2014), neurodegenerative diseases (e.g. Camargo et al., 2015; Glodzik, Randall, Rusinek & de Leon, 2013; Marshall et al., 2014), hypertension (e.g. Iadecola & Davisson, 2008; Leoni et al., 2011; Tchistiakova, Anderson, Greenwood & Macintosh, 2014), lifestyle habits (e.g. Friedman et al., 2008; Gonzales et al., 2014), sleep apnoea (e.g. Buterbaugh et al., 2015; Prilipko, Huynh, Thomason, Kushida & Guilleminault, 2014), and traumatic brain injury or concussions (e.g. Churchill, Hutchison, Graham & Schweizer, 2020; Markus & Cullinane, 2001).

One way to estimate CVR during BOLD-fMRI is by injection of acetazolamide, a chemical compound that decreases the pH in the vessels and elicits a vasodilatory response using in a similar way to hypercapnia (Settakis, Molnár et al., 2003; Vorstrup, Brun & Lassen, 1986). Acetazolamide injection can be easily performed, even with non-cooperating

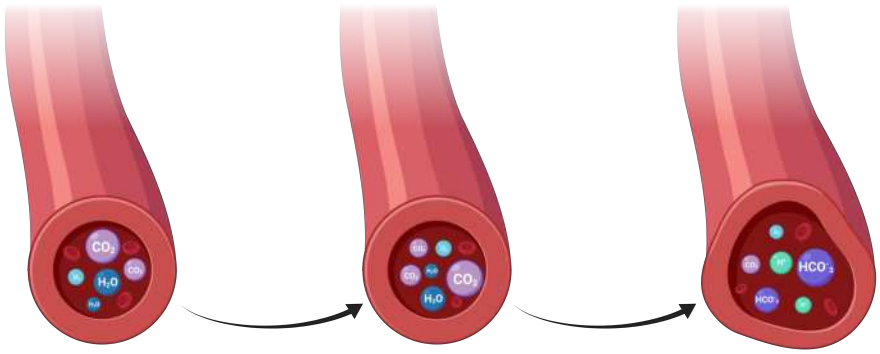

Figure 1.3: Representation of CVR responses. When the levels of CO_2 in the bloodstream increase, and the CO_2 and H_2O dissociate into protons and ions of bicarbonate (H^+ and HCO_3^-), the vessels dilate to provide more oxygen to the surrounding tissues. Note that the representation is a simplification of the content of the blood stream and the state of water and gas molecules (that are both free and bound to haemoglobin).

subjects, and it is a safe procedure (Fierstra et al., 2013). However, the high inter-subject response variability that reduces measurement reproducibility, its side effects, albeit mild, and overall its invasiveness limit its widespread use as a vasodilatory stimulus, particularly in experiments with healthy subjects (Fierstra et al., 2013).

Another option is to ask subjects to undergo a gas challenge, i.e. breathing air with a higher concentration of CO_2 than normal room environment at regular intervals, during which the subject is induced into temporary hypercapnia. The gas flow of the inspired air can be controlled manually by an operator or mechanically by a computerised system, while the pressure of gasses in the expired air can be recorded using a capnograph monitor, obtaining a measurement of the pressure of the (expired) end-tidal CO_2 ($P_{ET}CO_2$, Liu, De Vis & Lu, 2018). $P_{ET}CO_2$ is a close approximation of the pressure of the alveolar CO_2 (McSwain et al., 2010; Peebles et al., 2007; Sullivan, Kissoon & Goodwin, 2005), the real vasoactive stimulus, and despite being lower than the latter, it is also a non-invasive measurement, making it more suitable to estimate CVR in clinical and research settings. Hence, by comparing the increase in $P_{ET}CO_2$ to the changes in the BOLD signal, it is possible to obtain a quantitative, non-invasive, whole-brain measurement of CVR that is comparable to acetazolamide induced CVR (Gooskens et al., 2003; Markus & Harrison, 1992; Ringelstein, Van Eyck & Mertens, 1992).

While gas challenges are considered the non-invasive golden standard for CVR assessment, the need of specific materials and settings makes it more difficult to be broadly adapted (Pinto et al., 2021). Moreover, some subjects might present lower tolerance to the apparatus (e.g. face masks) or to the challenge itself, potentially experiencing anxiety or dizziness and thus biasing the CVR measurement (Urback, MacIntosh & Goldstein, 2017). A close alternative to gas challenges are respiratory challenges such as cued deep breathing (CDB) and Breath-Holding (BH). These challenges consist in inducing the subject into paced breathing patterns, causing changes in the percentage of CO_2 present in the blood.

A BH paradigm mainly consists in a period of apnoea concluded by either an inspiration or an exhalation followed by a period of normal breathing (Ratnatunga & Adiseshiah, 1990). It is possible to add one or more cycles of paced breathing before the apnoea as well. Due to the broad adoption of BH, different paradigms have been proposed, mainly varying for the length of the apnoea, the presence of paced breathing before the apnoea and the apnoea being followed by an exhalation or an inhalation. However, the recommended

paradigm for compliant subjects seems to consist of a paced breathing, followed by 15-20 seconds of apnoea ended by an exhalation, and a final period of self-paced recovery. With this paradigm, the variability of baseline CO_2 is minimised and the $P_{ET}CO_2$ response shape is simple and close to reach its limit (Pinto et al., 2021). BH paradigms can be successfully implemented in studies that include young children, elderly people and other groups of less cooperative subjects (Handwerker et al., 2007; Kannurpatti et al., 2010; Raut et al., 2016; Riecker et al., 2003; Thomas et al., 2013; Thomason et al., 2005), and they offer robust CVR measurements even when subjects are not able to hold their breath for as long as instructed (Bright & Murphy, 2013a). Moreover, they provide reliable results in the short and long term (Peng et al., 2019), both in terms of spatial reliability (i.e. comparing variability of voxels across multiple sessions in one subject) and general reliability (i.e. average CVR value across sessions and within subjects) (Lipp et al., 2015; Magon et al., 2009)), in a comparable way to gas challenges (Dengel et al., 2017; Evanoff et al., 2020; Leung, Kim & Kassner, 2016).

Conversely, CDB paradigms consists in successive cued deep breaths (typically two), lasting approximately 4 seconds each, followed by a few seconds of normal breathing. This is a very easy task for subjects that causes a mild and transient state of hypocapnia, a drop in CO_2, that despite being the opposite mechanism to BH, produces similarly reliable and comparable CVR estimations to BH (Bright et al., 2009; Sousa et al., 2014; Stickland et al., 2021).

Independently from the paradigm, it has been repeatedly shown that BH-induced CVR estimates are similar to CO_2 based CVR estimates (Biswal, Kannurpatti & Rypma, 2007; Bright et al., 2009; Kannurpatti & Biswal, 2008; Kastrup, Krüger, Neumann-Haefelin & Moseley, 2001; Tancredi & Hoge, 2013). Since they require a less complex (if any) set-up than gas challenges, and cause less discomfort in subjects, respiratory challenges can be easily implemented in research and clinical routines, offering a valid alternative to CO_2 challenges (Bright et al., 2009; Urback et al., 2017).

An even less invasive alternative to gas challenges consists in measuring poikilocapnia during a RS scan. If the $P_{ET}CO_2$ is recorded, and there is sufficient variability in the signal, it can be used to obtain a map of CVR (Chang & Glover, 2009; Wise et al., 2004) in a similar manner to respiratory challenges, although the latter family of techniques results in more reliable CVR estimations (Lipp et al., 2015). If it is not possible to record the $P_{ET}CO_2$, a qualitative CVR estimation can still be attempted, using the average signal of specific frequency bands (Liu, Li et al., 2017) or of specific tissues (e.g. the cerebrospinal fluid, see Jahanian et al., 2017). The advantage of this latter approach, besides its easy implementation, consists in the fact that while the sampling rate of $P_{ET}CO_2$ is de facto limited by the breathing rate, corresponding to the amplitude envelope of the CO_2 signal, the average BOLD signal will always be susceptible to faster fluctuations up to the sampling rate of the BOLD signal itself (Liu, Li et al., 2017). However, it is important to notice that while the two techniques produce estimations that are significantly correlated, the average signal is still characterised by neural component that cannot be estimated and treated as noise, and not using $P_{ET}CO_2$ will not allow a quantitative estimation of CVR. Moreover, it will not allow a precise estimation of the haemodynamic lag of CVR, although prepending few minutes of respiratory challenges to a RS scan can introduce enough variability to improve such estimation (Stickland et al., 2021).

The estimation of CVR through $P_{ET}CO_2$ fluctuations has been found to be similar to both RSFA (Kannurpatti & Biswal, 2008; Kannurpatti et al., 2014; Wang et al., 2019) and f/ALFF (De Vis et al., 2018; Golestani et al., 2016), at least in healthy subjects (De Vis et al., 2018). Interestingly, RS fluctuations have also been previously used to assess

intrinsic brain fluctuations that matched tIA, for instance matching working memory (Zou et al., 2013) and executive functions (Flanker task, see Mennes et al., 2011). Moreover, RS fluctuations have been used to rescale the amplitude of tIA in order to account for vascular effects (Kazan et al., 2016). These findings, as well as the impact that physiological signals can have on functional connectivity and RS fluctuations, might indicate that physiological fluctuations and CVR could actually constitute the basis or otherwise model the relationship between RS and tIA, indicating that at least part of what has been attributed to intrinsic brain patterns could actually be explained by stable physiological and vascular factors, such as CVR.

1.5 Introduction to the chapters and aim of the studies

For this reason, the aim of this work is not only to improve CVR estimation, but also to understand how cerebrovascular reactivity can impact the relationship between RS and tIA. In the following chapter, I will introduce the dataset built to investigate such impact. Following the model of dense mapping datasets, this dataset, named EuskalIBUR, features ten subjects undergoing ten sessions of BOLD-fMRI recordings, while performing a motor task, a Simon task, a Pinel functional localiser task, and a BH challenge, or being in a state of rest. Besides explaining the acquisition per sé and the methods of estimation of CVR maps, RS fluctuations, and task responses, the reliability of all tIA contrasts and RS will be tested, and the group-level responses for each task, besides the BH, will be estimated.

Since CVR does not happen simultaneously across the brain, taking into account local variation in the delay of the response can be a great advantage for CVR estimation. Chapter 3 will feature a technique to estimate voxelwise quantitative maps of BH-induced CVR by taking into account its haemodynamic lag, and will show how this technique outperforms CVR maps that are not optimised for spatial variability of the response delay. I will also show how simultaneously estimating both CVR and the impact of motion can improve CVR imaging compared to a sequential approach where the impact of motion (and other nuisances) is removed from the BOLD signal beforehand.

Then, to further explore methods for CVR mapping denoising, I will take into account the impact of ME-fMRI and ICA denoising on CVR in Chapter 4. The optimal combination of ME-fMRI signal will be compared to traditional approaches (namely, SE-fMRI) in terms of motion removal and reliability. Various denoising techniques based on ME-ICA denoising will also be considered to find what is the best balance between aggressivity in removing the noise and conservativity in maintaining the signal of interest.

In order to understand which individual effects can introduce spatial biases in CVR mapping, the impact of blood pressure will be studied in Chapter 5, in particular the effect of mean arterial pressure and pulse pressure over CVR and its lag. A Linear Mixed Effect model will be used to study the relationship between mean arterial pressure, pulse pressure, and cardiac pulse. Since previous literature reports an effect of sex, this variable will be taken into account in the model, as well as its interaction with the other variables. This relationship will be studied at the average grey matter level, as well as at the voxelwise level, in order to understand if different cerebral regions respond to changes of pressure and pulse in different ways.

Finally, Chapter 6 will be dedicated to study the impact of CVR on RS fluctuations and various tIA maps. First, the relationship between CVR and each metric of RS fluctuations (RSFA, ALFF, and fALFF) will be analysed both at the average grey matter level, as well as voxelwise. Then, the tIA associated to the motor task and the Simon task will be taken into account, in order to compare a higher cognitive level task and a simpler task.

2. Data acquisition: EuskalIBUR dataset

In 2012, Poldrack and colleagues, inspired by the *Quantified Self* movement and by the fruitful application of a similar approach in other fields of science (such as genomics, see Chen, Mias et al., 2012), started acquiring data from one individual (himself) twice a week for over a year and a half (Poldrack et al., 2015). Not too much time after, Gordon et al. (2017) created the Midnight Scan Club, a dataset of ten individuals undergoing twelve sessions of MRI composed by 30 minutes of RS and a motor, an incidental memory, a spatial coherence discrimination, and a semantic discrimination tasks. Around the same time Braga and Buckner (2017) started a similar collection of more than 30 sessions of RS, N-back working memory, and visuomotor tasks on two individuals. Challenging the common approach to MRI data acquisition by having few subjects undergo many scan hours, these datasets started a paradigm shift in cognitive neuroscience. In fact, this approach, called precision functional mapping or dense mapping (DM), started shifting the object of cognitive neuroscience's explanatory focus, from *any* brain to any *one* brain (Naselaris et al., 2021) in great detail.

DM presents many advantages compared to traditional group-based data acquisition. On the one hand, it makes subject recruitment easier and more adaptable to particular scanner access times (Gordon et al., 2017). On the other hand, it solves the problem of undersized experimental groups since the total amount of hours of data is higher than the common number of hours in a single session study (Naselaris et al., 2021; Poldrack, 2021). Moreover, DM can be seen as an extension of repeated measures (or test-retest) acquisitions, allowing improved estimation of the stability of neural activation and functional connectivity (Laumann et al., 2015; Lynch et al., 2020), functional network dynamics (Gratton et al., 2018) and interactions (Gordon et al., 2018), and how this stability is related to behaviour (Seitzman et al., 2019). It also serves as a perfect use-case to validate the reliability of analysis methods and pipelines (Fedorenko, 2021), for instance the estimation of cardiac signal from fMRI data (Aslan, Hocke, Schwarz & Frederick, 2019), and machine learning techniques (Hinrich et al., 2017; Huang et al., 2019). Conversely, it can open the possibility of studying variations in brain patterns over time (Shine et al., 2016), for in-

stance due to functional reconfiguration (Salehi et al., 2020), brain plasticity (Newbold & Dosenbach, 2021; Newbold et al., 2020), surprise and novelty (Betzel et al., 2017), or the effect of the endocrine system during the menstrual cycle (Arélin et al., 2015; Barth et al., 2016; Pritschet et al., 2020; Pritschet et al., 2021). In the past, DM also helped establish the impact of food and caffeine intake on functional connectivity (Poldrack et al., 2015), and on vasculature-related effects in RS (Yang et al., 2019).

Most of all, DM is the perfect data acquisition to explore individual idiosyncrasies, albeit the study of individual traits has been successfully carried out at the group level. For example, using the Human Connectome Project (Glasser et al., 2016), Finn et al. (2015) demonstrated that functional connectivity has individual characteristics that are independent from the type of task that the subject is carrying out, and can be discerned from other subjects See also, Finn et al. (2017). Using the same dataset, Bolton et al. (2020) showed that some subjects demonstrate idiosyncratic motion behaviour linked to behavioural and cognitive characteristics of the individual. Despite these individual-specific observations obtained from large populations datasets, DM specifically allows to understand whether the knowledge gathered from group analyses truly stands at the individual level, or if the latter can provide further insights into the brain structure and function (Fedorenko, 2021). For instance, Braga and colleagues showed how the default mode network (DMN), frequently reported in group analysis, is actually separated into two distinct, adjacent but not overlapping networks (Braga & Buckner, 2017), confirming this discovery with multiple data analyses (Braga, Van Dijk, Polimeni, Eldaief & Buckner, 2019), tracing a link with cognitive constructs (such as the theory of mind DiNicola, Braga & Buckner, 2020), and proposing interspecies similarities (Braga et al., 2019; Buckner & DiNicola, 2019). DMN sub-networks have been confirmed independently, finding up to 9 sub-networks interacting differently with other networks (Gordon et al., 2020). The sub-network organisation expands to other networks, such as the motor one, that was found to be multiple nested networks that match with the motor functional organisation from other species (Du & Buckner, 2021). Furthermore, DM allowed to improve the distinction of network variants (Gilmore, Nelson & McDermott, 2021) and the location of networks and functionality in areas characterised by high intersubject variability, such as the cerebellum (Marek et al., 2018; Xue et al., 2021) and the frontal lobe (Marek & Dosenbach, 2018; Smith, Perez, Porter, Dworetsky & Gratton, 2021), leading to new evolutionary models (DiNicola & Buckner, 2021).

DM can be used for clinical experimentation as well, especially in cohort of patients that are under continuous observation. Although longitudinal studies are well known in the clinical practice, DM can improve the observations on pathological variability over time (Lynch, Elbau & Liston, 2021; Poldrack, 2021), and allows personalised treatment and the development of personalised medicine (Chen, Mias et al., 2012; Chen & Snyder, 2012). The demonstration that advanced data acquisition techniques, such as ME-fMRI, can be used to lower the amount of necessary time to obtain reliable DM datasets (Lynch et al., 2020) further increases DM benefits to study psychiatric and neurological investigation and clinical applications (Gratton et al., 2020; Hampel et al., 2018; Padberg et al., 2017). Furthermore, combining DM with ME-fMRI not only ensures higher sensitivity, specificity, repeatability and reliability of fMRI mapping (Cohen et al., 2021; Cohen & Wang, 2019) enables to increase adopt denoising strategies such as ME-ICA (Kundu et al., 2013; Kundu et al., 2012; Kundu et al., 2017) that improve the mapping of task-induced activation (Amemiya et al., 2019; DuPre et al., 2016; Evans et al., 2015; Gonzalez-Castillo et al., 2016; Lombardo et al., 2016) and improves signal-to-noise ratio compared to single-echo acquisitions (Markello et al., 2018).

For these reason, we decided to collect a ME-fMRI based DM dataset to study the questions opened in the previous chapter. Each session includes a BH task and various RS runs to address the impact of CVR and RS fluctuations on tIA, including physiological recordings to quantitatively assess CVR. In order to generalise previous studies on the impact of RS fluctuations on tIA (e.g. Mennes et al., 2011; Zou et al., 2013), two different types of task with different experimental designs and involving different cognitive domains were implemented: a lower cognitive level, sensory, block designed motor task (Buckner et al., 2011) and a higher cognitive level, event related with random ISI designed Simon task (Simon & Rudell, 1967). The different cognitive level and the different design of the task should help ruling out eventual confounding factors related to the design of the task or the cognitive domain and effort involved in each task.

Note that a third type of task was collected for this dataset: an event related with fixed ISI designed Pinel functional localiser task (Pinel et al., 2007), eliciting various cognitive domains. However, the purposes of its collection and use are not in the scopes of this thesis. Hence, its results will be presented in this chapter, but not in further studies.

This chapter will introduce the dataset adopted in all further chapters, focusing on discussing the reliability of the three cognitive tasks and the four RS sessions, and analysing the group results of the contrasts of interest for each task. The reliability of the CVR and lag maps will be discussed in Chapter 4.

2.1 Methods

2.1.1 Participants

Ten healthy subjects with no record of psychiatric or neurological disorders (5F, age range 24-40 years at the start of the study) underwent ten MRI sessions in a 3T Siemens PrismaFit scanner with a 64-channel head coil. Each session took place one week apart, on the same day of the week and at the same time of the day to minimise effects related to circadian rhythms (see e.g. Shannon et al., 2013).

All participants had to meet several further requirements, i.e. being non-smokers and refrain from smoking for the whole duration of the experiment, and not suffering from respiratory or cardiac health issues. They were also instructed to refrain from consuming caffeinated drinks for two hours before the session. Informed consent was obtained before each session, and the study was approved by the local ethics committee.

2.1.2 Biometrics

Before the MRI session, subjects were instructed to lay in a supine position on a cot and relax. After approximately 5 minutes, blood pulse and pressure were measured once on the right arm and once on the left arm, using an OMRON M7 Intelli IT blood pressure monitor. Then, all subjects filled in a questionnaire on sleep and exercise habits, motivation, hydration, and consumption of alcohol, coffee, and liquids, adapted from Gorgolewski et al. (2015).

The original questionnaire (in Spanish) can be found as Appendix A

2.1.3 MRI data

Task instructions were explained before the first session, and then briefly reminded if required before each run took place in every subsequent session. All stimuli and in-task instructions were provided textually throughout the tasks through a mirror screen located in the head coil. All tasks were padded with a 15 seconds resting period to account for physiological signal alignment and/or shift during preprocessing.

Figure 2.1: Typical MRI session

All MRI sessions consisted of four resting state (RS) runs, a motor task (Buckner et al., 2011), a Simon task (Simon & Rudell, 1967), a Pinel functional localiser task (Pinel et al., 2007), a breath-hold (BH) challenge (Bright & Murphy, 2013a), as well as two anatomical images, a T2-weighted Turbo Spin Echo (Hennig, Nauerth & Friedburg, 1986) and a T1-weighted MP2RAGE (Marques et al., 2009) image (see Figure 2.1). Each MRI session began with the acquisition of the T2-weighted Turbo Spin Echo image, while the subjects fixated a cross on the screen or rested with their eyes closed. Next, all fMRI runs took place, always starting with a RS run and followed by the four tasks, which were interleaved by the three other runs of RS. Note that while the BH task always took place last, the order of the other three tasks is counterbalanced between sessions. Finally, the T1-weighted MP2RAGE image was acquired at the end of the session.

Resting State

During each RS run subjects were instructed to fixate a white cross in the middle of a black screen, maintaining the eyes open and staying as still as possible. Each RS run lasted 10 minutes (400 scans).

Motor task

The Motor task was adapted from Buckner et al. (2011). The task consisted in five repetitions of a trial module, including six blocks of 15 seconds each. Each block started with three seconds in which the type of movement to perform was shown as an image, followed by 12 seconds of the movement itself. The six blocks consisted in: (1)moving the tongue in the mouth; (2) touching each finger with the thumb in rapid succession in the right hand; and (3) left hand; (4)moving the toes of the left foot, and (5) right foot, or (6) fixating a star ("sham" condition). Their order was randomly set at each repetition and session (see Figure 2.2). The total duration of the run was 8.5 minutes (340 scans).

Simon task

The Simon task was adapted from Simon and Rudell (1967) (cfr. Hommel, 2011) and from the Flanker task in Mennes, Kelly, Colcombe, Xavier Castellanos and Milham (2013). It consisted of an event related design of 96 stimuli (average ISI = 5s, min ISI = 3s, max ISI = 9s, total duration = 8.5 minutes/340 scans). Each stimulus could be either a green or a red square appearing on the left or on the right of the screen. Subjects were instructed to press a button with the right hand when the red square was presented, and with the left hand when the green square was presented, as fast and exactly as they could (see Figure 2.2). 48 stimuli were congruent (red appearing on the right or green appearing on the left) and 48 were incongruent (red appearing on the left or green appearing on the right). Each response was recorded, taking into account if the response was correct or incorrect.

Pinel functional localiser task

A Pinel functional localiser task was adapted from Pinel et al. (2007) consisting of a rapid event related task with 30 auditory stimuli and 30 visual stimuli (ISI = 3s, min stimulus duration = 1.5s, max stimulus duration = 2.5s, total duration = 8.5 minutes/340 scans). Each group of stimuli was composed of 10 short sentences, 10 subtractions, and 10 motor instructions (press a button three times either with the left or the right hand). In addition,

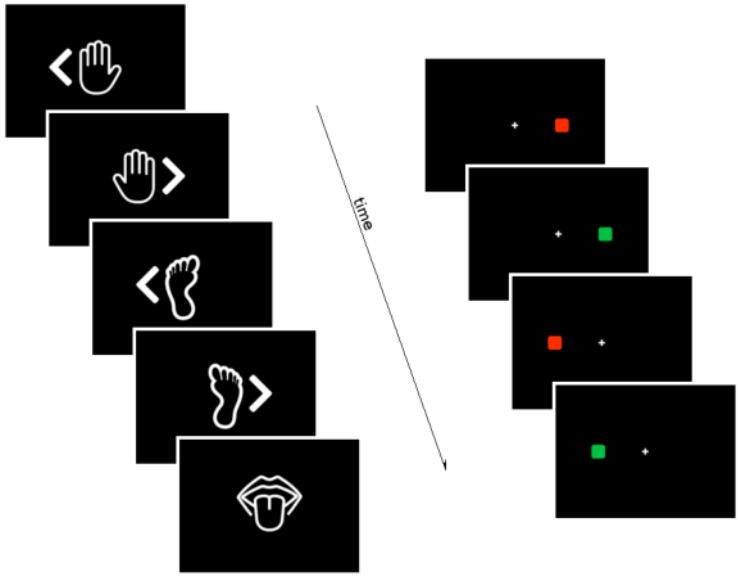

Figure 2.2: Left: stimuli of the Simon task. Right: stimuli of the motor task

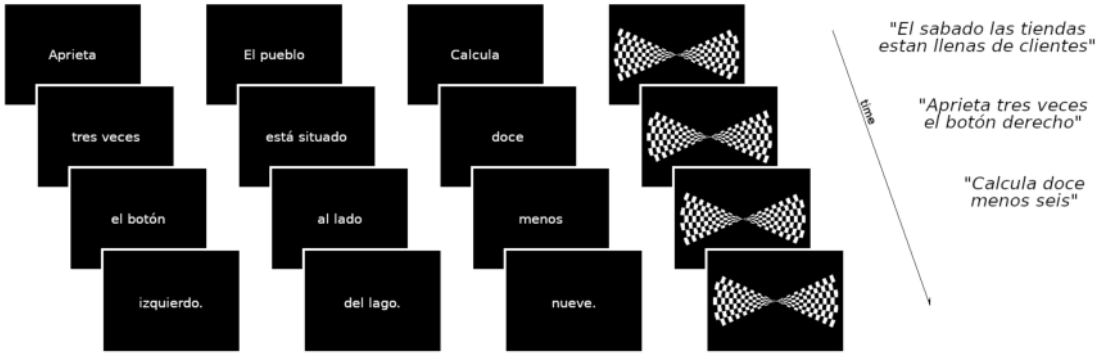

Figure 2.3: Stimuli of the Pinel task (adapted from Pinel et al. (2007))

there were 20 stimuli consisting of flashing chequerboards, oriented either vertically or horizontally (see Figure 2.3).

Breath-Hold task

The BH task followed the paradigm described by Bright and Murphy (2013a). It consisted of eight repetitions of a BH trial composed of four paced breathing cycles of 6 seconds each, an apnoea (BH) period of 20 seconds, an exhalation of 3 seconds, and 11 seconds of "recovery" (unpaced) breathing, for a total trial duration of 58 seconds (Figure 2.4). The total duration of the BH task was 8.5 minutes (340 scans).

Subjects were instructed prior to scanning about the importance of the exhalations preceding and following the apnoea (Pinto et al., 2021). Without these exhalations providing CO_2 measurements, the change in systemic CO_2 levels achieved by each BH cannot be robustly estimated and the CVR (%BOLD/mmHg CO_2 change) cannot be estimated quantitatively.

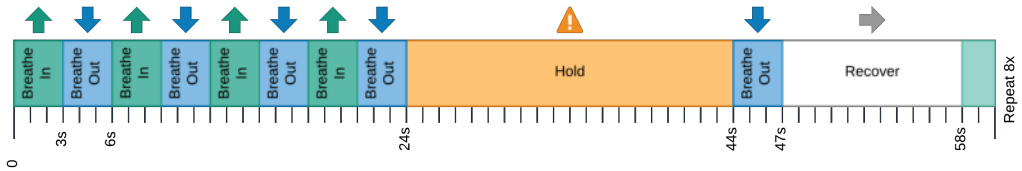

Figure 2.4: Schematic of Breath-Hold trial. Apnoea was preceded and followed by exhalations.

2.1.4 MRI data parameters

All functional MRI data was acquired with a T2*-weighted ME-fMRI data with the simultaneous multislice (a.k.a. multiband, MB) gradient-echo planar imaging sequence provided by the Center for Magnetic Resonance Research (CMRR, Minnesota) (Moeller et al., 2010; Setsompop et al., 2012). While the number of scans for each run was adapted according to the duration of each task, the rest of sequence parameters were identical: TR = 1.5 s, TEs = 10.6/28.69/46.78/64.87/82.96 ms, flip angle = 70°, MB acceleration factor = 4, GRAPPA = 2 with Gradient-echo reference scan, 52 slices with interleaved acquisition, Partial-Fourier = 6/8, FoV = 211x211 mm^2, voxel size = 2.4x2.4x3 mm^3, Phase Encoding = AP, bandwidth=2470 Hz/px, LeakBlock kernel reconstruction (Cauley, Polimeni, Bhat, Wald & Setsompop, 2014) and SENSE coil combination (Sotiropoulos et al., 2013). Single-band reference (SBRef) images were also acquired for each TE. In addition, a pair of Spin Echo echo planar images (EPI) with opposite phase-encoding (AP or PA) directions and identical volume layout (TR = 2920 ms, TE = 28.6 ms, flip angle = 70°) were collected before each functional run in order to be able to estimate field distortions, as suggested in the Human Connectome Project protocol (Glasser et al., 2016).

The T1-weighted MP2RAGE image had the following parameters: TR = 5 s, TE = 2.98 ms, TI1 = 700 ms, TI2 = 2.5 s,, flip angle 1 = 4°, flip angle 2 = 5°, GRAPPA = 3, 176 slices, FoV read = 256 mm, voxel size = 1x1x1 mm^3, TA = 662 s. The T2-weighted Turbo Spin Echo image had the following parameters: TR = 3.39 s, TE = 389 ms, GRAPPA = 2, 176 slices, FoV read = 256 mm, voxel size = 1x1x1 mm^3, TA = 300 s.

All DICOM files of the MRI data were transformed into nifti files with dcm2nii (Li, Morgan, Ashburner, Smith & Rorden, 2016) and formatted into Brain Imaging Data Structure (BIDS, Gorgolewski et al., 2016) with heudiconv (Halchenko et al., 2019).

2.1.5 Physiological parameters

During the fMRI acquisition runs exhaled CO_2 and O_2 levels were monitored and recorded using a nasal cannula (Intersurgical) connected to an ADInstruments ML206 gas analyser unit and transferred to a BIOPAC MP150 physiological monitoring system where scan triggers were simultaneously recorded, as well as cardiac pulse data using a photoplethysmogram (PPG, TSD200 transducer with an PPG100C-MRI amplifier), and respiration effort data (using either a TSD221-MRI or TSD110-MRI with a DA100C module, or a TSD201 transducer with an RSP100C amplifier). All signals were sampled at 10 kHz. The physiological recordings started before and lasted longer than the ME-fMRI data recording to enable the physiological regressors to be shifted, if necessary.

The files exported from the AcqKnowledge software were transformed and formatted into BIDS with phys2bids (phys2bids developers et al., 2019).

2.1.6 Data preprocessing

All MRI data were preprocessed with custom scripts based mainly in FSL (Jenkinson, Beckmann, Behrens, Woolrich & Smith, 2012), AFNI (Cox, 1996), and ANTs (Tustison et al., 2014). In brief, the T2-weighted image was skull-stripped and co-registered to the MP2RAGE image along with the brain mask. The latter was applied to the MP2RAGE image, that was then segmented into grey matter (GM), white matter (WM) and cerebrospinal fluid tissues using Atropos (Avants, Tustison, Wu, Cook & Gee, 2011). The MP2RAGE image was normalised to an asymmetric version of the MNI152 6th generation template at 1 mm resolution (Grabner et al., 2006), while the T2-weighted volume was co-registered to the skull-stripped SBRef of the first echo. The first 10 volumes of the functional data were discarded to allow the signal to achieve a steady state magnetisation. Image realignment to the SBRef was computed using the first echo with MCFLIRT (Jenkinson & Smith, 2001), and the estimated rigid-body spatial transformation was applied to all other echoes. A brain mask from the SBRef volume was obtained and applied to all echoes. The different echo timeseries were optimally combined (OC) voxelwise by weighting each timeseries contribution by its $T_2^\star$ value (Posse et al., 1999) and a ME-based Independent Component Analysis (ICA) was run with tedana (DuPre et al., 2019). A distortion field correction was then performed on the OC volume with Topup (Andersson et al., 2003), using the pair of spin-echo EPI images with reversed phase encoding acquired before the ME-EPI acquisition (Glasser et al., 2016). All fMRI timeseries were smoothed with a gaussian kernel of 5mm at FWHM, except for the BH task data. Finally, the fMRI voxel timeseries were transformed in signal percentage change (SPC).

2.1.7 Data analysis of Motor, Simon and Pinel functional localiser tasks

In order to analyse the functional data of the Motor, Simon and Pinel functional localiser tasks, a general linear model (GLM) was defined using 3dDeconvolve where the design matrix consisted of all task stimuli, the six demeaned realignments parameters and their first derivatives, Legendre polynomials up to the fourth order, and the timeseries of the independent components labelled as noise by ME-ICA (i.e. rejected ICs), after orthogonalisation with respect to the timeseries of the ICs labelled as signal (i.e. good ICs). The GLM was then applied on each voxel timeseries and solved using the Restricted Maximum Likelihood (ReML) estimation method considering an autoregressive moving average with order 1 (i.e. ARMA(1,1)) model of the residuals to find the optimal set of weights for each regressor in the design matrix.

Two different types of GLM analysis were performed: either considering each session independently (i.e. session-specific), and all sessions of the same subject together after temporal concatenation (i.e. subject-specific). The corresponding statistical parametric maps of the contrasts of interest (described below) were thresholded at $p < 0.05$ after correction for multiple comparisons with the False Discovery Rate (FDR) procedure implemented in AFNI (Benjamini, Krieger & Yekutieli, 2006).

Motor task

The following contrasts were modelled:

- tongue vs sham
- right finger vs sham
- left finger vs sham
- right toes vs sham

- left toes vs sham

Simon task

The following contrasts were modelled, considering only the correct responses:

- all congruent stimuli
- all incongruent stimuli
- congruent vs incongruent stimuli
- congruent and incongruent stimuli

In addition, the incorrect responses were modelled separately from the right ones as regressors of non-interest.

Pinel functional localiser task

The following contrasts were modelled:

- visual stimuli
- auditory stimuli
- motor stimuli
- sentences stimuli
- calculus stimuli
- motor vs sentences stimuli
- calculus vs sentences stimuli
- vertical vs horizontal chequerboards
- calculus vs non-calculus, auditory stimuli
- calculus vs non-calculus, visual stimuli
- auditory stimuli vs visual stimuli
- visual stimuli vs chequerboards
- right motor vs left motor

2.1.8 Resting State data analysis

The RS volumes were denoised by orthogonalising them with respect to the six demeaned motion parameters, their first derivative, Legendre polynomials up to the fourth order, and the timeseries of the rejected ICs (after orthogonalisation w.r.t. the timeseries of the good ICs) using 3dTproject. Then, ALFF (Zang et al., 2007, the the power of a specific frequency band, see), fALFF (Zou et al., 2008, the ALFF divided by the power of the full spectrum, see), and RSFA (Kannurpatti & Biswal, 2008, the standard deviation of a specific frequency band of the BOLD signal, see) were computed using 3dRSFC on each run of RS independently in the 0.01-0.1 Hz frequency band:

$$RSFA = \sigma_{t_x} \tag{2.1}$$

$$ALFF = 2 \int_{0.01}^{0.1} S_{xx}(f)\, df \tag{2.2}$$

$$fALFF = \frac{\int_{0.01}^{0.1} S_{xx}(f)\, df}{\int_{0}^{f_{max}} S_{xx}(f)\, df} \tag{2.3}$$

where t_x is the voxel timeseries, f_{max} is the maximum frequency of the data, and S_{xx} is the power spectral density of the band taken into account.

2.1.9 Breath-Hold task, CO_2 trace processing and CVR estimation

The CO_2 timecourse was processed using custom scripts in Python 3.6.7. Briefly, the CO_2 timecourse was downsampled to 40 Hz to reduce computational costs, then the end-tidal peaks were individuated automatically and manually. The amplitude envelope was obtained by linearly interpolating between the end-tidal peaks, then it was demeaned and convolved with a two gamma-variate SPM canonical HRF to obtain the $P_{ET}CO_2 hrf$ trace. In order to account for measurement delay, the $P_{ET}CO_2 hrf$ trace was shifted to maximise the cross-correlation with the average fMRI timecourse of an eroded version of the GM mask (bulk shift, see Yezhuvath, Lewis-Amezcua, Varghese, Xiao & Lu, 2009). A lagged general linear model (GLM) approach was adopted for CVR estimation in order to model temporal offsets between the $P_{ET}CO_2 hrf$ recording and the CVR response across voxels that occur due to measurement and physiological delays (Donahue et al., 2016; Geranmayeh, Wise, Leech & Murphy, 2015; Murphy, Harris & Wise, 2011; Sousa et al., 2014; Tong, Bergethon & Frederick, 2011). Sixty shifted versions of the $P_{ET}CO_2 hrf$ trace were created, ranging between ±9 seconds from the bulk shift, with a shift increment of 0.3 s (fine shift). This temporal range was based on previous literature, which rarely reports haemodynamic lags over ±8 s in healthy individuals (Bright et al., 2009; Donahue et al., 2016; Sousa et al., 2014).

For each shift, a lagged GLM was defined with a design matrix comprised of the shifted $P_{ET}CO_2 hrf$ timecourse as the regressor of interest, the demeaned motion parameters and their first derivative, and the Legendre polynomials up to the fourth order. The rationale and adequacy of this simultaneous lagged GLM model for CVR estimation is described in Chapter 3. The corresponding lagged GLM was fitted via orthogonal least squares using AFNI. Then, the beta coefficient (i.e. weight) of the best fine-shifted $P_{ET}CO_2 hrf$ trace were selected for each voxel, corresponding to the lagged GLM model with maximum coefficient of determination (R^2). Finally, the beta coefficients expressed in BOLD signal percentage change over Volts ($BOLD_{SPC}/V$) were rescaled to be expressed in BOLD percentage over millimetres of mercury (%BOLD/mmHg) as indicated by the gas analyser manufacturer[1], using the formula:

$$CO_2[mmHg] = (P_{atm} - P_{vap})[mmHg] \cdot 10 \cdot CO_2[V]/100[V], \tag{2.4}$$

where $CO_2[V]$ is the original CO_2 timeseries, P_{atm} is the atmospheric pressure in the laboratory at the moment of acquisition, and P_{vap} is the water vapour pressure associated with expired air. The values of $P_{atm} = 759$ and $P_{vap} = 47$ were used for all sessions.

In this way, a lag-optimised CVR map and a t-value map were obtained, together with the associated lag map representing the voxelwise delay from the bulk shift, for each

[1] https://www.adinstruments.com/support/knowledge-base/it-possible-measure-expired-gasses-partial-pressure-mmhg-rather-percentage

analysis pipeline. The CVR and lag maps were thresholded at p <0.05 adjusted with the Šidák correction (Bright, Tench & Murphy, 2017; Šidák, 1967) to account for sixty comparisons computed in the lagged GLM approach (one per regressor), and the voxels that were not statistically significant were excluded. The maps were further thresholded on the basis of the lag: those voxels in which the optimal lag was at or adjacent to the boundary (i.e. ±8.7s) were considered not truly optimised and not physiologically plausible in healthy subjects and therefore masked in all maps.

2.1.10 Group data analysis

One-sample test

In order to assess the statistical significance of the activation maps at the group level, all subject-specific maps of regression coefficients, or general linear contrasts among them, and associated t-statistics computed considering all sessions of the same subject were normalised to the MNI152 template (Grabner et al., 2006, 2.5 mm isotropic voxel resolution), with a nearest neighbour interpolation using ANTs. Then, a one-sample mixed effect meta-analysis using 3dMEMA (Chen, Saad, Nath, Beauchamp & Cox, 2012), that models both within- and across- subjects variability, was computed for each contrast of interest. All results were then thresholded at p <0.05 corrected for FDR (Benjamini et al., 2006) and found all clusters with a minimum size of 20 voxels (276.48 mm^3), considering a neighbourhood of 26 voxels. The same 3dMEMA model was also applied at the subject level, modelling only the within-subject variability, in order to compare such results with the group results.

Session reliability

In order to test the reliability of the results, all of the session-specific contrast, all of the resting state metrics, CVR, and lag maps, as well as the associated t-statistics maps (if any) were normalised to the MNI152 template (Grabner et al., 2006, 2.5mm isotropic voxel resolution), and they were used to compute the intraclass correlation coefficient (ICC). ICC was computed voxelwise using a regularized multilevel mixed effect model in 3dICC (AFNI) in order to take into account the voxelwise standard error of the estimate of the contrast, CVR, and lag maps for each session and run in the ICC estimation (Chen et al., 2018). ICC assesses the reliability of a metric by comparing the intersubject, intrasubject, and total variability of that metric, which is equivalent to:

$$ICC(2,1) \simeq \hat{\rho}_2 = \frac{MS_{subj} - MS_n}{\frac{k}{n}(MS_{sess} - MS_n) + MS_{subj} + (k-1)MS_n} \tag{2.5}$$

where MS_{subj}, MS_{sess}, and MS_n are the mean squares of the effects of subjects, sessions, and residuals respectively, k is the number of sessions and n the number of subjects (Chen et al., 2018; Mcgraw & Wong, 1996; Shrout & Fleiss, 1979). ICC(2,1) was chosen since both subjects and sessions were considered random effects. High ICC scores indicate high reliability, where the intrasubject variability is lower than the intersubject variability, and following the classification given by Cicchetti (2001), an ICC score above 0.75 is considered excellent, between 0.75 and 0.6 good, between 0.6 and 0.4 fair, and below 0.4 poor.

Since 3dICC uses the t-statistic map associated with the estimation of the beta coefficients and the CVR, beta maps were not thresholded, while CVR and lag maps used in this computation were only thresholded on the basis of the lag, and not on the basis of the t-statistic. Note that fALFF does not have an associated t-statistic map, so no error was taken into account.

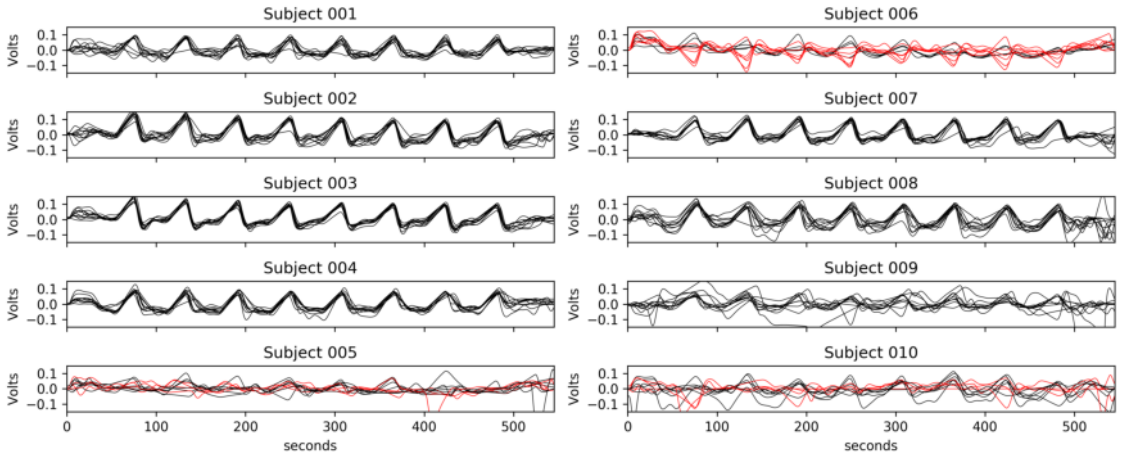

Figure 2.5: $P_{ET}CO_2 hrf$ trace for all subjects and all sessions. Rejected sessions are plotted in red. Rejection was based on having less than three proper $P_{ET}CO_2 hrf$ increases after breathholds or having more $P_{ET}CO_2 hrf$ decreases than increases after breathholds. Note that the first session of subject 10 was lost due to a software malfunction during acquisition.

2.2 Results

As it can be observed in Figure Figure 2.5, out of the ten subjects, subjects 005 (male), 006 (female) and 010 (male) did not perform the BH task correctly in one or more sessions. Therefore, these three subjects were excluded from further analyses for the sake of consistency across the different studies described in this thesis, with the exception of one session of subject 10, that was included in the analysis of Chapter 3

All CVR and lag maps, and related reliability maps, are discussed in more detail in Chapter 4.

2.2.1 Motor task

Figure 2.6 shows the results of the one-sample MEMA test for all motor task contrasts, while Tables B.1, B.3, B.5, B.7, and B.9 in Appendix B report all positive activation clusters and Tables B.2, B.4, B.6, B.8, and B.10 in Appendix B report all negative activation clusters, and Figure 2.8 shows the ICC reliability score of the BOLD activations.

The contrasts related to the tongue movement and to both finger tappings report positive activations in areas correspondent to the expected location in the motor homunculus projection on the cortex, as well as a strong reliability in the same areas. Moreover, they feature reliable subcortical and cerebellar activations that are bilateral (in the case of the tongue) or ipsilateral to the side of the movement. The negative clusters in the orbitofrontal cortex and on the edges of the brain in the contrast of tongue vs sham might be related to susceptibility and head movement artefacts induced by the task.

In both toes movements, there seems to be a small, yet reliable, activation in the cerebellum, ipsilateral to the movement. Despite high reliability values in the areas of the motor cortex associated to toe movements, that also extends to the medial portion of the cortex, there seems to be no group activation in the MEMA maps in those areas.

For comparison, Figure 2.7 shows the results of the MEMA test at the subject level, for a representative subject. Similar activations to the group can be seen, although the expected activations related to the toes movement in the medial motor cortex appear. However, when compared to the other subjects (see Figures B.1 to B.6 in Appendix B), it can be seen how the areas that show high reliability and no significant activation in the

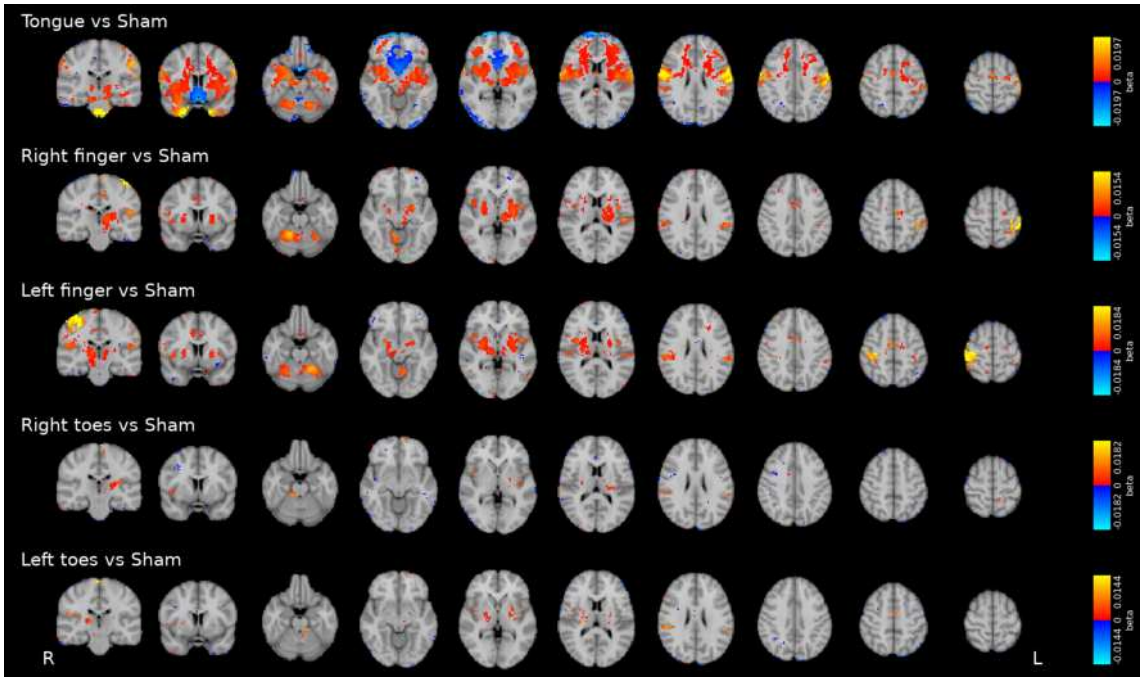

Figure 2.6: Results of the one-sample MEMA test **at the group level** for all contrasts of the motor task ($p < 0.05$, FDR corrected).

group MEMA present high spatial variability between subjects.

2.2.2 Simon task

Figure 2.9 plots the results of the one-sample MEMA test for all Simon task contrasts, while Tables B.11, B.13, and B.15 in Appendix B report all positive activation clusters and Tables B.12, B.14, B.16, and B.17 in Appendix B report all negative activation clusters, and Figure 2.11 shows the ICC reliability score of the activations.

Both congruent and incongruent reactions elicited a widespread and reliable activation across the whole GM and the cerebellum, including, but not limited to, occipital, parietal, temporal, and central lobes and the central core, interesting as well juxtapositional lobule (premotor cortex) and medial frontal cortex. Most of the GM, with the exception of the temporal poles and the orbitofrontal cortex, showed at least fair reliability, with peaks of excellent reliability in the angular gyrus, central pole, and juxtapositional lobule bilaterally, and left superior lateral occipital cortex.

For comparison, Figure 2.10 shows the results of the MEMA test at the subject level, for a representative subject. Similar results to the group level can be seen. Although minor differences between congruent and incongruent reactions can be noticed, the limited amount of difference might explain the lack of significant activations in the congruent vs incongruent contrast. The results of the other subjects are available in Appendix B (see Figures B.7 to B.12).

2.2.3 Pinel functional localiser task

Figure 2.12 depicts the results of the one-sample MEMA test for all Simon task contrasts, while Tables B.18, B.20, B.22, B.24, B.26, B.28, B.30, B.32, B.34, B.36, B.38, and B.40 in Appendix B report all positive activation clusters and Tables B.19, B.21, B.23, B.25, B.27, B.29, B.31, B.33, B.35, B.37, B.39, and B.41 in Appendix B report all negative activation

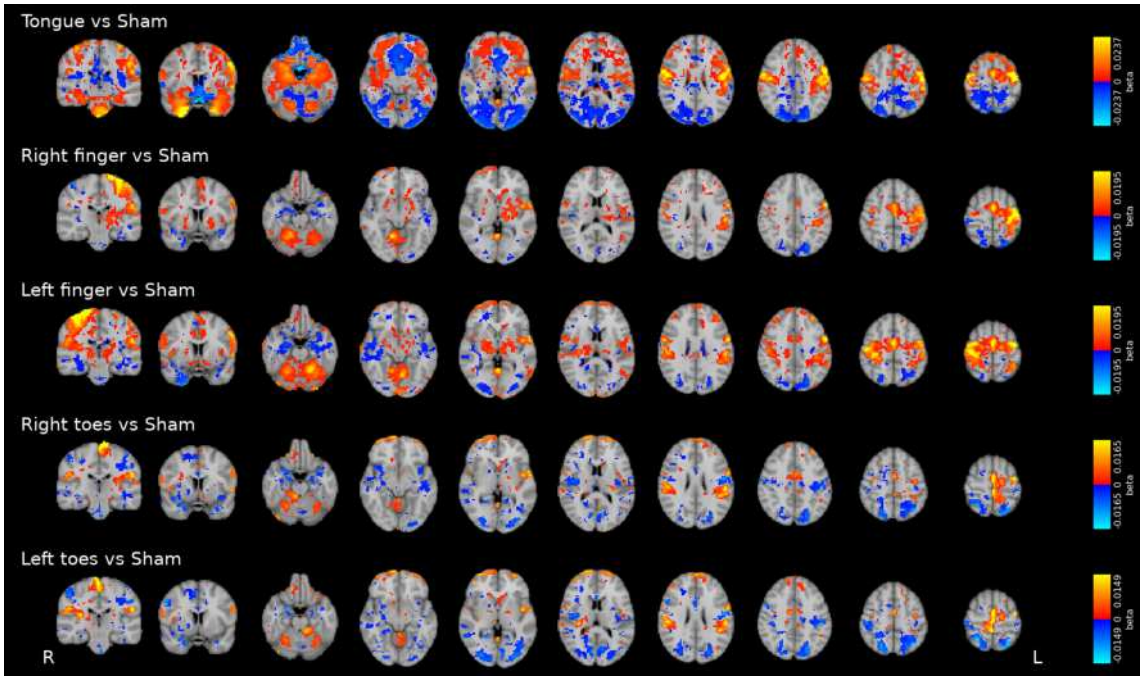

Figure 2.7: Results of the MEMA test **at the subject level**, for a representative subject (subject 007), for all contrasts of the motor task ($p < 0.05$, FDR corrected).

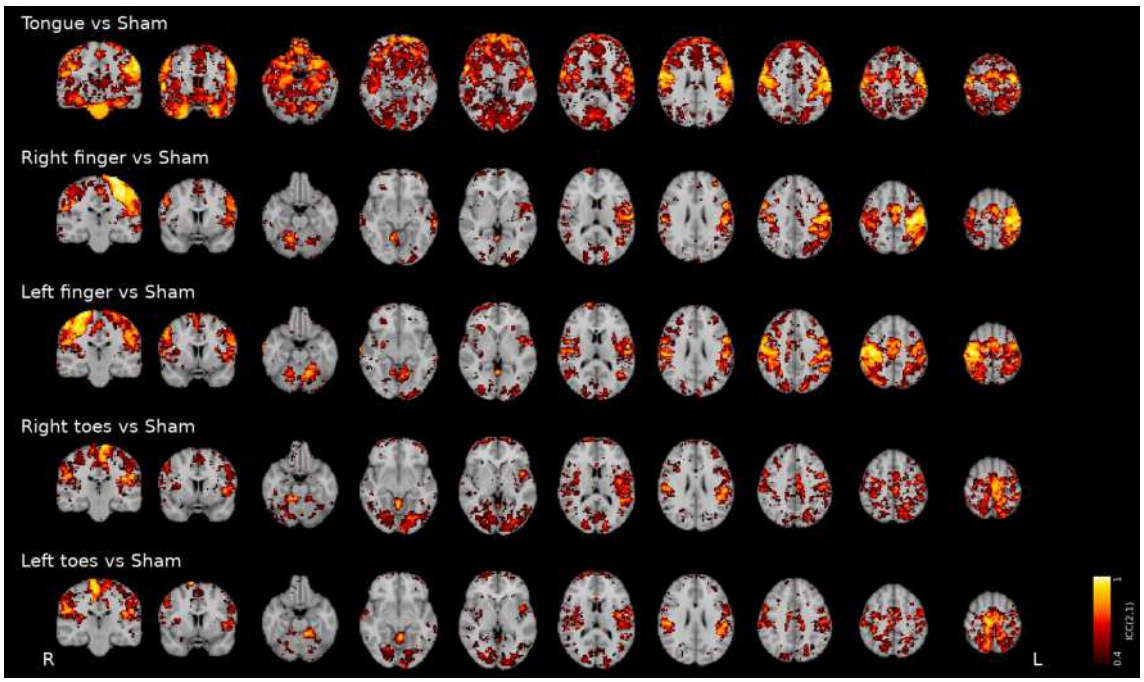

Figure 2.8: ICC(2,1) of all contrasts of the motor task. Maps are thresholded at 0.4, since values lower than that are considered poor reliability (Cicchetti, 2001).

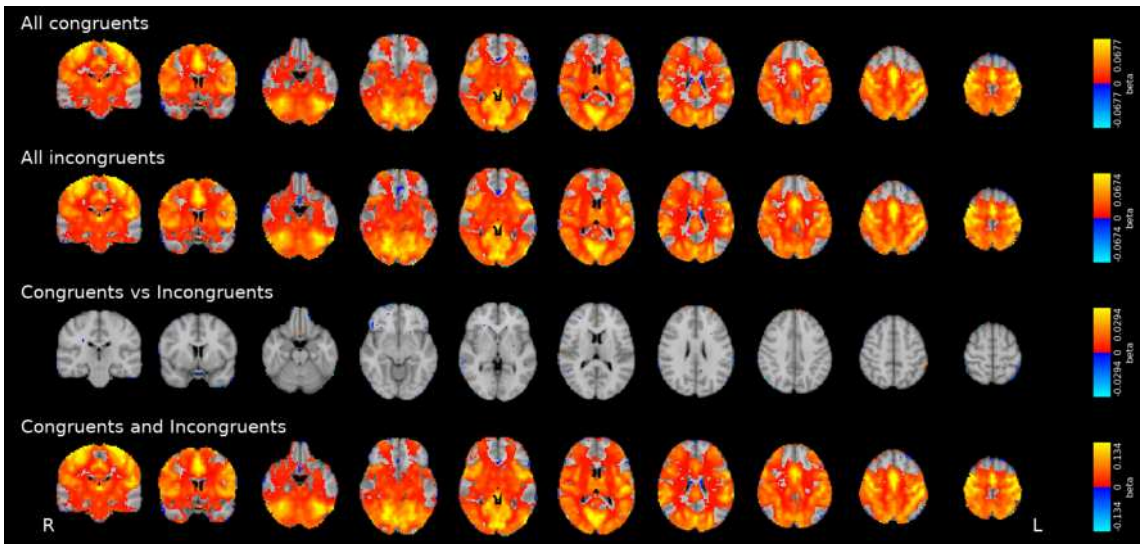

Figure 2.9: Results of the one-sample MEMA test **at the group level** for all contrasts of the Simon task (p <0.05, FDR corrected).

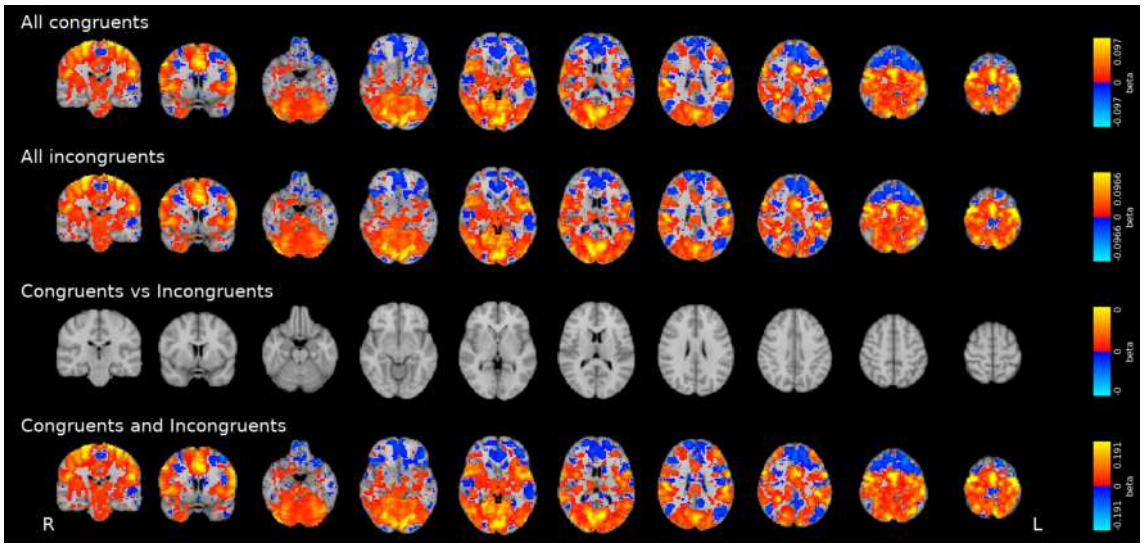

Figure 2.10: Results of the MEMA test **at the subject level**, for a representative subject (subject 007), for all contrasts of the Simon task (p <0.05, FDR corrected).

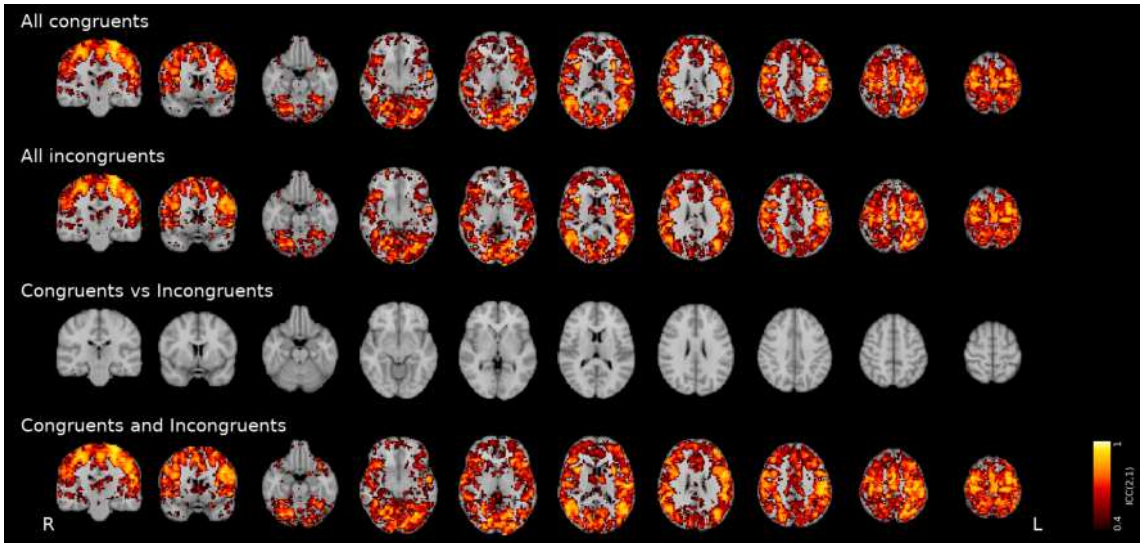

Figure 2.11: ICC(2,1) of all contrasts of the simon task. Maps are thresholded at 0.4, since values lower than that are considered poor reliability (Cicchetti, 2001).

clusters, and Figure 2.14 shows the ICC reliability score of the activations.

Visual stimuli presented a reliable bilateral co-activation of the lateral occipital lobe, as well as the motor cortex and the juxtapositional lobule (premotor cortex). They also presented good reliability in the lateral parietal cortex, and unreliable activations of subcortical areas such as the putamen and the pallidum, as well as in the frontal operculum (bilaterally). Auditory stimuli presented reliable activations in the Heschl's gyrus, as well as in the plani polare and temporale. Interestingly, areas typically associated to language (i.e. left Broca's and Wernicke's areas) showed a reliable, although non significant, activation. Motor stimuli elicited a reliable response in the motor cortices (bilaterally) and in the juxtapositional lobule. While both lateral parietal cortices presented a fairly reliable response, significant response, albeit unreliable, was also found in the cerebellum, in the subcortical areas, as well as in the visual and auditory areas. When modelled together, all sentence stimuli and all calculus stimuli (both visual and auditory) presented reliable activations mainly in the Heschl's gyrus and in the plani polare and temporale. Similarly to auditory responses, the left frontal opercoli and the posterior part of the superior temporal gyrus presented reliable activations. The main difference between sentences and calculus responses is that the activation induced by the latter was also present in subcortical areas and superior cerebellum, and that the reliability of calculus responses was more bilateral than that of sentences. Their contrast presented generally higher reliability and revealed positive activations in most subcortical areas and superior cerebellum, as well as in the superior lateral parietal cortex, in the juxtapositional lobule, and in the medial occipital cortex bilaterally, and negative activations across the planum temporale and frontal pole bilaterally and in the left temporal pole.

Comparing vertical vs horizontal chequerboards did not provide significant results at the group level, although a good to excellent reliability was found in the visual cortex (occipital pole). Comparing motor vs sentence stimuli provided positive activations not only in the areas activated by the motor task, with the exception of good part of the temporal gyrus, but also bilaterally across all of the central core, as well as in the medial occipital cortex and in the superior part of the cerebellum, in the cingulate gyrus, in the precuneous, and in the supramarginal gyrus. Conversely, negative activations were not

found in areas activated by the sentence stimuli, but mainly in the planum polare, in the amygdalae and hippocampi, and in the subcallosal cortex. Most of the GM showed fair reliability, with peaks of excellent reliability mainly in the precentral and postcentral gyri, and in the left temporal pole, frontal opercoli and superior parietal gyri.

Considering the contrast between auditory and visual stimuli, positive activations were found within the plani temporale and polare, the Heschl's gyrus bilaterally, and the intracalcarine sulcus bilaterally, and negative activations were found within the lateral occipital cortex and the lateral superior cerebellum (VI), as well as in the anterior cingulate gyrus, in line with the activations found considering each stimulus type on its own. Moreover, all activations related to the two types of stimuli were found having good to excellent reliability. In the contrast between visual stimuli and chequerboards, positive activity was found in the superior cerebellum, across the central core, in the frontal opercoli, and in the lateral precentral and postcentral gyri as well as in the juxtapositional lobule, while negative activations were found mainly in the lingual gyri and in the frontomedial cortex, as well as in the medial part of the frontal pole. Most of GM was found to be fairly reliable, with excellent reliability found in the occipital, parietal, and central lobes.

The comparison between calculus and non-calculus stimuli, for auditory presentations, revealed negative activations in the Heschl's gyrus and in the planum temporale, as well as in the anterior part of the cerebellum (V) bilaterally. Visual presentations featured the same areas of negative activations, with a stronger amplitude, as well as more negative activations in the postcentral gyrus and in the anterior cingulate gyrus bilaterally, and in the left superior lateral occipital cortex. Parietal, central, and posterior frontal lobes presented fair reliability with peaks of excellent reliability in the supramarginal gyrus.

Finally, in the contrast between right and left motor stimuli, while most of the brain presented negative activations, with a peak in the right motor cortex and left anterior superior cerebellum (I-IV), positive activations were found in the left motor cortex and in the right anterior superior cerebellum (I-IV). These peaks of activations presented good to excellent reliability as well.

For comparison, Figure 2.13 shows the results of the MEMA test at the subject level, for a representative subject. Similar results to the group level can be seen. Although small activations in the visual cortex can be seen in the contrast of vertical vs horizontal chequerboards, the comparison of this subject with all others (see Figures B.13 to B.18 in Appendix B) reveals high inter-subject variability, that could explain the lack of results in the MEMA test at the grup level.

2.2.4 Resting state

Figures 2.15 to 2.17 shows the reliability of the fALFF, ALFF, and RSFA maps respectively for each resting state run. The RSFA and ALFF ICC maps show generally good reliability across most of the brain, with few exceptions in the ventral portion of the brain and in the deep white matter. Some areas of the GM show excellent reliability, in particular the subcallosal cortex and the frontal pole, as well as the middle frontal gyri, the angular gyri, the precuneous, and the brain edges. While areas of excellent reliability seem to remain stable across runs, there appears to be a reduction of reliability in the other areas from the first to the last run, to the point that in the last run areas such as the pallidum and other subcortical structures have poor reliability. The fALFF maps show general good reliability across all brain, and particularly in the GM, although a very high reliability occurs in the subcallosal cortex, frontal pole, and brain edges. Noticeably, these latter areas present a neat separation, in terms of reliability, with the rest of the brain.

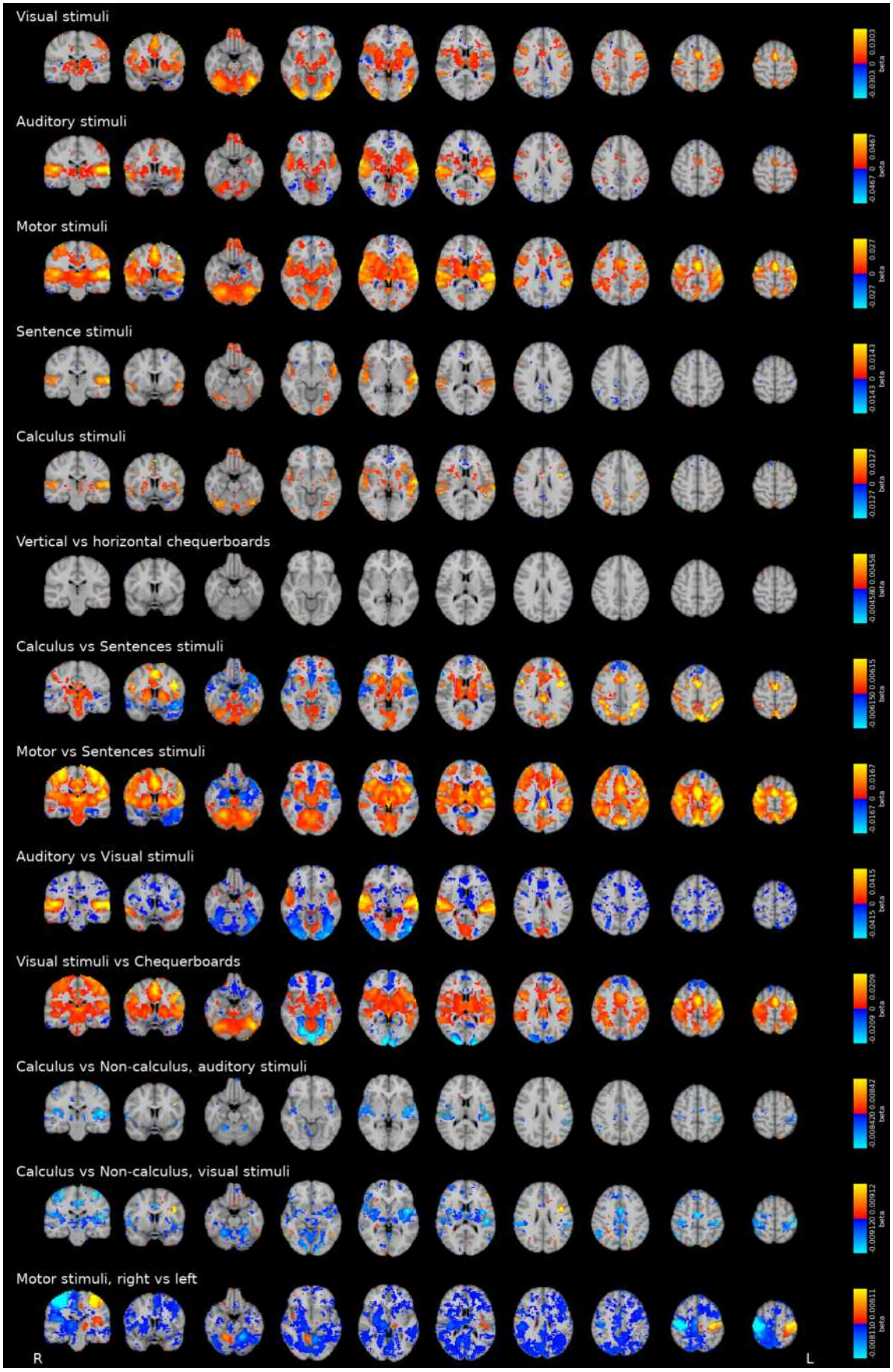

Figure 2.12: Results of the one-sample MEMA test for all contrasts of the pinel task ($p < 0.05$, FDR corrected).

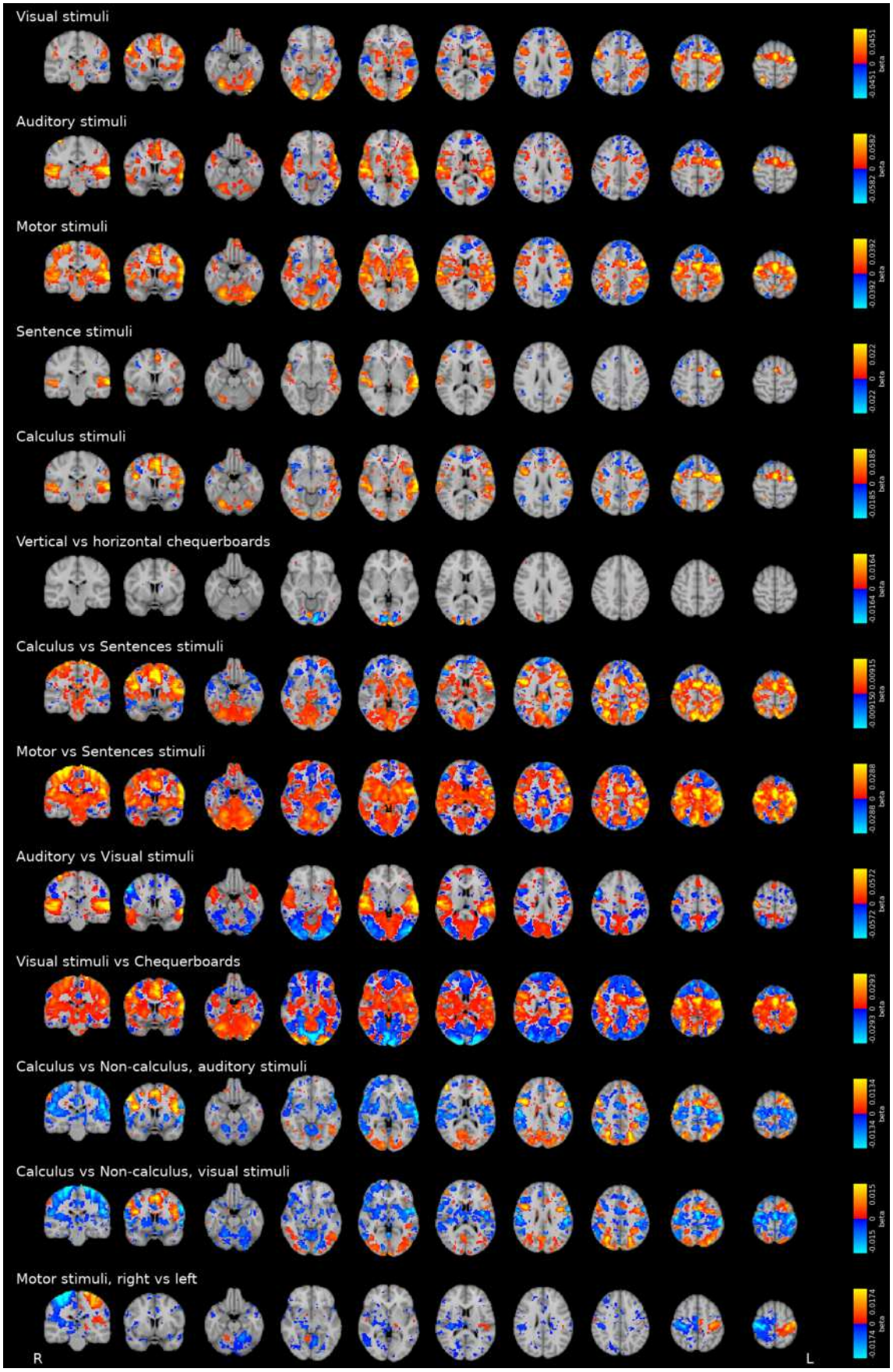

Figure 2.13: Results of the MEMA test **at the subject level**, for a representative subject (subject 007), for all contrasts of the Pinel task ($p < 0.05$, FDR corrected).

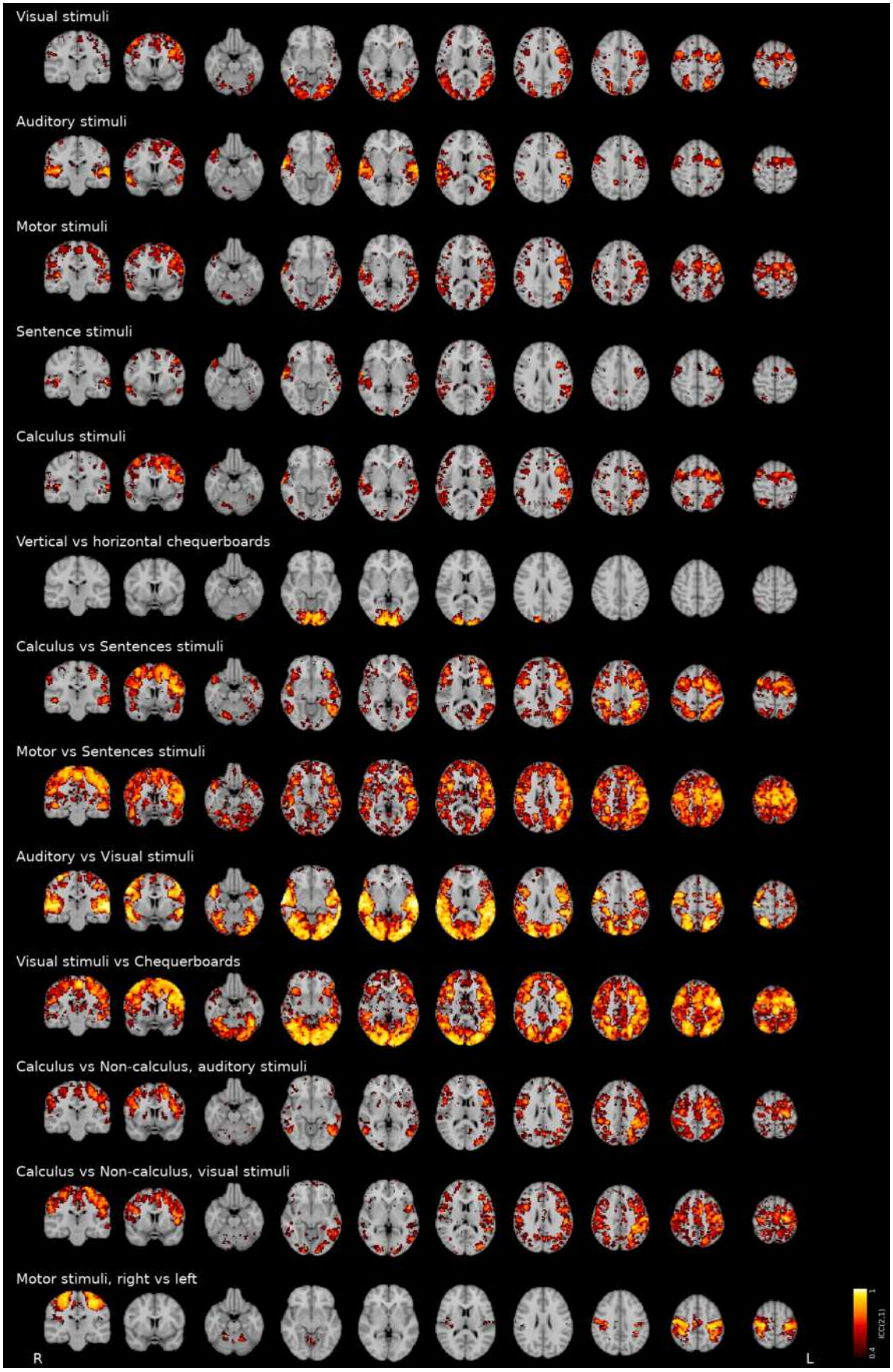

Figure 2.14: ICC(2,1) of all contrasts of the Pinel task. Maps are thresholded at 0.4, since values lower than that are considered poor reliability (Cicchetti, 2001).

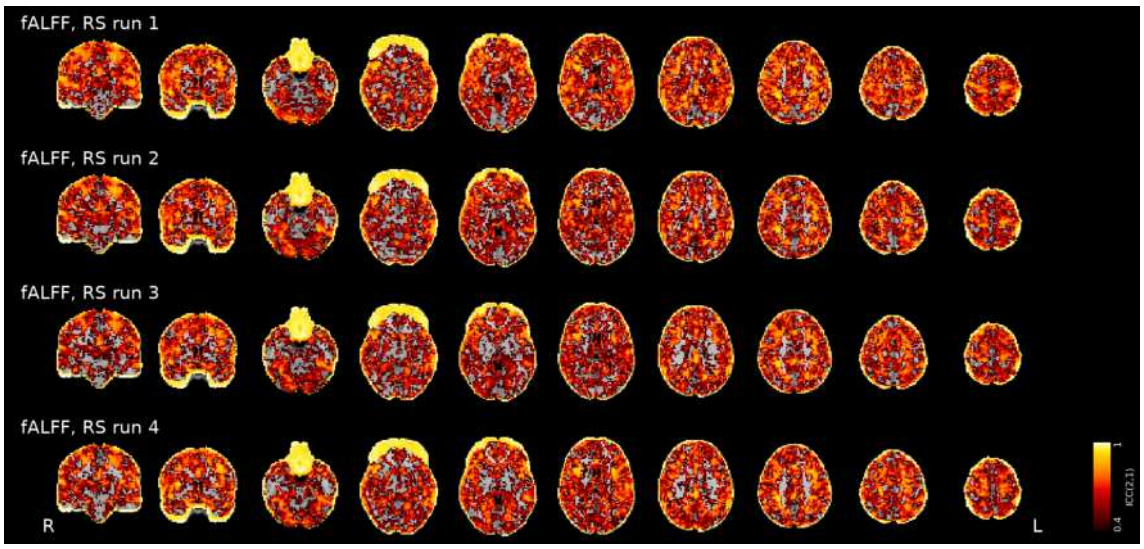

Figure 2.15: ICC(2,1) of all fALFF maps. Maps are thresholded at 0.4, since values lower than that are considered poor reliability (Cicchetti, 2001).

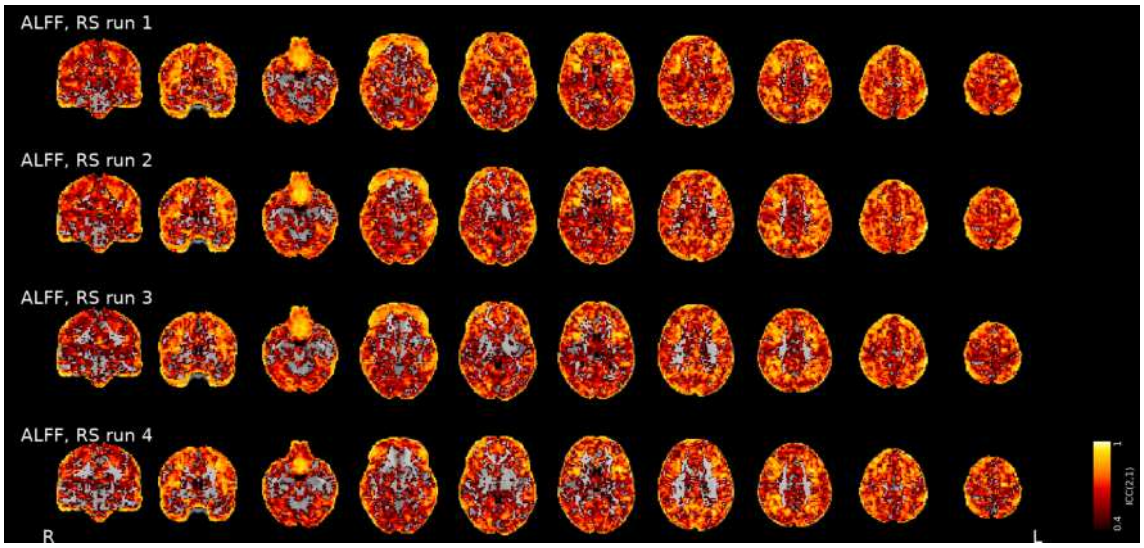

Figure 2.16: ICC(2,1) of all ALFF maps. Maps are thresholded at 0.4, since values lower than that are considered poor reliability (Cicchetti, 2001).

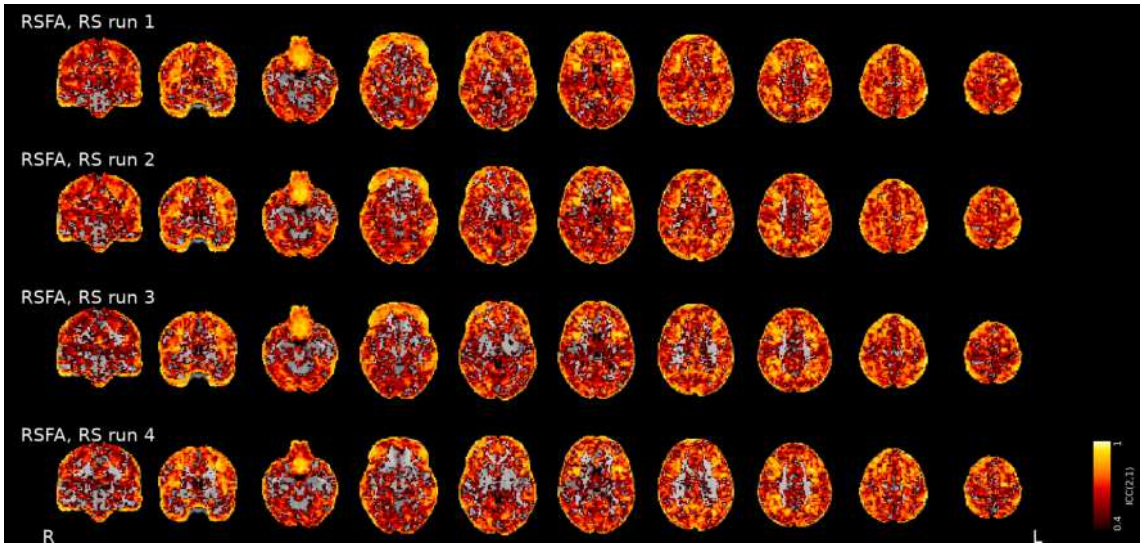

Figure 2.17: ICC(2,1) of all RSFA maps. Maps are thresholded at 0.4, since values lower than that are considered poor reliability (Cicchetti, 2001).

2.3 Discussion

This chapter described a dense mapping to study the effect of CVR on resting state and different types of tIA across different types of experimental designs and cognitive domains: a lower level, sensory, block designed motor task (Buckner et al., 2011), a higher level, event related with random ISI designed Simon task (Simon & Rudell, 1967), and a mixed, event related with fixed ISI designed Pinel functional localiser task (Pinel et al., 2007).

The motor task presented five different movement trials, i.e. tongue movement, lateral fingertapping, and lateral toe movement. The contrast of each trial was computed against a sham condition, similar to time of rest, consisting in fixating a star in the screen in order to reduce the effect of the visual cue of the motor action. For the tongue movement and finger tapping trials, reliable group activations were found in the expected areas of the homunculus projection on the primary motor cortex (Buckner et al., 2011), as well supplementary motor areas and subcortical areas (see e.g. Caballero-Gaudes et al., 2019). Nevertheless, no group activation was found in the medial motor cortex for the toe movements at the selected significance threshold ($p < 0.05$, FDR corrected). Conversely, these maps did exhibit robust group activation in subcortical areas associated to the toe movements, mainly the ipsilateral putamen and pallidum. Despite this, the medial motor cortex presented high reliability associated to the toe movement trials, suggesting highly subject-specific activations. The smaller size of the toes and foot motor cortices, compared to the rest of the homunculus, might lead to increased spatial variability across subjects. This observation is supported by the lack of agreement between subjects, that indicates highly subject-specific localization of the activations related to toe movement.

Interestingly, reliable and well localised group activations were found in the cerebellum for all types of movements, coherently with previous reports (e.g. Buckner et al., 2011), demonstrating the advantages of collecting a DM dataset along with a ME acquisition (Gonzalez-Castillo et al., 2016; Lynch et al., 2020): the higher amount of data and increased BOLD sensitivity enhances the power and reliability of the contrasts, giving the possibility of mapping the cerebellum in individual subjects (Marek & Dosenbach, 2018).

The same increase in sensitivity can be noticed for the Simon task. The corresponding group and ICC reliability maps depict not only the areas traditionally associated with

the task (Peterson et al., 2002), but also other areas involved in processing the task. For instance, occipital regions normally activated by visual stimuli (e.g. Pinel et al., 2007) are involved in seeing the task stimulus. Motor, premotor and cerebellar regions, normally activated by motor tasks (e.g. Buckner et al., 2011; Caballero-Gaudes et al., 2019; Pinel et al., 2007) , are involved in pressing the buttons, and premotor regions and parietal activations could be also related to spatial location and direction processing (Peterson et al., 2002) that characterise this task (Ivanoff & Peters, 2000). Finally, cingulate activity might be related to the continuous practice that the subjects underwent during the ten sessions, as it has been previously found both in the Simon task (Peterson et al., 2002) and in other tasks (Tracy et al., 2001).

All these regions present highly reliable group activations, and this widespread response is likely associated to an increase in sensitivity, due to both the high number of trials (960 trials, of which half congruent and half incongruent) and the use of ME acquisition with optimal combination of the echoes (Gonzalez-Castillo et al., 2016; Lynch et al., 2020). This could also explain the almost complete overlap of the incongruent and congruent responses, that resulted in no significant activation in the congruent versus incongruent contrast.

As for the functional localiser task (Pinel et al., 2007), almost all contrasts showed very high sensitivity at the group level in areas pertinent to the type of stimulus under observation (Pinel et al., 2007), as well as high reliability in both areas characterised by significant activations and not. The only exception was the contrast between vertical and horizontal flickering chequerboards, that showed no reliability and no significant activation at the group level, probably indicating the total overlap between the activations induced by horizontal and vertical chequerboards, possibly related, once again, to the high sensitivity of the dataset collection. However, most contrasts showed activations pertinent to other types of stimuli, indicating that the temporal sparsity of the trials was not sufficient to properly distinguish different types of stimuli from each others.

Finally, RSFA and ALFF maps presented fair to excellent reliability, but a decrease in reliability from the first to the last run. While further observations and tests are required to explain the observed decrease, a possible explanation might be the time spent in the scanner, and the fatigue or boredom of the subjects as the session progresses. fALFF maps presented generally good reliability, more stable across runs. They also showed excellent reliability in the subcallosal cortex, the frontal pole and brain edges. However, this high reliability might be artefactual and indicate a failure in recovering sufficient information on the signal of these areas, at least for some subjects.

2.4 Conclusion

This chapter describes the dense mapping (DM) dataset that will be used throughout this thesis. The group activation and reliability (in terms of ICC) maps of the relevant contrasts of a Motor, a Simon, and a Pinel functional localiser task were computed. Overall, leveraging ME-fMRI in a DM dataset resulted in highly increased sensitivity. RSFA, ALFF, and fALFF of the four runs of RS and their reliability maps were also computed. Almost all contrasts in the three tasks showed high reliability, as did RSFA, ALFF, and fALFF of the four runs. The contrasts in the Simon task, as well as the contrast inducing activation in large areas of the motor cortex in the motor task and most of the contrasts in the Pinel functional localiser, showed high sensitivity in the group analysis. The contrasts inducing activation in smaller areas of the motor cortex, as well as the contrast between differently oriented chequerboards in the Pinel functional localiser, showed small to no group activations, indicating heterogeneous, albeit stable, activations between subjects.

3. Voxelwise optimisation of haemodynamic lags to improve regional Cerebrovascular Reactivity estimates in breath-hold fMRI

Breath-hold induced CVR experiments require minimal additional equipment and are less prone to compliance issues compared to experiments involving gas inhalation, making them an attractive approach for clinical and research settings. However, subjects tend to take deep recovery breaths after the breath-hold, which can lead to severe task-correlated head motion (Bright et al., 2009) and respiratory-related susceptibility artefacts that can considerably corrupt the fMRI signal (see figure Figure 3.1).

In addition, in BH-induced CVR experiments with BOLD fMRI one must also consider the temporal offset between any recorded respiration trace ($P_{ET}CO_2$ or respiratory effort alike) and the local BOLD response. This offset results from the interplay of different factors: an inherent delay between the air exhalation inside the scanner and the sampling of CO_2 (and O_2) in the gas analyser (measurement delay), systemic changes in blood gases that travel with blood to arrive at local brain regions (vascular transit delay), and local arterioles responding to blood gas levels differently (vasodilatory dynamics) (see figure Figure 3.2). Correcting for this temporal offset can improve the estimation of CVR amplitude.

The challenge of accounting for temporal offsets in CVR studies has been previously addressed in multiple ways in the literature. For instance, simple averaging of breath-hold data was used to map CVR time-to-peak in healthy subjects (Bright et al., 2009), revealing consistent regional variability in CVR lags. In CO_2 inhalation studies, various approaches have been proposed to estimate the response lag. As an example, Duffin et al. (2015) implemented a Transfer Function Analysis with a Welch algorithm to measure the phase of the BOLD response considering the frequency of 0.01 Hz. Liu, Welch et al. (2017) used an iterative linear regression to first match a reference signal (i.e. the average signal of a ROI, e.g. cerebellum) to each voxel in the brain, and then to match the $P_{ET}CO_2$ to the reference signal, obtaining multi-parametric haemodynamic information including the bolus arrival time. This method provided similar information compared to regressing the BOLD response with a group of sines and cosines used to model a sinusoidal CO_2 paradigm (Blockley et al., 2017).

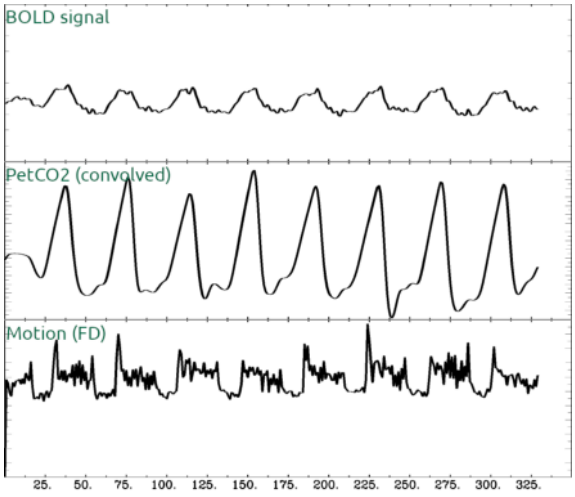

Figure 3.1: The average BOLD signal in the grey matter shows high collinearity not only with the $P_{ET}CO_2 hrf$ signal, but also with head motion (expressed here as Framewise Displacement)

Another alternative consists in Rapidtide, an algorithm that uses a recursive cross-correlation method to ascertain lags between fMRI data and a reference timeseries (Frederick, Salo & Drucker, 2020). Briefly, at each cycle this algorithm computes a voxelwise cross-correlation with a reference, such as the average timeseries of a ROI or a regressor of interest, and creates a shifted reference for each voxel according to the estimated lag. Then, it updates the reference timeseries by considering the first eigenvector of a principal component analysis or the weighted average of the obtained shifted regressors, repeating this cycle until a defined convergence or for a set number of times. In gas inhalation studies where $P_{ET}CO_2$ acted as the reference, this algorithm successfully mapped CVR latency in control and clinical populations, highlighting that haemodynamic lag is a sensitive measure of regional pathology (Donahue et al., 2016). Rapidtide can also estimate systemic vascular processes by using the global fMRI signal in resting state data as the reference, and extract similar haemodynamic lag maps (Tong & Frederick, 2014). Nevertheless, the global fMRI signal might include severe motion-related confounds and irrelevant physiological processes that can degrade the quality of the CVR and lag estimates, particularly in BH-induced CVR experiments.

In order to correct for the impact of motion on CVR and lag estimations, Sousa et al. (2014) proposed to use a lagged GLM approach that integrated motion parameters as nuisance regressors. The lagged GLM was preceded by the orthogonalization of the reference $P_{ET}CO_2$ signal to the motion parameters, and the lags were selected based on the highest Z score associated to the $P_{ET}CO_2$ regressor. Although this approach showed reproducible measures of BOLD CVR, modifying the $P_{ET}CO_2$ signal can potentially limit quantitative CVR estimation due to the aggressive removal of nuisance regressors (see Chapter 4 for further details).

This chapter proposes a framework similarly based on a lagged GLM analysis that estimates the haemodynamic lag in breath-hold BOLD fMRI data while preserving semi-quantitative measures of CVR amplitude. In order to properly take the impact of collinear motion into account, each GLM is defined including nuisance polynomial terms and motion parameters, as well as a shifted variant of the $P_{ET}CO_2 hrf$ regressor without prior orthogonalization, and the optimal temporal shift is identified by maximising the fit of the full

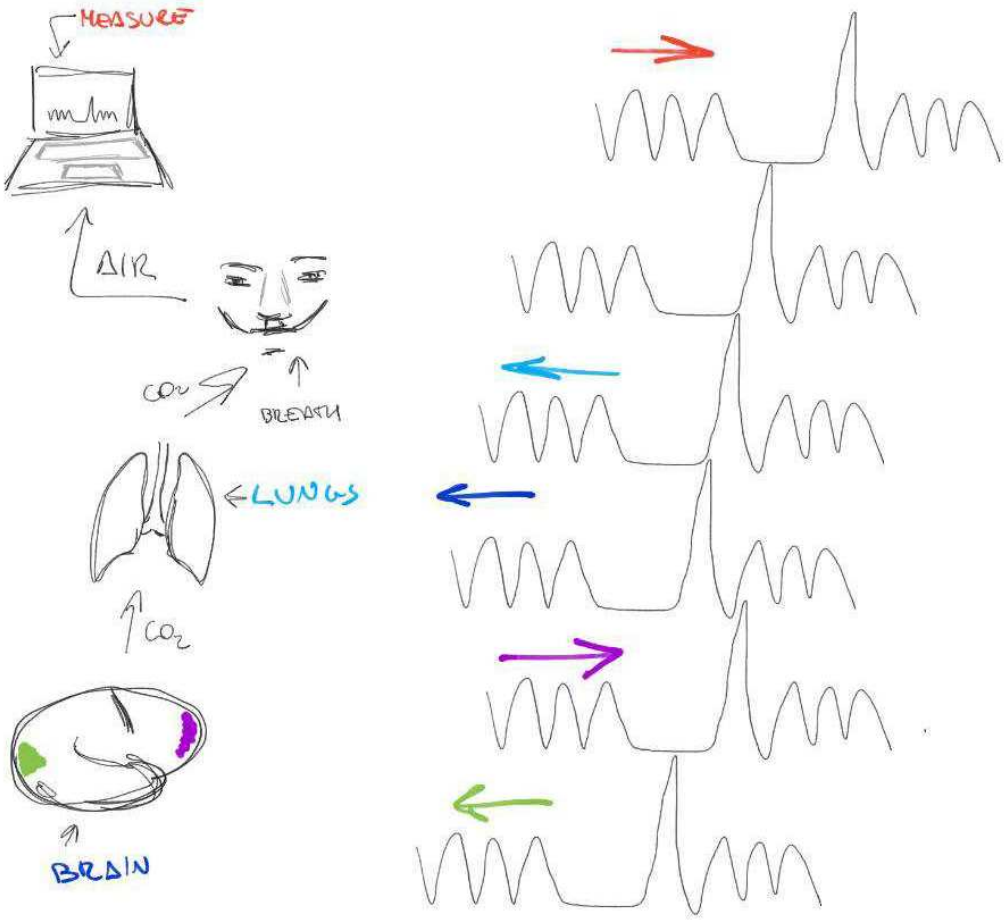

Figure 3.2: An illustration of the recorded CO_2 offset problem. While a person breathes, the air has to traverse the extent of the cannula to be sampled, introducing a measurement delay. This time lapse has to be summed to the time that is necessary for the the gas particles to move from the brain to the lungs (bulk shift). Moreover, each different area of the brain shows a different delay that should be taken into account for a precise CVR estimation.

model within physiological constraints. While motion regression prior to CVR estimation is a typical preprocessing step, having sequential steps for denoising and lag estimation, as done in cross-correlation approaches, might lead to biased estimates or the reintroduction of motion effects if the latter is not performed adequately (i.e. the variance removed during the initial denoising step is not removed from the regressors of interest used in the analysis as well Lindquist et al., 2019). Due to the unknown temporal offset between instantaneous local motion-related fMRI artefacts and delayed responses to $\mathrm{P_{ET}CO_2}hrf$ fluctuations, a simultaneous fit can address potential collinearities between regressors more accurately (Lindquist et al., 2019). This lag optimisation procedure is referred to as simultaneous motion fitting (**SimMot**). The proposed approach is compared with other lag-optimisation strategies incorporating motion correction, and is evaluated in terms of regional variability in haemodynamic lag across subjects, the contrast within lag maps, and how accounting for lag impacts regional CVR estimates.

3.1 Methods

This study employs the BH task fMRI data, the CO_2 traces, and the anatomical images from one session of eight subjects of the dataset described in the previous Chapter 2. The MRI and physiological data was analysed as described in Section 2.1.9, considering a range of ±9 seconds around the bulk shift with a step of 0.3 seconds for lag estimation.

3.1.1 Comparison of different Lag Optimization models

The lag-optimised (SimMot) model was compared with other three approaches. One approach did not consider a voxelwise lag optimisation, while the other two varied based on the way the motor regressors were treated in the analysis. In total, the four considered models were:

1. An non-optimised GLM model where only one $\mathrm{P_{ET}CO_2}hrf$ regressor was considered for all voxels, to study the impact of voxelwise lag optimisation. The regressor was shifted considering the bulk shift (**Non Opt**):

$$Y = P_{ET}CO_2hrf_{bulk} + n \tag{3.1}$$

2. The lag-optimised GLM where the design matrix included the motion parameters and their temporal derivatives (denoted as Mot), Legendre polynomials of up to the fourth order (denoted as $Poly$), together with a voxelwise shifted $\mathrm{P_{ET}CO_2}hrf$ trace (**SimMot**):

$$Y = P_{ET}CO_2hrf_{vx} + Mot + Poly + n \tag{3.2}$$

3. A lag-optimised GLM with no previous motion regression to assess the modelling of motion-related effects **NoMot**:

$$Y = P_{ET}CO_2hrf_{vx} + n \tag{3.3}$$

4. A lag-optimised GLM that included only shifted $\mathrm{P_{ET}CO_2}hrf$ regressors in the GLM but regressed out motion parameters and Legendre Polynomials beforehand (i.e. a sequential approach, **SeqMot**):

$$[Y \perp (Mot, Poly)] = P_{ET}CO_2hrf_{vx} \tag{3.4}$$

In the models above, Y represents the voxel timeseries, $P_{ET}CO_2hrf_{bulk}$ and $P_{ET}CO_2hrf_{vx}$ represents the non-optimised and lag-optimised $\mathrm{P_{ET}CO_2}hrf$ trace, and n denotes the random noise.

3.1.2 Group maps and summary statistics

In order to obtain group-level results and summary statistics, the CVR, t-statistics, and lag maps were warped to the MNI152 template (Grabner et al., 2006, 2.5 mm isotropic voxel resolution) using nearest neighbour interpolation, and averaged across subjects. Note that group average CVR maps do not include voxels from subjects where the lag was deemed implausible, or where the CVR fit was not deemed significant. Then, the NonOpt CVR maps were thresholded at t>1.65 (p<0.05, 313 DoF), while the lag-optimised CVR maps (SimMot, NoMot, and SeqMot) were thresholded at t >3.164 (p <0.05, 313 DoF) after adjustment with Šidák correction (Šidák, 1967) for the testing at multiple lags.

To assess the differences in CVR and lag estimates at the regional level, four regions of interest (ROIs) were defined by segmenting the MNI template into GM and WM (eroded with a 4 mm Gauss kernel to avoid partial volume effects), and considering a mask of the putamen (Harvard-Oxford Subcortical structural atlas) and a mask of cerebellar GM (Cerebellar MNI atlas), both subtracted from the GM mask to avoid overlaps between ROIs. Putamen and cerebellum ROIs were chosen due to their previously reported earlier and later haemodynamic lags, respectively (Bright et al., 2009). For each ROI, the average CVR value of each subject was extracted from the lag-optimised CVR maps and NonOpt CVR maps, and paired t-tests were computed to assess statistical differences between models. For each lag-optimised model, to asses how different the lag in each ROI was from that of the GM, the Contrast to Noise Ratio (CNR) between the average lag of the GM and each other ROI was computed as:

$$CNR = \frac{|\overline{Lag_{ROI_1}} - \overline{Lag_{ROI_2}}|}{\sqrt{\frac{\sigma_1^2}{n_1} + \frac{\sigma_2^2}{n_2}}} \tag{3.5}$$

where, for the i^{th} ROI, $\overline{Lag_{ROI_i}}$ is the average lag, σ_i^2 is the variance, and n_i is the number of voxels. Finally, the three CNR were compared between models using a t-test.

3.2 Results

Figure 3.4 shows CVR and lag maps of the NonOpt and SimMot models for an example subject and group averages, while the histograms for the ROI voxels are depicted in Figure 3.3 and the corresponding average CVr values are reported in the first two columns of Table 3.1. The results indicate that WM voxels exhibit a later lag (i.e. delayed CVR response) compared to GM voxels, whereas the putamen and cerebellum demonstrate much earlier and later responses, respectively, in agreement with previous literature (e.g. Bright et al., 2009). Moreover, average CVR significantly increases after lag optimisation (p<0.0001). Thus, fine correction for lag variability improves local CVR estimates that would otherwise be underestimated.

Figure 3.5 and Tables 3.1 and 3.2 compares lag and optimised CVR maps across the SimMot, SeqMot and NoMot methods, with accompanying CNR estimates in Table 3.3. Average CVR values are significantly lower in SimMot compared to both SeqMot and NoMot for GM and cerebellum and compared to NoMot for putamen. The average CVR value for the putamen was found significantly lower in SeqMot compared to NoMot as well (see Table 3.1). Average Lag values were found to be significantly lower for GM, putamen, and WM in SimMot compared to both SeqMot and NoMot. They were also found higher for cerebellum in SimMot compared to both SeqMot and NoMot, although not significantly (see Table 3.2). There was no significant difference between average lag values in SeqMot and NoMot (p>0.1). Lag CNR increases using the SimMot method, however only the

ROI	CVR (%BOLD/mmHg)			
	Non Opt	SimMot	SeqMot	NoMot
WM	0.09 + 0.02 *	0.16 + 0.03	0.16 + 0.03	0.16 + 0.03
GM	0.24 + 0.06 *	0.38 + 0.09	0.44 + 0.10 **	0.44 + 0.10 ‡
Putamen	0.18 + 0.05 *	0.28 + 0.07	0.30 + 0.07 ◇◇	0.30 + 0.06 ◇
Cerebellum	0.19 + 0.04 *	0.31 + 0.07	0.36 + 0.10 **	0.36 + 0.09 ‡

Table 3.1: Average CVR values of all considered ROI from each pipeline. Reported values are mean ± standard deviation across subjects. Note that the comparison between Non Opt and the SeqMot and NoMot approaches was not performed. * SimMot - Non Opt: significant t-test, DoF=7, $p<0.0001$, two-tailed. ** SimMot-SeqMot: significant t-test, DoF=7, $p<0.05$, two-tailed. ‡ SimMot-NoMot: significant t-test, DoF=7, $p<0.01$, two-tailed. ◇ SimMot-NoMot: significant t-test, DoF=7, $p<0.1$, two-tailed. ◇◇ SeqMot-NoMot: significant t-test, DoF=7, $p<0.1$, two-tailed.

ROI	Lag (sec)		
	SimMot	SeqMot	NoMot
WM	0.48 + 0.82	0.55 + 1.19	0.62 + 1.12
GM	-1.30 + 0.56	-1.00 + 0.60 **	-1.05 + 0.64 *
Putamen	-2.88 + 1.11	-2.49 + 1.11 *	-2.51 + 1.09 *
Cerebellum	1.53 + 0.72	1.37 + 0.80	1.34 + 0.73

Table 3.2: Average lag values of all considered ROI from each lag optimisation pipeline. Reported values are mean ± standard deviation across subjects. No significant difference was found between SeqMot and NoMot (DoF=7, $p>0.1$, two-tailed). * SimMot-SeqMot or SimMot-NoMot: significant t-test, DoF=7, $p<0.1$, two-tailed. ** SimMot-SeqMot: significant t-test, DoF=7, $p<0.05$, two-tailed.

contrast between cortical and cerebellar GM reaches significance, showing an average 18.8% increase.

3.3 Discussion

This study demonstrates that haemodynamic lag can be successfully mapped with BOLD fMRI in BH-induced CVR experiments. The proposed approach simultaneously fits for CO_2 CVR effects, low frequency trends and head motion to reduce the bias of task-correlated motion artefacts in the lag estimation. After lag optimisation, increases in CVR are observed in all ROIs, demonstrating that this is an important step to ensure accurate regional CVR values (see Figures 3.3 and 3.4).

Furthermore, the lag maps obtained with the SimMot model are spatially consistent with previous findings using alternative approaches and hypercapnic stimuli (e.g. Blockley, Driver, Francis, Fisher & Gowland, 2011; Bright et al., 2009). Although the different lag optimisation methods (SimMot, SeqMot and NoMot) show subtle variations, lag CNR was found always higher using the proposed simultaneous fitting approach. This was most notably observed in the cerebellum, a region that is particularly prone to motion artefacts.

While there were significant differences in CVR between the SimMot approach and all other methods, the only significant difference between NoMot and SeqMot was found in

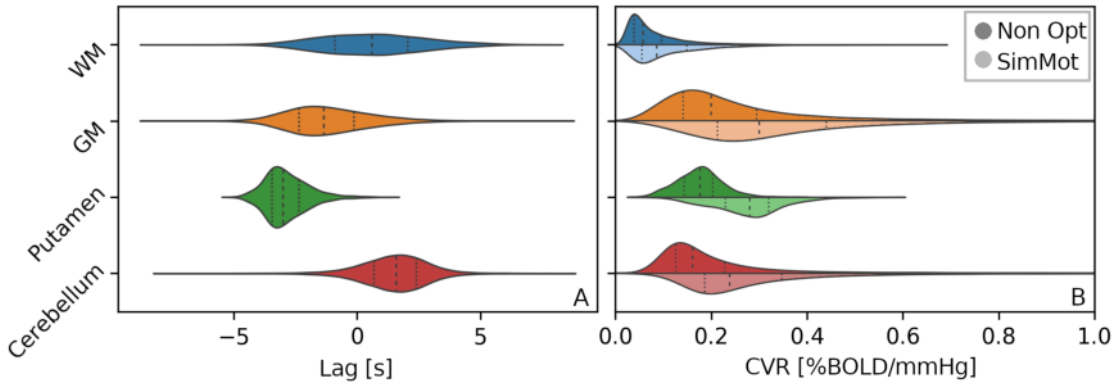

Figure 3.3: (A) Distribution of group mean lag values in each ROI. WM response is later than GM. Relative to the rest of the GM, the response in the Putamen happens earlier and the response in the cerebellar GM happens much later. (B) Distribution of group mean CVR values with (light colours, SimMot) and without (dark colours, Non Opt) incorporating the optimal lag. Note the general increase in CVR values in SimMot

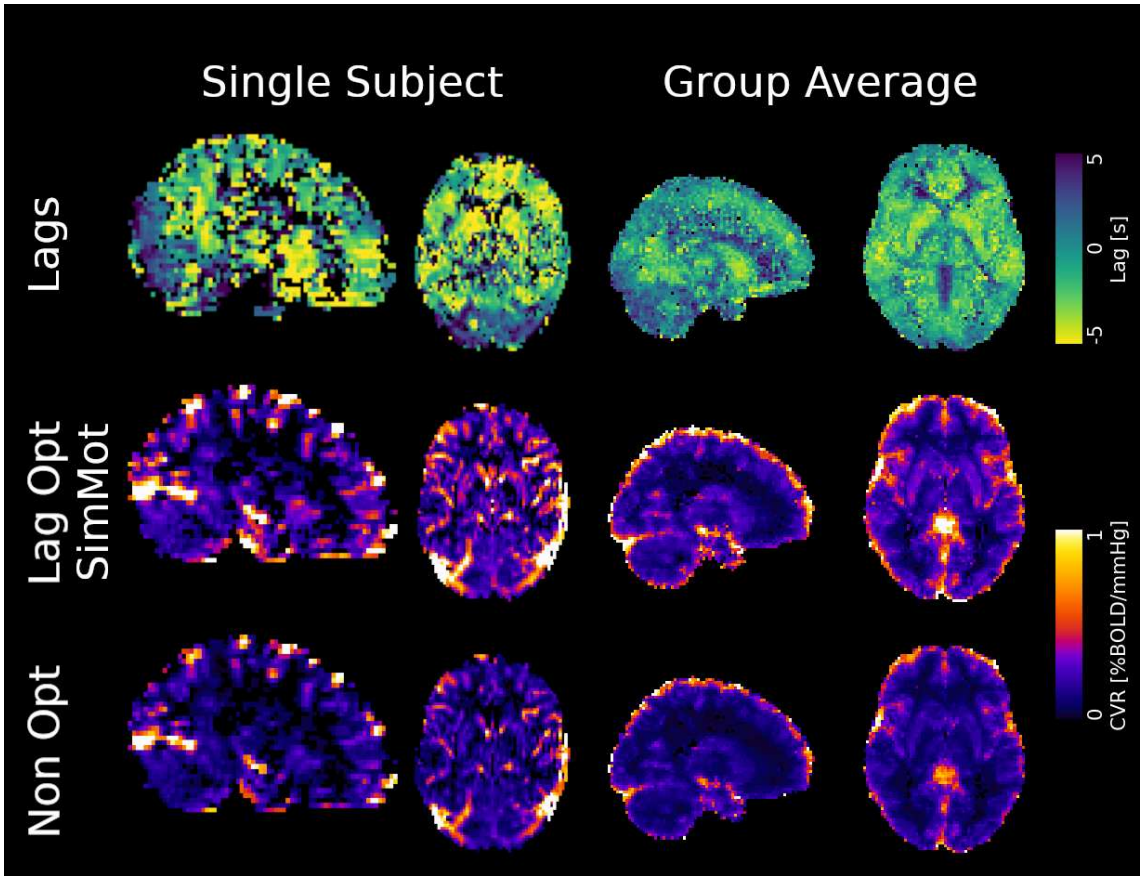

Figure 3.4: Maps of haemodynamic lag (clipped at ±8.4 s) and CVR, before and after optimisation of the temporal shift with the proposed approach (SimMot), for a representative subject and group average. Note the increased contrast between WM and GM after optimal shift, indicating an underestimation of CVR in most brain regions.

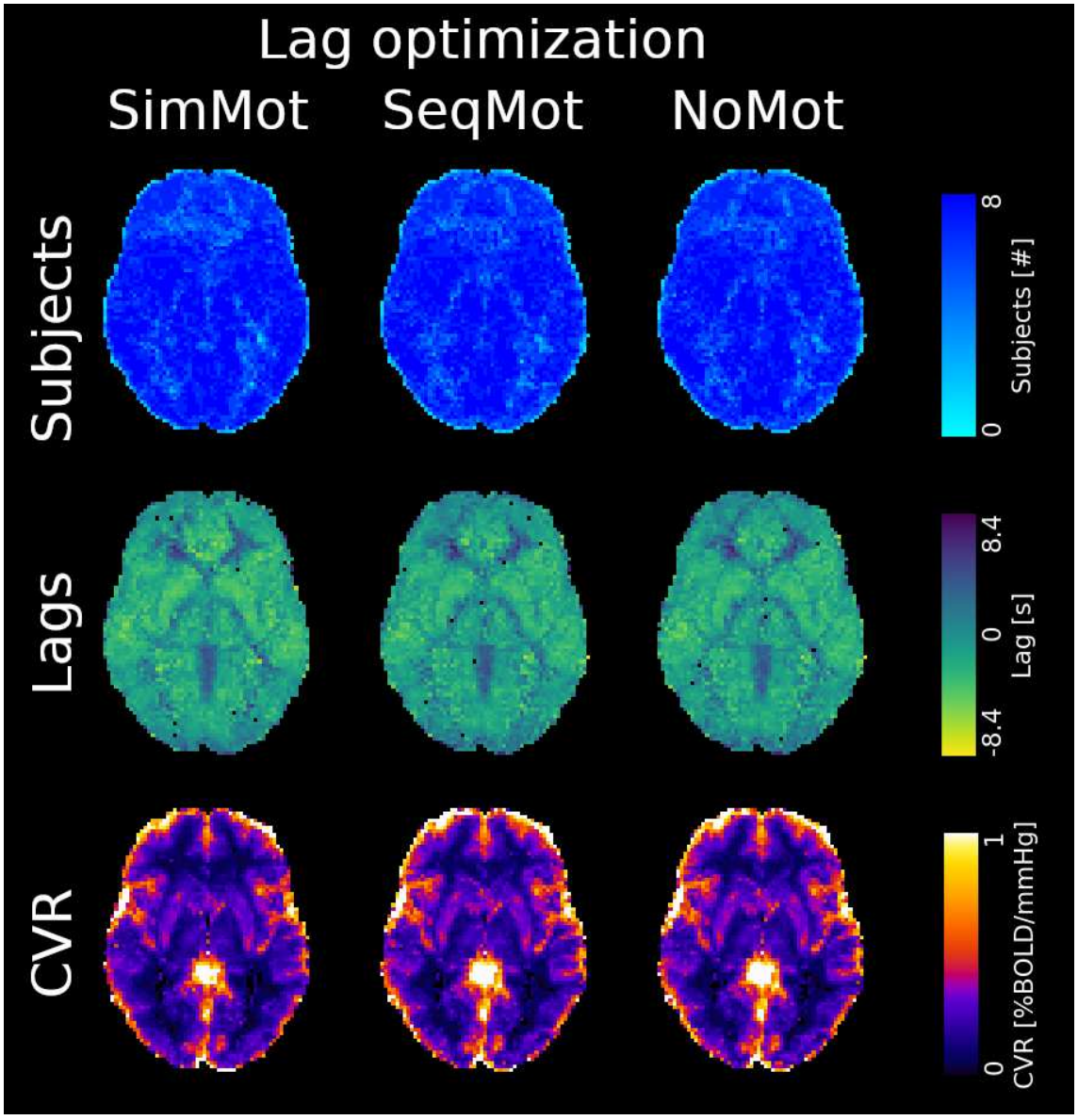

Figure 3.5: Group average maps of haemodynamic lag (second row) and CVR (third row) after optimal shift for simultaneous motion regression (SimMot), sequential motion regression (SeqMot) and no motion regression (NoMot). The maps of the first row depict the number of subjects contributing to each voxelwise estimate of lag and CVR after boundary conditions are considered, showing more subjects consistently at the boundary condition at the edges of the brain and WM. SimMot results in improved regional contrast in the lag maps as quantified in Table 3.3.

ROI 1 - ROI 2	CNR		
	SimMot	SeqMot	NoMot
GM-WM	0.52 + 0.21	0.46 + 0.26	0.49 + 0.25
GM-Putamen	0.47 + 0.22	0.44 + 0.21	0.44 + 0.21
GM-Cerebellum	0.82 + 0.15	0.69 + 0.17 *	0.69 + 0.16 *

Table 3.3: Lag CNR compared between different lag optimised methods. Reported values are mean ± standard deviation across subjects. * SimMot-SeqMot or SimMot-NoMot: significant t-test, DoF=7, $p<0.05$, two-tailed.

the Putamen (see Table 3.1). Furthermore, no difference in lag estimation was found in the latter two models, while there was a significant difference between them and the SimMot approach in the GM and Putamen, as well as a significantly higher CNR between GM and cerebellum. These results, taken all together, could indicate that the SimMot model takes into account motion-related effects better than the others, and may suggest that the higher CVR amplitude estimated in the NoMot and SeqMot approaches is an artificial increase due to unresolved collinearities with task-related motion effects. However, future studies are necessary to compare the CVR and lag estimates obtained with the three different approaches to those obtained with a gas challenge experiment.

The comparison between lag optimised and non-optimised CVR maps clearly illustrates that accurate measurement of CVR in a subcortical region using transient $P_{ET}CO_2$ manipulations must account for the vasodilatory lag being different from cortical GM. This is particularly relevant for clinical applications: for instance, one quarter of all first ischaemic infarcts are subcortical, and measuring CVR in these regions may be particularly important (Hartkamp et al., 2017). In line with the literature, the optimal lag was searched within a range of ±9 seconds relative to the bulk shift. This range should be adjusted in clinical or healthy ageing studies to adequately characterise expected pathological transits (Donahue et al., 2016; Stickland et al., 2021), although the maximum shift should not be longer than half a breath-hold period, as this may lead to spurious negative correlations between $P_{ET}CO_2 hrf$ and fMRI. While the application of this method showed interesting results in a single-case study of a subject with Moyamoya disease (Stickland et al., 2021), further evaluating the feasibility and utility of this method in clinical populations will be an interesting venue for future work. Moreover, the latency of these effects might facilitate the discrimination of neurovascular versus purely vascular signals in fMRI data (Bright & Murphy, 2013a; Stickland et al., 2021)

In this study, the negative CVR values were not taken into account in order to simplify the ROI average CVR estimations and comparisons. This choice could have led to miss possible significant differences in areas characterised by negative CVR values, such as the WM, and further studies should take this difference into account.

3.4 Conclusion

This chapter introduced a lagged-GLM approach that accounts for the impact of confounding factors, such as motion, while simultaneously estimating CVR amplitude and lag. This approach performed significantly better than a lack of lag optimisation, and showed less residual impact of motion than methods that did not correct for motion or that corrected for it in a sequential manner. In the next chapter, this method will be further expanded to also consider other source of noise than motion using denoising techniques based on ICA,

and the right rapport between aggressive denoising and conservative signal preservation.

4. ICA-based Denoising Strategies in Breath-Hold Induced Cerebrovascular Reactivity Mapping with Multi Echo BOLD fMRI

A valid approach to estimate Cerebrovascular reactivity (CVR) is the employment of breath-hold (BH) tasks during a BOLD fMRI session (Bright et al., 2009; Kastrup, Li, Takahashi, Glover & Moseley, 1998; Pinto et al., 2021). However, head motion is a particularly problematic source of noise in BH based experiments and respiration tasks for three main reasons. First, the experimental design is similar to that of block designs, that are less robust to motion artefacts (Johnstone et al., 2006) than event-related designs (Birn et al., 1999; Birn, Cox & Bandettini, 2004). Second, the amount of motion associated with paced breathing, deep breaths, or "recovery" breaths following a BH task can be very prominent and concur with the pattern of the task, similarly to overt speech production experiments (Barch et al., 1999; Soltysik & Hyde, 2006; Xu et al., 2014). Third, respiration can perturb the B0 field due to the change of air in the lungs (Raj et al., 2001) and introduce aliasing artefacts or pseudo-movement effects in the signal (Gratton et al., 2020; Pais-Roldán et al., 2018; Power, Lynch et al., 2019).

A first approach to correct for motion effects was discussed in the previous chapter. This chapter will expand this discussion by introducing other approaches to denoising, i.e. ME-fMRI and ICA decomposition, and expanding possible denoising to other sources, not only motion.

It has been shown that ME acquisitions, and in particular the optimal combination (OC) of multiple echo volumes can improve BH-induced CVR mapping sensitivity, specificity, repeatability and reliability (Cohen et al., 2021; Cohen & Wang, 2019). Furthermore, ME-ICA can improve the mapping of task-induced activation reducing sources of noise (Amemiya et al., 2019; DuPre et al., 2016; Evans et al., 2015; Gonzalez-Castillo et al., 2016; Lombardo et al., 2016), outperforming single-echo ICA-based denoising of resting-state fMRI data (Dipasquale et al., 2017; Lynch et al., 2020).

However, up to now, the operation of ME-ICA has not been evaluated thoroughly in experimental paradigms with unavoidable task-correlated artefacts. Under such scenarios, how to obtain the right trade-off between removing as much noise as possible while saving the signal of interest remains as an open question (Bright & Murphy, 2015; Griffanti

et al., 2014). This chapter investigates the efficiency of different regression models to remove artefacts that are highly correlated with the effect of interest, i.e. the CVR response, while also keeping the latter. In particular, the models under investigation include traditional nuisance regression approaches, applied to single- or multi-echo data, as well as three different ME-ICA denoising approaches ranging from an aggressive to a conservative denoising formulation. These modelling strategies is evaluated in terms of the correlation of the cleaned signal with measures of motion, and the physiological interpretability and inter-session reliability of the CVR amplitude and lag.

4.1 Materials and methods

4.1.1 Dataset

This study employs the BH task fMRI data, the CO_2 traces, and the anatomical images from ten sessions of seven subjects of the dataset described in Chapter 2. The MRI and physiological data was analysed as described in Section 2.1.9, considering a range of ±9 seconds around the bulk shift with a step of 0.3 seconds for lag estimation.

4.1.2 MRI data preprocessing

The BH task was preprocessed as described in Section 2.1.9. Moreover, we performed ME-ICA decomposition on the OC volume with tedana (DuPre et al., 2019) using the minimum description length criterion for estimation of the number of components (Li, Adali & Calhoun, 2007; Rissanen, 1978), before correcting for field distortions. Note that each run was treated independently from the others.

Since the automatic classification based on tedana did not classify the components correctly (see Figures 4.2 and 4.3 and the Results section), the independent components (ICs) were then manually classified by SM and CCG into two categories (rejected or accepted components) based on temporal, spatial, spectral and TE-dependence features of each component (Griffanti et al., 2017). The manual classifications are also available in the data repository.

For comparison, the dataset acquired at the second echo time (TE_2 = 28.6 ms) was used as a surrogate for standard single-echo (SE) acquisitions. This volume followed the same preprocessing steps as the OC volume, except for the optimal combination and the ICA decomposition.

4.1.3 CO_2 trace processing and CVR estimation

The CO_2 signal was preprocessed and analysed as described in Section 2.1.9 to obtain the $P_{ET}CO_2 hrf$ timecourse for each run. Chapter 3 demonstrated the appropriateness of lag optimization and simultaneous nuisance modelling for CVR estimation. Hence, the BH fMRI data was analysed using the same lagged-GLM approach where the design matrix comprises a time-shifted version of the $P_{ET}CO_2 hrf$ timecourse as the regressor of interest and different combinations of nuisance regressors (see below) in order to examine their efficiency in modelling artefactual signals of the voxel timeseries that might degrade CVR estimates. This led us to evaluate five different modelling strategies, varying the input data as well as which nuisance regressors were included in the design matrix or how they were derived from ME-ICA:

1. A lagged-GLM model on the SE data where the design matrix includes the motion parameters and their temporal derivatives (denoted as Mot), Legendre polynomials of up to the fourth order (denoted as $Poly$), together with the shifted $P_{ET}CO_2 hrf$

trace (**SE-MPR**):

$$Y_{SE} = P_{ET}CO_2hrf + Mot + Poly + n \tag{4.1}$$

2. The same model applied on the OC data (**OC-MPR**). Note that this model is the same as presented in Chapter 3 as SimMot:

$$Y_{OC} = P_{ET}CO_2hrf + Mot + Poly + n \tag{4.2}$$

3. An aggressive model applied on the OC data in which the design matrix also includes the timecourses of the ME-ICA rejected components (denoted as IC_{rej}), orthogonalised with respect to the motion parameters, their temporal derivatives, and Legendre polynomials of up to the fourth order. This orthogonalisation step (denoted as $A \perp B$, where A is orthogonalised with respect to B) was performed to maintain a low Variance Inflation Factor in this model, and thus not bias the CVR estimation, without altering the relative variance explained by the original nuisance regressors and the regressor of interest (Mumford, Poline & Poldrack, 2015) (**ME-AGG**):

$$Y_{OC} = P_{ET}CO_2hrf + Mot + Poly + [IC_{rej} \perp (Mot, Poly)] + n \tag{4.3}$$

4. A moderate model applied on the OC data in which the timecourses of the ME-ICA rejected components are also orthogonalised with respect to the $\mathrm{P_{ET}CO_2}hrf$ trace, i.e. the regressor of interest describing the CVR response (**ME-MOD**):

$$Y_{OC} = P_{ET}CO_2hrf + Mot + Poly + [IC_{rej} \perp (P_{ET}CO_2hrf, Mot, Poly)] + n \tag{4.4}$$

5. A conservative model applied on the OC data in which the timeseries of the ME-ICA rejected components are orthogonalised with respect to the $\mathrm{P_{ET}CO_2}hrf$ trace and the ME-ICA accepted components denoted as IC_{acc} (**ME-CON**):

$$Y_{OC} = P_{ET}CO_2hrf + Mot + Poly + [IC_{rej} \perp (P_{ET}CO_2hrf, IC_{acc}, Mot, Poly)] + n \tag{4.5}$$

In the models above, Y_{SE} and Y_{OC} are the SE and OC voxel timeseries respectively, and n denotes the random noise.

The corresponding lagged-GLM was fitted via orthogonal least squares using AFNI for each modelling strategy and each of the sixty shifted $\mathrm{P_{ET}CO_2}hrf$ traces. We then further processed the CVR and lag maps as described in Section 2.1.9, i.e. clipping the maps based on the voxel lag value and thresholding them for statistical significance.

4.1.4 Evaluation of motion removal across denoising strategies

To assess the efficiency of each modelling strategy to capture motion-related effects, the 4-D volumes representing the modelled noise variance for each type of lagged-GLM analysis was reconstructed by multiplying the estimated coefficient maps of the nuisance regressors by their corresponding timeseries using 3dSynthesize in AFNI. Then, the obtained 4D volumes were subtracted from the OC or the SE data to obtain five different denoised datasets. Afterwards, the root of the spatial mean square of the first derivative of the signal (a.k.a. DVARS) (Smyser et al., 2010) was calculated on each denoised dataset as:

$$DVARS_t = \sqrt{\langle [I_t(x) - I_{t-1}(x)]^2 \rangle}, \tag{4.6}$$

where $I_t(x)$ is the image intensity of voxel x and at time t and $\langle \cdots \rangle$ indicates the spatial average over the whole brain. In addition, Framewise Displacement (FD) timeseries (Power et al., 2012) were also computed for each run using the corresponding realignment parameters estimated during preprocessing using the fsl_motion_outliers tool as:

$$FD_t = |\Delta d_x| + |\Delta d_y| + |\Delta d_z| + |\Delta \alpha| + |\Delta \beta| + |\Delta \gamma| \tag{4.7}$$

where t denotes the time, d_x , d_y , d_z are the translational displacements along the three axes, α , β , γ are the rotational displacements of pitch, yaw, and roll, and $\Delta d_x = d_{x,t-1} - d_{x,t}$ (and similarly for the other parameters). DVARS was also computed on the SE volume before preprocessing (SE-PRE) to serve as a reference, as its relationship with FD should be at its maximum prior to the effects of motion being removed.

Next, a Linear Mixed Effects (LME) model analysis was carried out with the DVARS and FD timecourses in order to test the moderating effect of each analysis on the relationship between DVARS and FD, using the lme4 and lmer packages (Bates, Mächler, Bolker & Walker, 2015; Kuznetsova, Brockhoff & Christensen, 2017) in R (R Core Team, 2020), accounting for the random effect of subject and session and computing the statistical significance (i.e. p value) with Satterthwaite's method (Satterthwaite, 1946). The corresponding equation of the LME model in R notation is as follows:

$$DVARS \sim FD * model + (1|subject) + (1|session) \tag{4.8}$$

The same model was used to assess pairwise differences in motion removal between denoising strategies. The results were thresholded at $p \leq 0.05$ corrected with the Šidák correction (Šidák, 1967).

In addition, the average timeseries within GM was extracted for each dataset (i.e. SE-MPR, OC-MPR, ME-AGG, ME-MOD, ME-CON), as well as from SE-PRE, in order to visualise the CVR responses to a BH trial. These timeseries were then transformed to BOLD percentage signal change. In a similar manner, the responses to individual BH trials from each session were extracted using the timing of the third paced breathing cycle as a reference onset, and averaged for each subject. The DVARS and FD timeseries underwent the same process, except that the FD timeseries were not expressed in percentage changes.

Finally, the amount of BH trials necessary to converge to a robust estimate of the BH response was also examined for each denoising approach by computing the Manhattan distance from a pool of a gradually increasing number of trials to the average BOLD response over all BH trials (i.e., 80 trials in total across the ten sessions that was considered as the true CVR response) for each analysis model and subject.

4.1.5 Comparison of CVR and lag estimation and reliability across denoising strategies

The percentage of statistically significant voxels in the thresholded CVR maps, as well as the average CVR and lag values across significant voxels in GM and WM were calculated for each denoising strategy for all subjects and sessions.

In order to evaluate and compare the results of the different denoising strategies at the group level, the thresholded CVR map, the lag map and t-statistical map of each session were normalised to the MNI152 template (Grabner et al., 2006, 2.5 mm isotropic voxel resolution) with a nearest neighbour interpolation. A LME model was computed voxelwise using 3dLMEr (Chen, Saad, Britton, Pine & Cox, 2013) considering the effect of subjects and sessions as random effects. The LME model was formulated as the following R equation notation:

$$X \sim model + (1|subject) + (1|session), \tag{4.9}$$

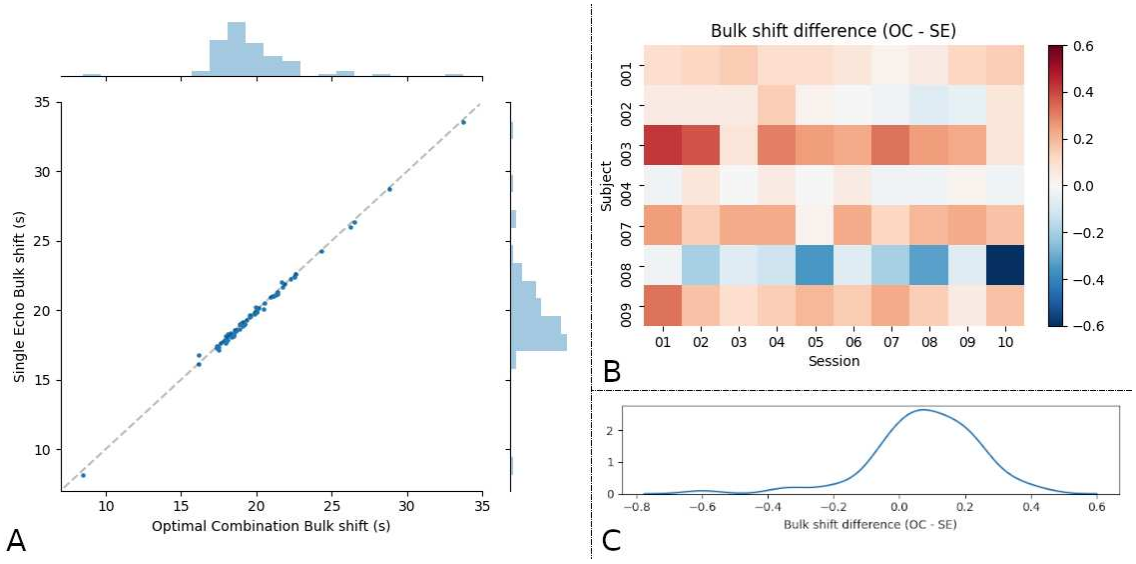

Figure 4.1: (A) Bulk shift of the alignment of the PETCO2 trace with the average GM timeseries of the Optimally Combined (OC) vs Second Echo (SE). (B) Bulk shift difference of the alignment of the PETCO2 trace with the average GM timeseries of the Optimally Combined (OC) vs Second Echo (SE). (C) Bulk shift difference distribution.

where X represents either the CVR or the lag value of each voxel. The same model was used to perform pairwise comparisons between the different strategies.

In addition, the intraclass correlation coefficient (ICC) was computed voxelwise using a regularised multilevel mixed effect model in 3dICC (AFNI) in order to take into account the standard error of CVR and lag for each session in the ICC estimation (Chen et al., 2018). Note that, since 3dICC uses the t-statistic map associated with the estimation of the CVR, CVR and lag maps used in this computation were only clipped on the basis of the lag, and not thresholded on the basis of the t-statistic.

4.2 Results

As reported in Chapter 2, three subjects were excluded due poor performance of the BH task in part of the sessions, mainly due to inadequate execution of the exhalations preceding and following the apnoea which prevented accurate determination of the $P_{ET}CO_2hrf$ traces. These traces are shown in red in Figure 2.5 that plots the $P_{ET}CO_2hrf$ trace for all subjects and sessions. Hence, only the seven subjects that had all ten session were used for subsequent analyses (4F, age 25-40y).

Figure 4.1 depicts the correlation and difference between the bulk shift optimisation for OC and SE data. As it can be seen in panel Figure 4.1A, the two bulk shifts are highly correlated with negligible differences compared with the bulk shift ($r=1$, $p<0.001$). The average bulk shift difference across all subjects and sessions was 0.08 ± 0.17, and their difference was not statistically significant (repeated measures paired t-test, $n=7$, $t = 1.22$, $p>0.1$). Besides, these differences are negligible with respect to the TR of the acquisition (1.5 s) and shift step used for the lag optimisation (0.3 s). Hence, this observation confirms that any reported difference on the results obtained with the SE and OC volumes cannot be due to differences in the bulk shift estimated with both volumes.

Figure 4.2 shows four representative ICs that were misclassified by the automatic algorithm in tedana. Figure 4.2A shows a component that follows the global BOLD oscilla-

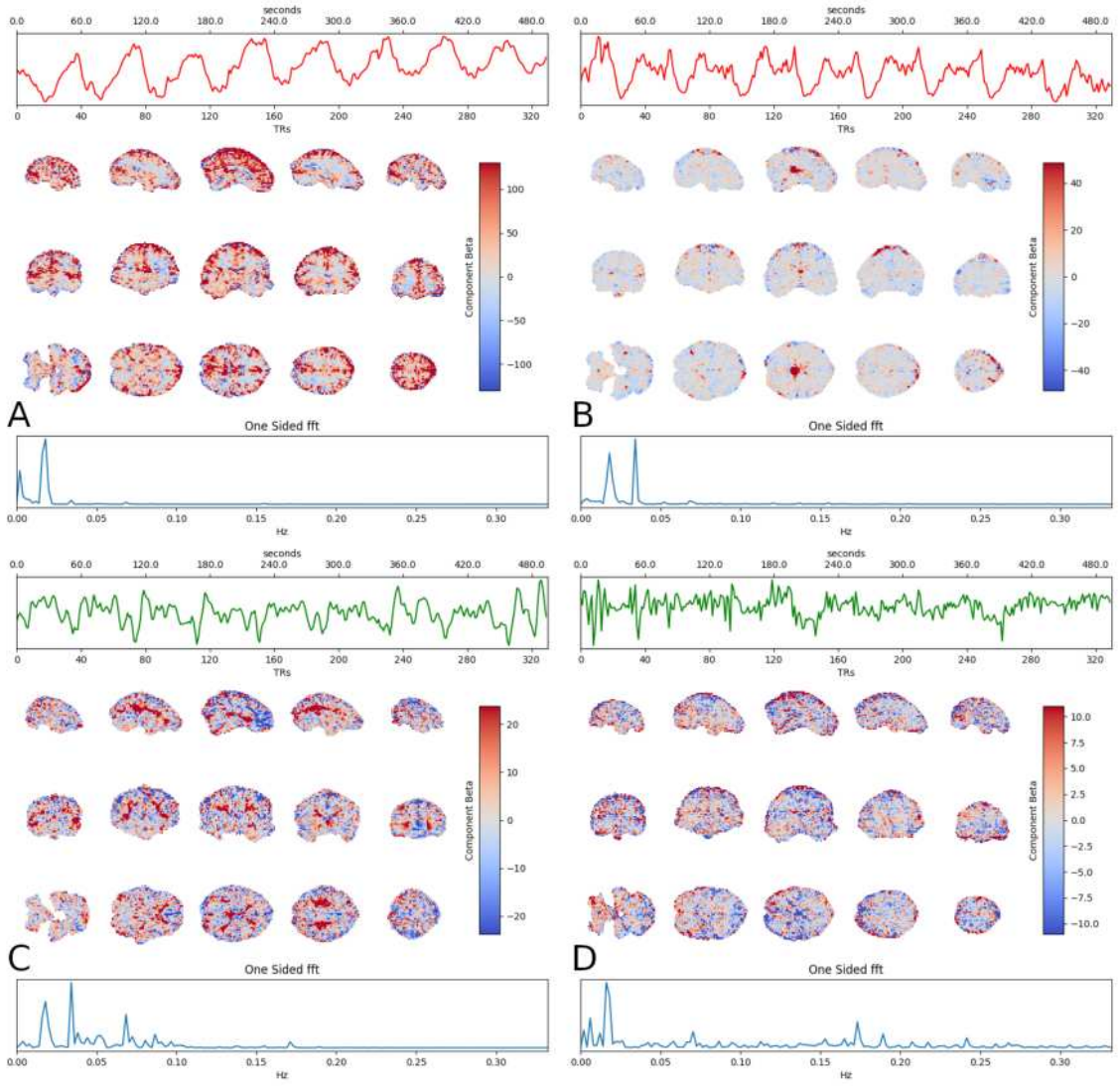

Figure 4.2: Four representative ICs that were misclassified by the automatic classification algorithm in tedana. Each panel is composed by three parts representing a characteristic of the IC: on the top, its timeseries; in the middle, its spatial distribution, on the bottom, its power spectra. A red timeseries indicates automatic rejection as "noise", while a green timeseries indicates automatic acceptance as "good signal".

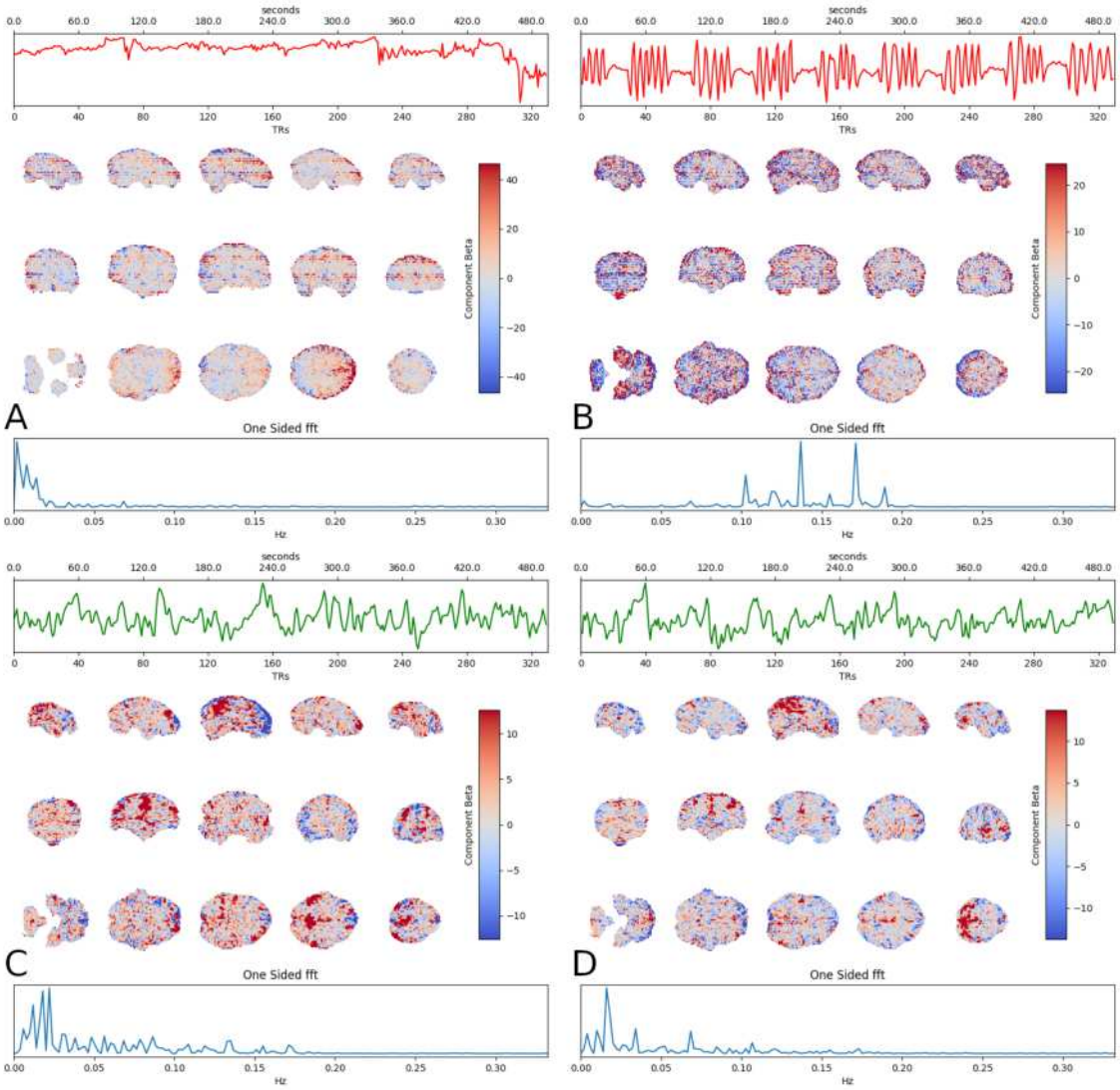

Figure 4.3: Four representative ICs that were classified correctly by the automatic classification algorithm in tedana. The composition of each panel and the color coding are the same as in Figure 4.2.

tions related to the BH task, its characterising frequency is that of the task, and it seems to be spread globally in the GM. The automatic misclassification as "noise" was probably related to the global increase proton density, that reflects in a higher $\Delta\rho$. Figure 4.2B shows a component of which timeseries is the opposite of the task. Due to the proximity of the activation with the central core, suggesting a possible activation of subcortical areas, and the collinearity with the task, we decided to conservatively classify it as a physiologically plausible source and to classify it as a "good" component. Figure 4.2C shows a component that seems to have the same cyclic pattern of the BH task, but due to its multiple main frequencies that are higher than that of the task, and its global WM localisation, it was classified as "noise". Figure 4.2D shows a component that despite having the right characterising frequency is a "noise" component, due to the noise in the timeseries and its spatial pattern. It is probably related to changes in field due to motion. These misclassification suggested the necessity of a manual classification of the components.

Conversely, Figure 4.3 shows four representative ICs that were correctly classified by tedana. Figure 4.3A shows a component with a stripe spatial pattern. This component is most probably associated to the multi-band induced artefacts, frequently removed automatically by tedana (Olafsson, Kundu, Wong, Bandettini & Liu, 2015). Figure 4.3B shows a component with a very irregular spatial pattern, and a timeseries (and main frequencies) that is synchronous to the paced breathings before each BH. Although the timeseries might indicate a relationship with the task, the spatial pattern suggests a source of artefactual nature, most probably related to changes in the field induced by the respiration. Figure 4.3C shows a component traditionally classified as Default Mode Network. Hence, this component is most probably neural in nature. Although the aim of this study relies in CVR, thus making neural events a source of "noise", we chose to keep this component due to the difficulty in disentangling neural and vascular events. Figure 4.3D shows a component that appears to be similarly distributed in space to the previous one, but the main frequency indicates a BH-related response, hence a proper CVR component.

4.2.1 Evaluation of motion removal across denoising strategies

Figure 4.4A illustrates the relationship between FD and DVARS in the raw data (SE-PRE) and after removing the reconstructed noise of each analysis model from the SE or OC volume for a representative subject, each point represents a timepoint and each line represents the linear regression between both timeseries in one session. The corresponding figures for the remaining subjects are available in Appendix C (Figures C.1 to C.3). Figure 4.4B shows the same plot considering all the subjects and sessions. The modulating effect of the denoising approaches on the relation between DVARS and FD was tested with a LME model that was found to be significant ($F(6,161181)=34597$, $p<0.001$). To further investigate the significant differences between analysis strategies, Table 4.1 reports the results of the same LME model considering pairwise combinations of all of the denoising approaches. From both Figure 4.4 and Table 4.1, it can be seen that the optimal combination (OC-MPR) of ME data reduces DVARS compared to single-echo (SE-MPR). Although a similar relationship is observed between DVARS and FD in both approaches, OC-MPR significantly reduces the impact of FD compared to SE-MPR (β=715.10, CI_{95} [710.17, 720.04], $p<0.001$). This relationship is even more mitigated in the moderate (ME-MOD) (β=145.40, CI_{95} [141.92, 148.88], $p<0.001$) and conservative (ME-CON) (β=146.69, CI_{95} [143.05, 150.33], $p<0.001$) denoising approaches, which show similar modulatory effects on it. Note that this similarity is common, but not the same for all the subjects. For instance, ME-MOD showed larger reduction of motion related effects than ME-CON for two subjects (subject 003 and 007, Figures C.1 and C.2 respectively), while the oppos-

ite pattern was clearly observed in two other subjects (subject 004 and 009, Figures C.2 and C.3 respectively), and there was no apparent difference in the remaining subjects. However, considering all subjects and all sessions together, the difference between these the ME-MOD and ME-CON approaches is statistically not significant (β=1.29, CI_{95} [-0.70, 3.27], p>0.5). Compared to OC-MPR, both ME-MOD and ME-CON reduce the impact of FD on DVARS (β=130.84, CI_{95} [127.89, 133.79], p<0.001 and β=132.13, CI_{95} [128.99, 135.27], p<0.001 respectively) The aggressive strategy (ME-AGG) is the most successful in reducing motion-related effects described by FD on DVARS of all approaches.

Figure 4.5A plots the average percentage DVARS (left column) and average GM percentage BOLD response (central column) of all the BH trials across all of the sessions of a representative subject. The FD trace features a clear peak right after the end of the apnoea (highlighted in grey), likely associated with large head movement artefacts caused by the recovery breaths following the apnoea period. The percentage DVARS curves of the SE-PRE, SE-MPR and OC-MPR denoised timeseries reflect this peak in FD, which is absent in the ME-ICA based denoising timeseries, indicating a strong influence of movement on the signal intensity changes. All DVARS curves present a peak at a later time (between timepoints 25 and 30) that, as DVARS is akin to the first derivative of the BOLD signal changes, may agree with the return to the baseline seen in the BOLD response. The percentage BOLD signal change curves feature a delayed peak compared to the FD trace, reflecting a delayed CVR response compared to instantaneous head movements associated with respiration. However, they also feature a modulation in the BOLD signal change in correspondence with the peak in the FD trace, with the exception of ME-MOD and ME-AGG. The flattened DVARS and BOLD responses seen for ME-AGG indicate that the inclusion of the ME-ICA rejected components substantially removes part of the true CVR response, compared with the OC-MPR time courses. The average percentage DVARS and percentage BOLD response of the other subjects can be found in Appendix C (Figures C.4 to C.6).

Figure 4.5B plots the Manhattan distance between the average of N trials and the average of all 80 BH trials as N increases from 1 to 80. ME-AGG tends to be more similar to the total average compared to all the other timeseries. For most of the subjects, SE-MPR, OC-MPR and ME-MOD have a similar behaviour and need more trials than SE-PRE, ME-CON and ME-AGG to converge to the total average. Note that the convergence to the analysis-specific 'ground truth' BH response is not monotonic and fluctuates across trials of the same session and across sessions, indicating that the convergence does not depend only on the number of BH trials, but also on their quality and possible physiological variability in the CVR response across trials and sessions.

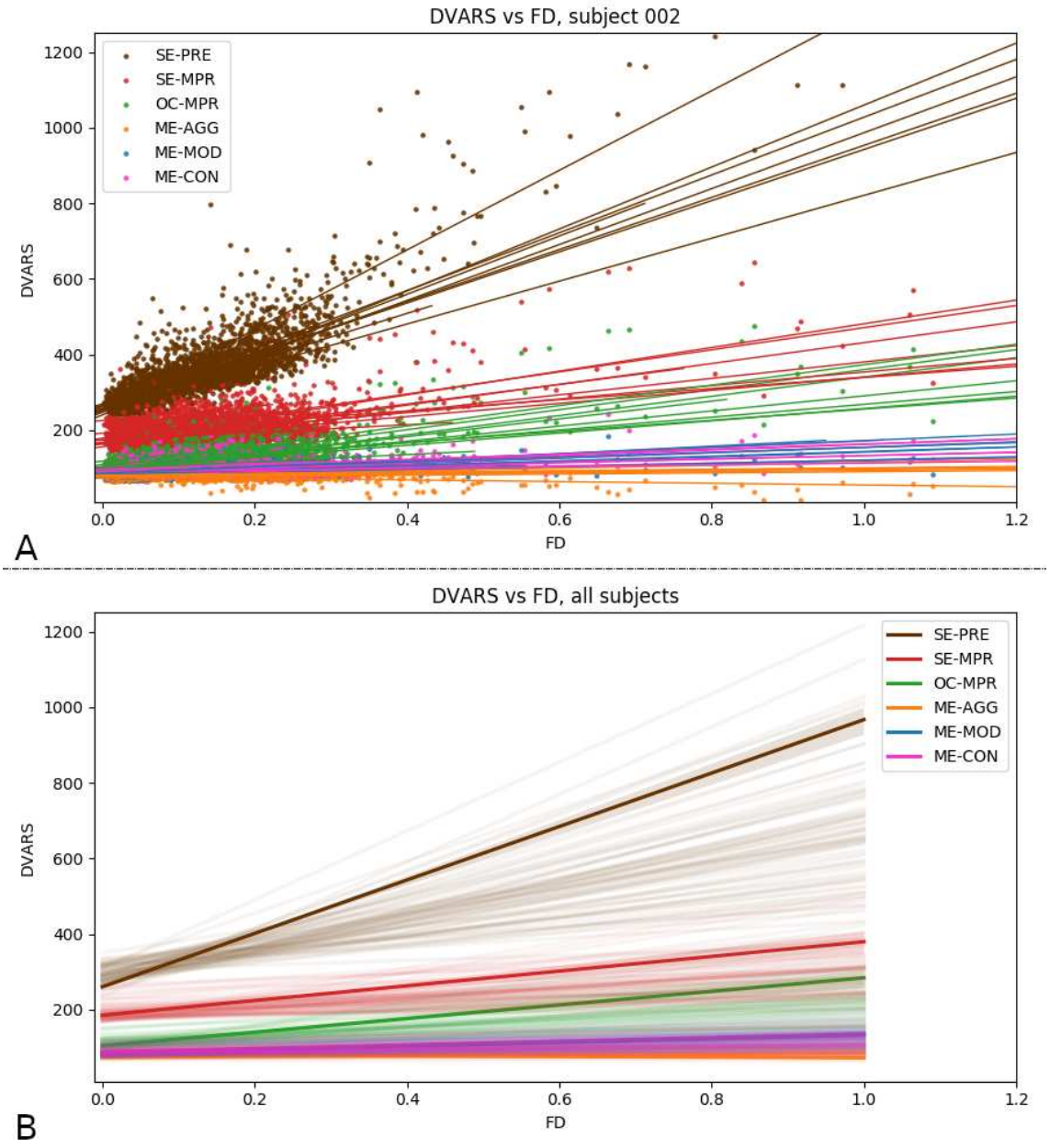

Figure 4.4: (A) Relation between the DVARS of the denoised data following different analysis pipelines and FD for a representative subject (subject 002). Each point represents a timepoint, each line represents the linear regression between both timeseries in a session. In general, OC-MPR shows lower DVARS than SE-MPR, but similar modulation of the DVARS-FD relationship. All the ICA denoising solutions performs better in reducing motion-related effects described by FD on DVARS. Between the ICA solutions, ME-AGG performs the best in reducing this relationship, while ME-MOD and ME-CON seem to be equivalent. (B) DVARS vs. FD for all the subjects. Each transparent line represents a session, the solid line represents the estimation across subjects and sessions. Similar patterns to the representative subject are shown. SE-PRE: raw data; SE-MPR: single-echo; OC-MPR: optimally combined; ME-AGG: aggressive; ME-MOD: moderate; ME-CON: conservative.

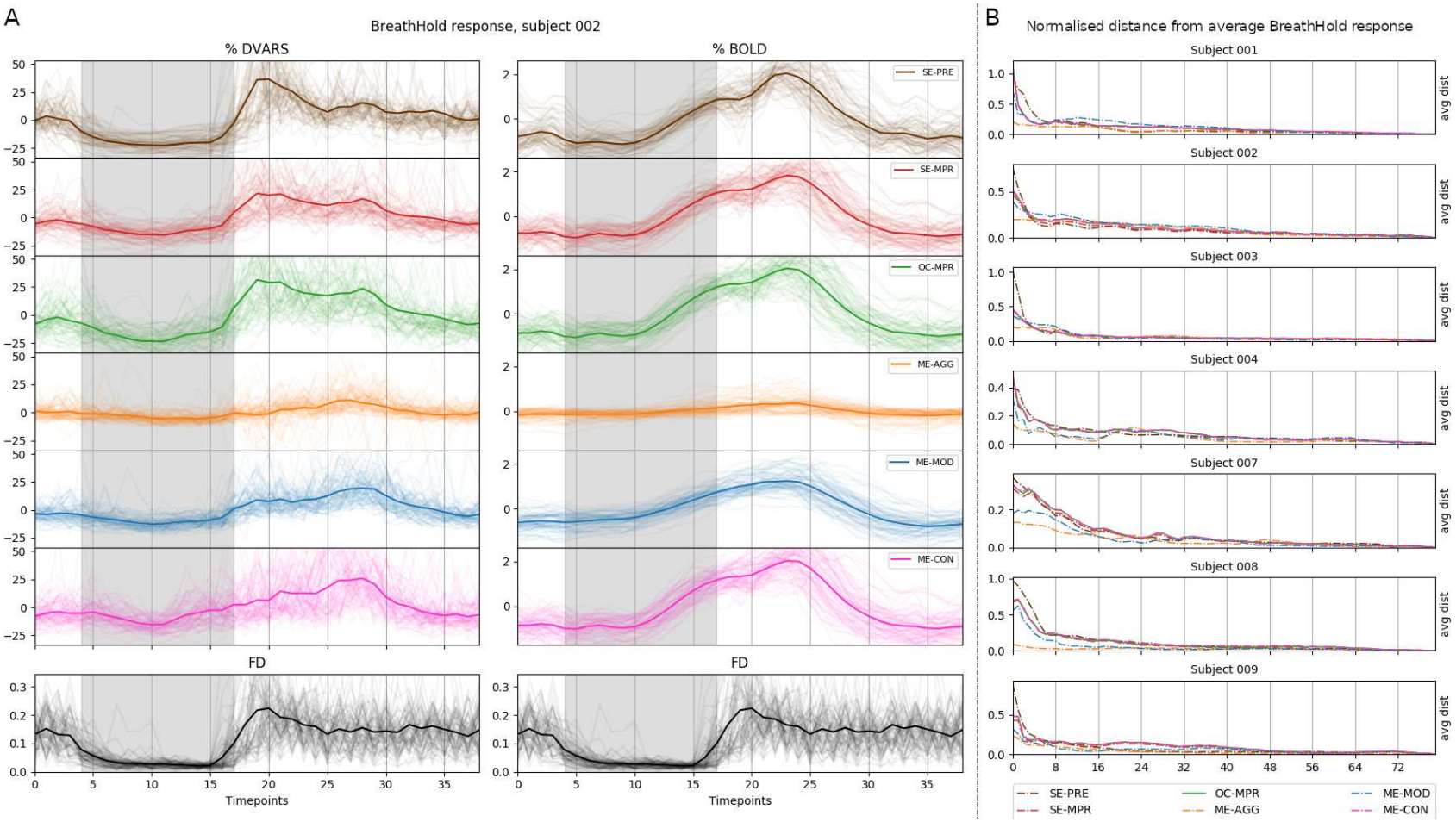

Figure 4.5: (A) Average GM %DVARS and %BOLD response of all BH trials across ten sessions for the same representative subject (subject 002). The apnoea period is highlighted in grey. Each transparent line is a trial, the solid line is the average across all the trials. (B) Manhattan distance between the average of N trials and the average of all 80 BH trials as N increases from 1 to 80 for each subject. Each vertical line divides the number of trials in each session. SE-PRE: raw data; SE-MPR: single-echo; OC-MPR: optimally combined; ME-AGG: aggressive; ME-MOD: moderate; ME-CON: conservative.

4.2.2 Cerebrovascular reactivity and lag maps

Figure 4.6 shows CVR (top) and lag (bottom) maps for all analysis strategies and all sessions of a representative subject (subject 002). The CVR and lag maps of other subjects are available in Appendix C (Figures C.7 to C.12). The CVR maps were masked to exclude the voxels that were not statistically significant or whose lag is at the boundary of the explored range and might not have been truly optimised or physiologically plausible. Across all subjects, SE-MPR features more spatial variation and speckled noise in CVR and lag estimates of voxels within the same brain region compared to ME approaches like OC-MPR or ME-CON. In general, the ME-AGG and ME-MOD approaches do not yield CVR maps with as much clear distinction between brain tissues or delineation of the cortical folding and subcortical structures (e.g. see putamen and caudate nucleus) as obtained with the OC-MPR and ME-CON models. Among the ICA-based approaches, the adoption of an aggressive (ME-AGG) or moderate (ME-MOD) modelling strategy results in lag maps without anatomically defined patterns, as well as a higher rate of voxels with a lag estimation that is not within physiologically plausible range, and in CVR maps with lower responses and fewer significant voxels. ME-AGG also produces CVR maps with a higher percentage of negative values than any other analysis model, and a reduced CVR response in voxels near the posterior part of the superior sagittal and transverse sinuses.

Figure 4.7 shows the distribution of the average values of CVR, lag, and the percentage of significant voxels for all subjects and sessions, and across all denoising strategies after thresholding. Considering the summaries within GM, although SE-MPR shows higher average CVR compared to the other approaches, it also features lower percentage of significant voxels compared to OC-MPR, ME-MOD and ME-CON. ME-AGG shows the lowest CVR value of all strategies, the most variable average of lag values, as well as the lowest percentage of significant voxels. ME-MOD features a lower percentage of significant voxels than SE-MPR, OC-MPR, and ME-CON. The same considerations can be extended to the WM. Table 4.2 reports the subject average CVR, lag, and the percentage of significant voxels across all denoising strategies after thresholding for GM only. For all models, the average CVR in the GM in the group and in each subjects are comparable or higher than the reported BH-induced CVR (in %BOLD/mmHg) in previous literature (Bright, Donahue, Duyn, Jezzard & Bulte, 2011; Bright & Murphy, 2013a; Lipp et al., 2015; Pinto, Jorge, Sousa, Vilela & Figueiredo, 2016). Table 4.3 reports the same values for WM.

4.2.3 Comparison of CVR and lag estimation and reliability across denoising strategies

Figure 4.8 shows the results of comparing the CVR and lag maps across all of the denoising strategies. The top row shows the thresholded χ score of the contrast between SE-MPR and all other denoising strategies, while the other maps depict the pairwise comparison between all of the denoising strategies. Among the most interesting comparisons, all of the strategies based on ME have lower CVR and an anticipated response in areas vascularised by big vessels (indicated by an arrow in the figure), where the blood transit time is usually faster compared to the rest of the brain. This could indicate that the response shown in SE-MPR could be overestimated due to the misestimation of its lag. Compared to SE-MPR, ME-MOD shows lower CVR and a delayed response in subcortical areas, while OC-MPR and ME-CON show higher CVR and an anticipated response in the insula, frontal, and parietal areas. OC-MPR shows no statistically significant differences with ME-CON, but a general higher CVR and an anticipated response compared to ME-MOD and ME-AGG, with the exception of the cerebellum, where it shows a delayed response. This difference could be related to the different local impact of motion artefacts, especially on the cerebellum. Between the three approaches based on ME-ICA, ME-AGG features generally lower CVR

SE-MPR	OC-MPR	ME-CON	ME-MOD	ME-AGG	
β =512.65*, CI_{95} [506.88, 518.42]	β =527.21*, CI_{95} [521.74, 532.68]	β =659.34*, CI_{95} [654.27, 664.41]	β =658.05*, CI_{95} [653.09, 663.01]	β =715.10*, CI_{95} [710.17, 720.04]	SE-PRE
	β =715.10*, CI_{95} [710.17, 720.04]	β =146.69*, CI_{95} [143.05, 150.33]	β =145.40*, CI_{95} [141.92, 148.88]	β =202.45*, CI_{95} [199.02, 205.88]	SE-MPR
		β =132.13*, CI_{95} [128.99, 135.27]	β =130.84*, CI_{95} [127.89, 133.79]	β =187.90*, CI_{95} [185.01, 190.78]	OC-MPR
			β =1.29, CI_{95} [-0.70, 3.27]	β =55.77*, CI_{95} [53.91, 57.63]	ME-CON
				β =57.05*, CI_{95} [55.59, 58.52]	ME-MOD

Table 4.1: Comparisons of motion dependence in image intensity and general noise between different denoising approaches. * significant for $p<0.001$, all p values are computed with Satterthwaite's method, and they are the equivalent of the p value after Šidák correction for multiple comparisons. SE-PRE: raw data, SE-MPR: single-echo, OC-MPR: optimally combined, ME-AGG: aggressive, ME-MOD: moderate, ME-CON: conservative.

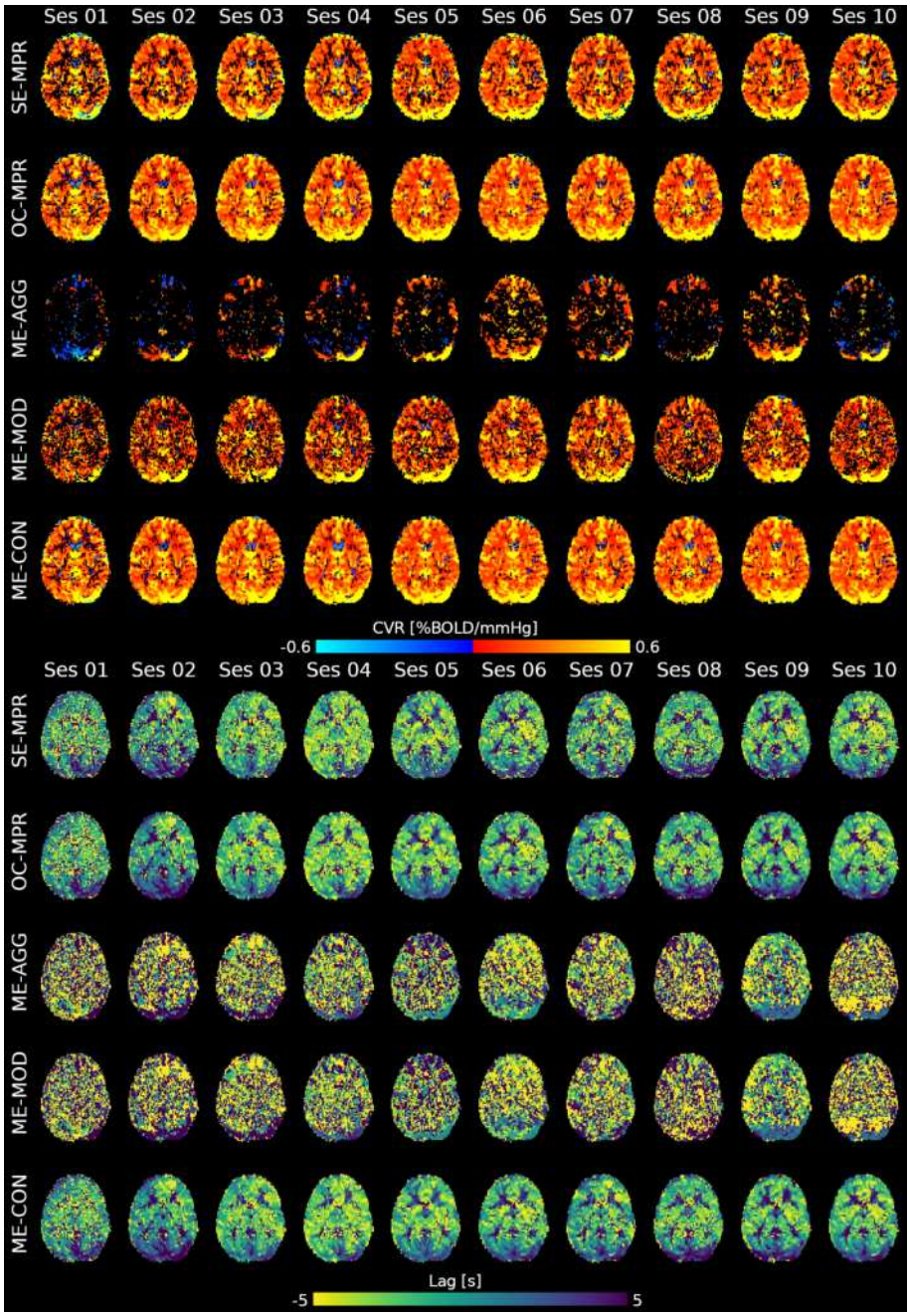

Figure 4.6: Top: Thresholded CVR map obtained with the different lagged-GLM analysis for all the sessions of a representative subject (subject 002). Note the low CVR response in ME-AGG, depicting numerous voxels with a negative values, as well as the increased amount of masked voxels in SE-MPR, ME-AGG and ME-MOD. Bottom: Unthresholded lag map obtained with the different lagged-GLM analysis, for all the sessions of the same subject. These lag maps represent the delay between the best shifted version of the PETCO2hrf trace and the bulk shift (i.e. the best match between average grey matter signal and PETCO2hrf trace). The scale from -5 to +5 represents earlier to later haemodynamic responses. Note the lack of anatomically informative patterns in ME-MOD and ME-AGG. SE-MPR: single-echo; OC-MPR: optimally combined; ME-AGG: aggressive; ME-MOD: moderate; ME-CON: conservative.

Subject	Average value	SE-MPR	OC-MPR	ME-AGG	ME-MOD	ME-CON
001	CVR [%BOLD/mmHg]	0.54	0.5	0.37	0.43	0.49
	Lag [s]	-0.54	-0.49	0.4	-0.11	-0.4
	% significant voxels	9.79	10.44	3.33	8.1	10.75
002	CVR [%BOLD/mmHg]	0.38	0.35	0.24	0.3	0.35
	Lag [s]	-0.38	-0.43	0.58	0	-0.42
	% significant voxels	10.67	11.65	3.29	8.61	11.92
003	CVR [%BOLD/mmHg]	0.4	0.34	0.18	0.31	0.33
	Lag [s]	-0.4	-0.28	-0.73	-0.74	-0.26
	% significant voxels	7.42	8.04	3.62	6.55	8.28
004	CVR [%BOLD/mmHg]	0.44	0.38	0.08	0.32	0.37
	Lag [s]	-1	-1.12	-0.57	-0.87	-1.1
	% significant voxels	8.46	9.27	2.87	6.57	9.56
007	CVR [%BOLD/mmHg]	0.33	0.29	0.17	0.28	0.29
	Lag [s]	-0.7	-0.61	0.95	-0.1	-0.53
	% significant voxels	7.98	9.19	2.6	6.31	9.44
008	CVR [%BOLD/mmHg]	0.34	0.14	-0.03	0.26	0.14
	Lag [s]	-0.98	-1.19	-0.28	-0.6	-1.18
	% significant voxels	6.34	6.89	1.5	4.9	7.19
009	CVR [%BOLD/mmHg]	0.44	0.38	-0.18	0.31	0.37
	Lag [s]	-1.75	-1.75	0.91	-0.11	-1.69
	% significant voxels	7.52	9.16	2.25	6.42	9.55
Total	CVR [%BOLD/mmHg]	0.41	0.34	0.12	0.32	0.33
	Lag [s]	-0.82	-0.84	0.18	-0.36	-0.80
	% significant voxels	8.31	9.23	2.78	6.78	9.53

Table 4.2: Subject average CVR, lag, and percentage of statistical voxels in the grey matter across strategies. The last three lines are the group average. SE-PRE: raw data, SE-MPR: single-echo, OC-MPR: optimally combined, ME-AGG: aggressive, ME-MOD: moderate, ME-CON: conservative. The same table for the WM voxels is available in Table 4.3.

Subject	Average value	SE-MPR	OC-MPR	ME-AGG	ME-MOD	ME-CON
001	CVR [%BOLD/mmHg]	0.26	0.25	0.1	0.22	0.24
	Lag [s]	-0.74	-0.6	-0.31	-0.39	-0.5
	% significant voxels	4.41	5.26	0.95	3.83	5.39
002	CVR [%BOLD/mmHg]	0.17	0.17	0.07	0.15	0.17
	Lag [s]	0.13	0.3	0.19	0.07	0.28
	% significant voxels	5.76	7.08	1.04	4.79	7.18
003	CVR [%BOLD/mmHg]	0.19	0.17	0.11	0.16	0.17
	Lag [s]	-0.23	0.01	-0.8	-0.5	0.04
	% significant voxels	4.75	6.01	1.71	4.45	6.17
004	CVR [%BOLD/mmHg]	0.21	0.2	0.07	0.17	0.2
	Lag [s]	-1.31	-1.3	-0.98	-0.98	-1.25
	% significant voxels	3.79	4.77	0.92	3.24	4.89
007	CVR [%BOLD/mmHg]	0.16	0.14	0.08	0.13	0.14
	Lag [s]	-1.03	-0.83	0.28	-0.5	-0.75
	% significant voxels	3.65	4.9	0.94	3.08	5
008	CVR [%BOLD/mmHg]	0.18	0.17	0.03	0.14	0.16
	Lag [s]	-1.1	-1.14	-0.36	-0.52	-1.08
	% significant voxels	4.43	5.5	0.79	3.71	5.69
009	CVR [%BOLD/mmHg]	0.2	0.19	-0.02	0.16	0.18
	Lag [s]	-2.16	-2.1	0.64	-0.56	-2.07
	% significant voxels	2.48	3.53	0.59	2.38	3.64
Total	CVR [%BOLD/mmHg]	0.2	0.18	0.06	0.16	0.18
	Lag [s]	-0.92	-0.81	-0.19	-0.48	-0.76
	% significant voxels	4.18	5.29	0.99	3.64	5.42

Table 4.3: Subject average CVR, lag, and percentage of statistical voxels in the white matter across strategies. SE-PRE: raw data; SE-MPR: single-echo; OC-MPR: optimally combined; ME-AGG: aggressive; ME-MOD: moderate; ME-CON: conservative.

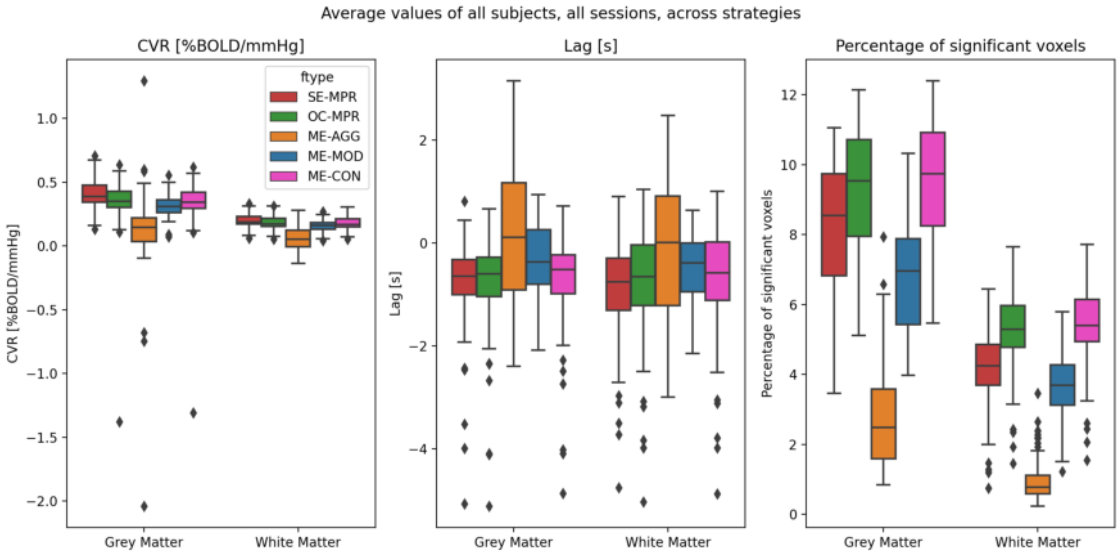

Figure 4.7: Average values of CVR, lag, and percentage of significant voxels, for voxels in the grey and white matter tissues separately, for all denoising strategies. The dots correspond to a singular session of a singular subject considered an outlier in the distribution. Note that all maps were thresholded before plotting. SE-MPR: single-echo; OC-MPR: optimally combined; ME-AGG: aggressive; ME-MOD: moderate; ME-CON: conservative.

compared to the other two, and a generally anticipated response compared to ME-MOD and a delayed response to ME-CON.

In order to assess the reliability of each model, voxelwise ICC(2,1) maps were also computed for both CVR and haemodynamic lag. Figure 4.9 depicts the ICC(2,1) maps for all analysis strategies for both CVR and lag maps, as well as their distributions. High ICC scores indicate that the intra-subject variability is lower than the inter-subject variability, hence the estimations of CVR or haemodynamic lag can be considered consistent across sessions. Conversely, low ICC scores indicate that the inter-subject variability is low compared to the intra-subject variability, hence the estimations of CVR and haemodynamic lag cannot be considered consistent across sessions. Following the classification given by (Cicchetti, 2001), an ICC score lower than 0.4 is considered poor, lower than 0.6 fair, lower than 0.75 good, and equal or higher than 0.75 excellent.

In terms of whole brain CVR reliability, the ME-CON demonstrated excellent reliability (spatial average across the whole brain of 0.86 ± 0.16) as well as the highest ICC values among all methods tested, closely followed by the OC-MPR (excellent, 0.85 ± 0.16), SE-MPR (excellent, 0.81 ± 0.19), and ME-MOD (excellent, 0.79 ± 0.19), while ME-AGG had a fair reliability (0.46 ± 0.22). If only voxels in GM are considered, the ICC of all approaches increases slightly (0.88 ± 0.14, 0.87 ± 0.15, 0.85 ± 0.17, 0.82 ± 0.17, and 0.49 ± 0.22 for ME-CON, OC-MPR, SE-MPR, ME-MOD, and ME-AGG respectively). Despite the average fair reliability observed for ME-AGG, it can be observed that this approach exhibits a considerable number of voxels with poor reliability (ICC below 0.4). These voxels are mostly located in white matter, which also exhibit lower ICC values in the other analyses. In terms of whole-brain lag reliability, OC-MPR performed the best (good reliability, 0.67 ± 0.21), closely followed by ME-CON (good reliability, 0.66 ± 0.21). SE-MPR, ME-MOD, and ME-AGG demonstrated fair lag reliability (0.6 ± 0.22 and 0.42 ± 0.19, 0.41 ± 0.20, respectively). Considering only GM voxels, the reliability of all the

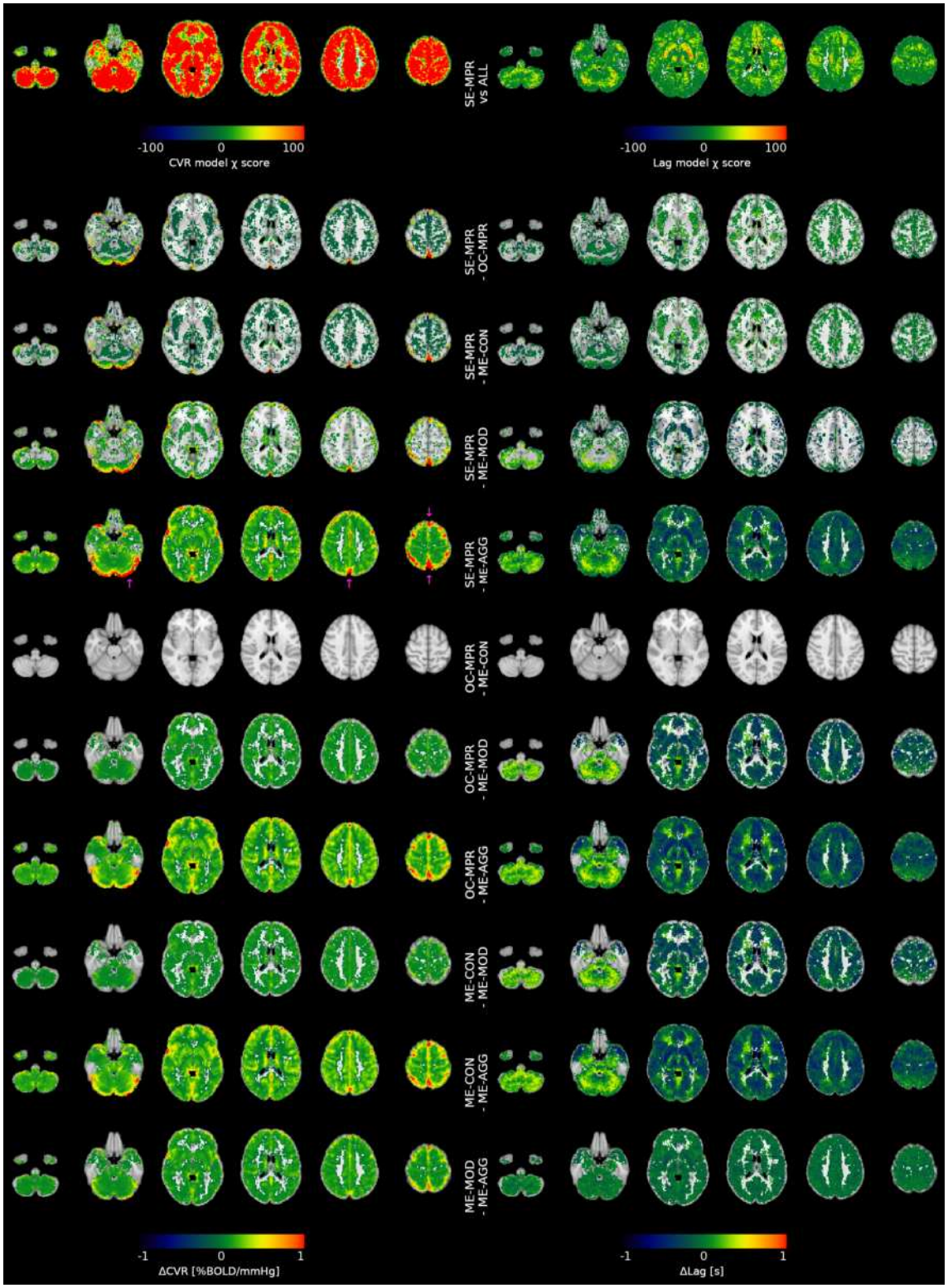

Figure 4.8: Top row: Thresholded χ value of the LME model used for the comparison of CVR (left) and lag (right) maps across all denoising strategies. Other rows: Pairwise comparison between denoising strategies. Arrows indicate areas vascularised by big vessels. SE-MPR: single-echo; OC-MPR: optimally combined; ME-AGG: aggressive; ME-MOD: moderate; ME-CON: conservative.

approaches increases minimally (0.68 ± 0.21, 0.67 ± 0.21, 0.61 ± 0.21, 0.43 ± 0.19, 0.42 ± 0.20, for OC-MPR, ME-CON, SE-MPR, ME-MOD, and ME-AGG respectively). The reliability of CVR lag estimates was lower than that of CVR amplitude estimates, even though certain cortical regions, such as the visual and motor cortices, also show excellent ICC values for the OC-MPR and ME-CON denoising approaches. Interestingly, it can be observed that ME-MOD offers excellent ICC values for the CVR response amplitude in grey matter voxels, whereas they are poor for the lag estimates. Note that the reliability of OC-MPR CVR maps is generally higher, at least in the GM, than the reliability of RSFA, ALFF, or fALFF (see Figures 2.15 to 2.17 respectively)

4.3 Discussion

This study compared five different analysis strategies based on a lagged-GLM model (Moia et al., 2020) to simultaneously remove motion-related effects and non-BOLD artefacts in the BOLD fMRI signal while estimating CVR and haemodynamic lag in order to identify the best modelling approach for BH paradigms in which prominent task-correlated artefacts coexist with the effect of interest. The lagged-GLM model adopted in this study is similar to other models for CVR estimation that take into account local variations in the haemodynamic lag (Donahue et al., 2016; Geranmayeh et al., 2015; Murphy et al., 2011; Sousa et al., 2014; Tong et al., 2011). The main difference with such models is that, in this lagged-GLM approach, after a first bulk shift that matches the average GM response with the $P_{ET}CO_2 hrf$ regressor, the denoising and the voxelwise optimised response estimation take place simultaneously. This ensures that the interaction between regressors is properly taken into account and that the degrees of freedom of the model are properly accounted for in statistical inference.

Among all possible modelling strategies, the five presented here were included in our analysis for different reasons. The optimal combination of ME-fMRI data, with subsequent motion and Legendre polynomial regression (MPR), was expected to remove more noise and improve reliability of the CVR estimation due to its increased BOLD sensitivity compared to MPR on single-echo data, which is the standard approach for BH CVR estimation (Cohen & Wang, 2019). While optimal combination of ME volumes alone can partially reduce the random noise present in the data, it still cannot remove artefactual signals, such as motion-related effects, as illustrated in Figure 4.4 in which SE-MPR and OC-MPR exhibit the same dependence of signal changes (DVARS) with motion (FD). For this reason, we further adopted three different ME-ICA based approaches, ranging from a conservative to an aggressive motion removal. ICA-based approaches are known to outperform traditional nuisance regression, such as MPR, in typical denoising fMRI data, possibly because they can identify and separate artefactual sources in the data in a data-driven and non-linear manner (Griffanti et al., 2014; Pruim, Mennes, Buitelaar & Beckmann, 2015; Pruim, Mennes, Rooij et al., 2015; Salimi-Khorshidi et al., 2014). In the current study, ICA was not applied to single-echo data because it has already been demonstrated that ICA-based denoising applied to OC data outperforms ICA denoising applied to single-echo data (Dipasquale et al., 2017) and the ICs estimated from OC data might not have matched the ICs obtained from single-echo data, making such comparison less straight forward than the one based on MPR.

Furthermore, spatial ICA decomposition was applied rather than temporal ICA decomposition because the latter requires many more observations than normally available. Having many sessions for each subject, temporal ICA could have been leveraged in this study which could be more appropriate than spatial ICA to estimate a proper decomposition of timeseries sources (Smith et al., 2012), improving the modelling of temporal noise

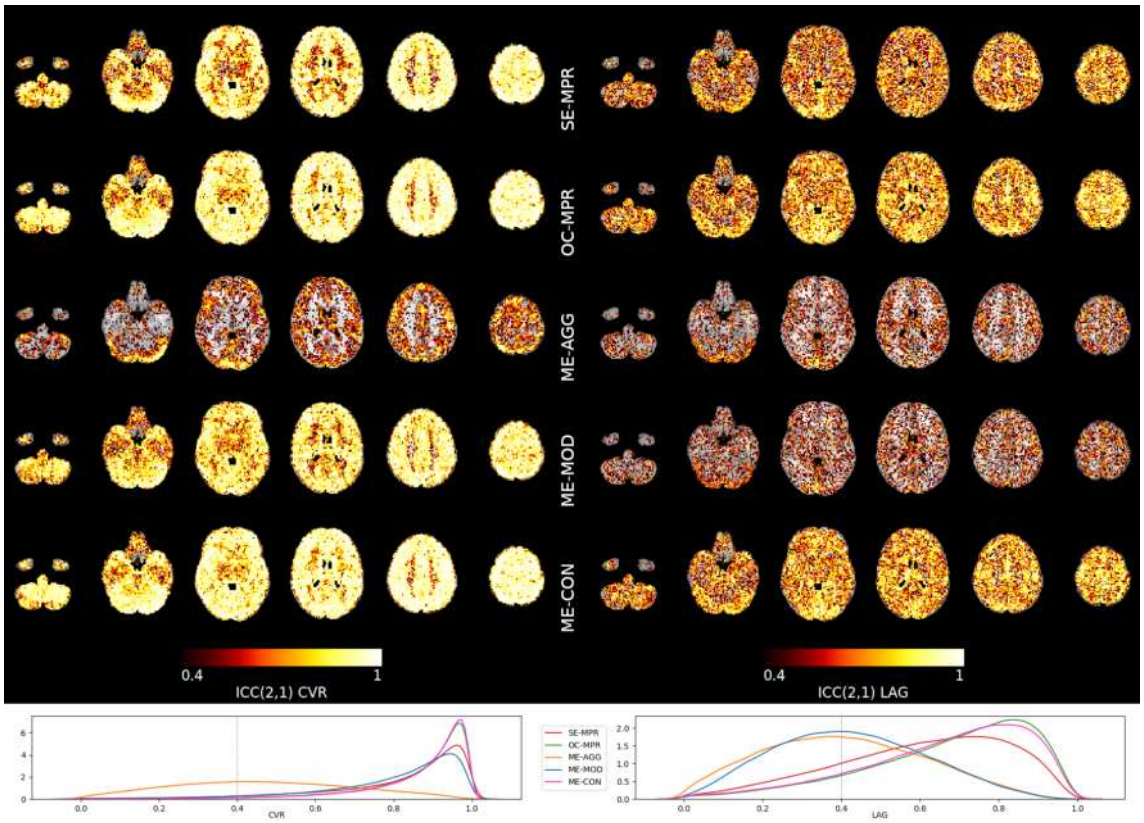

Figure 4.9: ICC(2,1) maps of CVR (left) and haemodynamic lag (right) for each analysis pipeline. The maps are thresholded at 0.4 since scores lower than it indicate poor reliability. A high ICC score indicates that the inter-subject variability is higher than the intra-session variability, while a low ICC score suggest that the variability across sessions is the same as the one across subjects. Following the classification given by Cicchetti (2001), an ICC score lower than 0.4 is considered poor, lower than 0.6 fair, lower than 0.75 good, and equal or higher than 0.75 excellent. The bottom rows depict the whole brain distribution of ICC scores across voxels. Note how OC-MPR and ME-CON have generally higher ICC scores than the other approaches, and are very similar to each other, while ME-AGG has the lowest ICC scores for both CVR and lag maps. SE-MPR: single-echo; OC-MPR: optimally combined; ME-AGG: aggressive; ME-MOD: moderate; ME-CON: conservative. The distribution of ICC scores across grey matter voxels only is available in Figure 4.10

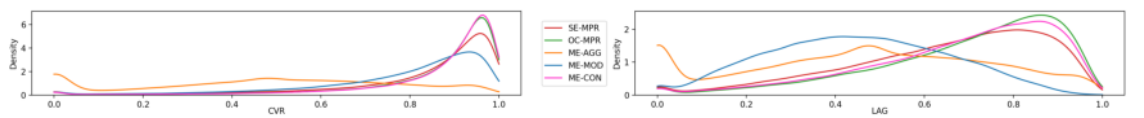

Figure 4.10: Grey matter distribution of ICC scores across voxels for all the pipelines. SE-PRE: raw data; SE-MPR: single-echo; OC-MPR: optimally combined; ME-AGG: aggressive; ME-MOD: moderate; ME-CON: conservative.

(Glasser et al., 2018) and potentially leading to better disentanglement of noise from CVR effects. However, spatial ICA was chosen in order to maintain the independence of each session, both to simulate a more common denoising approach to fMRI data, and to be able to capture session-specific noise contributions that could have been missed otherwise. Further studies could compare temporal and spatial ICA denoising for CVR mapping when many temporal samples have been collected in the same session, for instance reducing the TR by acquiring fewer echoes. Here, instead of conventional multi-echo protocols with three or four echoes, five echoes were acquired to facilitate and improve the classification of the ICs based on their TE-dependence (Kundu et al., 2013).

The choice of comparing different levels of orthogonalisation of only the ICA-based nuisance regressors compared to regressors of interest might seem in contrast with previous literature suggesting that orthogonalisation of collinear confounding factors could lead to misinterpreted results (Mumford et al., 2015). Our results clearly demonstrated that using the original (e.g., non orthogonalised) rejected ICs as nuisance regressors in the analysis (ME-AGG) removes the CVR effect of interest (see Figures 4.6, 4.7, 4.9, and 4.10). To decide which regressors should be orthogonalised, and with respect to what, we considered the different origin of the nuisance regressors. While Legendre polynomials and motion parameters can be considered adequate models of noise sources in the data, intrinsic data-driven regressors may well contain variance related to the effect of interest, especially as spatial ICA was adopted and because of the high collinearity between the $P_{ET}CO_2hrf$, motion, physiological adaptations to vascular dilation (e.g. cerebrospinal fluid flows), or changes in the magnetisation related to breathing (Raj et al., 2001). In these scenarios, it becomes more important to understand how to properly implement ICA denoising in order to preserve the effect of interest. For these reasons, three different ICA-based approaches were selected, from an aggressive strategy to a conservative approach, to assess if they preserved the BOLD effects related to the CVR response happening at different lags.

As hypothesised, all of the ME-based solutions outperformed the SE-MPR model in their ability to account for the effect of motion, summarized in terms of FD, on the fMRI signal intensity changes, described in terms of DVARS (see Figure 4.4). Furthermore, all of the ICA-based strategies outperformed traditional MPR, and within ICA-based strategies, the aggressive one (ME-AGG) showed the best performance to remove these motion-related effects in the signal. However, observing the average DVARS and BOLD response time-courses (Figure 4.5) and the CVR and lag maps (Figure 4.6) it becomes evident how aggressive and moderate approaches result in poor estimates of CVR responses, even compared to the SE-MPR approach. Similarly, these two approaches result in the estimated haemodynamic lag hitting the boundaries of a physiologically plausible lag range in healthy adults. The substantial reduction in the CVR estimates in the aggressive approach (Figures 4.5 and 4.6) occurs because the effect of interest can also be explained as a linear combination of the timecourses of rejected ICs related to motion, vascular effects or large susceptibility changes due to chest expansions and contractions while performing the BH task (Caballero-Gaudes & Reynolds, 2017; Griffanti et al., 2017). As for the moderate approach, the lower estimates of CVR could be because orthogonalising data-driven nuisance regressors with respect to the $P_{ET}CO_2hrf$ trace per sé is not sufficient to save all the variance associated to real CVR. The $P_{ET}CO_2$ trace can only be estimated during exhalations, hence it is unable to capture local dynamic signal changes that are captured by ICs timeseries. Furthermore, CVR has a sigmoidal non-linear relation with the $P_{ET}CO_2hrf$ trace (Bhogal et al., 2014), and the local BH-induced BOLD response has a complex shape, in terms of response amplitude and temporal delays, due to multiple physiological factors (Magon et al., 2009) that must be accounted for in order to improve its estimation and

characterization. These results illustrate that these local complexities might be adequately captured by the accepted ICs timecourses. Hence, not removing this CVR-related variance from the rejected ICs prior to their inclusion as nuisance regressors in the model is detrimental as it is observed with the ME-MOD and ME-AGG approaches. In other words, only a conservative approach (ME-CON) that preserves the BOLD variance associated with local CVR responses performs well, while also reducing motion-related effects more than conventional MPR models.

To further explore the benefit of different modelling strategies, the intraclass coefficient coefficient ICC(2,1) was used to assess the reliability of the resulting CVR and haemodynamic lag maps over the course of two and a half months (ten sessions). This was the first time that CVR reliability was tested over the course of ten sessions in individual subjects, and the first time that intersession haemodynamic lag reliability was tested. The ME-CON and OC-MPR strategies featured the greatest reliability for CVR and lag estimation, while the ME-AGG and ME-MOD approaches produced lower reliability values than even the simple SE-MPR model.

The lag maps are computed as the temporal offset related to the bulk shift, which is obtained by aligning the average GM BOLD response with the $P_{ET}CO_2 hrf$ trace. If the bulk shift computation is misestimated this would create a systematic bias in the estimated lag maps, potentially reducing the apparent intersession reliability. While the CVR reliability should not be affected by this issue, due to the use of a lagged-GLM approach that can overcome bulk shift misestimation (see session 4 of subject 007 in Figure C.10), the true lag map reliability might be higher than reported here.

Regarding CVR reliability, the whole-brain average reliability of SE-MPR was comparable to long-term reliability (days or weeks apart) found in previous studies of CVR induced by BH (Peng et al., 2019), by paced deep breathing (Sousa et al., 2014), or by gas challenges (Leung et al., 2016), and higher than that reported in other studies on BH induced CVR estimated with a non-lagged optimized $P_{ET}CO_2 hrf$ trace (Lipp et al., 2015) or with Fourier modelling (Pinto et al., 2016), and by gas challenges (Dengel et al., 2017; Evanoff et al., 2020). Consequently, the reliability of CVR estimates obtained with the optimal combination dataset and conservative ME-ICA modelling approaches were found higher than those previously reported in the literature. However, all strategies produced a reliability that was lower than the short-term (within-session) reliability reported in BH induced CVR (Peng et al., 2019), resting state based CVR (Liu, Li et al., 2017), and gas challenge induced CVR (Leung et al., 2016), although lower intersession reliability in gas challenges has also been reported (Dengel et al., 2017; Evanoff et al., 2020). Note that the reliability observed in this study seems to be globally higher and spatially less variable than that reported in previous studies (Lipp et al., 2015; Sousa et al., 2014). However, discrepancies in the reliability measurements might be related to the different methods used to compute the CVR maps and the ICC score itself.

Using ICC to test reliability has the drawback that higher scores might be related to the presence of residual task-correlated motion effects that artificially stabilise the CVR estimation and reduce intrasubject variability compared to intersubject variability. In fact, recent studies have shown that individuals have particular movement patterns during fMRI sessions that may be a stable characteristic of a person (Bolton et al., 2020) related to stable physical characteristics, such as body mass index (Ekhtiari, Kuplicki, wen Yeh & Paulus, 2019) and could even be a heritable characteristic (Couvy-Duchesne et al., 2014; Hodgson et al., 2017). If subjects have similar motion patterns across the 10 repeated sessions, fMRI responses might appear more similar than they truly are, and the ICC might be inflated by such effects. Moreover, higher spatial reliability does not necessarily

mean higher accuracy: a denoising strategy might be systematically misestimating CVR or haemodynamic lag. The fact that both optimal combination with traditional nuisance regression and the conservative ME-ICA denoising approaches resulted in similar CVR and lag spatial patterns and exhibited higher reliability than the single-echo model, while at the same time reduced the apparent effect of motion on the data variance, suggests that such drawbacks are mitigated in our data. However, further studies could compare different BH analysis strategies with a CVR estimation based on an independent computerised gas delivery protocol.

Another possibility would be to assess CVR in resting state fMRI, either measuring resting fluctuations in exhaled CO_2 levels (Golestani et al., 2016; Lipp et al., 2015), or by using a band of the power spectrum of the global signal as a regressor of interest (Liu, Li et al., 2017; Liu et al., 2020). Such method might be more robust to motion collinearity, as the amount of movement in each breath is less pronounced and not consistently time-locked to the paradigm cues. At the same time, the lower amplitude of intrinsic CO_2 fluctuations relative to BH CO_2 change might also make this approach more susceptible to general motion effects and other sources of variance (e.g. neural or artefactual) unrelated to CO_2. Moreover, previous work has shown that the optimal temporal shift between BOLD and $P_{ET}CO_2$ is hard to reliably identify in resting state data alone, in contrast to BH datasets where the temporal shift can be reliably identified (Bright et al., 2017; Stickland et al., 2021). Current resting state fMRI methods for CVR mapping may therefore be inappropriate to use with the lagged-GLM approach that was applied here. Either way, the analyses presented in this study can be easily implemented in other CVR assessment pipelines to mitigate the dependence of the response on motion. Beyond BH-based CVR studies, similar conclusions might be applicable to other experimental paradigms that present high collinearity between the expected task induced activity and artefactual sources, such as in overt speech production with long trial durations (Birn et al., 1999; Birn et al., 2004; Gracco, Tremblay & Pike, 2005), that aim to use (ME-)ICA-based nuisance regressors as part of the model.

Note that MPR and ICA denoising are not the only viable options to reduce motion effects on fMRI and BH-induced CVR in particular, and advanced setups can be used to reduce motion during the acquisition itself. For instance, subject specific moulded head casts can be used to reduce head motion (Power, Silver et al., 2019). Mounting an MRI compatible camera or tracker in the scanner enables prospective motion correction techniques (Faraji-Dana, Tam, Chen & Graham, 2016; Maziero, Rondinoni, Marins, Stenger & Ernst, 2020; Parkes, Fulcher, Yücel & Fornito, 2018; Schulz et al., 2014; Zaitsev, Akin, LeVan & Knowles, 2017) or concurrent field monitoring enables the dynamic correction of field distortions dynamically (Vannesjo et al., 2015; Wilm et al., 2015) in order to effectively reduce effects of motion and magnetic field susceptibility changes. However, such advanced setups are available in typical MRI laboratories.

A limitation of the present study is that the results are influenced by the manual ICA classification. Despite being based on the automatic classification made by tedana, a manual approach was adopted because often multiple ICs clearly exhibiting CVR-related timeseries and spatial maps were misclassified as noise. This manual classification was made with a cautious approach: if an IC seemed to be temporally and spatially related to the CVR response, it was accepted. Manual classification is still considered the gold standard for the classification of ICA components when performed by experts, despite the introduction of automatic classification algorithms (Griffanti et al., 2017), calling for further improvements in the automatic classification of (ME-)ICA components for BH tasks.

Another limitation is the lack of a CO_2 automated delivery protocol. The choice not to

include one was driven by the necessity to reduce the discomfort of the participants during the imaging sessions, and because experiments with gas challenges require dedicated setups that are not typically available. Nevertheless, future studies should compare denoised CVR maps to a CVR estimation based on independent computerised gas delivery protocols. This would also help estimating the accuracy of the denoised results on top of the reliability analysis featured in the present study.

Moreover, despite the fact that a BH task can be a valid alternative to gas delivery protocols for CVR estimation and its easy implementation, not all the subjects in this study could perform the task during all of the sessions. In total, 86% of the sessions were completed successfully by the subjects, although three subjects had to be excluded due to poor performance or non-compliance to the task in a subset of the sessions (four in two subjects and six in the third, see Figure 2.5).

Finally, it is worth noticing that the adoption of ME imaging requires an increase in TR or a decrease in the spatial resolution. A way to cope for this issue is the adoption of simultaneous multi-slice (a.k.a. multiband) acquisition, and despite the fact that this choice might introduce additional slice-leaking artefacts, a ME-ICA based denoising approach can successfully deal with their removal (Olafsson et al., 2015).

Furthermore, This study adopted one of the echo volumes as an approximation of a single-echo acquisition. Further studies could evaluate if this solution improves the estimation of CVR compared to SE imaging with higher spatial or temporal resolution.

4.4 Conclusion

Breath Holding (BH) is a non-invasive, robust way to estimate cerebrovascular reactivity (CVR). However, due to the task-correlated movement introduced by the BH task, attention has to be paid when choosing an appropriate modelling strategy to remove movement-related effects while preserving the effect of interest ($P_{ET}CO_2 hrf$). We compared different multi-echo (ME) independent component analysis (ICA) based denoising strategies to the standard data acquisition and analysis procedure, i.e. single-echo motion parameters regression. We found that a conservative ICA-based approach, but not an aggressive or moderate ICA approach, best removes motion-related effects while obtaining reliable CVR and lag responses, although a simple optimal combination of ME data with motion parameters regression provides similar CVR and lag estimations, and both ME-based approaches offer improvements in reliability compared with single-echo data acquisition.

5. Cerebrovascular Reactivity and blood pressure

Changes in blood acidity induced by changes in CO_2 or acetazolamide injection are not the only triggers for CVR. Due to its nature as homeostatic process, like cerebral autoregulation and cerebral blood flow CVR can also be triggered during systemic changes in blood pressure (Fierstra et al., 2013; Panerai, 1998). Techniques such as thigh cuffs release (see Aaslid et al., 1989; Mahony, Panerai, Deverson, Hayes & Evans, 2000) or lower body negative pressure (LBNP, see Tan, 2012; Thrall et al., 2021) have been successfully implemented to measure cerebral autoregulation and blood flow with Transcranial Doppler ultrasound (TCD). Using the thigh cuffs release approach, Aaslid et al. (1989) showed that changes in blood pressure and CO_2 might modulate each other's effect on cerebrovascular resistance, although such findings were not replicated with LBNP (Thrall et al., 2021). However, it is plausible that since vasodilatory mechanisms are equally initiated by pressure and CO_2 variations, independently of whether they are related to cerebral autoregulation or CVR (Carr et al., 2021), changes in blood pressure may act as confounding factors when measuring CVR (Hetzel et al., 1999; Pericot Nierga et al., 2000; Regan et al., 2014), since changes in Mean Arterial Pressure (MAP) during hypercapnia might not be correlated with the increase in CO_2 (Smielewski et al., 1995).

This is more evident in pathology, since abnormal blood pressure states can alter the response to CO_2 variations. Artru and Colley (1984) demonstrated the lack of CVR to hypocapnia during induced hypotension in dogs, and the absence of autoregulation was equally found in hypertensive dogs (Harper, 1965). Although vasoreactivity to acetazolamide was found to be higher during hypertension in humans (Ficzere et al., 1997), there have been multiple reports of reduced reactivity to changes in CO_2, both in hypertensive rats (Leoni et al., 2011; Li et al., 2021) and in hypertensive humans (Dumville et al., 1998; Settakis, Páll et al., 2003), for which such reduced reactivity was associated with worse executive functions (Hajjar et al., 2014).

Moreover, it has been shown that blood pressure influences BOLD fMRI measurements, since BOLD is sensitive to changes in MAP (Whittaker, Driver, Venzi, Bright & Murphy, 2019). Hence, the role of pressure as a confounding factor in CVR measurement might

be even more important when the latter is estimated with BOLD-fMRI. However, to our knowledge, the impact of pressure on local CVR estimations in individuals has not been studied yet. As a consequence, the aim of this study is to investigate the relationship between CVR responses and lag with blood pressure measurements.

5.1 Material and Methods

5.1.1 Dataset

This study uses the BOLD fMRI data corresponding to the BH task and the corresponding CO_2 traces from all the sessions, as well as the anatomical T1-weighted and T2-weighted images from the first session, of the dataset described in chapter Chapter 2. In addition, it also uses part of the biometrics collected in each participant before each MRI session, in particular the pulse, the systolic and diastolic pressure.

5.1.2 Data analysis

BH data were preprocessed and analysed with the OC-MPR model described in Section 2.1.9 so as to obtain the CVR and lag maps for all subjects and sessions. The CVR and lag maps were then normalised to the MNI152 template (Grabner et al., 2006, 2.5 mm isotropic voxel resolution), spatially smoothed with a Gaussian kernel with 5 mm FWHM within a dilated GM mask (dilation of 1 voxel, considering only face neighbours), and all volumes were masked with the same mask.

The two measurements (once per arm) of systolic and diastolic pressure and cardiac pulse were averaged to provide one value per session. Then, Pulse Pressure (PP) and MAP were computed, as:

$$\begin{aligned} PP &= SP - DP \\ MAP &= DP + 1/3 PP \end{aligned} \tag{5.1}$$

The impact of MAP, PP, and cardiac pulse on the CVR and lag maps was evaluated with a Linear Mixed Effect (LME) model using 3dLMEr (Chen et al., 2013). Since the literature reports differences in CVR between males and females (see Barnes & Charkoudian, 2020; Carr et al., 2021), and difference of the impact of cardiac pulse on CVR between males and females (Sabra et al., 2020), the interactions between the sex of each participant and the other variables were added to the model. Finally, the random effects of session and subject and the interactions of subject with all other variables were modelled. In sum, the resulting model in R notation is given by:

$$CVR \sim sex \cdot (MAP + PP + pulse) + (1|ses) + ((MAP + PP + pulse)|subj) \tag{5.2}$$

This model was evaluated voxelwise and on the average value of CVR or lag across all the voxels within the dilated GM mask used for smoothing. To assess the statistical significance, the voxelwise results were thresholded at $p < 0.05$ after controlling for false discovery rate (Benjamini et al., 2006). In addition, clusters with a minimum size of 20 voxels (312.5 mm^3) with a neighbourhood of 26 voxels are reported.

5.2 Results

5.2.1 Average GM analysis

Considering the average GM value, the only significant effect was the mild and negative effect of cardiac pulse on lag ($\beta = -0.0369$, $z = -1.986$, see Table 5.1), indicating a relationship between higher cardiac pulse and an average earlier CVR onset in the GM.

	CVR (β)	Lag (β)
MAP	0.154	0.049
PP	0.336	0.023
Pulse	0.077	-0.037$\diamond$
Sex	-10.630	-0.903
MAP * Sex	-0.178	0.079
PP * Sex	-0.804	0.031
Pulse * Sex	-0.135	-0.002
MAP * M	0.065	0.089
PP * M	-0.066	0.039
Pulse * M	0.009	-0.038
MAP * F	0.242	0.010
PP * F	0.738	0.008
Pulse * F	0.144	-0.036

Table 5.1: Results of the LME model considering the average GM. $\diamond$ significant relationship, $p<0.05$.

5.2.2 Voxelwise analysis

The first three rows of Figure 5.2 depict the maps of voxelwise effects of MAP (top), PP (second), and sex (third) on CVR in our healthy cohort. As it can be observed in the top panel, multiple GM regions spreading across the entire cortex as well as the cerebellum exhibit a significant positive effect of MAP in CVR, that involves bilaterally the cerebellum, the medial occipital cortex, the parietal opercular cortex, the temporooccipital part of the middle temporal gyrus, the superior temporal gyrus, the posterior insular cortex, the cingulate gyrus, the postcentral gyrus, and the precuneous cortex (see Table D.1 in Appendix D). The maps shown in the second panel illustrate that the positive effects of PP on CVR exhibit a reduced extent than the effects of MAP, mainly involving clusters in regions of the left insula, the right auditory cortex, the middle temporal gyrus, and the medial superior frontal gyrus (see Table D.2 in Appendix D). No clusters of negative impact of MAP or PP on CVR were found significant with sufficient size. The bottom row of Figure 5.2 shows the impact of MAP (red), PP (green), and the overlap between the two (yellow). Interestingly, the overlap between the two is very limited, involving mainly only a small portion of the cerebellum (VI, bilateral), the right cingulate gyrus and temporooccipital part of the middle temporal gyrus, and the left posterior insular cortex and superior lateral occipital cortex. This fact indicates spatial independency between the impact of MAP and PP on CVR, and suggests the importance of considering both PP and MAP when assessing the effects of blood pressure on CVR.

The bottom panel of Figure 5.2 depicts the map of effects of sex on CVR, where positive effects indicate higher CVR in males versus females, and negative effects indicate the reverse. At the group level, females largely showed a higher CVR response compared to males across most of the GM, with the exception of the medial orbitofrontal gyrus. Table D.3 in Appendix D reports the extent and location of each cluster with a positive effect (i.e. males showed higher CVR than females), while Table D.4 in Appendix D reports the clusters of negative effects (i.e. males showed lower CVR than females).

A stricter statistical threshold was adopted to identify better the cluster of negative effects of sex over CVR. Hence, Table D.5 in Appendix D reports the cluster of negat-

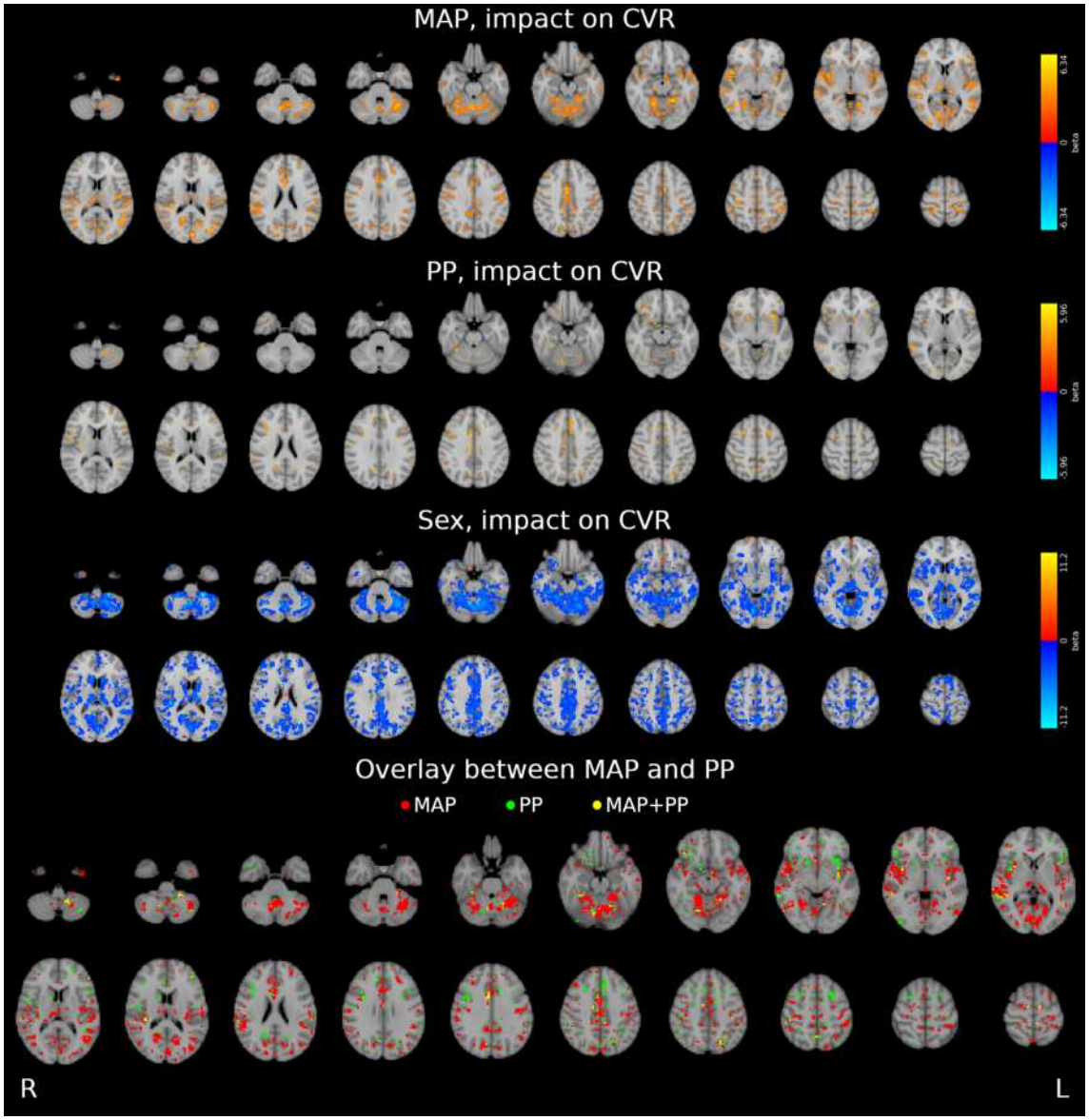

Figure 5.1: Top three rows: Local impact of MAP, PP, and sex on CVR. All results are FDR corrected and thresholded at $p < 0.05$. Bottom row: Overlap of significant voxels ($p < 0.05$) of the MAP and PP impact on CVR. Very few voxels (271) show overlapping effects, indicating that the impacts of MAP and PP are almost spatially independent.

ive effects for p <0.005, after FDR correction, revealing clusters across the cerebellum, the inferior and lateral occipital lobe, the medial parietal lobe, the postcentral gyrus, the cingulate and paracingulate gyri, the middle frontal gyrus, the insula, and the putamen bilaterally, across the temporooccipital part of the middle temporal gyrus and the superior temporal gyrus in the right hemisphere, and across the superior parietal lobule, the middle temporal gyrus, the central opercular cortex, the Juxtapositional Lobule Cortex, the superior frontal gyrus, and the amigdala in the left hemisphere.

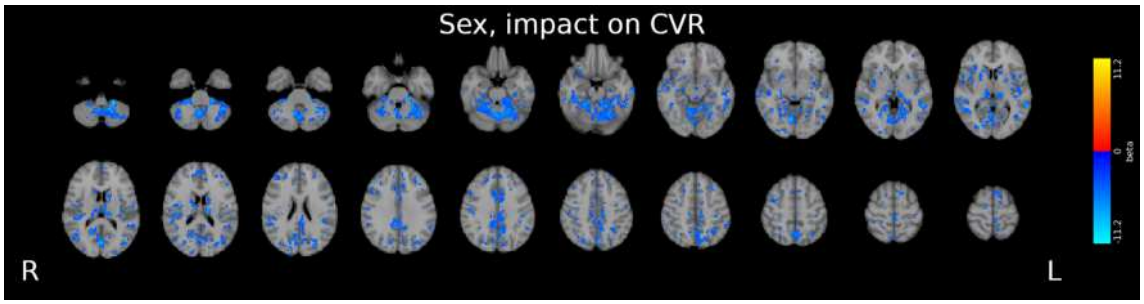

Figure 5.2: Local impact of sex on CVR, thresholded at p <0.005 (FDR corrected).

No significant effects were found for cardiac pulse or the interactions of the variables. Notably, no significant effects on the lag were found for any variable (MAP, PP, cardiac pulse, or sex), nor for their interactions.

5.3 Discussion

This study demonstrates that two blood pressure measurements, namely MAP and PP, as measured immediately prior to the MRI session, show a significant relationship with BOLD fMRI-based CVR during BH, and this relationship varies across brain regions. This is in line with previous findings that reported an interaction between blood pressure and CVR, although the polarity of the interaction observed in our data is opposite to that reported by Dumville et al. (1998), Regan et al. (2014), who show a negative effect of MAP on CVR, estimated with TCD, between subjects.

Furthermore, a widespread effect of sex on CVR was found, with generally higher CVR in females compared to males. These results are in line with previous evidence observed with TCD-derived CVR measurements, where CVR was found to be higher in females compared to males (Kastrup, Dichgans, Niemeier & Schabet, 1998; Kastrup, Thomas, Hartmann & Schabet, 1997; Tallon, Barker, Nowak-Flück, Ainslie & McManus, 2020), although care must be taken when comparing CVR measurements derived from TCD and BOLD-fMRI (Burley et al., 2021). However, our results are in contrast with previous reports that measure CVR with BOLD fMRI, which report higher GM CVR in males (Kassner, Winter, Poublanc, Mikulis & Crawley, 2010) or no difference at all (Chen, Yang et al., 2021; Jiménez Caballero & Segura Martín, 2006), albeit these comparisons were conducted on the average GM CVR only.

A possible reason for this difference might be related to the phase of the menstrual cycle in which our female participants were during the MRI sessions. Whereas Kassner et al. (2010) did not take into account the phase of the menstrual cycle of their female participants, our data were collected each week over a two and a half months period of time, and therefore might result in a more homogeneous sample of different menstrual cycle phases (cfr. Carr et al., 2021). In that sense, our study was not able to control for the different stages in the menstrual cycle due to the lack of sufficient observations

in the final cohort of female subjects. Given the importance of the role of the endocrine system observed in BOLD fMRI based studies (Arélin et al., 2015; Barth et al., 2016; Pritschet et al., 2020; Pritschet et al., 2021), this might explain the contrasting reports of the difference in CVR between males and females emerging in the literature, especially considering previous observations of the changes in CVR during different phases of the menstrual cycle (Krejza, Rudzinski, Arkuszewski, Onuoha & Melhem, 2013). All in all, further in-depth studies on the difference in CVR across the menstrual cycle and on the role that hormones play in this context are needed.

Furthermore, high spatial independence was found between the relationship of PP and that of MAP. While MAP has been vastly used as an estimation of blood pressure and compared to CVR and BOLD fMRI, PP has been overlooked in this context. Instead, our observations indicate that not taking into account PP could lead to missing important local effects of blood pressure.

Our data did not show any relationship of cardiac pulse and CVR, nor an interaction between sex and PP or MAP. These observations contrast with previous evidence of a relationship between cardiovascular pulse and CVR, as measured by magnetic resonance encephalography (Raitamaa et al., 2018), and of the modulatory effect of the sex of a subject on this relationship (Sabra et al., 2020), that might be mainly driven by the effect of oestrogen on the tone and reactivity of the blood vessels (Barnes & Charkoudian, 2020; Tallon et al., 2020). Multiple methodological factors might have played a role on this difference, since Sabra et al. (2020) used arterial spin labelling with a gas challenge instead of BH-induced BOLD fMRI. Moreover, given the evidence of changes in CVR related to age (Burley et al., 2021), and the complex relationship between CVR, sex and age of the participants (Barnes, 2017), the different age of the two cohorts (elderly participants vs adults) might have been another important cause. Future studies should investigate the effect of age on the relationship of pulse and pressure and CVR.

Despite the fact that our cohort is composed by healthy volunteers, our results might provide further insight into the impact of hypertension on BH-induced CVR assessed with BOLD fMRI. Previous studies employing TCD (Dumville et al., 1998; Hajjar et al., 2014; Settakis, Páll et al., 2003), or using animal models (rat) (Leoni et al., 2011; Li et al., 2021), reported impaired CVR caused by systemic hypertension. In apparent contrast, our results were characterised by local positive relationships between MAP and PP and CVR. Together with the studies of Li et al. (2021) and Settakis, Páll et al. (2003), which showed complex, almost biphasic effects that different stages of hypertension have on CVR, our findings might suggest an "exhaustion" scenario: temporary increased blood pressure in otherwise healthy conditions increases CVR, but if the high blood pressure becomes systemic, it might compromise the vasodilatory properties of the vessels, resulting in lower regulatory capacities and impaired CVR. Moreover, the different effects of PP and MAP on CVR also suggest that different types of hypertension, such as isolated hypertension, should be taken into account and studied separately from primary hypertension.

Finally, a limitation of the current study is that pressure measurements were taken only before the MRI session. Future work could examine how dynamic changes of blood pressure (e.g. via cuffless continuous measurements), simultaneously recorded to expired-air CO_2 concentrations, could influence the dynamics of CVR, either measured with BOLD fMRI, ASL MRI, or alternative techniques such as TCD (Artru & Colley, 1984; Dumville et al., 1998; Hetzel et al., 1999) and functional near infrared spectroscopy (Smielewski et al., 1995).

5.4 Conclusion

This study demonstrates that higher MAP and PP, as measured before the MRI session, are associated with distinct regional increases in CVR. This evidence suggests that not measuring MAP and PP might produce biases in studies comparing CVR between cohorts or across timepoints, and that both MAP and PP should be measured and modeled. Moreover, these results, in conjunction with previous studies, suggest a possible distinction between the effect of temporary and chronic elevations in blood pressure. Finally, the results showed that females presents higher CVR compared to males, with mixed agreement with the existing literature, calling for further studies on sex difference of CVR.

6. Impact of Cerebrovascular reactivity on Resting State and task Induced Activity

In the last 20 years the relationship between RS fluctuations or functional connectivity and behaviour gathered considerable attention among cognitive neuroscientists. Several studies gave evidence of a link between the intrinsic, spontaneous brain fluctuations observed in resting state (RS) fMRI data and functional connectivity with various traits of cognitions (See van den Heuvel & Hulshoff Pol, 2010, for a complete review), followed by various attempts of linking them with behavioural outcomes and scores in domains such as language development and production (e.g. Gilbert et al., 2021; Qi, Schaadt & Friederici, 2021; Xiao, Friederici, Margulies & Brauer, 2016). Beside finding links between the amplitude and the strength of RS fluctuations and functional connectivity, a few studies tried to understand the relationship between RS fluctuations and task Induced Activity (tIA), which will be the focus of this chapter.

For instance, Mennes et al. (2011) showed that the fALFF scores estimated during RS was related to estimated responses of a Flanker task, linking RS fluctuations to executive function outcomes. Similarly, Zou et al. (2013) reported direct links between tIA of a working memory task and the fALFF of a preceding RS scan. Moreover, RS functional connectivity has been similarly linked to task based functional connectivity (Finn et al., 2017; Finn et al., 2015), proportionally to behavioural outcome (Sala-Llonch et al., 2012), in a reliable manner (Gratton et al., 2018), especially when considering its latent counterpart (McCormick, Arnemann, Ito, Hanson & Cole, 2021). However, previous results reported a close relationship between tIA and RS that was competitive (He, 2013; Ito et al., 2020), i.e. that tIA reduced signal variability in RS, and that increased stimulus response resulted in lower fluctuations at a later time, and that this competitiveness was not limited to fMRI imaging, but extended to neural activations in animal models (Ito et al., 2020).

Similarly, RS fluctuations have also been used to rescale the amplitude of tIA in order to account for vascular effects (Kazan et al., 2016), providing similar results to corrections induced by using BH data (Murphy et al., 2011). Furthermore, they have been proposed as an alternative to CVR mapping with RS-fMRI and no physiological measurement (De Vis et al., 2018; Golestani et al., 2016; Kannurpatti & Biswal, 2008; Kannurpatti et al.,

2014; Wang et al., 2019), although the relationship between RS fluctuations and CVR was not always found optimal (Golestani et al., 2016; Lipp et al., 2015). These findings, as well as the impact that physiological signals and vascular sources can have on functional connectivity and RS fluctuations (Bright, Whittaker, Driver & Murphy, 2020; Chen et al., 2020), might indicate that these factors could actually explain a considerable variability the relationship between RS, tIA and behaviour.

The study presented in this chapter investigates the relationship between BH-induced CVR and different metrics of RS fluctuations (RSFA, ALFF, and fALFF) that have been proposed as counterparts to CVR, as well as tIA observed in a simple Motor task and an event-related, high-level cognitive task (Simon). In that sense, it also aims to generalise the results of Mennes et al. (2011) and those of Golestani et al. (2016), and observe if CVR has direct causation on tIA.

6.1 Material and Methods

6.1.1 Dataset

In this study the motor, Simon, and BH task, the first RS run of each session, the CO_2 traces, and the T1-weighted and T2-weighted anatomical images from the first session of the dataset described in Chapter 2 were used.

6.1.2 Data analysis

All functional volumes were preprocessed and analysed as described in Chapter 2. For the motor task, the maps of the contrasts between the five motor conditions and the sham condition were averaged to obtain one map representing all motor activations. For the Simon task, three contrasts were considered: all the congruent responses, all the incongruent responses, and all the responses together. As noted in Chapter 2, only the correct responses were taken into account for these contrasts, whereas the wrong responses were modelled in the design matrix with regressors of non-interest. Note that the Pinel functional localiser task shown in Chapter 2 was not used in this analysis, as its collection served other purposes outside of the scope of this study.

RSFA, ALFF, and fALFF were estimated from the first RS run with 3dRSFC, in the 0.01-0.1 Hz band, as explained in Chapter 2 (see Equation (2.1)).

Finally, all maps were normalised to the MNI152 template (Grabner et al., 2006, 2.5 mm isotropic voxel resolution) with a nearest neighbours interpolation. Since the BH task fMRI volumes were not smoothed before the GLM computation in order not to bias the adopted lagged-GLm estimation method, the normalised CVR maps were smoothed within the same dilated GM mask used in Chapter 5 (1 voxel dilation), with a 5mm FWHM gaussian filter.

The average CVR, ALFF, RSFA, and fALFF GM value was extracted for each subject and session using the same dilated GM mask, and the obtained values were used to create three scatterplots comparing CVR and each of the three RS fluctuations measures.

Then, in order to understand the role that CVR plays in the relationship between intrinsic RS fluctuations and tIA (Mennes et al., 2011; Zou et al., 2013), the following three LME models were modelled using 3dLMEr (Chen et al., 2013) to obtain a voxelwise map of the impact of each independent variable on each dependent one:

1. A LME model to estimate the impact of CVR on RSFA, ALFF, and fALFF:

$$RSFL \sim 1 + cvr + (cvr|ses) + (cvr|subj), \tag{6.1}$$

	RSFA	ALFF	fALFF
CVR	$\beta = 22.438$, CI_{95} [17.486, 27.390]	$\beta = 4480.721$, CI_{95} [3620.913, 5340.529]	$\beta = 0.029$, CI_{95} [0.018, 0.0401]

Table 6.1: Impact of CVR on RS fluctuations considering an average GM value. No impact was found significant.

where $RSFL$ denotes either the RSFA, ALFF, or fALFF map. This model was also adopted to estimate the impact of CVR on RSFA, ALFF, and fALFF considering the average value of the aforementioned dilated GM mask.

2. A LME model to estimate the impact of RSFA, ALFF, and fALFF on tIA:

$$tIA \sim 1 + RSFL + (RSFL|ses) + (RSFL|subj), \tag{6.2}$$

where tIA is either the averaged contrast map of the motor task, or one of the contrast maps of the Simon task.

3. A LME model to estimate the impact of CVR on tIA:

$$tIA \sim 1 + cvr + (cvr|ses) + (cvr|subj), \tag{6.3}$$

Since no significant results were observed using a threshold of $p \leq 0.05$ after controlling for multiple comparisons with the FDR procedure (Benjamini et al., 2006), the results at an uncorrected threshold of $p \leq 0.01$ are reported. In addition, only clusters of at least 20 voxels (312.5 mm^3) with a neighbourhood of 26 voxels were considered.

6.2 Results

6.2.1 Relationship between CVR and RS fluctuations

Figure 6.1 shows the CVR, RSFA, ALFF, and fALFF maps of a representative session of a representative subject. Note that although the different metrics adopt different scales and ranges, and their amplitude was not rescaled or normalised, the adopted display ranges are the same relatively to each metric amplitude distribution. RSFA and ALFF maps are equivalent, and seem to be similar to the CVR map, in particular for the peaks of amplitude. The fALFF amplitude distribution appears much more skewed toward higher values, but with a similar spatial distribution compared to the other three.

Table 6.1 and Figure 6.2 show the relationship between CVR and ALFF (6.2A, 6.2D), RSFA (6.2B, 6.2E), and fALFF (6.2C, 6.2F). The top lines shows the the relationship between CVR and RS fluctuations for each subject independently, and the bottom line considering all sessions and subjects together. While there seems to be a good relationship between CVR and RS fluctuations when all subjects and sessions are pooled together, considering each subject independently shows a much higher inter-subject and inter-session variability.

Figure 6.3 depicts the results of the model in Equation (6.1) for RSFA, ALFF, and fALFF, while Tables E.1 to E.3 in Appendix E report the clusters of positive impact of CVR on the RS fluctuations. Note that no cluster of negative impact of sufficient size was found. Figure 6.4 shows the overlap between the different maps. While there is a large agreement between the areas of impact of CVR over ALFF and RSFA, fewer voxels show

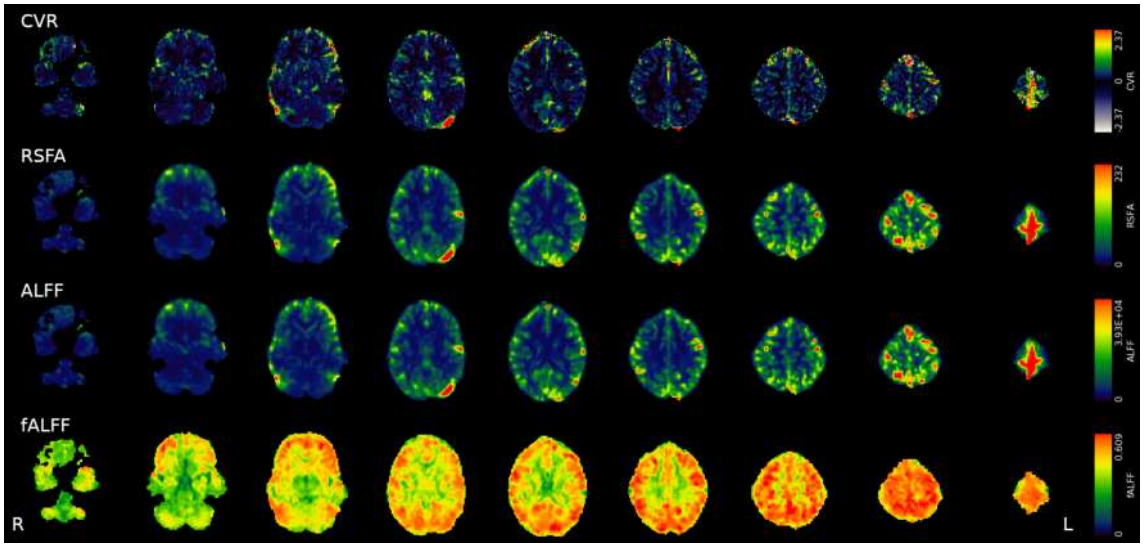

Figure 6.1: CVR, RSFA, ALFF, and fALFF maps of a representative session of a representative subject. Note that the display range is different for each map, but the upper limit is consistently the 99$^{\text{th}}$ percentile of each amplitude distribution, considering positive, non-zero voxels only.

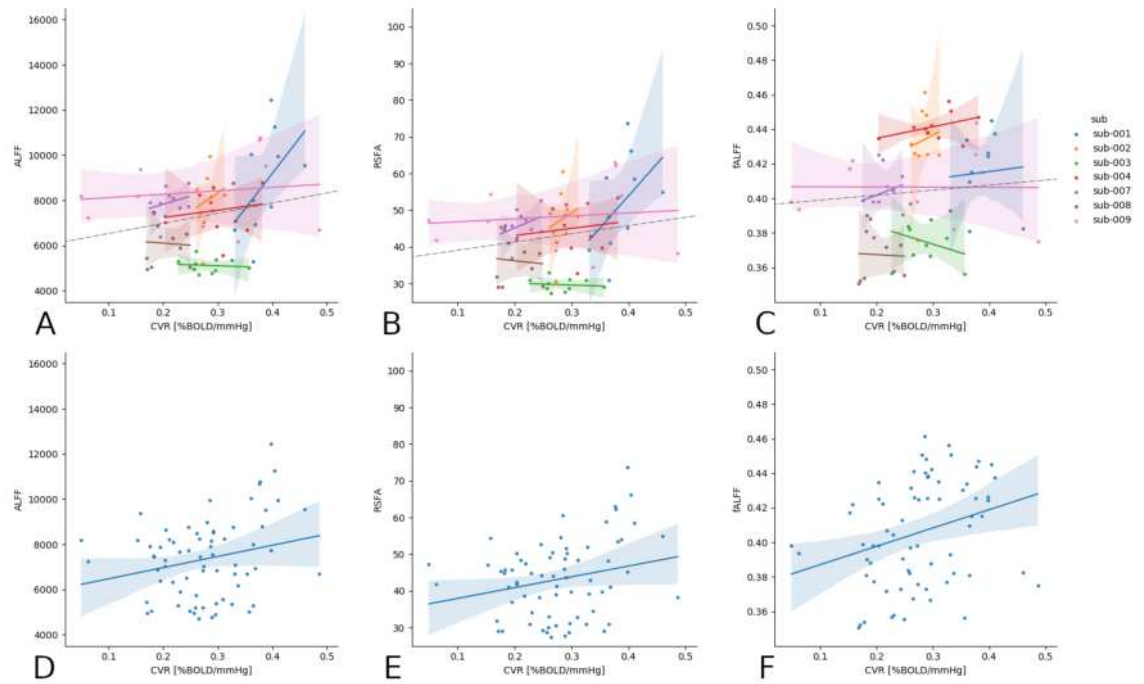

Figure 6.2: Scatterplots of the relationships between the average GM value of CVR and RSFA, ALFF, and fALFF. The top line reports the relationship of each subject independently, the bottom line of all subjects and all sessions together. In the top line, the grey line represents the LME model coefficient.

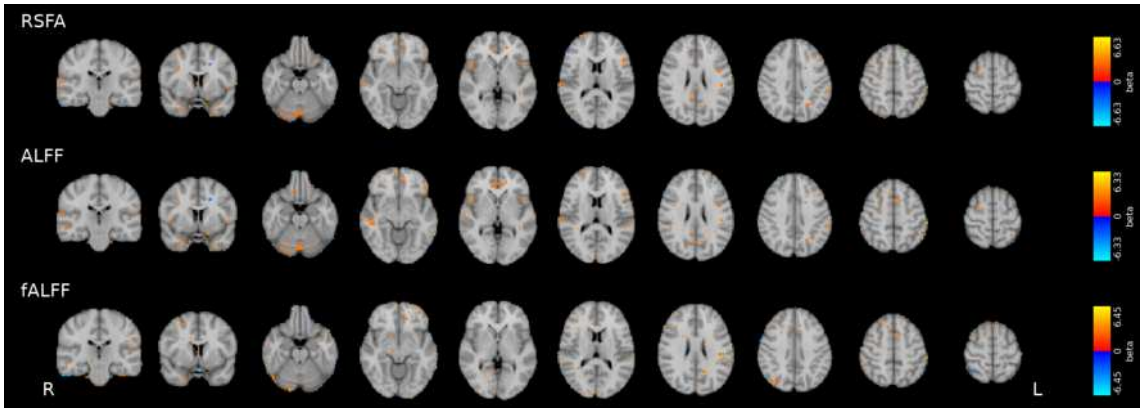

Figure 6.3: Local effect of CVR on RS fluctuations ($p \leq 0.01$ uncorrected).

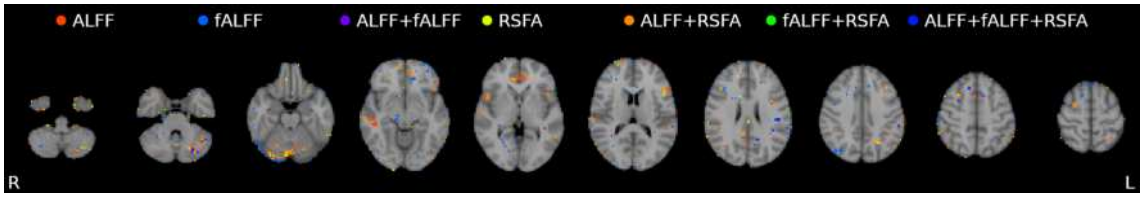

Figure 6.4: Overlap of the positive values of the maps shown in Figure 6.3.

an overlap between areas related to ALFF, fALFF, and RSFA, and even less between ALFF or RSFA and fALFF.

The largest positive impact of CVR on ALFF was found in the cerebellum, in the left crus (I) and in the vermis (VI). Positive impact was also found in the right middle temporal gyrus, temporal pole, and planum temporale, in the right superior frontal gyrus, in the left superior frontomedial and frontal operculum cortices, in the left supramarginal gyrus, and bilaterally in the posterior and anterior cingulate gyrus. The positive impact on RSFA was almost completely overlapping to that of ALFF, except for the anterior cingulate gyrus and the frontal operculum cortex, while the impact on fALFF was localised at the edges of the cerebellum, in the left anterior supramarginal gyrus, and in the superior frontomedial gyrus (bilaterally).

6.2.2 Relationship between RS fluctuations, CVR, and the motor task

Figure 6.5 shows the results of the model in Equations (6.2) and (6.3) for the motor task contrast, while Table E.4 reports the clusters of positive impact of CVR, Table E.5 in Appendix E reports the clusters of negative impact of CVR, Tables E.6 and E.8 in Appendix E reports the clusters of positive impact of RS fluctuations, and Tables E.7, E.9, and E.10 in Appendix E reports the clusters of negative impact of RS fluctuations. No statistically significant positive impact of fALFF was found.

The impact of ALFF and RSFA on the motor vs sham contrast was characterised by a negative impact mainly across the caudal half of the brain, from the left lateral occipital cortex to the left cingulate gyrus, extending bilaterally to the precentral and postcentral gyri, the juxtapositional lobule cortex (supplementary motor cortex) and the posterior insular cortices. The negative impact of fALFF was localised similarly to the impact of ALFF and RSFA, with the exception of the superior precentral and postcentral gyri and the bilateral occipital and insular cortices, and the addition of the precuneous, bilaterally. A positive impact of ALFF and RSFA was found around the anterior horn of the right

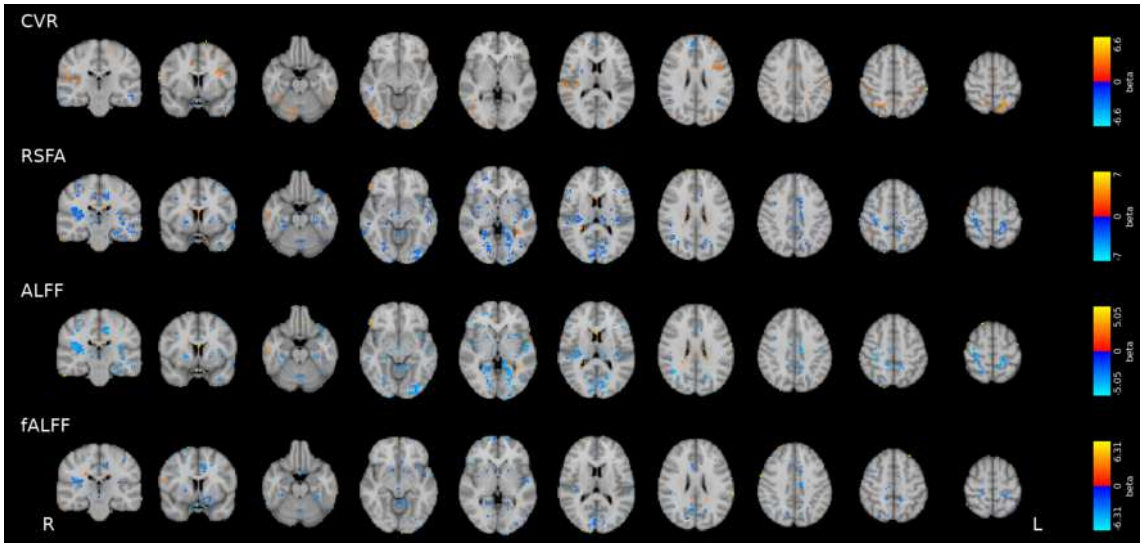

Figure 6.5: Local effect of RS fluctuations and CVR on the motor task ($p \leq 0.01$ uncorrected).

lateral ventricle.

The impact of CVR was mainly positive in the left anterior inferior cerebellum (VIIIa), left inferior frontal gyrus, left posterior supramarginal gyrus and superior parietal lobule, in the left inferior temporal gyrus, in the right parietal operculum cortex, in the right posterior inferior cerebellum (VI and VIIb), and bilaterally in the superior and inferior lateral occipital cortex. Negative impact of CVR was found bilaterally in the middle temporal gyrus and in the right paracingulate gyrus.

6.2.3 Relationship between RS fluctuations, CVR, and the Simon task

Figures 6.6 to 6.8 shows the results of the model in Equations (6.2) and (6.3) for all considered contrasts of the Simon task, while Tables E.11, E.15, and E.17 in Appendix E report the clusters of positive impact of CVR, Tables E.12, E.13, E.18, and E.19 in Appendix E report the clusters of positive impact of ALFF and RSFA, and Tables E.14 and E.16 in Appendix E report the clusters of negative impact of fALFF. Note that no cluster of negative impact of CVR, ALFF or RSFA of sufficient size, or any cluster of positive impact of fALFF, was found.

For the congruent responses condition, a positive impact of ALFF and RSFA was found in the right superior parietal lobule and cerebellum (crus II), in the left superior lateral occipital cortex, and bilaterally in the juxtapositional lobule cortex (supplementary motor cortex). Positive RSFA impact was found in the left superior parietal lobule as well. The negative impact of fALFF was localised in the anterior cingulate gyri (bilaterally). The impact of CVR on the same condition was positive and located in the left superior and middle frontal gyrus, in the left superior lateral occipital cortex, in the left cerebellum (VI), in the right putamen, in the right occipital fusiform gyrus, in the right cerebellum (crus I), and bilaterally in the precuneous cortex. As for the incongruent responses condition, the impact of CVR was found positive in the right precentral and postcentral gyri, and in the left middle frontal and angular gyri. We also found a negative impact of fALFF in the cerebellum (vermis VIIIa), but no effect of ALFF or RSFA. Considering both congruent and incongruent responses together showed similar patterns of positive impact of ALFF and RSFA when considering only the congruent responses, and of positive impact of CVR

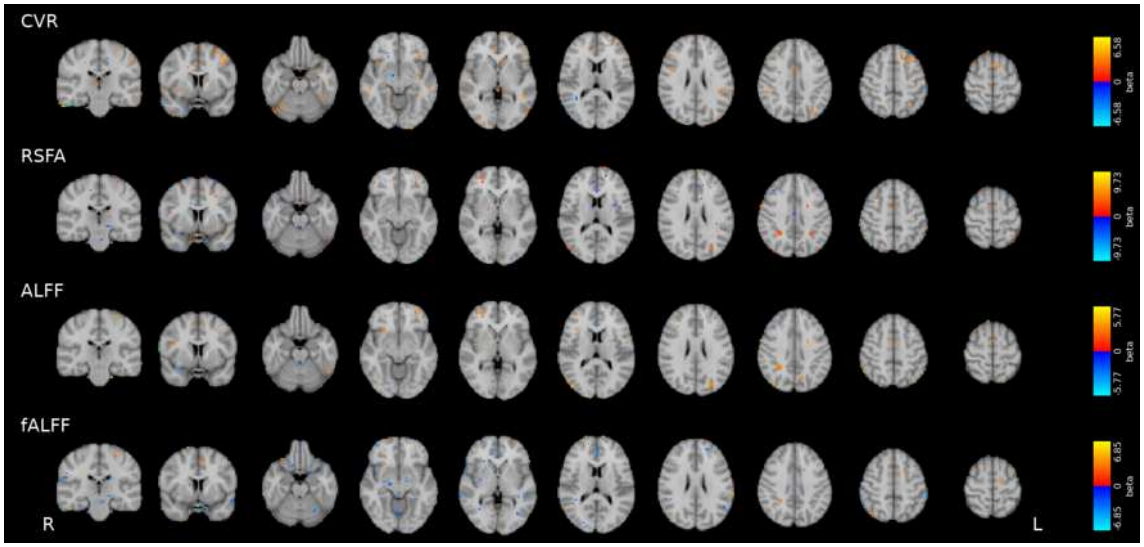

Figure 6.6: Local effect of RS fluctuations and CVR on all congruent responses contrast ($p \leq 0.01$ uncorrected).

when considering only the incongruent responses.

6.3 Discussion

This study evaluated the relationship between BH-induced CVR, RS fluctuations as measured in terms of RSFA, ALFF and fALFF, as well as between these metrics and task induced activations (tIA), considering two different types of task: a block design, low cognitive level, motor task and an event related, high cognitive level, Simon task. Leveraging the 70 sessions of the dataset presented in Chapter 2, and using a voxelwise LME model to take into account repeated measures for each subject, the results revealed that the impact of CVR on RS fluctuations and on tIA, as well as of RS fluctuations on tIA, is localised on particular areas that do not overlap with those activated by the task (see Chapter 2). Albeit not completely, a large concordance between all results regarding ALFF or RSFA was observed for all LME analyses, independently of whether they were treated as dependent or independent variables in the model. This could be explained by the maps plotted in Figure 6.1, that show a complete overlap between RSFA and ALFF maps, but not with fALFF, in a representative subject.

Considering the relationship between RS fluctuations and CVR, few areas of impact of CVR on RSFA and ALFF were observed (see Figure 6.3, mainly in the cerebellum and in small portions of the temporal and frontal lobes. This observation seems to contradict previous results shown in the literature, as well as the maps plotted in Figure 6.1. For instance, Golestani et al. (2016) reported higher group spatial agreement between RSFA (and ALFF) and CVR across the whole GM. Independently, Lipp et al. (2015) showed even higher group agreement between RSFA and BH-induced CVR.

A possible reason for the observed differences could be the voxelwise analysis used in the current study versus the averaged-GM analysis examined in previous studies. Beyond this, our dense mapping dataset enables us to formulate another possible cause, that is the high between-subject variability observed in these relationships in previous studies (see Golestani et al., 2016). Since the current dataset includes 7 subjects, each with 10 sessions, and the estimated maps have high repeatability over time (see Chapter 2), it is possible that our observations only fall within a small range of the true link between CVR and RS

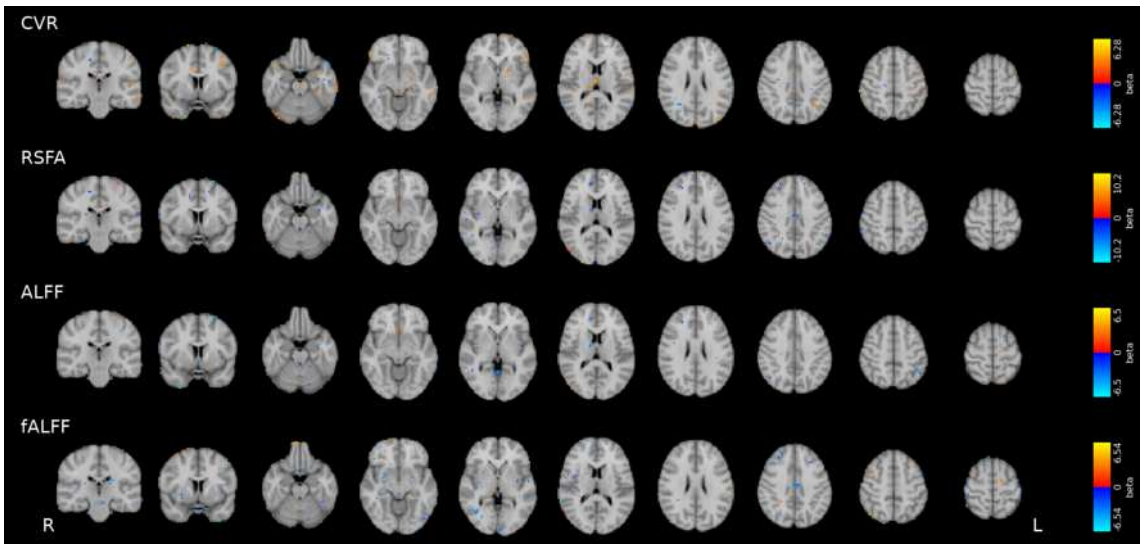

Figure 6.7: Local effect of RS fluctuations and CVR on all incongruent responses contrast ($p \leq 0.01$ uncorrected).

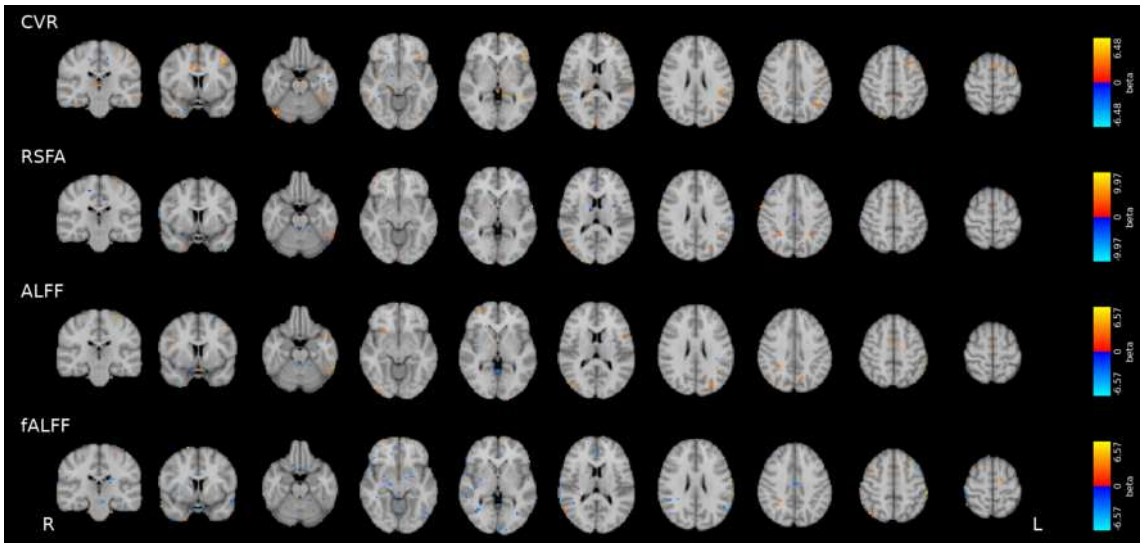

Figure 6.8: Local effect of RS fluctuations and CVR on all congruent and incongruent responses contrast ($p \leq 0.01$ uncorrected).

fluctuations, thereby biasing toward a weaker relationship between CVR and RSFA (or ALFF).

For these reasons, we plotted the relationship between average GM value of CVR and ALFF, RSFA and fALFF(see Figure 6.2). The latter figure revealed that considering all subjects and sessions together seem to inflate the relationship between CVR and RS fluctuations. However, considering each subject independently from the others revealed not only a high between-subject variability, but also an interacting effect of different within-subject (across sessions) variability, that could confirm a generally low reproducibility, or sample specificity, of previous results reported in the literature.

Considering the relationship between fALFF and tIA, our results did not replicate and generalize the findings described by Mennes et al. (2011), that reported greater spatial relationships between fALFF and task, especially in motor areas. A possible reason might be related to the different tasks considered: although the Flanker and the Simon tasks activate very similar neural correlates and trigger the same cognitive domains, they are not completely overlapping (see Kawai, Kubo-Kawai, Kubo, Terazawa & Masataka, 2012; Keye, Wilhelm, Oberauer & van Ravenzwaaij, 2009; Wager et al., 2005, for commonalities and differences). This fact might have plaid a role in the failed generalisation.

Another difference between the two setups consists in the distance between the RS run and the task run: while in Mennes et al. (2011) the RS took place right before or after the Flanker task, our analyses considered the initial RS run of each session in order not to induce any bias due to subsequent tasks performed during the MRI session. Therefore, both RS and each of task runs, which the tIA map was estimated from, might be spaced by the other tasks and additional RS runs, due to the counterbalancing of the tasks in the the dataset design. This could indicate that the relationship between RS fluctuations and tIA is a transient phenomenon with limited duration, or interfered by other tasks. Future analyses will address this point and differentiate the RS run, considering their relative position with respect to the tasks.

The observed discrepancy might also be due to the small subject sample size. If the between-subject variance of the effects under study is not negligible, this dense mapping dataset might have failed to sample it, calling for a larger group of subjects with acceptable CO2 recordings and task performance. However, Chen, Pine et al. (2021) demonstrated that increasing the number of sessions should be comparable to a bigger sample size, suggesting that these effects should be evident even with this small sample size. Performing a power analysis in terms of the number of subjects and thresholds while planning the experiment could be beneficial. Such power analysis was not carried out due to the difficulty of determining proper values for the multiple effect sizes and sources of variability (within- and between-subject) for the different tasks and this type of data analysis and the absence of sufficient examples and/or information in previous studies. Our choice for the number of sessions and subjects was based instead on the size of previous DM datasets (10 subjects and 10 sessions, see Gordon et al., 2017), although we discarded three subject due to bad compliance with the BH task (see results in Chapter 2. Consequently, we conjecture that while the sample size of this dataset is normally enough, it might not be sufficient to study more complex relationships between physiological, vascular metrics, RS and tIA under observation in this chapter. Indeed, while it is generally expected that observations at the group level are replicable at the subject level, the different type of dataset might reveal patterns of relationships that do not hold when an individual is highly sampled.

Using CVR estimates obtained from CO_2 recording during the RS runs nearby the tasks (Golestani et al., 2016) could be an alternative approach to using BH-induced CVR estimates. The main reason behind the current choice is that estimating the vascular lag

is more challenging without the presence of a CVR inducing task (Stickland et al., 2021) because it is more difficult to individuate true peaks in the CO_2 signal during normal breathing and the fMRI signal during spontaneous fluctuations exhibits lower variability (i.e. contrast-to-noise ratio). However, Lipp et al. (2015) showed that the RSFA computed during a BH task is more similar to a BH-induced CVR estimation, and that similarly the CO_2 fluctuation regression in RS is more similar to RSFA patterns. Consequently, future analysis will consider all CO_2 signals and fluctuation measurements.

6.4 Conclusion

This study investigated the relationship between CVR, RS fluctuations, and task Induced Activation, considering a motor task and a Simon task. Although results were not significant after FDR correction ($p < 0.05$), at $p < 0.01$ uncorrected we found an impact of CVR on RS fluctuations and tIA, and an impact of RS fluctuations on tIA. The impact of CVR on RSFA and ALFF is widely overlapping, and partially overlapping with the impact on fALFF as well. Considering tIA, the impact of RS fluctuations and CVR is localised in specific areas of the GM, albeit not those involved in the task. However, further studies are necessary to properly characterise the relationship between CVR, RS fluctuations, and tIA, both short and long term.

7. Conclusions and future work

The recognition of BOLD based fMRI as a fundamentally metabolic and physiological measurement is still ignored by the largest part of the neuroimaging community. Be it for simplicity or convenience, it is far more easy to skip a step in the interpretation of the BOLD signal and its fluctuations and observe only its meaning as neural mechanism, related to neuronal activity. However, the potential of fMRI as a non-invasive imaging tool to investigate cerebral physiology is indisputable, and deserves further methodological improvement and deeper understanding of its nature. Equally, more knowledge is required to understand the impact of physiological factors on the interpretation of BOLD signal and the neural mechanics underlying it.

Consequently, a rich fMRI dataset was collected to pursue this thesis comprising a variety of cognitive and sensory tasks (motor task, Simon task and the Pinel functional localizer task), four RS, and a BH task to estimate CVR and its lag, along with anatomical MR images and physiological recordings ($P_{ET}CO_2$, respiratory belt, and cardiac pulse). Following the design of DM datasets (e.g. Braga & Buckner, 2017; Gordon et al., 2017; Poldrack et al., 2015), the subject sample size is small ($n = 10$), but the session sample size is higher ($n = 10$) than traditional datasets, thus being associated to bigger datasets in terms of statistical power (Chen, Pine et al., 2021).

Chapter 2 described the dataset acquisition, computed group activation maps, and checked the reliability of the tIA maps, as well as of the fALFF of the RS runs. fALFF maps reliability was good, and tIA contrasts reliability was excellent in the areas involved in the processing of the different tasks. Leveraging ME-fMRI for a DM dataset showed to increase the sensitivity of various tasks and contrasts, as shown by previous studies (Gonzalez-Castillo et al., 2016; Lynch et al., 2020), especially for the Simon and the Pinel functional localiser task. However, our results at the group level, that considered an unconventional mixed-effects analysis (i.e. modelling both within- and across- subjects variability), demonstrated that some contrasts, for instance toe movements or the contrast between vertical and horizontal visual chequerboards, might not be detectable at the group level, having high spatial subject specificity. This specificity, together with inter-subject spatial

variability, might be the cause of the lack of detection of these contrasts at the group level. Indeed, one of the main reasons to collect a DM dataset is to focus on subject specific spatial patterns of brain activations (cfr. Fedorenko, 2021). Nevertheless, another cause of lack of results at the group level could be the method used to normalise the results to a common space, as previous studies showed that surface-based spatial registrations might be more appropriate for group analyses (Coalson, Van Essen & Glasser, 2018). Hence, we plan to further explore this possibility by comparing different types of registrations in future studies.

The collection of BH tasks in this dataset was driven by the idea that while some studies traced a link between RS fluctuations and tIA (Kazan et al., 2016; Mennes et al., 2011; Zou et al., 2013, e.g.), other traced a link between CVR and RS fluctuations (De Vis et al., 2018; Golestani et al., 2016; Kannurpatti & Biswal, 2008; Kannurpatti et al., 2014; Wang et al., 2019), introducing the possibility that CVR can be a modulating factor of tIA. However, in order to correctly assess any relationship between CVR, RS and tIA, we first aimed to investigate new methods to improve CVR modelling and characterization (see Chapters 3 and 4), especially leveraging ME-fMRI data, due to its capability of improving not only tIA and RS imaging, but also CVR mapping (Cohen et al., 2021; Cohen & Wang, 2019).

To begin with, due to the unknown time that gasses need to transit from the brain to the lungs and then be sampled, it is necessary to take into account the delay in the response. It is also important to take into account that different areas of the brain do not have an immediate and synchronous response, hence the estimation of the delay needs to be local. Moreover, respiratory challenges, such as a BH task, are characterised by considerable motion, collinear to the CO_2 fluctuations of interest.

Chapter 3 described an approach that accounts for local variability in CVR lag and simultaneous modelling of nuisance regressors. This approach performed better than not optimising for the response delay and reduced confounding effects resulting from not applying nuisance regression (e.g. motion) or applying it sequentially to CVR estimation (see Lindquist et al., 2019). Moreover, in contrast with sequential approaches, simultaneous regression enables to maintain quantitative information in the CVR estimate in terms of %BOLD / mmHg.

Although the method described in Chapter 3 was tested using only one session of eight subjects, the rich DM dataset collected for this thesis could serve as a benchmark to evaluate methods for BH-induced CVR estimation in future studies. In particular, we plan to compare the proposed approach with previous methods that also consider regional variability in vascular lags (e.g. Donahue et al., 2016; Frederick et al., 2020; Geranmayeh et al., 2015; Murphy et al., 2011; Sousa et al., 2014; Tong et al., 2011) in terms of the accuracy and reliability of CVR and lag estimates.

The topic of CVR modelling and denoising was elaborated further in Chapter 4 by taking into account the use of ME-BOLD acquisition and ICA-based denoising. A ME acquisition along with tailored ME-based denoising (e.g. ME-ICA) had been proven successful in removing motion artefacts and other sources of noise, such as acquisition artefacts or magnetic field artefacts induced by respiration, in multiple task and resting state experiments. Nevertheless, these potential advantages had not been evaluated before for BH-induced CVR estimation. Thus, this study examined their efficacy in improving CVR estimation comprehensively, in terms of motion removal, estimation accuracy and reliability.

Our results revealed that a conservative ICA-based approach in which the noisy IC components are orthogonalised with respect to the $P_{ET}CO_2 hrf$ signal and the good IC components removes motion-related effects while obtaining reliable CVR and lag responses.

Notably, our analyses also demonstrated that simple optimal combination of ME data with modelling of motion and low frequency polynomial regressors provides similar CVR and lag estimations, and shows a clear improvement over using SE data with the same model.

In future work, we intend to assess the generalization of these observations with other type of tasks (e.g. speech production tasks, block-design motor tasks, slow and rapid event-related designs) and RS analysis, aiming to help researchers make a more informed decision on the benefits of ME-ICA. Indeed, it is important to weight the possible improvement in data denoising introduced by ME-ICA and the additional work required for its correct operation (e.g. manual classification) compared with simple optimal combination.

Moreover, it is important to highlight that our study did not compare ME based approaches with optimised SE sequences (i.e. with faster TR). Future studies could evaluate if the higher temporal resolution achievable in SE acquisitions is more beneficial to CVR than ME acquisitions.

Having obtained reliable CVR estimations, we progressed in studying their relation with with variations in blood pressure metrics, such as mean arterial pressure (MAP) and pulse pressure (PP), and other individual characteristics in Chapter 5. This assessment was performed by means of a linear mixed effects (LME) model to assess the impact that subject-specific, repeated measures of blood pressure and pulse have on CVR and its lag.

Our results demonstrated that both MAP and PP can have regional effects on CVR and the spatial distribution of their impact is highly divergent. This spatial divergence is particularly interesting, and deserves further attention, especially to understand its origin and its implication in pathologies that affect blood pressure. Furthermore, in our dataset, we only collected a single static assessment of vital signals at the beginning of each MR session. Future studies could consider how dynamic fluctuations of blood pressure, pulse, and other endogenous physiological fluctuations, might impact the estimation of CVR, and, to a further extent, tIA and RS fluctuations.

Our results also showed a difference between males and females, where females showed higher CVR than males. However, these results should be interpreted with caution, not only due to the few individuals in each sex group considered in the current study, but also because although a difference in CVR between males and females has been reported previously (see Barnes & Charkoudian, 2020; Carr et al., 2021), such difference in CVR between sexes is still under debate. More observations are required to understand if such difference between males and females is consistent, and what role the menstrual cycle might play in it, especially considering the effect that hormones have on blood vessels and their function.

Finally, Chapter 6 addressed the question of how CVR impacts RS fluctuations and tIA, with the intention of generalising the results shown by Golestani et al. (2016) and Mennes et al. (2011), respectively. Our analyses demonstrated that the impact of CVR on RS fluctuations, and the impact of CVR and RS fluctuations and tIA is highly spatially confined. Moreover, the impact of CVR on RSFA and ALFF is highly overlapping, and partially overlapping with that of fALFF as well. Despite having few localisations, the impact of RS fluctuations or CVR on tIA does not involve areas normally related to the tasks taken into exam. Furthermore, no result was significant after applying FDR correction, so further studies are needed to properly address this question and understand if the lack of significant results is due to previous studies not being generalisable, or due to a lack of necessary power. Although we did not manage to generalise previous results reported in the literature (e.g. Golestani et al., 2016; Mennes et al., 2011), this lack of generalisation leaves open questions. For instance, the implication of the temporal delay between different task, rest, and BH is a topic that requires further exploration. Indeed,

attention should be paid to the time and order between tasks, RS, and CVR estimation, in order to assess if the relationship between the three has a transient nature, and if that is the case, the amount of its duration. Equally, how CO_2 fluctuations during the performance of the tasks and RS, respectively, might impact the observed relationship between tIA and RS fluctuations could also be considered. Finally, in this study we did not take into account the relationship between RS fluctuations and pure behavioural performance, as other studies have investigated before (e.g. Mennes et al., 2011; Sala-Llonch et al., 2012). Further studies will take into account this comparison as well.

Overall, these series of studies demonstrated how to obtain reliable, optimised CVR estimations that take into account the haemodynamic lag of the process, and they helped inserting BOLD fMRI based CVR mapping in a broader context. At the individual level, they explored how other physiological characteristics such as blood pressure can impact CVR measurement. This is not new information if other methods to estimate CVR are taken into account (e.g. TCD), but their role in fMRI is still unknown and deserves further exploration. In the context of BOLD fMRI methodology, these studies started addressing the effect that endogenous CO_2 fluctuations can have on tIA and RS fluctuations. More studies are required to scope the full extent of such effects at the group level, in order not only to improve the estimation and characterization of the BOLD response to different cognitive events, but also to understand how these effects might be affected by pathologies that alter normal physiology.

With these efforts, the neuroimaging community could once again appreciate the physiological aspects of the BOLD signal, and how physiological processes might influence the investigation of neuronal activity, cognition and behaviour with BOLD fMRI.

Bibliography

Aaslid, R., Lindegaard, K. F., Sorteberg, W. & Nornes, H. (1989). Cerebral autoregulation dynamics in humans. *Stroke*, *20*(1), 45–52. doi:10.1161/01.STR.20.1.45

Amemiya, S., Yamashita, H., Takao, H. & Abe, O. (2019). Integrated multi-echo denoising strategy improves identification of inherent language laterality. *Magnetic Resonance in Medicine*, *81*(5), 3262–3271. doi:10.1002/mrm.27620

Anderson, J. S., Druzgal, T. J., Lopez-Larson, M., Jeong, E. K., Desai, K. & Yurgelun-Todd, D. (2011). Network anticorrelations, global regression, and phase-shifted soft tissue correction. *Human Brain Mapping*, *32*(6), 919–934. doi:10.1002/hbm.21079

Andersson, J. L., Skare, S. & Ashburner, J. (2003). How to correct susceptibility distortions in spin-echo echo-planar images: Application to diffusion tensor imaging. *NeuroImage*, *20*(2), 870–888. doi:10.1016/S1053-8119(03)00336-7

Arélin, K., Mueller, K., Barth, C., Rekkas, P. V., Kratzsch, J., Burmann, I., ... Sacher, J. (2015). Progesterone mediates brain functional connectivity changes during the menstrual cycle-a pilot resting state MRI study. *Frontiers in Neuroscience*, *9*(FEB), 1–11. doi:10.3389/fnins.2015.00044

Arichi, T., Fagiolo, G., Varela, M., Melendez-Calderon, A., Allievi, A., Merchant, N., ... Edwards, A. D. (2012). Development of BOLD signal hemodynamic responses in the human brain. *NeuroImage*, *63*(2), 663–673. doi:10.1016/j.neuroimage.2012.06.054

Artru, A. A. & Colley, P. S. (1984). Cerebral blood flow responses to hypocapnia during hypotension. *Stroke*, *15*(5), 878–883. doi:10.1161/01.STR.15.5.878

Aslan, S., Hocke, L., Schwarz, N. & Frederick, B. (2019). Extraction of the cardiac waveform from simultaneous multislice fMRI data using slice sorted averaging and a deep learning reconstruction filter. *NeuroImage*, *198*(January), 303–316. doi:10.1016/j.neuroimage.2019.05.049

Attarpour, A., Ward, J. & Chen, J. J. (2021). Vascular origins of low-frequency oscillations in the cerebrospinal fluid signal in resting-state fMRI: Interpretation using photoplethysmography. *Human Brain Mapping*, (December 2020), 2606–2622. doi:10.1002/hbm.25392

Atwi, S., Metcalfe, A. W., Robertson, A. D., Rezmovitz, J., Anderson, N. D. & MacIntosh, B. J. (2018). Attention-related brain activation is altered in older adults with white matter hyperintensities using multi-echo fMRI. *Frontiers in Neuroscience*, *12*(OCT), 1–14. doi:10.3389/fnins.2018.00748

Avants, B. B., Tustison, N. J., Wu, J., Cook, P. A. & Gee, J. C. (2011). An open source multivariate framework for N-tissue segmentation with evaluation on public data. *Neuroinformatics*, *9*(4), 381–400. doi:10.1007/s12021-011-9109-y

Barch, D. M., Sabb, F. W., Carter, C. S., Braver, T. S., Noll, D. C. & Cohen, J. D. (1999). Overt verbal responding during fMRI scanning: empirical investigations of problems and potential solutions. *NeuroImage*, *10*(6), 642–657.

Barnes, J. N. (2017). Sex-specific factors regulating pressure and flow. *Experimental Physiology*, *102*(11), 1385–1392. doi:10.1113/EP086531

Barnes, J. N. & Charkoudian, N. (2020). Integrative cardiovascular control in women: Regulation of blood pressure, body temperature, and cerebrovascular responsiveness. *FASEB Journal*, (September), 1–11. doi:10.1096/fj.202001387R

Barth, C., Steele, C. J., Mueller, K., Rekkas, V. P., Arélin, K., Pampel, A., ... Sacher, J. (2016). In-vivo Dynamics of the Human Hippocampus across the Menstrual Cycle. *Scientific Reports*, *6*(April), 1–9. doi:10.1038/srep32833

Bates, D., Mächler, M., Bolker, B. M. & Walker, S. C. (2015). Fitting linear mixed-effects models using lme4. *Journal of Statistical Software*, *67*(1). doi:10.18637/jss.v067.i01. arXiv: 1406.5823

Beall, E. B. & Lowe, M. J. (2007). Isolating physiologic noise sources with independently determined spatial measures. *NeuroImage*, *37*(4), 1286–1300. doi:10.1016/j.neuroimage.2007.07.004

Beckmann, C. & Smith, S. (2004). Probabilistic Independent Component Analysis for Functional Magnetic Resonance Imaging. *IEEE Transactions on Medical Imaging*, *23*(2), 137–152. doi:10.1109/TMI.2003.822821

Behzadi, Y., Restom, K., Liau, J. & Liu, T. T. (2007). A component based noise correction method (CompCor) for BOLD and perfusion based fMRI. *NeuroImage*, *37*(1), 90–101. doi:10.1016/j.neuroimage.2007.04.042. arXiv: NIHMS150003

Belliveau, J. W., Kennedy, D. N., Mckinstry, R. C., Buchbinder, B. R., Weisskoff, R. M., Cohen, M. S., ... Rosen, B. R. (1991). Functional Mapping of the Human Visual Cortex by Magnetic Resonance Imaging. *Science*, *254*, 716–719.

Benjamini, Y., Krieger, A. M. & Yekutieli, D. (2006). Adaptive linear step-up procedures that control the false discovery rate. *Biometrika*, *93*(3), 491–507. doi:10.1093/biomet/93.3.491

Betzel, R. F., Satterthwaite, T. D., Gold, J. I. & Bassett, D. S. (2017). Positive affect, surprise, and fatigue are correlates of network flexibility. *Scientific Reports*, *7*(1), 1–10. doi:10.1038/s41598-017-00425-z

Bhogal, A. A., Siero, J. C., Fisher, J. A., Froeling, M., Luijten, P., Philippens, M. & Hoogduin, H. (2014). Investigating the non-linearity of the BOLD cerebrovascular reactivity response to targeted hypo/hypercapnia at 7T. *NeuroImage*, *98*, 296–305. doi:10.1016/j.neuroimage.2014.05.006

Bianciardi, M., Fukunaga, M., van Gelderen, P., Horovitz, S. G., de Zwart, J. A., Shmueli, K. & Duyn, J. H. (2009). Sources of functional magnetic resonance imaging signal fluctuations in the human brain at rest: a 7 T study. *Magnetic Resonance Imaging*, *27*(8), 1019–1029. doi:10.1016/j.mri.2009.02.004

Birn, R. M., Bandettini, P. A., Cox, R. W. & Shaker, R. (1999). Event-related fMRI of tasks involving brief motion. *Human Brain Mapping*, *7*(2), 106–114. doi:10.1002/(SICI)1097-0193(1999)7:2<106::AID-HBM4>3.0.CO;2-O

Birn, R. M., Cox, R. W. & Bandettini, P. A. (2004). Experimental designs and processing strategies for fMRI studies involving overt verbal responses. *NeuroImage*, *23*(3), 1046–1058. doi:10.1016/j.neuroimage.2004.07.039

Birn, R. M., Diamond, J. B., Smith, M. A. & Bandettini, P. A. (2006). Separating respiratory-variation-related fluctuations from neuronal-activity-related fluctuations in fMRI. *NeuroImage*, *31*(4), 1536–1548. doi:10.1016/j.neuroimage.2006.02.048

Birn, R. M., Smith, M. A., Jones, T. B. & Bandettini, P. A. (2008). The respiration response function: The temporal dynamics of fMRI signal fluctuations related to changes in respiration. *NeuroImage*, *40*(2), 644–654. doi:10.1016/j.neuroimage.2007.11.059

Biswal, B., Yetkin, F., Haughton, V. & Hyde, J. (1995). Functional connectivity in the motor cortex of resting human brain using. *Magn Reson Med*, *34*(9), 537–541. doi:10.1002/mrm.1910340409

Biswal, B., DeYoe, E. A. & Hyde, J. S. (1996). Reduction of physiological fluctuations in fMRI using digital filters. *Magnetic Resonance in Medicine*, *35*(1), 107–113. doi:10.1002/mrm.1910350114

Biswal, B. B., Kannurpatti, S. S. & Rypma, B. (2007). Hemodynamic scaling of fMRI-BOLD signal: validation of low-frequency spectral amplitude as a scalability factor. *Magnetic Resonance Imaging*, *25*(10), 1358–1369. doi:10.1016/j.mri.2007.03.022

Bloch, F. (1946). Nuclear induction. *Physical Review*, *70*(7-8), 460–474. doi:10.1103/PhysRev.70.460

Blockley, N. P., Driver, I. D., Francis, S. T., Fisher, J. A. & Gowland, P. A. (2011). An improved method for acquiring cerebrovascular reactivity maps. *Magnetic Resonance in Medicine*, *65*(5), 1278–1286. doi:10.1002/mrm.22719

Blockley, N. P., Harkin, J. W. & Bulte, D. P. (2017). Rapid cerebrovascular reactivity mapping: Enabling vascular reactivity information to be routinely acquired. *NeuroImage*, *159*(January), 214–223. doi:10.1016/j.neuroimage.2017.07.048

Bolton, T. A., Kebets, V., Glerean, E., Zöller, D., Li, J., Yeo, B. T., ... Van De Ville, D. (2020). Agito ergo sum: Correlates of spatio-temporal motion characteristics during fMRI. *NeuroImage*, *209*(June 2019). doi:10.1016/j.neuroimage.2019.116433. arXiv: 1906.06445

Braga, R. M. & Buckner, R. L. (2017). Parallel Interdigitated Distributed Networks within the Individual Estimated by Intrinsic Functional Connectivity. *Neuron*, *95*(2), 457–471.e5. doi:10.1016/j.neuron.2017.06.038

Braga, R. M., Van Dijk, K. R., Polimeni, J. R., Eldaief, M. C. & Buckner, R. L. (2019). Parallel distributed networks resolved at high resolution reveal close juxtaposition of distinct regions. *Journal of Neurophysiology*, *121*(4), 1513–1534. doi:10.1152/jn.00808.2018

Bright, M. G., Whittaker, J. R., Driver, I. D. & Murphy, K. (2020). Vascular physiology drives functional brain networks. *NeuroImage*, *217*. doi:10.1101/475491

Bright, M. G., Bulte, D. P., Jezzard, P. & Duyn, J. H. (2009). Characterization of regional heterogeneity in cerebrovascular reactivity dynamics using novel hypocapnia task and BOLD fMRI. *NeuroImage*, *48*(1), 166–175. doi:10.1016/j.neuroimage.2009.05.026

Bright, M. G., Donahue, M. J., Duyn, J. H., Jezzard, P. & Bulte, D. P. (2011). The effect of basal vasodilation on hypercapnic and hypocapnic reactivity measured using magnetic resonance imaging. *Journal of Cerebral Blood Flow and Metabolism*, *31*(2), 426–438. doi:10.1038/jcbfm.2010.187

Bright, M. G. & Murphy, K. (2013a). Reliable quantification of BOLD fMRI cerebrovascular reactivity despite poor breath-hold performance. *NeuroImage*, *83*, 559–568. doi:10.1016/j.neuroimage.2013.07.007

Bright, M. G. & Murphy, K. (2013b). Removing motion and physiological artifacts from intrinsic BOLD fluctuations using short echo data. *NeuroImage*, *64*(1), 526–537. doi:10.1016/j.neuroimage.2012.09.043

Bright, M. G. & Murphy, K. (2015). Is fMRI "noise"really noise? Resting state nuisance regressors remove variance with network structure. *NeuroImage*, *114*, 158–169. doi:10.1016/j.neuroimage.2015.03.070

Bright, M. G., Tench, C. R. & Murphy, K. (2017). Potential pitfalls when denoising resting state fMRI data using nuisance regression. *NeuroImage*, *154*(December 2016), 159–168. doi:10.1016/j.neuroimage.2016.12.027

Buckner, R. L. & DiNicola, L. M. (2019). The brain's default network: updated anatomy, physiology and evolving insights. *Nature reviews. Neuroscience*. doi:10.1038/s41583-019-0212-7

Buckner, R. L., Krienen, F. M., Castellanos, A., Diaz, J. C. & Yeo, B. T. T. (2011). The organization of the human cerebellum estimated by intrinsic functional connectivity. *J Neurophysiol*, *106*(July 2011), 2322–2345. doi:10.1152/jn.00339.2011.. arXiv: NIHMS150003

Buckner, R. L., Andrews-Hanna, J. R. & Schacter, D. L. (2008). The brain's default network: Anatomy, function, and relevance to disease. *Annals of the New York Academy of Sciences*, *1124*, 1–38. doi:10.1196/annals.1440.011

Burley, C. V., Francis, S. T., Thomas, K. N., Whittaker, A. C., Lucas, S. J. & Mullinger, K. J. (2021). Contrasting Measures of Cerebrovascular Reactivity Between MRI and Doppler: A Cross-Sectional Study of Younger and Older Healthy Individuals. *Frontiers in Physiology*, *12*(April), 1–17. doi:10.3389/fphys.2021.656746

Buterbaugh, J., Wynstra, C., Provencio, N., Combs, D., Gilbert, M. & Parthasarathy, S. (2015). Cerebrovascular Reactivity in Young Subjects with Sleep Apnea. *Sleep*, *38*(2), 241–250. doi:10.5665/sleep.4406

Caballero-Gaudes, C., Karahanoğlu, F. I., Lazeyras, F. & Van De Ville, D. (2012). Structured sparse deconvolution for paradigm free mapping of functional MRI data. *Proceedings - International Symposium on Biomedical Imaging*, 322–325. doi:10.1109/ISBI.2012.6235549

Caballero-Gaudes, C., Moia, S., Panwar, P., Bandettini, P. A. & Gonzalez-Castillo, J. (2019). A deconvolution algorithm for multi-echo functional MRI: Multi-echo Sparse Paradigm Free Mapping. *NeuroImage*, *202*(August), 1–15. doi:10.1016/j.neuroimage.2019.116081

Caballero-Gaudes, C., Petridou, N., Dryden, I. L., Bai, L., Francis, S. T. & Gowland, P. A. (2011). Detection and characterization of single-trial fMRI bold responses: Paradigm free mapping. *Human Brain Mapping*, *32*(9), 1400–1418. doi:10.1002/hbm.21116

Caballero-Gaudes, C. & Reynolds, R. C. (2017). Methods for cleaning the BOLD fMRI signal. *NeuroImage*, *154*(December 2016), 128–149. doi:10.1016/j.neuroimage.2016.12.018

Camargo, C. H. F., Martins, E. A., Lange, M. C., Hoffmann, H. A., Luciano, J. J., Young Blood, M. R., ... Miyoshi, E. (2015). Abnormal Cerebrovascular Reactivity in Patients with Parkinson's Disease. *Parkinson's Disease*, *2015*. doi:10.1155/2015/523041

Carr, J. M. J. R., Caldwell, H. G. & Ainslie, P. N. (2021). Cerebral blood flow, cerebrovascular reactivity and their influence on ventilatory sensitivity. *Experimental Physiology*, (April), 1–24. doi:10.1113/ep089446

Cauley, S. F., Polimeni, J. R., Bhat, H., Wald, L. L. & Setsompop, K. (2014). Interslice leakage artifact reduction technique for simultaneous multislice acquisitions. *Magnetic Resonance in Medicine*, *72*(1), 93–102. doi:10.1002/mrm.24898

Chang, C., Cunningham, J. P. & Glover, G. H. (2009). Influence of heart rate on the BOLD signal: The cardiac response function. *NeuroImage*, *44*(3), 857–869. doi:10.1016/j.neuroimage.2008.09.029

Chang, C. & Glover, G. H. (2009). Relationship between respiration, end-tidal CO2, and BOLD signals in resting-state fMRI. *NeuroImage*, *47*(4), 1381–1393. doi:10.1016/j.neuroimage.2009.04.048. arXiv: NIHMS150003

Chen, C. M., Yang, H. C., Hsieh, H. H., Liao, T. Y., Huang, Y. C. & Peng, S. L. (2021). Characterization of regional differences in cerebral vascular response to breath holding using BOLD fMRI. *International Journal of Imaging Systems and Technology*, *31*(1), 180–188. doi:10.1002/ima.22473

Chen, G., Pine, D. S., Brotman, M. A., Smith, A. R., Cox, R. W., Taylor, P. A. & Haller, S. P. (2021). Hyperbolic trade-off : the importance of balancing trial and subject sample sizes in neuroimaging. *bioRxiv*. doi:10.1101/2021.07.15.452548

Chen, G., Saad, Z. S., Britton, J. C., Pine, D. S. & Cox, R. W. (2013). Linear mixed-effects modeling approach to FMRI group analysis. *NeuroImage*, *73*, 176–190. doi:10.1016/j.neuroimage.2013.01.047

Chen, G., Saad, Z. S., Nath, A. R., Beauchamp, M. S. & Cox, R. W. (2012). FMRI group analysis combining effect estimates and their variances. *NeuroImage*, *60*(1), 747–765. doi:10.1016/j.neuroimage.2011.12.060

Chen, G., Taylor, P. A., Haller, S. P., Kircanski, K., Stoddard, J., Pine, D. S., ... Cox, R. W. (2018). Intraclass correlation: Improved modeling approaches and applications for neuroimaging. *Human Brain Mapping*, *39*(3), 1187–1206. doi:10.1002/hbm.23909

Chen, J. E., Lewis, L. D., Chang, C., Tian, Q., Fultz, N. E., Ohringer, N. A., ... Polimeni, J. R. (2020). Resting-state "physiological networks". *NeuroImage*, *213*(March), 116707. doi:10.1016/j.neuroimage.2020.116707

Chen, R., Mias, G. I., Li-Pook-Than, J., Jiang, L., Lam, H. Y., Chen, R., ... Snyder, M. (2012). Personal omics profiling reveals dynamic molecular and medical phenotypes. *Cell*, *148*(6), 1293–1307. doi:10.1016/j.cell.2012.02.009

Chen, R. & Snyder, M. (2012). Systems biology: Personalized medicine for the future? *Current Opinion in Pharmacology*, *12*(5), 623–628. doi:10.1016/j.coph.2012.07.011

Chuang, K. H. & Chen, J. H. (2001). IMPACT: Image-based physiological artifacts estimation and correction technique for functional MRI. *Magnetic Resonance in Medicine*, *46*(2), 344–353. doi:10.1002/mrm.1197

Churchill, N. W., Hutchison, M. G., Graham, S. J. & Schweizer, T. A. (2020). Cerebrovascular reactivity after sport concussion: From acute injury to 1 year after medical clearance. *Frontiers in Neurology*, *11*(July), 1–11. doi:10.3389/fneur.2020.00558

Cicchetti, D. V. (2001). The precision of reliability and validity estimates re-visited: Distinguishing between clinical and statistical significance of sample size requirements. *Journal of Clinical and Experimental Neuropsychology*, *23*(5), 695–700. doi:10.1076/jcen.23.5.695.1249

Coalson, T. S., Van Essen, D. C. & Glasser, M. F. (2018). The impact of traditional neuroimaging methods on the spatial localization of cortical areas. *Proceedings of the National Academy of Sciences of the United States of America*, *115*(27), E6356–E6365. doi:10.1073/pnas.1801582115

Cohen, A. D., Jagra, A. S., Visser, N. J., Yang, B., Fernandez, B., Banerjee, S. & Wang, Y. (2021). Improving the Breath-Holding CVR Measurement Using the Multiband

Multi-Echo EPI Sequence. *Frontiers in Physiology*, *12*(February), 1–14. doi:10.3389/fphys.2021.619714

Cohen, A. D. & Wang, Y. (2019). Improving the Assessment of Breath-Holding Induced Cerebral Vascular Reactivity Using a Multiband Multi-echo ASL/BOLD Sequence. *Scientific Reports*, *9*(1), 1–12. doi:10.1038/s41598-019-41199-w

Couvy-Duchesne, B., Blokland, G. A., Hickie, I. B., Thompson, P. M., Martin, N. G., de Zubicaray, G. I., ... Wright, M. J. (2014). Heritability of head motion during resting state functional MRI in 462 healthy twins. *NeuroImage*, *102*(P2), 424–434. doi:10.1016/j.neuroimage.2014.08.010

Cox, R. W. (1996). AFNI: software for analysis and visualization of functional magnetic resonance neuroimages. *Computers and Biomedical Research*, *29*(29), 162–173. doi:10.1006/cbmr.1996.0014

Damadian, R. (1971). Tumor detection by nuclear magnetic resonance. *Science*, *171*(3976), 1151–1153. doi:10.1126/science.171.3976.1151

De Vis, J. B., Bhogal, A. A., Hendrikse, J., Petersen, E. T. & Siero, J. C. (2018). Effect sizes of BOLD CVR, resting-state signal fluctuations and time delay measures for the assessment of hemodynamic impairment in carotid occlusion patients. *NeuroImage*, *179*(June), 530–539. doi:10.1016/j.neuroimage.2018.06.017

Dengel, D. R., Evanoff, N. G., Marlatt, K. L., Geijer, J. R., Mueller, B. A. & Lim, K. O. (2017). Reproducibility of blood oxygen level-dependent signal changes with end-tidal carbon dioxide alterations. *Clinical Physiology and Functional Imaging*, *37*(6), 794–798. doi:10.1111/cpf.12358

DiNicola, L. M., Braga, R. M. & Buckner, R. L. (2020). Parallel distributed networks dissociate episodic and social functions within the individual. *Journal of Neurophysiology*, *123*(3), 1144–1179. doi:10.1152/JN.00529.2019

DiNicola, L. M. & Buckner, R. L. (2021). Precision estimates of parallel distributed association networks: evidence for domain specialization and implications for evolution and development. *Current Opinion in Behavioral Sciences*, *40*, 120–129. doi:10.1016/j.cobeha.2021.03.029

Dipasquale, O., Sethi, A., Marcella Laganà, M., Baglio, F., Baselli, G., Kundu, P., ... Cercignani, M. (2017). Comparing resting state fMRI de-noising approaches using multi- and single-echo acquisitions. *Clinical Imaging Sciences Centre, Brighton and Sussex Medical School*, (3). doi:10.1371/journal.pone.0173289

Donahue, M. J., Strother, M. K., Lindsey, K. P., Hocke, L. M., Tong, Y. & Frederick, B. D. B. (2016). Time delay processing of hypercapnic fMRI allows quantitative parameterization of cerebrovascular reactivity and blood flow delays. *Journal of Cerebral Blood Flow and Metabolism*, *36*(10), 1767–1779. doi:10.1177/0271678X15608643

Du, J. & Buckner, R. L. (2021). Precision estimates of macroscale network organization in the human and their relation to anatomical connectivity in the marmoset monkey. *Current Opinion in Behavioral Sciences*, *40*, 144–152. doi:10.1016/j.cobeha.2021.04.010

Duffin, J., Sobczyk, O., Crawley, A. P., Poublanc, J., Mikulis, D. J. & Fisher, J. A. (2015). The dynamics of cerebrovascular reactivity shown with transfer function analysis. *NeuroImage*, *114*, 207–216. doi:10.1016/j.neuroimage.2015.04.029

Dumville, J., Panerai, R. B., Lennard, N. S., Naylor, A. R. & Evans, D. H. (1998). Can Cerebrovascular Reactivity Be Assessed Without Measuring Blood Pressure in Patients With Carotid Artery Disease? *Stroke*, *29*(5), 968–974. doi:10.1161/01.STR.29.5.968

DuPre, E., Luh, W. M. & Spreng, R. N. (2016). Multi-echo fMRI replication sample of autobiographical memory, prospection and theory of mind reasoning tasks. *Scientific Data*, *3*(October), 1–9. doi:10.1038/sdata.2016.116

DuPre, E., Salo, T., Markello, R., Kundu, P., Whitaker, K. & Handwerker, D. (2019). ME-ICA/tedana: 0.0.6. doi:10.5281/ZENODO.2558498

Ekhtiari, H., Kuplicki, R., wen Yeh, H. & Paulus, M. P. (2019). Physical characteristics not psychological state or trait characteristics predict motion during resting state fMRI. *Scientific Reports*, *9*(1), 1–8. doi:10.1038/s41598-018-36699-0

Evanoff, N. G., Mueller, B. A., Marlatt, K. L., Geijer, J. R., Lim, K. O. & Dengel, D. R. (2020). Reproducibility of a ramping protocol to measure cerebral vascular reactivity using functional magnetic resonance imaging. *Clinical Physiology and Functional Imaging*, *40*(3), 183–189. doi:10.1111/cpf.12621

Evans, J. W., Kundu, P., Horovitz, S. G. & Bandettini, P. A. (2015). Separating slow BOLD from non-BOLD baseline drifts using multi-echo fMRI. *NeuroImage*, *105*, 189–197. doi:10.1016/j.neuroimage.2014.10.051

Fair, D. A., Miranda-Dominguez, O., Snyder, A. Z., Perrone, A., Earl, E. A., Van, A. N., ... Dosenbach, N. U. (2020). Correction of respiratory artifacts in MRI head motion estimates. *NeuroImage*, *208*(November 2019), 116400. doi:10.1016/j.neuroimage.2019.116400

Faraji-Dana, Z., Tam, F., Chen, J. J. & Graham, S. J. (2016). A robust method for suppressing motion-induced coil sensitivity variations during prospective correction of head motion in fMRI. *Magnetic Resonance Imaging*, *34*(8), 1206–1219. doi:10.1016/j.mri.2016.06.005

Fedorenko, E. (2021). The early origins and the growing popularity of the individual-subject analytic approach in human neuroscience. *Current Opinion in Behavioral Sciences*, *40*, 105–112. doi:10.1016/j.cobeha.2021.02.023

Fernandez, B., Leuchs, L., Sämann, P. G., Czisch, M. & Spoormaker, V. I. (2017). Multi-echo EPI of human fear conditioning reveals improved BOLD detection in ventromedial prefrontal cortex. *NeuroImage*, *156*(May), 65–77. doi:10.1016/j.neuroimage.2017.05.005

Ficzere, A., Valikovics, A., Fülesdi, B., Juhász, A., Czuriga, I. & Csiba, L. (1997). Cerebrovascular reactivity in hypertensive patients: A transcranial Doppler study. *Journal of Clinical Ultrasound*, *25*(7), 383–389. doi:10.1002/(SICI)1097-0096(199709)25:7<383::AID-JCU6>3.0.CO;2-6

Fierstra, J., Sobczyk, O., Battisti-Charbonney, A., Mandell, D. M., Poublanc, J., Crawley, A. P., ... Fisher, J. A. (2013). Measuring cerebrovascular reactivity: what stimulus to use? *The Journal of Physiology*, *591*(23), 5809–5821. doi:10.1113/jphysiol.2013.259150

Fierstra, J., van Niftrik, C., Piccirelli, M., Bozinov, O., Pangalu, A., Krayenbühl, N., ... Regli, L. (2018). Diffuse gliomas exhibit whole brain impaired cerebrovascular reactivity. *Magnetic Resonance Imaging*, *45*(September 2017), 78–83. doi:10.1016/j.mri.2017.09.017

Finn, E. S., Scheinost, D., Finn, D. M., Shen, X., Papademetris, X. & Constable, R. T. (2017). Can brain state be manipulated to emphasize individual differences in functional connectivity? *NeuroImage*, *160*(March), 140–151. doi:10.1016/j.neuroimage.2017.03.064

Finn, E. S., Shen, X., Scheinost, D., Rosenberg, M. D., Huang, J., Chun, M. M., ... Constable, R. T. (2015). Functional connectome fingerprinting: Identifying individu-

als using patterns of brain connectivity. *Nature Neuroscience*, *18*(11), 1664–1671. doi:10.1038/nn.4135. arXiv: 15334406

Fox, M. D., Snyder, A. Z., Vincent, J. L., Corbetta, M., Van Essen, D. C. & Raichle, M. E. (2005). The human brain is intrinsically organized into dynamic, anticorrelated functional networks. *Proceedings of the National Academy of Sciences of the United States of America*, *102*(27), 9673–9678. doi:10.1073/pnas.0504136102

Frederick, B. d. B., Salo, T. & Drucker, D. M. (2020). bbfrederick/rapidtide: January 6, 2020 checkpoint release. doi:10.5281/ZENODO.3598720

Friedman, L., Turner, J. A., Stern, H., Mathalon, D. H., Trondsen, L. C. & Potkin, S. G. (2008). Chronic smoking and the BOLD response to a visual activation task and a breath hold task in patients with schizophrenia and healthy controls. *NeuroImage*, *40*(3), 1181–1194. doi:10.1016/j.neuroimage.2007.12.040

Friston, K. J., Holmes, A. P., Worsley, K. J., Poline, J.-B., Frith, C. D. & Frackowiak, R. S. (1995). Statistical parametric maps in functional imaging: a general linear model approach. *Human Brain Mapping*, *2*(081), 189–210. doi:10.1002/hbm.460020402

Friston, K. J., Ashburner, J., Frith, C. D., Poline, J. .-B., Heather, J. D. & Frackowiak, R. S. (1995). Spatial registration and normalization of images. *Human Brain Mapping*, *3*(3), 165–189. doi:10.1002/hbm.460030303

Geranmayeh, F., Wise, R. J., Leech, R. & Murphy, K. (2015). Measuring vascular reactivity with breath-holds after stroke: A method to aid interpretation of group-level BOLD signal changes in longitudinal fMRI studies. *Human Brain Mapping*, *36*(5), 1755–1771. doi:10.1002/hbm.22735

Gilbert, K. E., Wheelock, M. D., Kandala, S., Eggebrecht, A. T., Luby, J. L. & Barch, D. M. (2021). Associations of observed preschool performance monitoring with brain functional connectivity in adolescence. *Cortex*, *142*, 15–27. doi:10.1016/j.cortex.2021.05.015

Gilmore, A. W., Nelson, S. M. & McDermott, K. B. (2021). Precision functional mapping of human memory systems. *Current Opinion in Behavioral Sciences*, *40*, 52–57. doi:10.1016/j.cobeha.2020.12.013

Glasser, M. F., Coalson, T. S., Bijsterbosch, J. D., Harrison, S. J., Harms, M. P., Anticevic, A., ... Smith, S. M. (2018). Using temporal ICA to selectively remove global noise while preserving global signal in functional MRI data. *NeuroImage*, *181*(December 2017), 692–717. doi:10.1016/j.neuroimage.2018.04.076

Glasser, M. F., Smith, S. M., Marcus, D. S., Andersson, J. L. R., Auerbach, E. J., Behrens, T. E. J., ... Van Essen, D. C. (2016). The Human Connectome Project's neuroimaging approach. *Nature Neuroscience*, *19*(9), 1175–1187. doi:10.1038/nn.4361

Glodzik, L., Randall, C., Rusinek, H. & de Leon, M. J. (2013). Cerebrovascular Reactivity to Carbon Dioxide in Alzheimer's Disease. *Journal of Alzheimer's Disease*, *35*(3), 427–440. doi:10.3233/JAD-122011

Glover, G. H., Li, T.-q. & Ress, D. (2000). Image-Based Method for Retrospective Correction of Physiological Motion Effects in fMRI: RETROICOR. *Magnetic Resonance in Medicine*, *44*(1), 162–167. doi:10.1002/1522-2594(200007)44:1<162::AID-MRM23>3.0.CO;2-E

Golestani, A. M., Chang, C., Kwinta, J. B., Khatamian, Y. B. & Jean Chen, J. (2015). Mapping the end-tidal CO2 response function in the resting-state BOLD fMRI signal: Spatial specificity, test-retest reliability and effect of fMRI sampling rate. *NeuroImage*, *104*, 266–277. doi:10.1016/j.neuroimage.2014.10.031

Golestani, A. M., Wei, L. L. & Chen, J. J. (2016). Quantitative mapping of cerebrovascular reactivity using resting-state BOLD fMRI: Validation in healthy adults. *NeuroImage*, *138*, 147–163. doi:10.1016/j.neuroimage.2016.05.025

Gonzales, M. M., Tarumi, T., Mumford, J. A., Ellis, R. C., Hungate, J. R., Pyron, M., ... Haley, A. P. (2014). Greater BOLD response to working memory in endurance-trained adults revealed by breath-hold calibration. *Human Brain Mapping*, *35*(7), 2898–2910. doi:10.1002/hbm.22372

Gonzalez-Castillo, J., Panwar, P., Buchanan, L. C., Caballero-Gaudes, C., Handwerker, D. A., Jangraw, D. C., ... Bandettini, P. A. (2016). Evaluation of multi-echo ICA denoising for task based fMRI studies: Block designs, rapid event-related designs, and cardiac-gated fMRI. *NeuroImage*, *141*, 452–468. doi:10.1016/j.neuroimage.2016.07.049

Gooskens, I., Schmidt, E. A., Czosnyka, M., Piechnik, S. K., Smielewski, P., Kirkpatrick, P. J., ... Mendelow, A. D. (2003). Pressure-autoregulation, CO2 reactivity and asymmetry of haemodynamic parameters in patients with carotid artery stenotic disease. A clinical appraisal. *Acta Neurochirurgica*, *145*(7), 527–532. doi:10.1007/s00701-003-0045-y

Gordon, E. M., Laumann, T. O., Gilmore, A. W., Newbold, D. J., Greene, D. J., Berg, J. J., ... Dosenbach, N. U. (2017). Precision Functional Mapping of Individual Human Brains. *Neuron*, *95*(4), 791–807.e7. doi:10.1016/j.neuron.2017.07.011

Gordon, E. M., Laumann, T. O., Marek, S., Raut, R. V., Gratton, C., Newbold, D. J., ... Nelson, S. M. (2020). Default-mode network streams for coupling to language and control systems. *Proceedings of the National Academy of Sciences of the United States of America*, *117*(29), 17308–17319. doi:10.1073/pnas.2005238117

Gordon, E. M., Lynch, C. J., Gratton, C., Laumann, T. O., Gilmore, A. W., Greene, D. J., ... Nelson, S. M. (2018). Three Distinct Sets of Connector Hubs Integrate Human Brain Function. *Cell Reports*, *24*(7), 1687–1695.e4. doi:10.1016/j.celrep.2018.07.050

Gorgolewski, K. J., Auer, T., Calhoun, V. D., Craddock, R. C., Das, S., Duff, E. P., ... Poldrack, R. A. (2016). The brain imaging data structure, a format for organizing and describing outputs of neuroimaging experiments. *Scientific Data*. doi:10.1007/978-1-4020-6754-9_1720

Gorgolewski, K. J., Mendes, N., Wilfling, D., Wladimirow, E., Gauthier, C. J., Bonnen, T., ... Margulies, D. S. (2015). A high resolution 7-Tesla resting-state fMRI test-retest dataset with cognitive and physiological measures. *Scientific Data*, *2*, 1–13. doi:10.1038/sdata.2014.54

Gorter, C. J. & Broer, L. J. (1942). Negative result of an attempt to observe nuclear magnetic resonance in solids. *Physica*, *9*(6), 591–596. doi:10.1016/S0031-8914(42)80073-7

Grabner, G., Janke, A. L., Budge, M. M., Smith, D., Pruessner, J. & Collins, D. L. (2006). Symmetric Atlasing and Model Based Segmentation: An Application to the Hippocampus in Older Adults. In R. Larsen, M. Nielsen & J. Sporring (Eds.), *Medical image computing and computer-assisted intervention – miccai 2006: 9th international conference, copenhagen, denmark, october 1-6, 2006. proceedings, part ii* (pp. 58–66). doi:10.1007/11866763_8

Gracco, V. L., Tremblay, P. & Pike, B. (2005). Imaging speech production using fMRI. *NeuroImage*, *26*(1), 294–301. doi:10.1016/j.neuroimage.2005.01.033

Gratton, C., Dworetsky, A., Coalson, R. S., Adeyemo, B., Laumann, T. O., Wig, G. S., ... Campbell, M. C. (2020). Removal of high frequency contamination from motion

estimates in single-band fMRI saves data without biasing functional connectivity. *NeuroImage*, *217*(April), 116866. doi:10.1016/j.neuroimage.2020.116866

Gratton, C., Laumann, T. O., Nielsen, A. N., Greene, D. J., Gordon, E. M., Gilmore, A. W., ... Petersen, S. E. (2018). Functional Brain Networks Are Dominated by Stable Group and Individual Factors, Not Cognitive or Daily Variation. *Neuron*, 439–452. doi:10.1016/j.neuron.2018.03.035

Griffanti, L., Douaud, G., Bijsterbosch, J., Evangelisti, S., Alfaro-Almagro, F., Glasser, M. F., ... Smith, S. M. (2017). Hand classification of fMRI ICA noise components. *NeuroImage*, *154*(June 2016), 188–205. doi:10.1016/j.neuroimage.2016.12.036

Griffanti, L., Salimi-Khorshidi, G., Beckmann, C. F., Auerbach, E. J., Douaud, G., Sexton, C. E., ... Smith, S. M. (2014). ICA-based artefact removal and accelerated fMRI acquisition for improved resting state network imaging. *NeuroImage*, *95*, 232–247. doi:10.1016/j.neuroimage.2014.03.034

Hajjar, I., Marmerelis, V., Shin, D. C. & Chui, H. (2014). Assessment of cerebrovascular reactivity during resting state breathing and its correlation with cognitive function in hypertension. *Cerebrovascular Diseases*, *38*(1), 10–16. doi:10.1159/000365349

Halchenko, Y., Goncalves, M., di Oleggio Castello, M. V., Ghosh, S., Hanke, M., Dae, ... Kahn, A. (2019). Nipy/heudiconv v0.6.0. doi:10.5281/zenodo.3579455

Hampel, H., Toschi, N., Babiloni, C., Baldacci, F., Black, K. L., Bokde, A. L., ... Lista, S. (2018). Revolution of Alzheimer Precision Neurology. Passageway of Systems Biology and Neurophysiology. *Journal of Alzheimer's Disease*, *64*(s1), S47–S105. doi:10.3233/JAD-179932

Handwerker, D. A., Gazzaley, A., Inglis, B. A. & D'Esposito, M. (2007). Reducing vascular variability of fMRI data across aging populations using a breathholding task. *Human Brain Mapping*, *28*(9), 846–859. doi:10.1002/hbm.20307

Harper, A. M. (1965). THE INTER-RELATIONSHIP BETWEEN aPco2 AND BLOOD PRESSURE IN THE REGULATION OF BLOOD FLOW THROUGH THE CEREBRAL CORTEX. *Acta Neurologica Scandinavica*, *41*, 94–103. doi:10.1111/j.1600-0404.1965.tb01964.x

Harrison, S. J., Bianchi, S., Heinzle, J., Stephan, K. E., Iglesias, S. & Kasper, L. (2021). A Hilbert-based method for processing respiratory timeseries. *NeuroImage*, *230*(September 2020), 117787. doi:10.1016/j.neuroimage.2021.117787

Hartkamp, N. S., Bokkers, R. P., van Osch, M. J., de Borst, G. J. & Hendrikse, J. (2017). Cerebrovascular reactivity in the caudate nucleus, lentiform nucleus and thalamus in patients with carotid artery disease. *Journal of Neuroradiology*, *44*(2), 143–150. doi:10.1016/j.neurad.2016.07.003

He, B. J. (2013). Spontaneous and task-evoked brain activity negatively interact. *Journal of Neuroscience*, *33*(11), 4672–4682. doi:10.1523/JNEUROSCI.2922-12.2013

Hennig, J., Nauerth, A. & Friedburg, H. (1986). RARE imaging: A fast imaging method for clinical MR. *Magnetic Resonance in Medicine*, *3*(6), 823–833. doi:10.1002/mrm.1910030602

Hetzel, A., Braune, S., Guschlbauer, B. & Dohms, K. (1999). CO 2 Reactivity Testing Without Blood Pressure Monitoring? *Stroke*, *30*(2), 398–401. doi:10.1161/01.STR.30.2.398

Hillman, E. M. (2014). Coupling mechanism and significance of the BOLD signal: A status report. *Annual Review of Neuroscience*, *37*, 161–181. doi:10.1146/annurev-neuro-071013-014111

Hinrich, J. L., Nielsen, S. F. V., Riis, N. A. B., Eriksen, C. T., Frøsig, J., Kristensen, M. D. F., ... Mørup, M. (2017). SCALABLE GROUP LEVEL PROBABILISTIC

SPARSE FACTOR ANALYSIS DTU Compute , Technical University of Denmark , Denmark Danish Research Centre for Magnetic Resonance , Copenhagen University Hospital Hvidovre , Denmark. *IEEE International Conference on Acoustics, Speech, and Signal Processing (ICASSP) 2017*, 6314–6318.

Hodgson, K., Poldrack, R. A., Curran, J. E., Knowles, E. E., Mathias, S., Göring, H. H., ... Glahn, D. C. (2017). Shared Genetic Factors Influence Head Motion During MRI and Body Mass Index. *Cerebral cortex (New York, N.Y. : 1991)*, *27*(12), 5539–5546. doi:10.1093/cercor/bhw321

Hommel, B. (2011). The Simon effect as tool and heuristic. *Acta Psychologica*, *136*(2), 189–202. doi:10.1016/j.actpsy.2010.04.011

Huang, B., Zhang, K., Xie, P., Gong, M., Xing, E. & Glymour, C. (2019). Specific and shared causal relation modeling and mechanism-based clustering. *Advances in Neural Information Processing Systems*, *32*(NeurIPS), 1–12.

Iadecola, C. & Davisson, R. L. (2008). Hypertension and Cerebrovascular Dysfunction. *Cell Metabolism*, *7*(6), 476–484. doi:10.1016/j.cmet.2008.03.010

Ito, T., Brincat, S. L., Siegel, M., Mill, R. D., He, B. J., Miller, E. K., ... Cole, M. W. (2020). *Task-evoked activity quenches neural correlations and variability across cortical areas*. doi:10.1371/JOURNAL.PCBI.1007983

Ivanoff, J. & Peters, M. (2000). A shift of attention may be necessary, but it is not sufficient, for the generation of the Simon effect. *Psychological Research*, *64*(2), 117–135. doi:10.1007/s004260000033

Jahanian, H., Christen, T., Moseley, M. E., Pajewski, N. M., Wright, C. B., Tamura, M. K. & Zaharchuk, G. (2017). Measuring vascular reactivity with resting-state blood oxygenation level-dependent (BOLD) signal fluctuations: A potential alternative to the breath-holding challenge? *Journal of Cerebral Blood Flow and Metabolism*, *37*(7), 2526–2538. doi:10.1177/0271678X16670921

Jenkinson, M., Beckmann, C. F., Behrens, T. E. J., Woolrich, M. W. & Smith, S. M. (2012). FSL. *NeuroImage*, *62*(2), 782–790. doi:10.1016/j.neuroimage.2011.09.015. arXiv: arXiv:1401.4122v2

Jenkinson, M. & Smith, S. (2001). A global optimisation method for robust affine registration of brain images. *Medical Image Analysis*, *5*(2), 143–156. doi:10.1016/S1361-8415(01)00036-6

Jiménez Caballero, P. E. & Segura Martín, T. (2006). Valores de normalidad de la reactividad vasomotora cerebral mediante el test de apnea voluntaria. *Revista de Neurología*, *43*(10), 598. doi:10.33588/rn.4310.2005544

Jo, H. J., Saad, Z. S., Simmons, W. K., Milbury, L. A. & Cox, R. W. (2010). Mapping sources of correlation in resting state FMRI, with artifact detection and removal. *NeuroImage*, *52*(2), 571–582. doi:10.1016/j.neuroimage.2010.04.246

Johnstone, T., Ores Walsh, K. S., Greischar, L. L., Alexander, A. L., Fox, A. S., Davidson, R. J. & Oakes, T. R. (2006). Motion correction and the use of motion covariates in multiple-subject fMRI analysis. *Human Brain Mapping*, *27*(10), 779–788. doi:10.1002/hbm.20219

Jorge, J., Figueiredo, P., van der Zwaag, W. & Marques, J. P. (2013). Signal fluctuations in fMRI data acquired with 2D-EPI and 3D-EPI at 7 Tesla. *Magnetic Resonance Imaging*, *31*(2), 212–220. doi:10.1016/j.mri.2012.07.001

Kannurpatti, S. S. & Biswal, B. B. (2008). Detection and scaling of task-induced fMRI-BOLD response using resting state fluctuations. *NeuroImage*, *40*(4), 1567–1574. doi:10.1016/j.neuroimage.2007.09.040

Kannurpatti, S. S., Motes, M. A., Biswal, B. B. & Rypma, B. (2014). Assessment of unconstrained cerebrovascular reactivity marker for large age-range fMRI studies. *PLoS ONE*, *9*(2). doi:10.1371/journal.pone.0088751

Kannurpatti, S. S., Motes, M. A., Rypma, B. & Biswal, B. B. (2010). Neural and vascular variability and the fMRI-BOLD response in normal aging. *Magnetic Resonance Imaging*, *28*(4), 466–476. doi:10.1016/j.mri.2009.12.007

Karahanoğlu, F. I., Caballero-Gaudes, C., Lazeyras, F. & Van De Ville, D. (2013). Total activation: FMRI deconvolution through spatio-temporal regularization. *NeuroImage*, *73*, 121–134. doi:10.1016/j.neuroimage.2013.01.067

Kassinopoulos, M. & Mitsis, G. D. (2019). Identification of physiological response functions to correct for fluctuations in resting-state fMRI related to heart rate and respiration. *NeuroImage*, *202*(September), 116150. doi:10.1016/j.neuroimage.2019.116150

Kassner, A., Winter, J. D., Poublanc, J., Mikulis, D. J. & Crawley, A. P. (2010). Blood-oxygen level dependent MRI measures of cerebrovascular reactivity using a controlled respiratory challenge: Reproducibility and gender differences. *Journal of Magnetic Resonance Imaging*, *31*(2), 298–304. doi:10.1002/jmri.22044

Kastrup, A., Dichgans, J., Niemeier, M. & Schabet, M. (1998). Changes of cerebrovascular CO2 reactivity during normal aging. *Stroke*, *29*(7), 1311–1314. doi:10.1161/01.STR.29.7.1311

Kastrup, A., Krüger, G., Neumann-Haefelin, T. & Moseley, M. E. (2001). Assessment of cerebrovascular reactivity with functional magnetic resonance imaging: Comparison of CO2 and breath holding. *Magnetic Resonance Imaging*, *19*(1), 13–20. doi:10.1016/S0730-725X(01)00227-2

Kastrup, A., Li, T.-q., Takahashi, A., Glover, G. H. & Moseley, M. E. (1998). Functional Magnetic Resonance Imaging of Regional Cerebral Blood Oxygenation Changes During Breath Holding. *Stroke*, *29*(12), 2641–2645. doi:doi:10.1161/01.STR.29.12.2641

Kastrup, A., Thomas, C., Hartmann, C. & Schabet, M. (1997). Sex dependency of cerebrovascular CO2 reactivity in normal subjects. *Stroke*, *28*(12), 2353–2356. doi:10.1161/01.STR.28.12.2353

Kawai, N., Kubo-Kawai, N., Kubo, K., Terazawa, T. & Masataka, N. (2012). Distinct aging effects for two types of inhibition in older adults: A near-infrared spectroscopy study on the Simon task and the flanker task. *NeuroReport*, *23*(14), 819–824. doi:10.1097/WNR.0b013e3283578032

Kazan, S. M., Mohammadi, S., Callaghan, M. F., Flandin, G., Huber, L., Leech, R., ... Weiskopf, N. (2016). Vascular autorescaling of fMRI (VasA fMRI) improves sensitivity of population studies: A pilot study. *NeuroImage*, *124*, 794–805. doi:10.1016/j.neuroimage.2015.09.033

Keye, D., Wilhelm, O., Oberauer, K. & van Ravenzwaaij, D. (2009). Individual differences in conflict-monitoring: Testing means and covariance hypothesis about the Simon and the Eriksen flanker task. *Psychological Research*, *73*(6), 762–776. doi:10.1007/s00426-008-0188-9

Krainik, A., Hund-Georgiadis, M., Zysset, S. & Von Cramon, D. Y. (2005). Regional impairment of cerebrovascular reactivity and BOLD signal in adults after stroke. *Stroke*, *36*(6), 1146–1152. doi:10.1161/01.STR.0000166178.40973.a7

Krejza, J., Rudzinski, W., Arkuszewski, M., Onuoha, O. & Melhem, E. R. (2013). Cerebrovascular reactivity across the menstrual cycle in young healthy women. *Neuroradiology Journal*, *26*(4), 413–419. doi:10.1177/197140091302600406

Kundu, P., Brenowitz, N. D., Voon, V., Worbe, Y., Vertes, P. E., Inati, S. J., ... Bullmore, E. T. (2013). Integrated strategy for improving functional connectivity mapping using

multiecho fMRI. *Proceedings of the National Academy of Sciences*, *110*(40), 16187–16192. doi:10.1073/pnas.1301725110. arXiv: arXiv:1408.1149

Kundu, P., Inati, S. J., Evans, J. W., Luh, W.-M. & Bandettini, P. A. (2012). Differentiating BOLD and non-BOLD signals in fMRI time series using multi-echo EPI. *NeuroImage*, *60*, 1759–1770. doi:10.1016/j.neuroimage.2011.12.028

Kundu, P., Voon, V., Balchandani, P., Lombardo, M. V., Poser, B. A. & Bandettini, P. A. (2017). Multi-echo fMRI: A review of applications in fMRI denoising and analysis of BOLD signals. *NeuroImage*, *154*(March), 59–80. doi:10.1016/j.neuroimage.2017.03.033

Kuznetsova, A., Brockhoff, P. B. & Christensen, R. H. B. (2017). lmerTest Package: Tests in Linear Mixed Effects Models. *Journal of Statistical Software*, *82*(13). doi:10.18637/jss.v082.i13

Laumann, T. O., Gordon, E. M., Adeyemo, B., Snyder, A. Z., Joo, S. J., Chen, M. Y., ... Petersen, S. E. (2015). Functional System and Areal Organization of a Highly Sampled Individual Human Brain. *Neuron*, *87*(3), 657–670. doi:10.1016/j.neuron.2015.06.037

Lauterbur, P. C. (1973). Image Formation by Induced Local Interactions: Examples Employing Nuclear Magnetic Resonance. *Nature*, *242*, 190–191.

Leoni, R. F., Paiva, F. F., Henning, E. C., Nascimento, G. C., Tannús, A., De Araujo, D. B. & Silva, A. C. (2011). Magnetic resonance imaging quantification of regional cerebral blood flow and cerebrovascular reactivity to carbon dioxide in normotensive and hypertensive rats. *NeuroImage*, *58*(1), 75–81. doi:10.1016/j.neuroimage.2011.06.030

Leung, J., Kim, J. A. & Kassner, A. (2016). Reproducibility of cerebrovascular reactivity measures in children using BOLD MRI. *Journal of Magnetic Resonance Imaging*, *43*(5), 1191–1195. doi:10.1002/jmri.25063

Li, X., Morgan, P. S., Ashburner, J., Smith, J. & Rorden, C. (2016). The first step for neuroimaging data analysis: DICOM to NIfTI conversion. *Journal of Neuroscience Methods*, *264*, 47–56. doi:10.1016/j.jneumeth.2016.03.001

Li, Y. O., Adali, T. & Calhoun, V. D. (2007). Estimating the number of independent components for functional magnetic resonance imaging data. *Human Brain Mapping*, *28*(11), 1251–1266. doi:10.1002/hbm.20359

Li, Y., Li, R., Liu, M., Nie, Z., Muir, E. R. & Duong, T. Q. (2021). MRI study of cerebral blood flow, vascular reactivity, and vascular coupling in systemic hypertension. *Brain Research*, *1753*(September 2020), 147224. doi:10.1016/j.brainres.2020.147224

Lindquist, M. A., Geuter, S., Wager, T. D. & Caffo, B. S. (2019). Modular preprocessing pipelines can reintroduce artifacts into fMRI data. *Human Brain Mapping*, *40*(8), 2358–2376. doi:10.1002/hbm.24528

Lipp, I., Murphy, K., Caseras, X. & Wise, R. G. (2015). Agreement and repeatability of vascular reactivity estimates based on a breath-hold task and a resting state scan. *NeuroImage*, *113*, 387–396. doi:10.1016/j.neuroimage.2015.03.004

Liu, P., De Vis, J. B. & Lu, H. (2018). Cerebrovascular reactivity (CVR) MRI with CO2 challenge: A technical review. *NeuroImage*, *187*(February), 104–115. doi:10.1016/j.neuroimage.2018.03.047

Liu, P., Li, Y., Pinho, M., Park, D. C., Welch, B. G. & Lu, H. (2017). Cerebrovascular reactivity mapping without gas challenges. *NeuroImage*, *146*(November 2016), 320–326. doi:10.1016/j.neuroimage.2016.11.054

Liu, P., Welch, B. G., Li, Y., Gu, H., King, D., Yang, Y., ... Lu, H. (2017). Multiparametric imaging of brain hemodynamics and function using gas-inhalation MRI. *NeuroImage*, *146*(May 2016), 715–723. doi:10.1016/j.neuroimage.2016.09.063

Liu, P., Xu, C., Lin, Z., Sur, S., Li, Y., Yasar, S., ... Lu, H. (2020). Cerebrovascular reactivity mapping using intermittent breath modulation. *NeuroImage*, *215*(March), 116787. doi:10.1016/j.neuroimage.2020.116787

Liu, T. T. (2016). Noise contributions to the fMRI signal: An overview. *NeuroImage*, *143*, 141–151. doi:10.1016/j.neuroimage.2016.09.008

Liu, X., Chang, C. & Duyn, J. H. (2013). Decomposition of spontaneous brain activity into distinct fMRI co-activation patterns. *Frontiers in systems neuroscience*, *7*(December), 101. doi:10.3389/fnsys.2013.00101

Liu, X. & Duyn, J. H. (2013). Time-varying functional network information extracted from brief instances of spontaneous brain activity. *Proceedings of the National Academy of Sciences of the United States of America*, *110*(11), 4392–7. doi:10.1073/pnas.1216856110

Liu, X., Zhang, N., Chang, C. & Duyn, J. H. (2018). Co-activation patterns in resting-state fMRI signals. *NeuroImage*, (January), 1–10. doi:10.1016/j.neuroimage.2018.01.041

Lombardo, M. V., Auyeung, B., Holt, R. J., Waldman, J., Ruigrok, A. N., Mooney, N., ... Kundu, P. (2016). Improving effect size estimation and statistical power with multi-echo fMRI and its impact on understanding the neural systems supporting mentalizing. *NeuroImage*, *142*, 55–66. doi:10.1016/j.neuroimage.2016.07.022

Lowe, M. J., Mock, B. J. & Sorenson, J. A. (1998). Functional connectivity in single and multislice echoplanar imaging. *Neuroimage*, *7*(7), 119–132.

Lynch, C. J., Elbau, I. & Liston, C. (2021). Improving precision functional mapping routines with multi-echo fMRI. *Current Opinion in Behavioral Sciences*, *40*, 113–119. doi:10.1016/j.cobeha.2021.03.017

Lynch, C. J., Power, J. D., Scult, M. A., Dubin, M., Gunning, F. M. & Liston, C. (2020). Rapid Precision Functional Mapping of Individuals Using Multi-Echo fMRI. *Cell Reports*, *33*(12), 108540. doi:10.1016/j.celrep.2020.108540

Magon, S., Basso, G., Farace, P., Ricciardi, G. K., Beltramello, A. & Sbarbati, A. (2009). Reproducibility of BOLD signal change induced by breath holding. *NeuroImage*, *45*, 702–712. doi:10.1016/j.neuroimage.2008.12.059

Mahony, P. J., Panerai, R. B., Deverson, S. T., Hayes, P. D. & Evans, D. H. (2000). Assessment of the thigh cuff technique for measurement of dynamic cerebral autoregulation. *Stroke*, *31*(2), 476–480. doi:10.1161/01.STR.31.2.476

Mansfield, P. & Grannell, P. K. (1973). NMR 'diffraction' in solids? *Journal of Physics C: Solid State Physics*, *6*(22), L422–L426. doi:10.1088/0022-3719/6/22/007

Marek, S. & Dosenbach, N. U. (2018). The frontoparietal network: Function, electrophysiology, and importance of individual precision mapping. *Dialogues in Clinical Neuroscience*, *20*(2), 133–141. doi:10.31887/dcns.2018.20.2/smarek

Marek, S., Siegel, J. S., Gordon, E. M., Raut, R. V., Gratton, C., Newbold, D. J., ... Dosenbach, N. U. (2018). Spatial and Temporal Organization of the Individual Human Cerebellum. *Neuron*, *100*(4), 977–993.e7. doi:10.1016/j.neuron.2018.10.010

Markello, R. D., Spreng, R. N., Luh, W. M., Anderson, A. K. & De Rosa, E. (2018). Segregation of the human basal forebrain using resting state functional MRI. *NeuroImage*, *173*(October 2017), 287–297. doi:10.1016/j.neuroimage.2018.02.042

Markus, H. & Cullinane, M. (2001). Severely impaired cerebrovascular reactivity predicts stroke and TIA risk in patients with carotid artery stenosis and occlusion. *Brain*, *124*(3), 457–467. doi:10.1093/brain/124.3.457

Markus, H. S. & Harrison, M. J. (1992). Estimation of cerebrovascular reactivity using transcranial doppler, including the use of breath-holding as the vasodilatory stimulus. *Stroke*, *23*(5), 668–673. doi:10.1161/01.STR.23.5.668

Marques, J. P., Kober, T., Krueger, G., Van Der Zwaag, W., Van De Moortele, P.-F. & Gruetter, R. (2009). MP2RAGE, a self bias-field corrected sequence for improved segmentation and T 1 -mapping at high field. *NeuroImage*, *49*, 1271–1281. doi:10.1016/j.neuroimage.2009.10.002

Marshall, O., Lu, H., Brisset, J. C., Xu, F., Liu, P., Herbert, J., ... Ge, Y. (2014). Impaired cerebrovascular reactivity in multiple sclerosis. *JAMA Neurology*, *71*(10), 1275–1281. doi:10.1001/jamaneurol.2014.1668

Mascali, D., Moraschi, M., DiNuzzo, M., Tommasin, S., Fratini, M., Gili, T., ... Giove, F. (2021). Evaluation of denoising strategies for task-based functional connectivity: Equalizing residual motion artifacts between rest and cognitively demanding tasks. *Human Brain Mapping*, *42*(6), 1805–1828. doi:10.1002/hbm.25332

Maziero, D., Rondinoni, C., Marins, T., Stenger, V. A. & Ernst, T. (2020). Prospective motion correction of fMRI: Improving the quality of resting state data affected by large head motion. *NeuroImage*, *212*(August 2019), 116594. doi:10.1016/j.neuroimage.2020.116594

McCormick, E. M., Arnemann, K. L., Ito, T., Hanson, S. J. & Cole, M. W. (2021). Latent functional connectivity underlying multiple brain states. *bioRxiv*, 2021.04.05.438534. Retrieved from https://doi.org/10.1101/2021.04.05.438534

Mcgraw, K. O. & Wong, S. (1996). Forming Inferences About Some Intraclass Correlation Coefficients. *Psychological Methods*, *1*(1), 30–46. doi:10.1037/1082-989X.1.1.30

Mckeown, M. J., Makeig, S., Brown, G. G., Jung, T.-P., Kindermann, S. S., Bell, A. J. & Sejnowski, T. J. (1998). Analysis of fMRI data by blind separation into independent spatial components. *Human Brain Mapping*, *6*(3), 160–188. doi:10.1002/(sici)1097-0193(1998)6:3<160::aid-hbm5>3.3.co;2-r

McRobbie, D. W., Moore, E. A., Graves, M. J. & Prince, M. R. (2017). *MRI from Picture to Proton* (3rd ed.). doi:10.1017/9781107706958

McSwain, S. D., Hamel, D. S., Smith, P. B., Gentile, M. A., Srinivasan, S., Meliones, J. N. & Cheifetz, I. M. (2010). End-tidal and arterial carbon dioxide measurements correlate across all levels of physiologic dead space. *Respiratory Care*, *55*(3), 288–293.

Mennes, M., Kelly, C., Colcombe, S., Xavier Castellanos, F. & Milham, M. P. (2013). The extrinsic and intrinsic functional architectures of the human brain are not equivalent. *Cerebral Cortex*, *23*(1), 223–229. doi:10.1093/cercor/bhs010

Mennes, M., Zuo, X. N., Kelly, C., Di Martino, A., Zang, Y. F., Biswal, B., ... Milham, M. P. (2011). Linking inter-individual differences in neural activation and behavior to intrinsic brain dynamics. *NeuroImage*, *54*(4), 2950–2959. doi:10.1016/j.neuroimage.2010.10.046. arXiv: NIHMS150003

Moeller, S., Yacoub, E., Olman, C. A., Auerbach, E., Strupp, J., Harel, N. & Uğurbil, K. (2010). Multiband multislice GE-EPI at 7 tesla, with 16-fold acceleration using partial parallel imaging with application to high spatial and temporal whole-brain FMRI. *Magnetic Resonance in Medicine*, *63*(5), 1144–1153. doi:10.1002/mrm.22361

Moia, S., Stickland, R. C., Ayyagari, A., Termenon, M., Caballero-Gaudes, C. & Bright, M. G. (2020). Voxelwise optimization of hemodynamic lags to improve regional CVR estimates in breath-hold fMRI. In *2020 42nd annual international conference of the ieee engineering in medicine & biology society (embc)* (pp. 1489–1492). doi:10.1109/EMBC44109.2020.9176225

Monti, M. M. (2011). Statistical analysis of fMRI time-series: A critical review of the GLM approach. *Frontiers in Human Neuroscience*, *5*(MARCH), 1–13. doi:10.3389/fnhum.2011.00028

Mosso, A. (1883). Applicazione della bilancia allo studio della circolazione del sangue nell'uomo. *Reale Accademia delle Scienze di Torino*, *17*, 534–535.

Mumford, J. A., Poline, J. B. & Poldrack, R. A. (2015). Orthogonalization of regressors in fMRI models. *PLoS ONE*, *10*(4), 1–11. doi:10.1371/journal.pone.0126255

Murphy, K., Harris, A. D. & Wise, R. G. (2011). Robustly measuring vascular reactivity differences with breath-hold: Normalising stimulus-evoked and resting state BOLD fMRI data. *NeuroImage*, *54*(1), 369–379. doi:10.1016/j.neuroimage.2010.07.059

Muschelli, J., Nebel, M. B., Caffo, B. S., Barber, A. D., Pekar, J. J. & Mostofsky, S. H. (2014). Reduction of motion-related artifacts in resting state fMRI using aCompCor. *NeuroImage*, *96*, 22–35. doi:10.1016/j.neuroimage.2014.03.028

Naselaris, T., Allen, E. & Kay, K. (2021). Extensive sampling for complete models of individual brains. *Current Opinion in Behavioral Sciences*, *40*, 45–51. doi:10.1016/j.cobeha.2020.12.008

Newbold, D. J. & Dosenbach, N. U. (2021). Tracking plasticity of individual human brains. *Current Opinion in Behavioral Sciences*, *40*, 161–168. doi:10.1016/j.cobeha.2021.04.018

Newbold, D. J., Laumann, T. O., Hoyt, C. R., Hampton, J. M., Montez, D. F., Raut, R. V., ... Dosenbach, N. U. (2020). Plasticity and Spontaneous Activity Pulses in Disused Human Brain Circuits. *Neuron*, *107*(3), 580–589.e6. doi:10.1016/j.neuron.2020.05.007

Ogawa, S. & Lee, T. M. (1990). Magnetic resonance imaging of blood vessels at high fields: in vivo and in vitro measurements and image simulation. *Magnetic resonance in medicine : official journal of the Society of Magnetic Resonance in Medicine / Society of Magnetic Resonance in Medicine*, *16*(1), 9–18. doi:10.1002/mrm.1910160103

Ogawa, S., Tank, D. W., Menon, R., Ellermann, J. M., Kim, S. G., Merkle, H. & Ugurbil, K. (1992). Intrinsic signal changes accompanying sensory stimulation: functional brain mapping with magnetic resonance imaging. *Proceedings of the National Academy of Sciences*, *89*(13), 5951–5955. doi:10.1073/pnas.89.13.5951

Olafsson, V., Kundu, P., Wong, E. C., Bandettini, P. A. & Liu, T. T. (2015). Enhanced identification of BOLD-like components with multi-echo simultaneous multi-slice (MESMS) fMRI and multi-echo ICA. *NeuroImage*, *112*, 43–51. doi:10.1016/j.neuroimage.2015.02.052. arXiv: 15334406

Padberg, F., Brem, A. K., Palm, U., Pogarell, O., Hasan, A., Brunelin, J., ... Keeser, D. (2017). Discovering the individual brain: brain stimulation in psychiatry: Editorial I to the supplement from the 2nd European conference on brain stimulation in psychiatry. *European Archives of Psychiatry and Clinical Neuroscience*, *267*(s2), 109–112. doi:10.1007/s00406-017-0853-3

Pais-Roldán, P., Biswal, B., Scheffler, K. & Yu, X. (2018). Identifying respiration-related aliasing artifacts in the rodent resting-state fMRI. *Frontiers in Neuroscience*, *12*(NOV), 1–14. doi:10.3389/fnins.2018.00788

Panerai, R. B. (1998). Assessment of cerebral pressure autoregulation in humans - A review of measurement methods. *Physiological Measurement*, *19*(3), 305–338. doi:10.1088/0967-3334/19/3/001

Parker, D. B. & Razlighi, Q. R. (2019). The benefit of slice timing correction in common fMRI preprocessing pipelines. *Frontiers in Neuroscience*, *13*(JUL). doi:10.3389/fnins.2019.00821

Parkes, L., Fulcher, B., Yücel, M. & Fornito, A. (2018). An evaluation of the efficacy, reliability, and sensitivity of motion correction strategies for resting-state functional MRI. doi:10.1016/j.neuroimage.2017.12.073

Parri, R. & Crunelli, V. (2003). An astrocyte bridge from synapse to blood flow. *Nature neuroscience*, *6*(1), 5–6. doi:10.1038/nn0103-5

Peebles, K., Celi, L., McGrattan, K., Murrell, C., Thomas, K. & Ainslie, P. N. (2007). Human cerebrovascular and ventilatory CO2 reactivity to end-tidal, arterial and internal jugular vein PCO2. *Journal of Physiology*, *584*(1), 347–357. doi:10.1113/jphysiol.2007.137075

Peng, S.-L., Yang, H.-C., Chen, C.-M. & Shih, C.-T. (2019). Short- and long-term reproducibility of BOLD signal change induced by breath-holding at 1.5 and 3 T. *NMR in Biomedicine*. doi:10.1002/nbm.4195

Pericot Nierga, I., Molina Cateriano, C. A., Álvarez Sabín, J. & Codina Puiggrós, A. (2000). Influencia de la presión arterial en el estudio de la reactividad cerebrovascular en oclusiones carotídeas. *Revista de Neurología*, *31*(11), 1015. doi:10.33588/rn.3111.2000380

Perlbarg, V., Bellec, P., Anton, J. L., Pélégrini-Issac, M., Doyon, J. & Benali, H. (2007). CORSICA: correction of structured noise in fMRI by automatic identification of ICA components. *Magnetic Resonance Imaging*, *25*(1), 35–46. doi:10.1016/j.mri.2006.09.042

Peterson, B. S., Kane, M. J., Alexander, G. M., Lacadie, C., Skudlarski, P., Leung, H.-C., ... Gore, J. C. (2002). An event-related functional MRI study comparing interference effects in the Simon and Stroop tasks. *Cognitive Brain Research*, *13*(3), 427–440. doi:10.1016/S0926-6410(02)00054-X

phys2bids developers, T., Alcalá, D., Ayyagari, A., Bright, M., Ferrer, V., Gaudes, C. C., ... Zvolanek, K. (2019). physiopy/phys2bids: BIDS formatting of physiological recordings. doi:10.5281/zenodo.3586045

Pinel, P., Thirion, B., Meriaux, S., Jobert, A., Serres, J., Le Bihan, D., ... Dehaene, S. (2007). Fast reproducible identification and large-scale databasing of individual functional cognitive networks. *BMC Neuroscience*, *8*(1), 91. doi:10.1186/1471-2202-8-91

Pinto, J., Bright, M. G., Bulte, D. P. & Figueiredo, P. (2021). Cerebrovascular reactivity mapping without gas challenges: A Methodological Guide. *Frontiers in Physiology*, *11*, 1711. doi:10.3389/fphys.2020.608475

Pinto, J., Jorge, J., Sousa, I., Vilela, P. & Figueiredo, P. (2016). Fourier modeling of the BOLD response to a breath-hold task: Optimization and reproducibility. *NeuroImage*, *135*, 223–231. doi:10.1016/j.neuroimage.2016.02.037

Poldrack, R. A. (2021). Diving into the deep end: a personal reflection on the MyConnectome study. *Current Opinion in Behavioral Sciences*, *40*, 1–4. doi:10.1016/j.cobeha.2020.10.008

Poldrack, R. A., Laumann, T. O., Koyejo, O., Gregory, B., Hover, A., Chen, M. Y., ... Mumford, J. A. (2015). Long-term neural and physiological phenotyping of a single human. *Nature Communications*, *6*. doi:10.1038/ncomms9885

Poline, J. B. & Brett, M. (2012). The general linear model and fMRI: Does love last forever? *NeuroImage*, *62*(2), 871–880. doi:10.1016/j.neuroimage.2012.01.133

Poppe, T., Willers Moore, J. & Arichi, T. (2021). Individual focused studies of functional brain development in early human infancy. *Current Opinion in Behavioral Sciences*, *40*, 137–143. doi:10.1016/j.cobeha.2021.04.017

Poser, B. A., Versluis, M. J., Hoogduin, J. M. & Norris, D. G. (2006). BOLD contrast sensitivity enhancement and artifact reduction with multiecho EPI: Parallel-acquired inhomogeneity-desensitized fMRI. *Magnetic Resonance in Medicine*, *55*(6), 1227–1235. doi:10.1002/mrm.20900

Posse, S., Wiese, S., Gembris, D., Mathiak, K., Kessler, C., Grosse-Ruyken, M. L., ... Kiselev, V. G. (1999). Enhancement of BOLD-contrast sensitivity by single-shot multi-echo functional MR imaging. *Magnetic Resonance in Medicine*, *42*(1), 87–97. doi:10.1002/(SICI)1522-2594(199907)42:1<87::AID-MRM13>3.0.CO;2-O. arXiv: NIHMS150003

Power, J. D., Barnes, K. A., Snyder, A. Z., Schlaggar, B. L. & Petersen, S. E. (2012). Spurious but systematic correlations in functional connectivity MRI networks arise from subject motion. *NeuroImage*, *59*(3), 2142–2154. doi:10.1016/j.neuroimage.2011.10.018. arXiv: NIHMS150003

Power, J. D., Lynch, C. J., Silver, B. M., Dubin, M. J., Martin, A. & Jones, R. M. (2019). Distinctions among real and apparent respiratory motions in human fMRI data. *NeuroImage*, *201*(July), 116041. doi:10.1016/j.neuroimage.2019.116041

Power, J. D., Plitt, M., Gotts, S. J., Kundu, P., Voon, V., Bandettini, P. A. & Martin, A. (2018). Ridding fMRI data of motion-related influences: Removal of signals with distinct spatial and physical bases in multiecho data. *Proceedings of the National Academy of Sciences*, *115*(9), E2105–E2114. doi:10.1073/pnas.1720985115

Power, J. D., Plitt, M., Laumann, T. O. & Martin, A. (2017). Sources and implications of whole-brain fMRI signals in humans. *NeuroImage*, *146*(September 2016), 609–625. doi:10.1016/j.neuroimage.2016.09.038

Power, J. D., Silver, B. M., Silverman, M. R., Ajodan, E. L., Bos, D. J. & Jones, R. M. (2019). Customized head molds reduce motion during resting state fMRI scans. *NeuroImage*, *189*(October 2018), 141–149. doi:10.1016/j.neuroimage.2019.01.016

Prilipko, O., Huynh, N., Thomason, M. E., Kushida, C. A. & Guilleminault, C. (2014). An fMRI study of cerebrovascular reactivity and perfusion in obstructive sleep apnea patients before and after CPAP treatment. *Sleep Medicine*, *15*(8), 892–898. doi:10.1016/j.sleep.2014.04.004

Pritschet, L., Santander, T., Taylor, C. M., Layher, E., Yu, S., Miller, M. B., ... Jacobs, E. G. (2020). Functional reorganization of brain networks across the human menstrual cycle. *NeuroImage*, *220*(December 2019), 117091. doi:10.1016/j.neuroimage.2020.117091

Pritschet, L., Taylor, C. M., Santander, T. & Jacobs, E. G. (2021). Applying dense-sampling methods to reveal dynamic endocrine modulation of the nervous system. *Current Opinion in Behavioral Sciences*, *40*, 72–78. doi:10.1016/j.cobeha.2021.01.012

Pruim, R. H. R., Mennes, M., Buitelaar, J. K. & Beckmann, C. F. (2015). Evaluation of ICA-AROMA and alternative strategies for motion artifact removal in resting state fMRI. *NeuroImage*, *112*, 278–287. doi:10.1016/j.neuroimage.2015.02.063

Pruim, R. H. R., Mennes, M., Rooij, D. V., Llera, A., Buitelaar, J. K., Beckmann, C. F., ... Beckmann, C. F. (2015). ICA-AROMA: A robust ICA-based strategy for removing motion artifacts from fMRI data. *NeuroImage*, *112*, 267–277. doi:10.1016/j.neuroimage.2015.02.064

Puckett, A. M., Bollmann, S., Poser, B. A., Palmer, J., Barth, M. & Cunnington, R. (2018). Using multi-echo simultaneous multi-slice (SMS) EPI to improve functional MRI of the subcortical nuclei of the basal ganglia at ultra-high field (7T). *NeuroImage*, *172*(December 2017), 886–895. doi:10.1016/j.neuroimage.2017.12.005

Purcell, E. M., Torrey, H. C. & Pound, R. V. (1945). Resonance Absorption by Nuclear Magnetic Moments in a Solid. *Phys. Rev*, *69*.

Qi, T., Schaadt, G. & Friederici, A. D. (2021). Associated functional network development and language abilities in children. *NeuroImage*, *242*(August), 118452. doi:10.1016/j.neuroimage.2021.118452

R Core Team. (2020). R: A Language and Environment for Statistical Computing. Vienna, Austria. Retrieved from https://www.r-project.org/

Rabi, I. I. (1937). Space quantization in a gyrating magnetic field. *Physical Review*, *51*(8), 652–654. doi:10.1103/PhysRev.51.652

Raitamaa, L., Korhonen, V., Huotari, N., Raatikainen, V., Hautaniemi, T., Kananen, J., ... Kiviniemi, V. (2018). Breath hold effect on cardiovascular brain pulsations – A multimodal magnetic resonance encephalography study. *Journal of Cerebral Blood Flow and Metabolism*. doi:10.1177/0271678X18798441

Raj, D., Anderson, A. W. & Gore, J. C. (2001). Respiratory effects in human functional magnetic resonance imaging due to bulk susceptibility changes. *Physics in Medicine and Biology*, *46*(12), 3331–3340. doi:10.1088/0031-9155/46/12/318

Ratnatunga, C. & Adiseshiah, M. (1990). Increase in middle cerebral artery velocity on breath holding: A simplified test of cerebral perfusion reserve. *European Journal of Vascular Surgery*, *4*(5), 519–523. doi:10.1016/S0950-821X(05)80795-9

Raut, R. V., Nair, V. A., Sattin, J. A. & Prabhakaran, V. (2016). Hypercapnic evaluation of vascular reactivity in healthy aging and acute stroke via functional MRI. *NeuroImage: Clinical*, *12*, 173–179. doi:10.1016/j.nicl.2016.06.016

Regan, R. E., Fisher, J. A. & Duffin, J. (2014). Factors affecting the determination of cerebrovascular reactivity. *Brain and Behavior*, *4*(5), 775–788. doi:10.1002/brb3.275

Riecker, A., Grodd, W., Klose, U., Schulz, J. B., Gröschel, K., Erb, M., ... Kastrup, A. (2003). Relation between regional functional MRI activation and vascular reactivity to carbon dioxide during normal aging. *Journal of Cerebral Blood Flow and Metabolism*, *23*(5), 565–573. doi:10.1097/01.WCB.0000056063.25434.04

Ringelstein, E. B., Van Eyck, S. & Mertens, I. (1992). Evaluation of cerebral vasomotor reactivity by various vasodilating stimuli: Comparison of CO2 to acetazolamide. *Journal of Cerebral Blood Flow and Metabolism*, *12*(1), 162–168. doi:10.1038/jcbfm.1992.20

Rissanen, J. (1978). Modelling by the shortest data description. *Automatica*, *14*, 465–471.

Sabra, D., Intzandt, B., Desjardins-Crepeau, L., Langeard, A., Steele, C., Frouin, F., ... Gauthier, C. (2020). Sex moderates the relationship between aortic stiffness, cognition and cerebrovascular reactivity in healthy older adults. *bioRxiv*, (514). doi:10.1101/2020.02.18.955146

Sacco, K. (2012). *Le Neuroimmagini, nuove frontiere per lo studio del cervello umano in vivo* (Idelson-Gnocchi, Ed.).

Sala-Llonch, R., Peña-Gómez, C., Arenaza-Urquijo, E. M., Vidal-Piñeiro, D., Bargalló, N., Junqué, C. & Bartrés-Faz, D. (2012). Brain connectivity during resting state and subsequent working memory task predicts behavioural performance. *Cortex*, *48*(9), 1187–1196. doi:10.1016/j.cortex.2011.07.006

Salehi, M., Karbasi, A., Barron, D. S., Scheinost, D. & Constable, R. T. (2020). Individualized functional networks reconfigure with cognitive state. *NeuroImage*, *206*(September 2019), 116233. doi:10.1016/j.neuroimage.2019.116233

Salimi-Khorshidi, G., Douaud, G., Beckmann, C. F., Glasser, M. F., Griffanti, L. & Smith, S. M. (2014). Automatic denoising of functional MRI data: Combining independent component analysis and hierarchical fusion of classifiers. *NeuroImage*, *90*, 449–468. doi:10.1016/j.neuroimage.2013.11.046

Satterthwaite, F. E. (1946). An Approximate Distribution of Estimates of Variance Components. *Biometrics Bulletin*, *2*(6), 110–114.

Schulz, J., Siegert, T., Bazin, P. L., Maclaren, J., Herbst, M., Zaitsev, M. & Turner, R. (2014). Prospective slice-by-slice motion correction reduces false positive activ-

ations in fMRI with task-correlated motion. *NeuroImage*, *84*, 124–132. doi:10.1016/j.neuroimage.2013.08.006

Seitzman, B. A., Gratton, C., Laumann, T. O., Gordon, E. M., Adeyemo, B., Dworetsky, A., ... Petersen, S. E. (2019). Trait-like variants in human functional brain networks. *Proceedings of the National Academy of Sciences of the United States of America*, *116*(45), 22851–22861. doi:10.1073/pnas.1902932116

Setsompop, K., Gagoski, B. A., Polimeni, J. R., Witzel, T., Wedeen, V. J. & Wald, L. L. (2012). Blipped-controlled aliasing in parallel imaging for simultaneous multislice echo planar imaging with reduced g-factor penalty. *Magnetic Resonance in Medicine*, *67*(5), 1210–1224. doi:10.1002/mrm.23097

Settakis, G., Molnár, C., Kerényi, L., Kollár, J., Legemate, D., Csiba, L. & Fülesdi, B. (2003). Acetazolamide as a vasodilatory stimulus in cerebrovascular diseases and in conditions affecting the cerebral vasculature. *European Journal of Neurology*, *10*(6), 609–620. doi:10.1046/j.1468-1331.2003.00675.x

Settakis, G., Páll, D., Molnár, C., Bereczki, D., Csiba, L. & Fülesdi, B. (2003). Cerebrovascular reactivity in hypertensive and healthy adolescents: TCD with vasodilatory challenge. *Journal of Neuroimaging*, *13*(2), 106–112. doi:10.1177/1051228403251265

Shannon, B. J., Dosenbach, R. A., Su, Y., Vlassenko, A. G., Larson-Prior, L. J., Nolan, T. S., ... Raichle, M. E. (2013). Morning-evening variation in human brain metabolism and memory circuits. *Journal of Neurophysiology*, *109*(5), 1444–1456. doi:10.1152/jn.00651.2012

Shine, J. M., Koyejo, O. & Poldrack, R. A. (2016). Temporal metastates are associated with differential patterns of time-resolved connectivity, network topology, and attention. *Proceedings of the National Academy of Sciences of the United States of America*, *113*(35), 9888–9891. doi:10.1073/pnas.1604898113

Shmueli, K., van Gelderen, P., de Zwart, J. A., Horovitz, S. G., Fukunaga, M., Jansma, J. M. & Duyn, J. H. (2007). Low-frequency fluctuations in the cardiac rate as a source of variance in the resting-state fMRI BOLD signal. *NeuroImage*, *38*(2), 306–320. doi:10.1016/j.neuroimage.2007.07.037

Shrout, P. E. & Fleiss, J. L. (1979). Intraclass correlations: Uses in assessing rater reliability. *Psychological Bulletin*, *86*(2), 420–428. doi:10.1037/0033-2909.86.2.420

Šidák, Z. (1967). Rectangular Confidence Regions for the Means of Multivariate Normal Distributions. *Journal of the American Statistical Association*, *62*(318), 626–633.

Simon, J. R. & Rudell, A. P. (1967). Auditory S-R compatibility: The effect of an irrelevant cue on information processing. *Journal of Applied Psychology*, *51*(3), 300–304. doi:10.1037/h0020586

Smielewski, P., Kirkpatrick, P., Minhas, P., Pickard, J. D. & Czosnyka, M. (1995). Can cerebrovascular reactivity be measured with near-infrared spectroscopy? *Stroke*, *26*(12), 2285–2292. doi:10.1161/01.STR.26.12.2285

Smith, D. M., Perez, D. C., Porter, A., Dworetsky, A. & Gratton, C. (2021). Light through the fog: using precision fMRI data to disentangle the neural substrates of cognitive control. *Current Opinion in Behavioral Sciences*, *40*, 19–26. doi:10.1016/j.cobeha.2020.12.004

Smith, S. M., Miller, K. L., Moeller, S., Xu, J., Auerbach, E. J., Woolrich, M. W., ... Ugurbil, K. (2012). Temporally-independent functional modes of spontaneous brain activity. *Proceedings of the National Academy of Sciences of the United States of America*, *109*(8), 3131–3136. doi:10.1073/pnas.1121329109

Smyser, C. D., Inder, T. E., Shimony, J. S., Hill, J. E., Degnan, A. J., Snyder, A. Z. & Neil, J. J. (2010). Longitudinal analysis of neural network development in preterm infants. *Cerebral Cortex*, *20*(12), 2852–2862. doi:10.1093/cercor/bhq035

Soltysik, D. A. & Hyde, J. S. (2006). Strategies for block-design fMRI experiments during task-related motion of structures of the oral cavity. *NeuroImage*, *29*(4), 1260–1271. doi:10.1016/j.neuroimage.2005.08.063

Sotiropoulos, S. N., Moeller, S., Jbabdi, S., Xu, J., Andersson, J. L., Auerbach, E. J., ... Lenglet, C. (2013). Effects of image reconstruction on fiber orientation mapping from multichannel diffusion MRI: Reducing the noise floor using SENSE. *Magnetic Resonance in Medicine*, *70*(6), 1682–1689. doi:10.1002/mrm.24623

Sousa, I., Vilela, P. & Figueiredo, P. (2014). Reproducibility of hypocapnic cerebrovascular reactivity measurements using BOLD fMRI in combination with a paced deep breathing task. *NeuroImage*, *98*, 31–41. doi:10.1016/j.neuroimage.2014.04.049

Stickland, R. C., Zvolanek, K. M., Moia, S., Ayyagari, A., Caballero-Gaudes, C. & Bright, M. G. (2021). A practical modification to a resting state fMRI protocol for improved characterization of cerebrovascular function. *NeuroImage*, *239*(June), 118306. doi:10.1016/j.neuroimage.2021.118306

Sullivan, K. J., Kissoon, N. & Goodwin, S. R. (2005). End-tidal carbon dioxide monitoring in pediatric emergencies. *Pediatric Emergency Care*, *21*(5), 327–333. doi:10.1097/01.pec.0000159064.24820.bd

Tagliazucchi, E., Balenzuela, P., Fraiman, D. & Chialvo, D. R. (2011). Point process analysis of large-scale brain fMRI dynamics. arXiv: arXiv:1107.4572v1

Tallon, C. M., Barker, A. R., Nowak-Flück, D., Ainslie, P. N. & McManus, A. M. (2020). The influence of age and sex on cerebrovascular reactivity and ventilatory response to hypercapnia in children and adults. *Experimental Physiology*, *105*(7), 1090–1101. doi:10.1113/EP088293

Tan, C. O. (2012). Defining the characteristic relationship between arterial pressure and cerebral flow. *Journal of Applied Physiology*, *113*(8), 1194–1200. doi:10.1152/japplphysiol.00783.2012

Tancredi, F. B. & Hoge, R. D. (2013). Comparison of Cerebral Vascular Reactivity Measures Obtained Using Breath-Holding and CO 2 Inhalation. *Journal of Cerebral Blood Flow & Metabolism*, *33*(7), 1066–1074. doi:10.1038/jcbfm.2013.48

Tchistiakova, E., Anderson, N. D., Greenwood, C. E. & Macintosh, B. J. (2014). Combined effects of type 2 diabetes and hypertension associated with cortical thinning and impaired cerebrovascular reactivity relative to hypertension alone in older adults. *NeuroImage: Clinical*, *5*, 36–41. doi:10.1016/j.nicl.2014.05.020

Thomas, B., Logan, W., Donner, E. J. & Shroff, M. (2013). Assessment of cerebrovascular reactivity using real-time BOLD fMRI in children with moyamoya disease: A pilot study. *Child's Nervous System*, *29*(3), 457–463. doi:10.1007/s00381-012-1952-0

Thomason, M. E., Burrows, B. E., Gabrieli, J. D. & Glover, G. H. (2005). Breath holding reveals differences in fMRI BOLD signal in children and adults. *NeuroImage*, *25*(3), 824–837. doi:10.1016/j.neuroimage.2004.12.026

Thrall, S. F., Tymko, M. M., Green, C. L., Wynnyk, K. I., Brandt, R. A. & Day, T. A. (2021). The effect of hypercapnia on regional cerebral blood flow regulation during progressive lower-body negative pressure. *European Journal of Applied Physiology*, *121*(1), 339–349. doi:10.1007/s00421-020-04506-2

Tong, Y., Bergethon, P. R. & Frederick, B. d. B. (2011). An improved method for mapping cerebrovascular reserve using concurrent fMRI and near-infrared spectroscopy with

Regressor Interpolation at Progressive Time Delays (RIPTiDe). *NeuroImage*, *56*(4), 2047–2057. doi:10.1016/j.neuroimage.2011.03.071

Tong, Y. & Frederick, B. d. B. (2014). Tracking cerebral blood flow in BOLD fMRI using recursively generated regressors. *Human Brain Mapping*, *35*(11), 5471–5485. doi:10.1002/hbm.22564

Tracy, J. I., Faro, S. S., Mohammed, F., Pinus, A., Christensen, H. & Burkland, D. (2001). A comparison of 'early' and 'late' stage brain activation during brief practice of a simple motor task. *Cognitive Brain Research*, *10*(3), 303–316. doi:10.1016/S0926-6410(00)00045-8

Tustison, N. J., Cook, P. A., Klein, A., Song, G., Das, S. R., Duda, J. T., ... Avants, B. B. (2014). Large-scale evaluation of ANTs and FreeSurfer cortical thickness measurements. *NeuroImage*, *99*, 166–179. doi:10.1016/j.neuroimage.2014.05.044

Urback, A. L., MacIntosh, B. J. & Goldstein, B. I. (2017). Cerebrovascular reactivity measured by functional magnetic resonance imaging during breath-hold challenge: A systematic review. *Neuroscience and Biobehavioral Reviews*, *79*(April), 27–47. doi:10.1016/j.neubiorev.2017.05.003

van den Heuvel, M. P. & Hulshoff Pol, H. E. (2010). Exploring the brain network: A review on resting-state fMRI functional connectivity. *European Neuropsychopharmacology*, *20*(8), 519–534. doi:10.1016/j.euroneuro.2010.03.008

Van Oers, C. A., Van Der Worp, H. B., Kappelle, L. J., Raemaekers, M. A., Otte, W. M. & Dijkhuizen, R. M. (2018). Etiology of language network changes during recovery of aphasia after stroke. *Scientific Reports*, *8*(1), 1–12. doi:10.1038/s41598-018-19302-4

Vannesjo, S. J., Wilm, B. J., Duerst, Y., Gross, S., Brunner, D. O., Dietrich, B. E., ... Pruessmann, K. P. (2015). Retrospective correction of physiological field fluctuations in high-field brain MRI using concurrent field monitoring. *Magnetic Resonance in Medicine*, *73*(5), 1833–1843. doi:10.1002/mrm.25303

Vorstrup, S., Brun, B. & Lassen, N. A. (1986). Evaluation of the cerebral vasodilatory capacity by the acetazolamide test before ec-ic bypass surgery in patients with occlusion of the internal carotid artery. *Stroke*, *17*(6), 1291–1298. doi:10.1161/01.STR.17.6.1291

Wager, T. D., Sylvester, C. Y. C., Lacey, S. C., Nee, D. E., Franklin, M. & Jonides, J. (2005). Common and unique components of response inhibition revealed by fMRI. *NeuroImage*, *27*(2), 323–340. doi:10.1016/j.neuroimage.2005.01.054

Wang, J., Chen, H., Liang, H., Wang, W., Liang, Y., Liang, Y. & Zhang, Y. (2019). Low-frequency fluctuations amplitude signals exhibit abnormalities of intrinsic brain activities and reflect cognitive impairment in leukoaraiosis patients. *Medical Science Monitor*, *25*, 5219–5228. doi:10.12659/MSM.915528

Webster, M. W., Makaroun, M. S., Steed, D. L., Smith, H. A., Johnson, D. W. & Yonas, H. (1995). Compromised cerebral blood flow reactivity is a predictor of stroke in patients with symptomatic carotid artery occlusive disease. *Journal of Vascular Surgery*, *21*(2), 338–345. doi:10.1016/S0741-5214(95)70274-1

Whittaker, J. R., Driver, I. D., Venzi, M., Bright, M. G. & Murphy, K. (2019). Cerebral autoregulation evidenced by synchronized low frequency oscillations in blood pressure and resting-state fMRI. *Frontiers in Neuroscience*, *13*(MAY), 1–13. doi:10.3389/fnins.2019.00433

Wilm, B. J., Nagy, Z., Barmet, C., Vannesjo, S. J., Kasper, L., Haeberlin, M., ... Pruessmann, K. P. (2015). Diffusion MRI with concurrent magnetic field monitoring. *Magnetic Resonance in Medicine*, *74*(4), 925–933. doi:10.1002/mrm.25827

Wise, R. G., Ide, K., Poulin, M. J. & Tracey, I. (2004). Resting fluctuations in arterial carbon dioxide induce significant low frequency variations in BOLD signal. *NeuroImage*, *21*(4), 1652–1664. doi:10.1016/j.neuroimage.2003.11.025

Xiao, Y., Friederici, A. D., Margulies, D. S. & Brauer, J. (2016). Longitudinal changes in resting-state fMRI from age 5 to age 6years covary with language development. *NeuroImage*, *128*, 116–124. doi:10.1016/j.neuroimage.2015.12.008

Xu, Y., Tong, Y., Liu, S., Chow, H. M., AbdulSabur, N. Y., Mattay, G. S. & Braun, A. R. (2014). Denoising the speaking brain: Toward a robust technique for correcting artifact-contaminated fMRI data under severe motion. *NeuroImage*, *103*, 33–47. doi:10.1016/j.neuroimage.2014.09.013

Xue, A., Kong, R., Yang, Q., Eldaief, M. C., Angeli, P. A., DiNicola, L. M., ... Thomas Yeo, B. T. (2021). The detailed organization of the human cerebellum estimated by intrinsic functional connectivity within the individual. *Journal of Neurophysiology*, *125*(2), 358–384. doi:10.1152/jn.00561.2020

Yang, H. C. (, Liang, Z., Yao, J. (, Shen, X., Frederick, B. d. B. & Tong, Y. (2019). Vascular effects of caffeine found in BOLD fMRI. *Journal of Neuroscience Research*, *97*(4), 456–466. doi:10.1002/jnr.24360

Yezhuvath, U. S., Lewis-Amezcua, K., Varghese, R., Xiao, G. & Lu, H. (2009). On the assessment of cerebrovascular reactivity using hypercapnia BOLD MRI. *NMR in Biomedicine*, *22*(7), 779–786. doi:10.1002/nbm.1392

Zacà, D., Jovicich, J., Nadar, S. R., Voyvodic, J. T. & Pillai, J. J. (2014). Cerebrovascular reactivity mapping in patients with low grade gliomas undergoing presurgical sensorimotor mapping with BOLD fMRI. *Journal of Magnetic Resonance Imaging*, *40*(2), 383–390. doi:10.1002/jmri.24406

Zaitsev, M., Akin, B., LeVan, P. & Knowles, B. R. (2017). Prospective motion correction in functional MRI. *NeuroImage*, *154*(November 2016), 33–42. doi:10.1016/j.neuroimage.2016.11.014

Zang, Y.-F., He, Y., Zhu, C.-Z., Cao, Q.-J., Sui, M.-Q., Liang, M., ... Wang, Y.-F. (2007). Altered baseline brain activity in children with ADHD revealed by resting-state functional MRI. *Brain Dev*, *29*(2), 83–91. doi:10.1016/j.braindev.2006.07.002

Zang, Y., Jiang, T., Lu, Y., He, Y. & Tian, L. (2004). Regional homogeneity approach to fMRI data analysis. *NeuroImage*, *22*(1), 394–400. doi:10.1016/j.neuroimage.2003.12.030

Zhou, T. & Tao, D. (2011). GoDec: Randomized Low-rank & Sparse Matrix Decomposition in Noisy Case. *Proceedings of the28th International Conference on Machine Learning*. Retrieved from https://opus.lib.uts.edu.au/bitstream/10453/19145/1/2011001843OK.pdf

Ziyeh, S., Rick, J., Reinhard, M., Hetzel, A., Mader, I. & Speck, O. (2005). Blood oxygen level-dependent MRI of cerebral CO2 reactivity in severe carotid stenosis and occlusion. *Stroke*, *36*(4), 751–756. doi:10.1161/01.STR.0000157593.03470.3d

Zonta, M., Angulo, M. C., Gobbo, S., Rosengarten, B., Hossmann, K.-A., Pozzan, T. & Carmignoto, G. (2003). Neuron-to-astrocyte signaling is central to the dynamic control of brain microcirculation. *Nature neuroscience*, *6*(1), 43–50. doi:10.1038/nn980

Zou, Q. H., Zhu, C. Z., Yang, Y., Zuo, X. N., Long, X. Y., Cao, Q. J., ... Zang, Y. F. (2008). An improved approach to detection of amplitude of low-frequency fluctuation (ALFF) for resting-state fMRI: Fractional ALFF. *Journal of Neuroscience Methods*, *172*(1), 137–141. doi:10.1016/j.jneumeth.2008.04.012. arXiv: NIHMS150003

Zou, Q., Ross, T. J., Gu, H., Geng, X., Zuo, X. N., Hong, L. E., ... Yang, Y. (2013). Intrinsic resting-state activity predicts working memory brain activation and behavioral performance. *Human Brain Mapping*, *34*(12), 3204–3215. doi:10.1002/hbm.22136

A. Questionnaire on sleep, hydration, physical activity, and caffeine and alcohol intake habits

Cuestionario

Por favor, conteste a las siguientes preguntas

*Campo obbligatorio

1. Número de participante *

2. Fecha *

Esempio: 7 gennaio 2019

3. Tensión sistólica brazo derecho *

4. Tensión diastólica brazo derecho *

5. Pulso brazo derecho *

6. Tensión sistólica brazo izquierdo *

7. Tensión diastólica brazo izquierdo *

8. Pulso brazo izquierdo *

9. De media, ¿cuántas horas duermes cada noche?

10. De media, ¿cuántas horas has dormido por día en esta semana? *

A

11. ¿Cuántas horas has dormido esta noche? *

_____

12. En una escala de 1 a 9, ¿cuán cansado te sientes en este momento? *

Contrassegna solo un ovale.

	1	2	3	4	5	6	7	8	9	
Extremamente cansado	◯	◯	◯	◯	◯	◯	◯	◯	◯	Perfectamente reposado

13. ¿Cómo has dormido esta noche? *

Contrassegna solo un ovale.

	1	2	3	4	5	6	7	8	9	
He dormido muy mal	◯	◯	◯	◯	◯	◯	◯	◯	◯	He dormido muy bien

14. En una escala de 1 a 9, ¿cuán motivado te sientes en este momento? *

Contrassegna solo un ovale.

	1	2	3	4	5	6	7	8	9	
Poco motivado	◯	◯	◯	◯	◯	◯	◯	◯	◯	Muy motivado

15. De media, ¿cuántas horas de ejercicio haces en una semana?

_____

16. ¿Que tipo de ejercicio haces?

_____

_____

_____

_____

_____

17. ¿Cuántas horas de ejercicio has hecho esta semana en total? *

_____

18. ¿Cuánto tiempo ha pasado desde el ultimo periodo de ejercicio? *

_____

19. En una escala de 1 a 9, ¿cuán hidratado te sientes en este momento? *

Contrassegna solo un ovale.

	1	2	3	4	5	6	7	8	9	
Completamente deshidratado										Perfectamente hidratado

20. De media, ¿cuántos litros de agua (y otros líquidos sin alcohol o cafeína) bebes cada día?

_____

21. De media, ¿cuántos litros de agua (y otros líquidos sin alcohol o cafeína) has bebido por día esta semana? *

_____

22. En comparación con otros días, ¿has bebido más o menos líquidos hoy? (5=igual) *

Contrassegna solo un ovale.

	1	2	3	4	5	6	7	8	9	
Muchos menos										Muchos más

23. En media, ¿cuántos cafés (y otras bebidas con cafeína) bebes cada día?

_____

24. En media, ¿cuántos cafés (y otras bebidas con cafeína) has bebido por día esta semana? *

_____

25. En comparación con otros días, ¿has bebido más o menos cafés (y otras bebidas con cafeína) hoy? (5=igual) *

Contrassegna solo un ovale.

	1	2	3	4	5	6	7	8	9	
Muchos más										Muchos menos

A

26. De media, ¿cuántas unidades de bebidas alcohólicas bebes cada semana en total?

_____

Unidades
Una pinta = 1 ud;
Una caña = 0.5 ud;
Un vaso de sidra = 0.5 ud;
Un vaso de vino = 1 ud;
Otras bebidas alcohólicas = 1 ud.

27. ¿Cuántas unidades de bebidas alcohólicas has bebido esta semana en total? *

_____

28. En comparación con otras semanas, ¿has bebido más o menos unidades de bebidas alcohólicas en total? (5=igual) *

Contrassegna solo un ovale.

	1	2	3	4	5	6	7	8	9	
Muchas menos	◯	◯	◯	◯	◯	◯	◯	◯	◯	Muchas más

29. Si eres mujer, ¿estás en el periodo de menstruación?

Contrassegna solo un ovale.

◯ Si
◯ No

30. Si eres mujer, ¿cuándo comenzó tu último periodo de menstruación?

_____
Esempio: 7 gennaio 2019

31. ¿Estás tomando medicinas? ¿Cuáles?

_____
_____
_____
_____
_____

A

A

B. Tables of activation for the three tasks in Chapter 2

B.1 Figures

B.1.1 Motor task

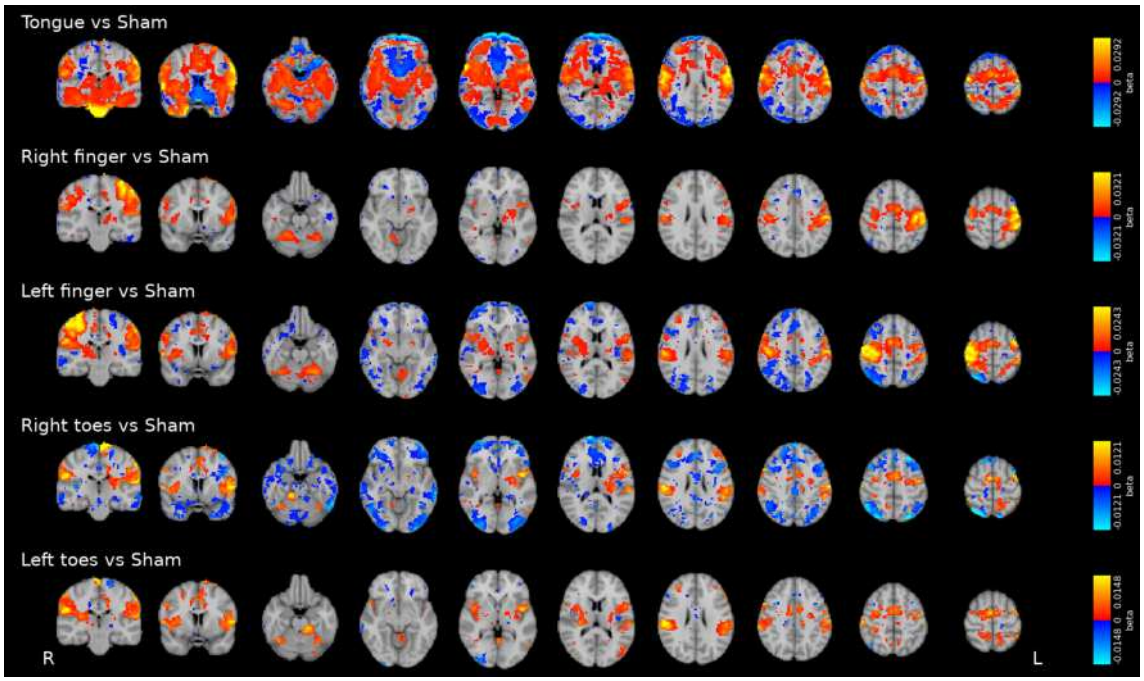

Figure B.1: Results of the one-sample MEMA test at the subject level, for subject 001, for all contrasts of the motor task ($p < 0.05$, FDR corrected).

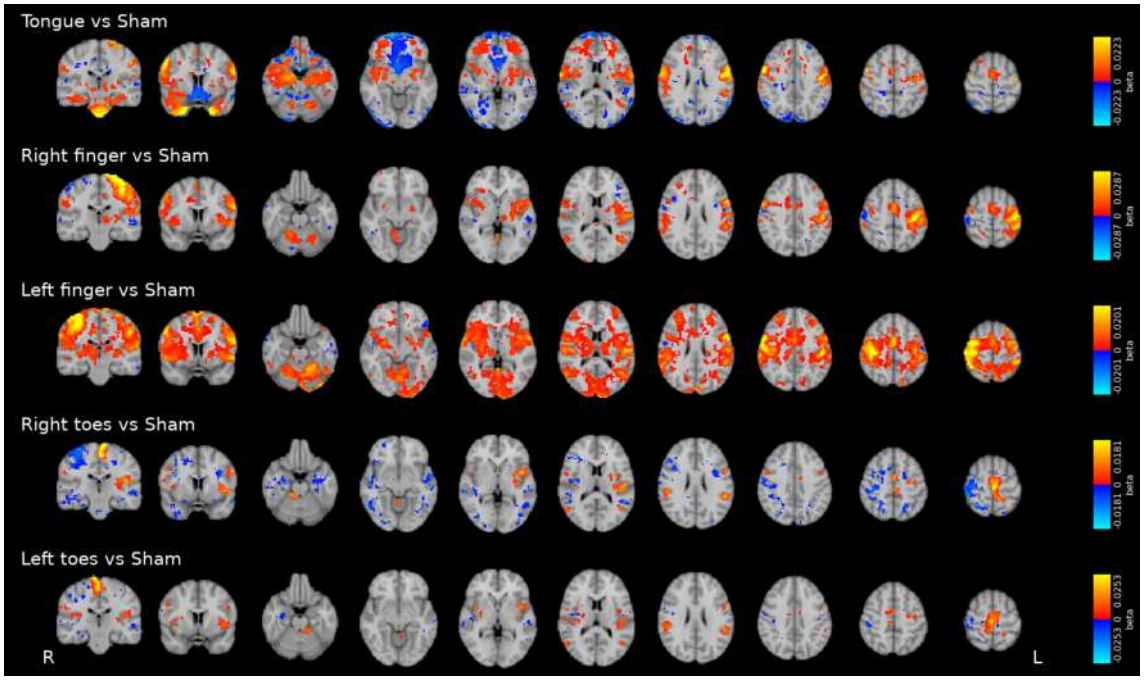

Figure B.2: Results of the one-sample MEMA test at the subject level, for subject 002, for all contrasts of the motor task (p <0.05, FDR corrected).

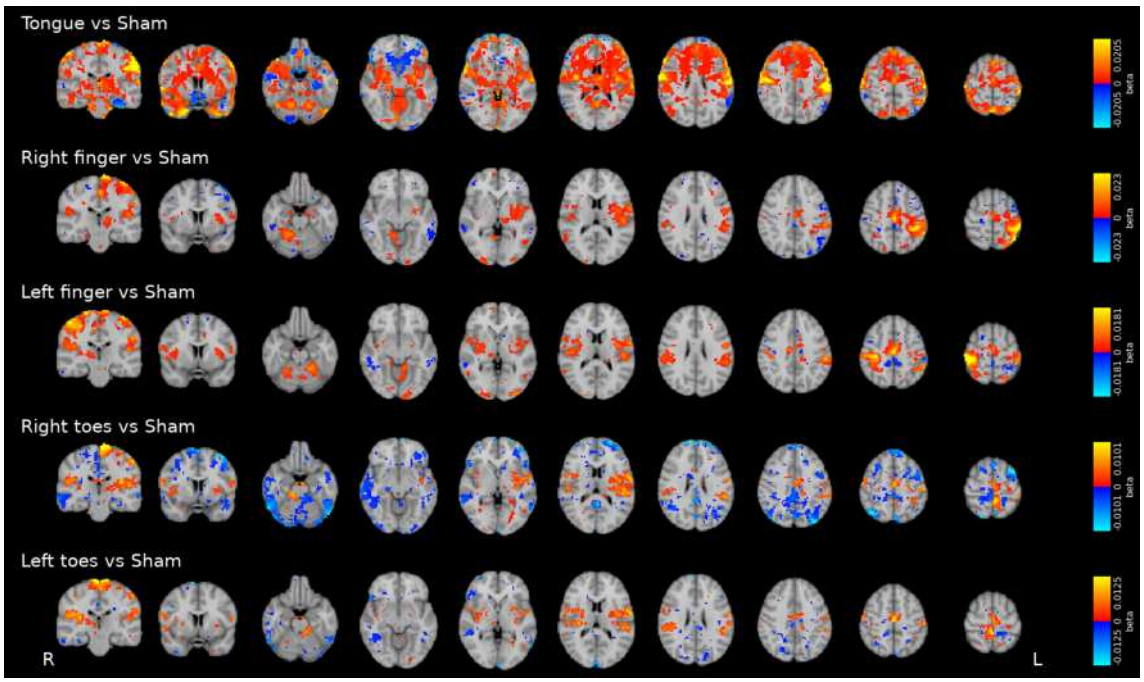

Figure B.3: Results of the one-sample MEMA test at the subject level, for subject 003, for all contrasts of the motor task (p <0.05, FDR corrected).

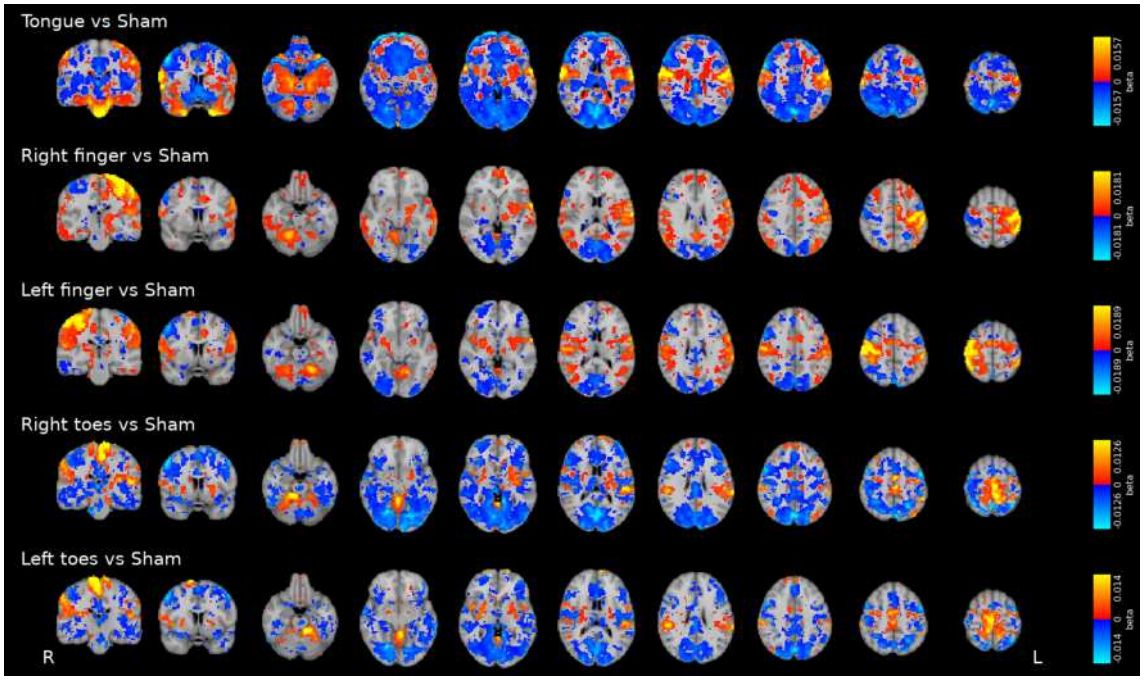

Figure B.4: Results of the one-sample MEMA test at the subject level, for subject 004, for all contrasts of the motor task ($p < 0.05$, FDR corrected).

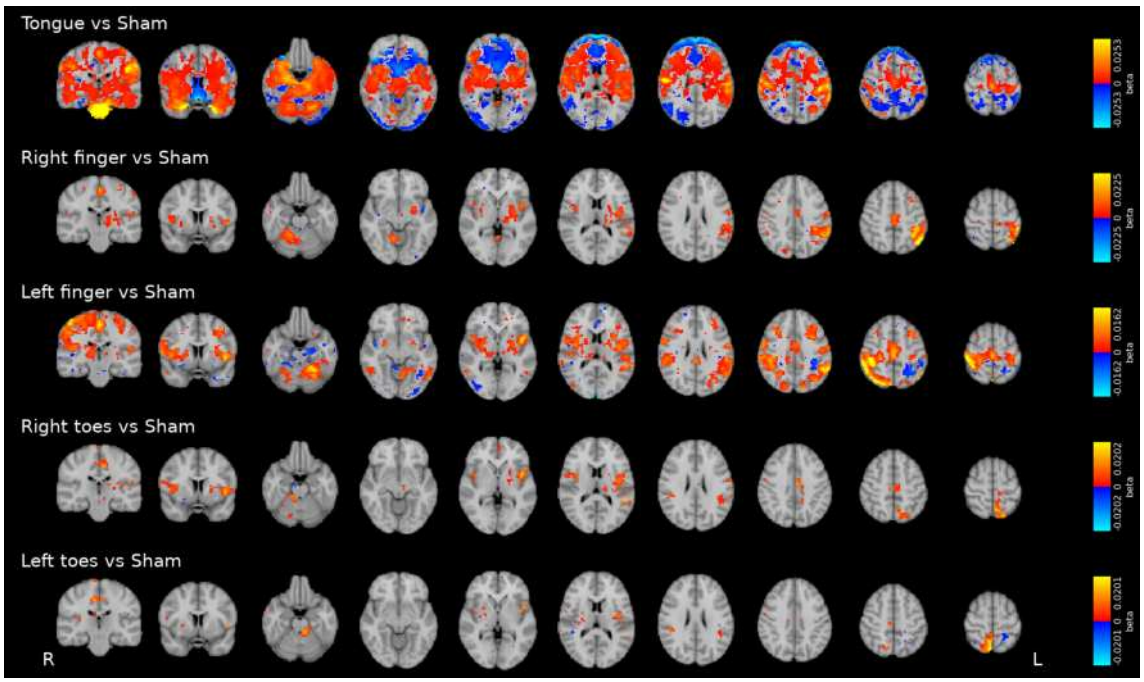

Figure B.5: Results of the one-sample MEMA test at the subject level, for subject 008, for all contrasts of the motor task ($p < 0.05$, FDR corrected).

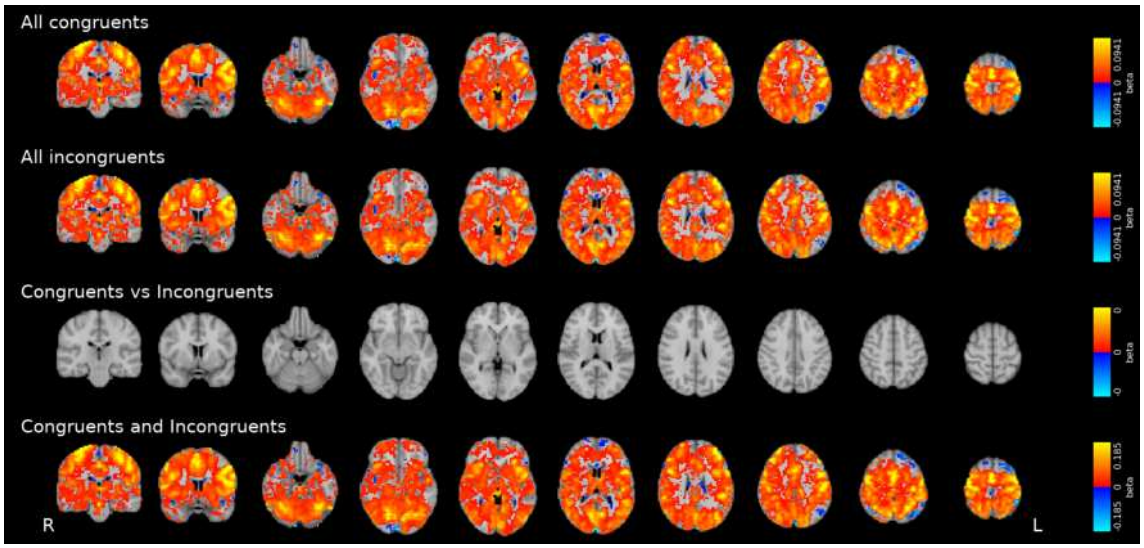

Figure B.6: Results of the one-sample MEMA test at the subject level, for subject 009, for all contrasts of the motor task ($p < 0.05$, FDR corrected).

B.1.2 Simon task

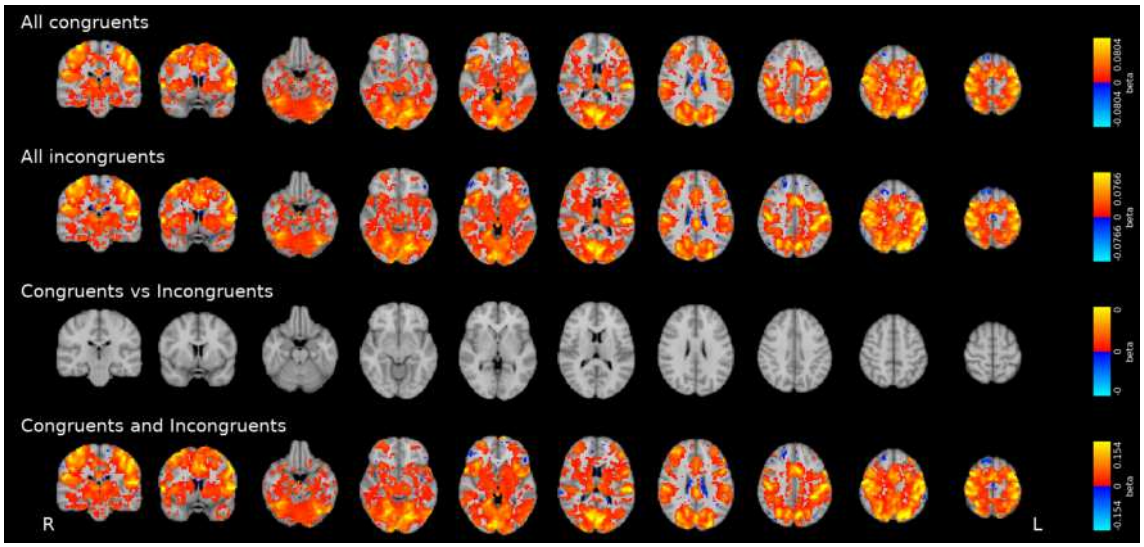

Figure B.7: Results of the one-sample MEMA test at the subject level, for subject 001, for all contrasts of the Simon task (p <0.05, FDR corrected).

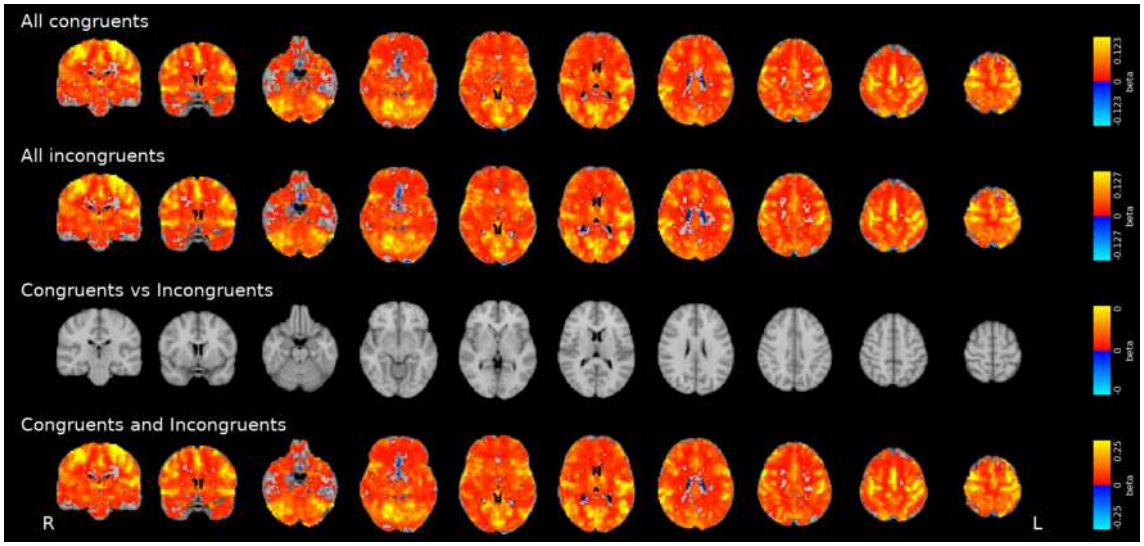

Figure B.8: Results of the one-sample MEMA test at the subject level, for subject 002, for all contrasts of the Simon task (p <0.05, FDR corrected).

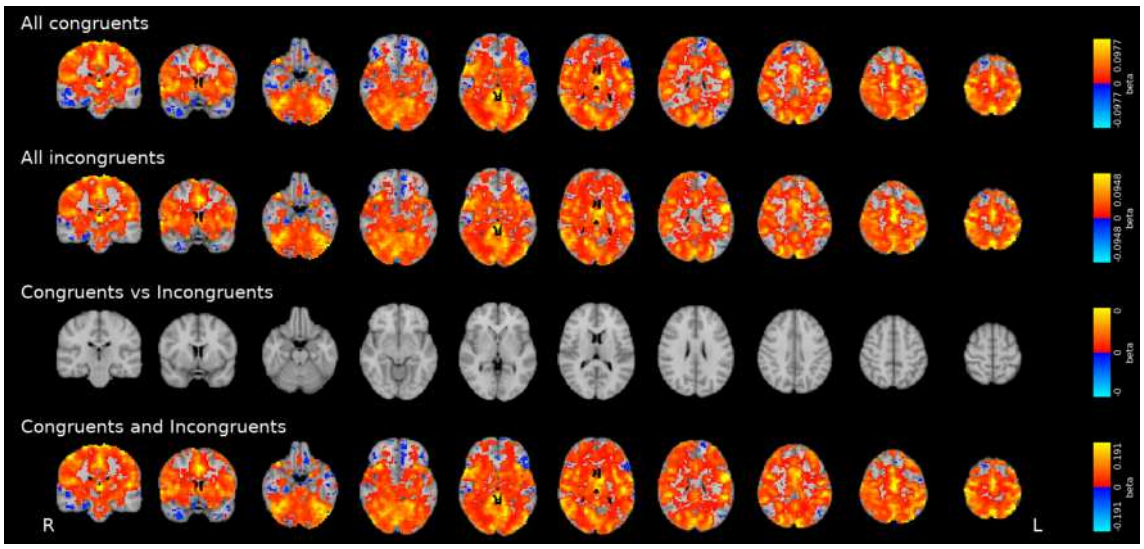

Figure B.9: Results of the one-sample MEMA test at the subject level, for subject 003, for all contrasts of the Simon task ($p < 0.05$, FDR corrected).

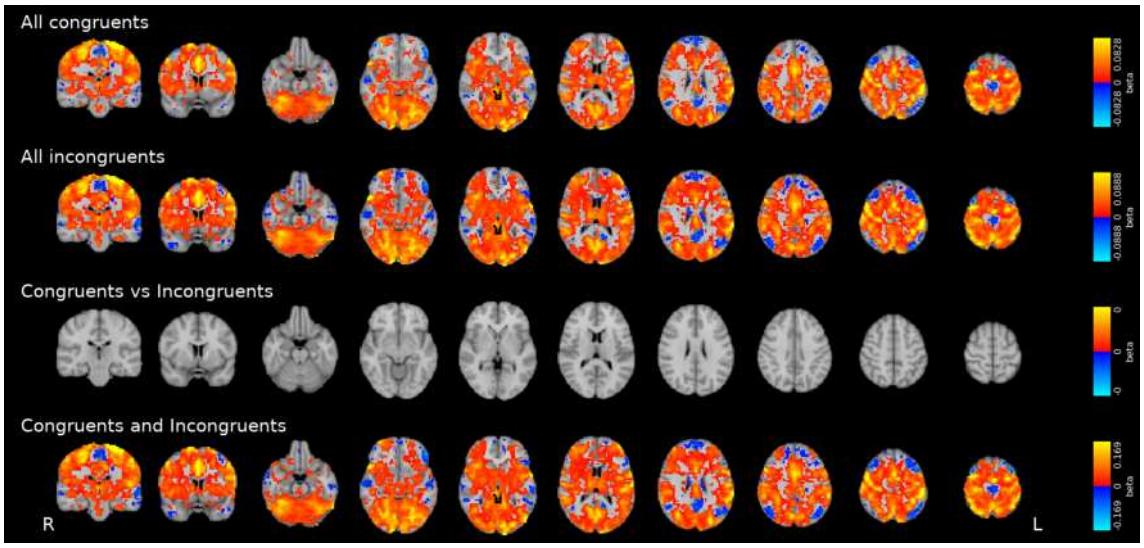

Figure B.10: Results of the one-sample MEMA test at the subject level, for subject 004, for all contrasts of the Simon task ($p < 0.05$, FDR corrected).

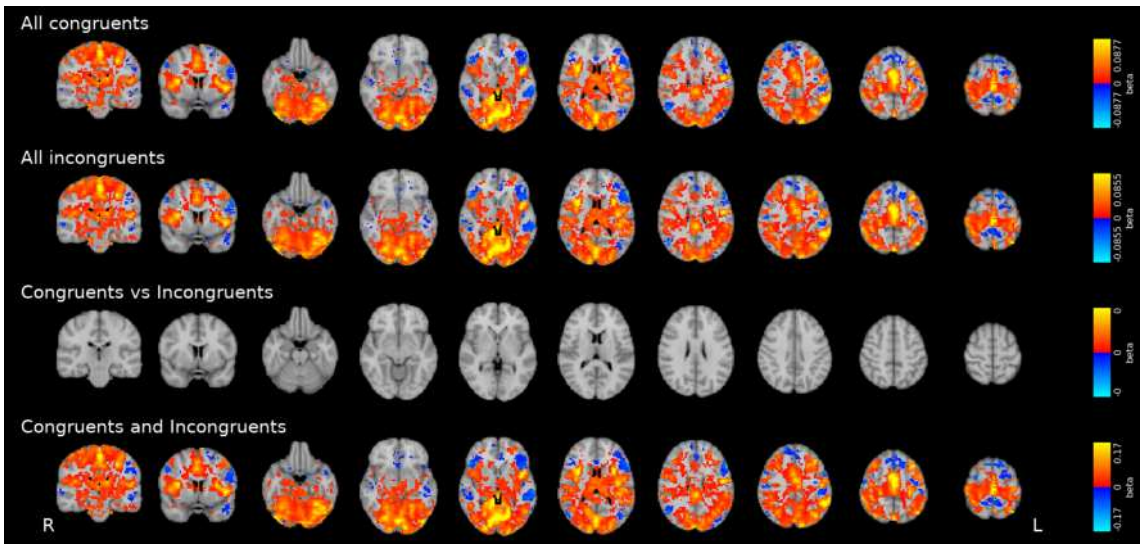

Figure B.11: Results of the one-sample MEMA test at the subject level, for subject 008, for all contrasts of the Simon task ($p < 0.05$, FDR corrected).

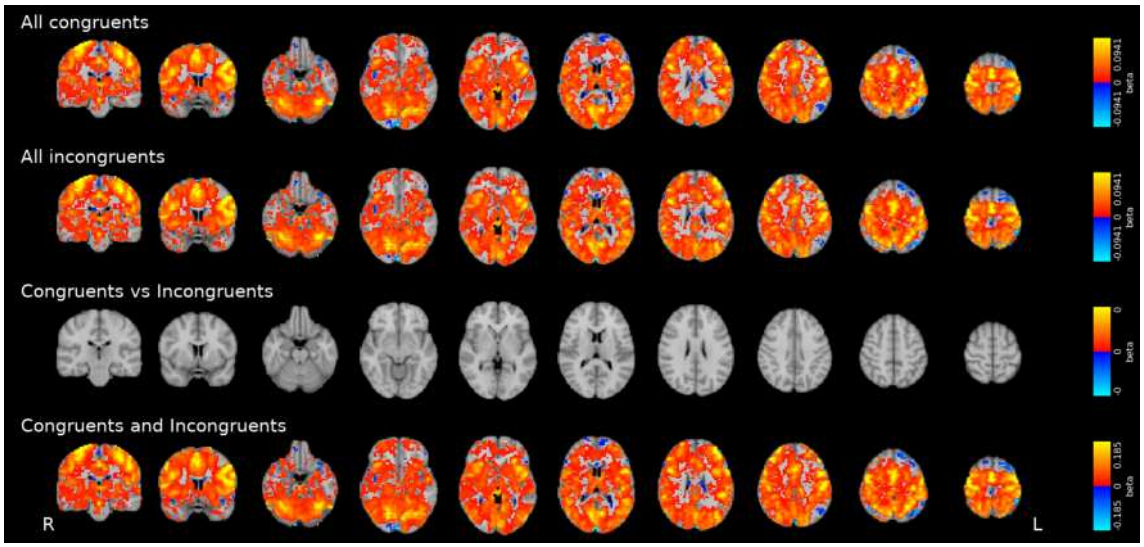

Figure B.12: Results of the one-sample MEMA test at the subject level, for subject 009, for all contrasts of the Simon task ($p < 0.05$, FDR corrected).

B.1.3 Pinel functional localiser task

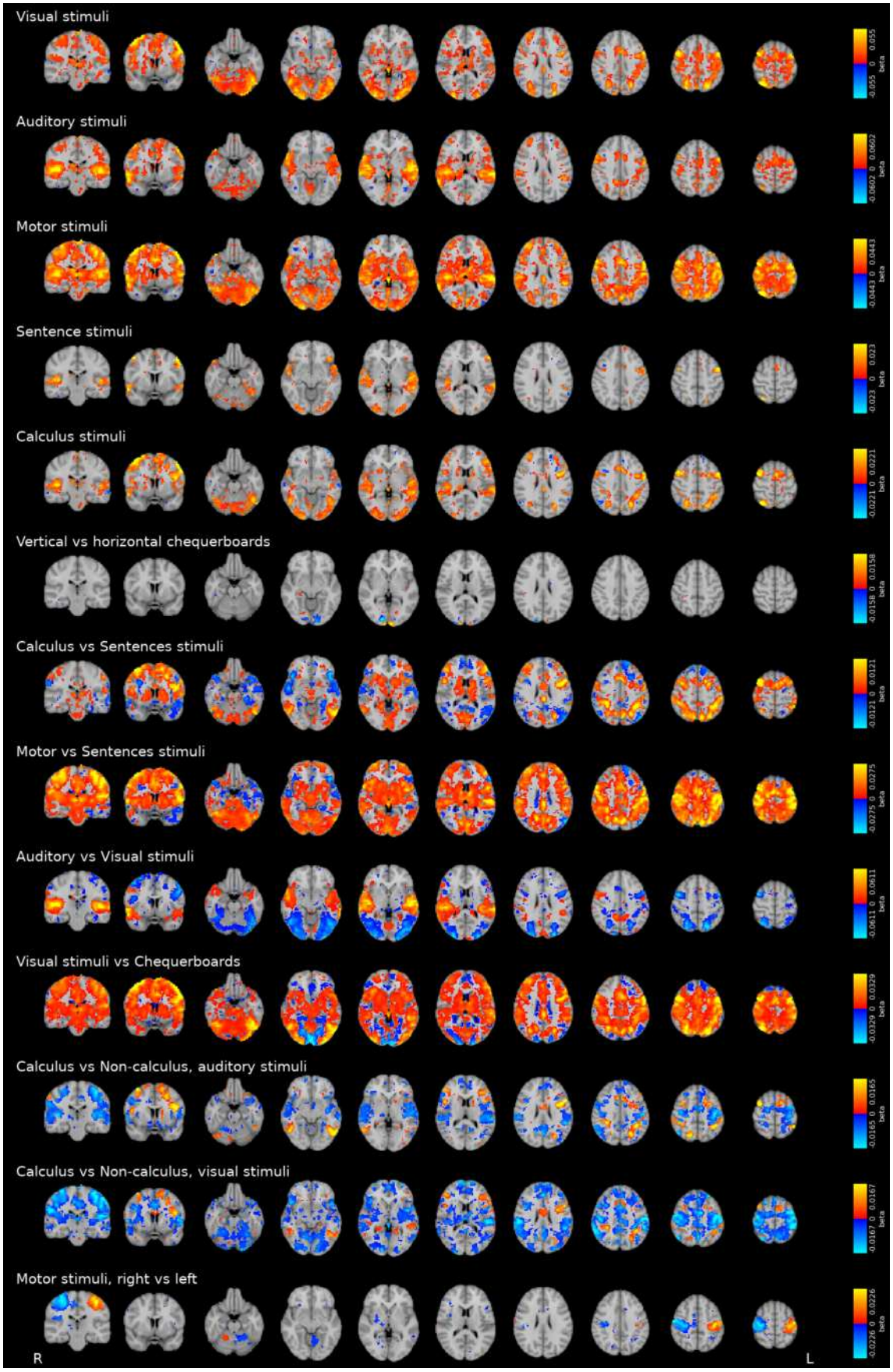

Figure B.13: Results of the one-sample MEMA test at the subject level, for subject 001, for all contrasts of the Pinel task ($p < 0.05$, FDR corrected).

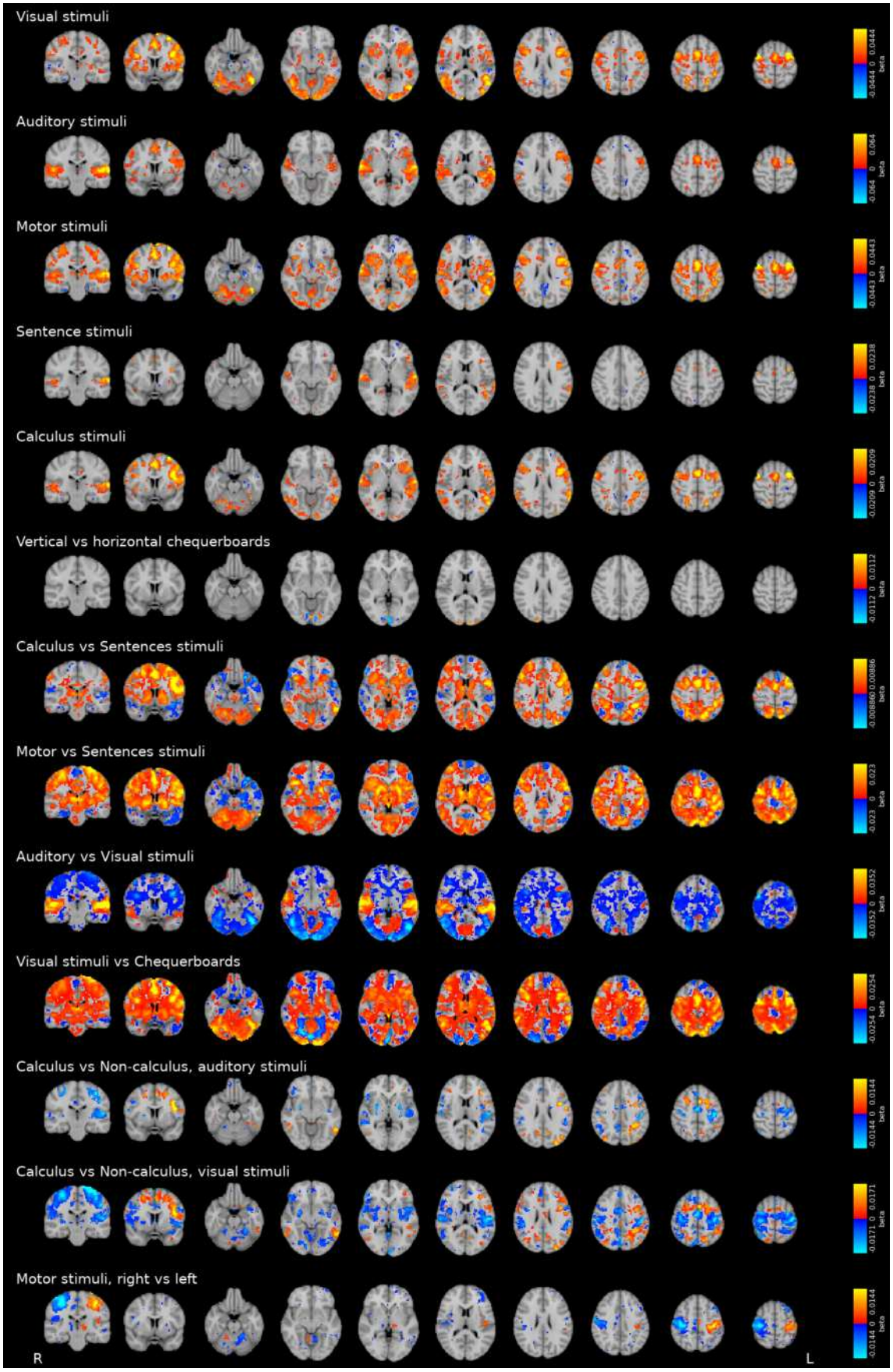

Figure B.14: Results of the one-sample MEMA test at the subject level, for subject 002, for all contrasts of the Pinel task ($p < 0.05$, FDR corrected).

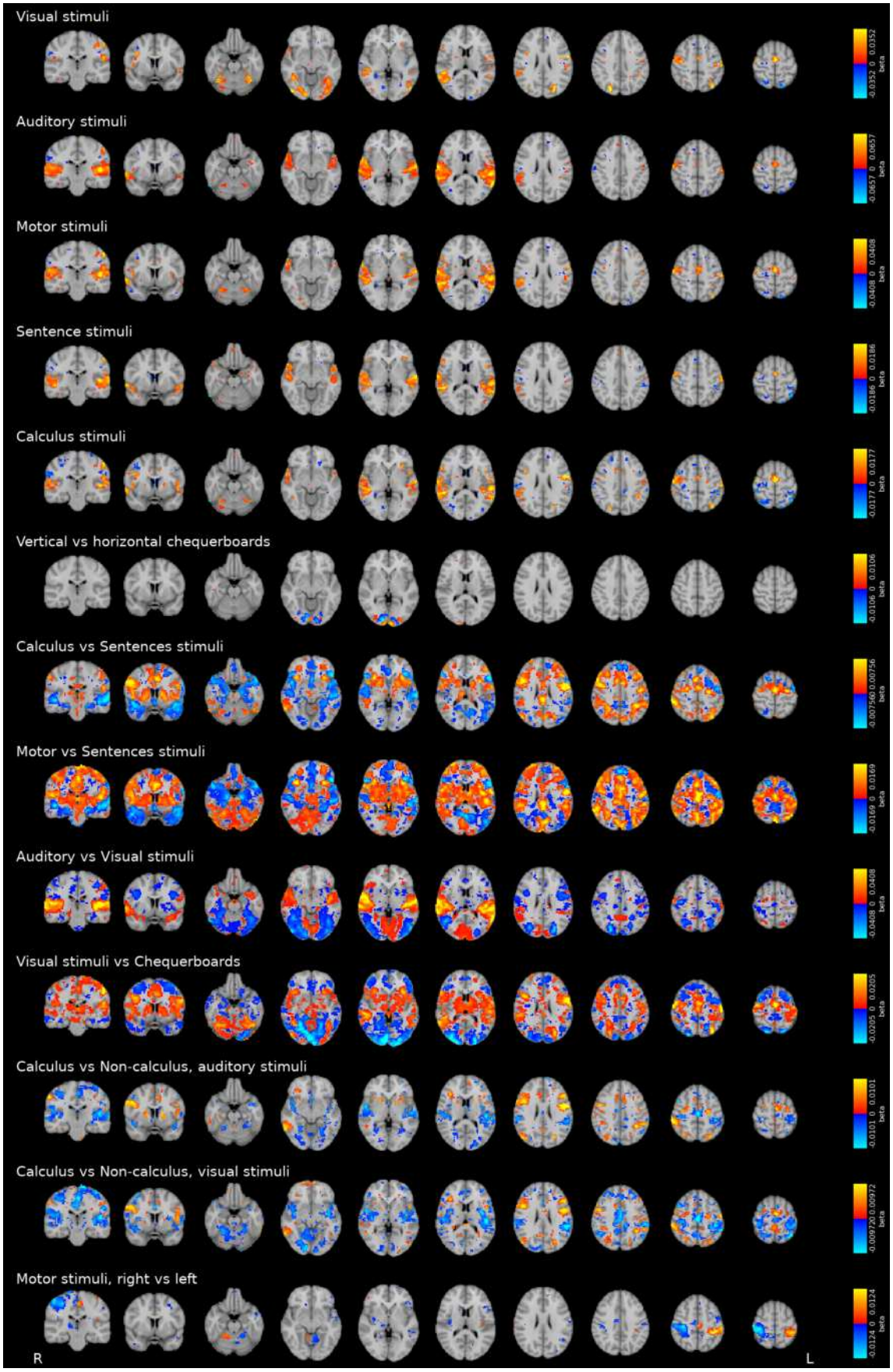

Figure B.15: Results of the one-sample MEMA test at the subject level, for subject 003, for all contrasts of the Pinel task ($p < 0.05$, FDR corrected).

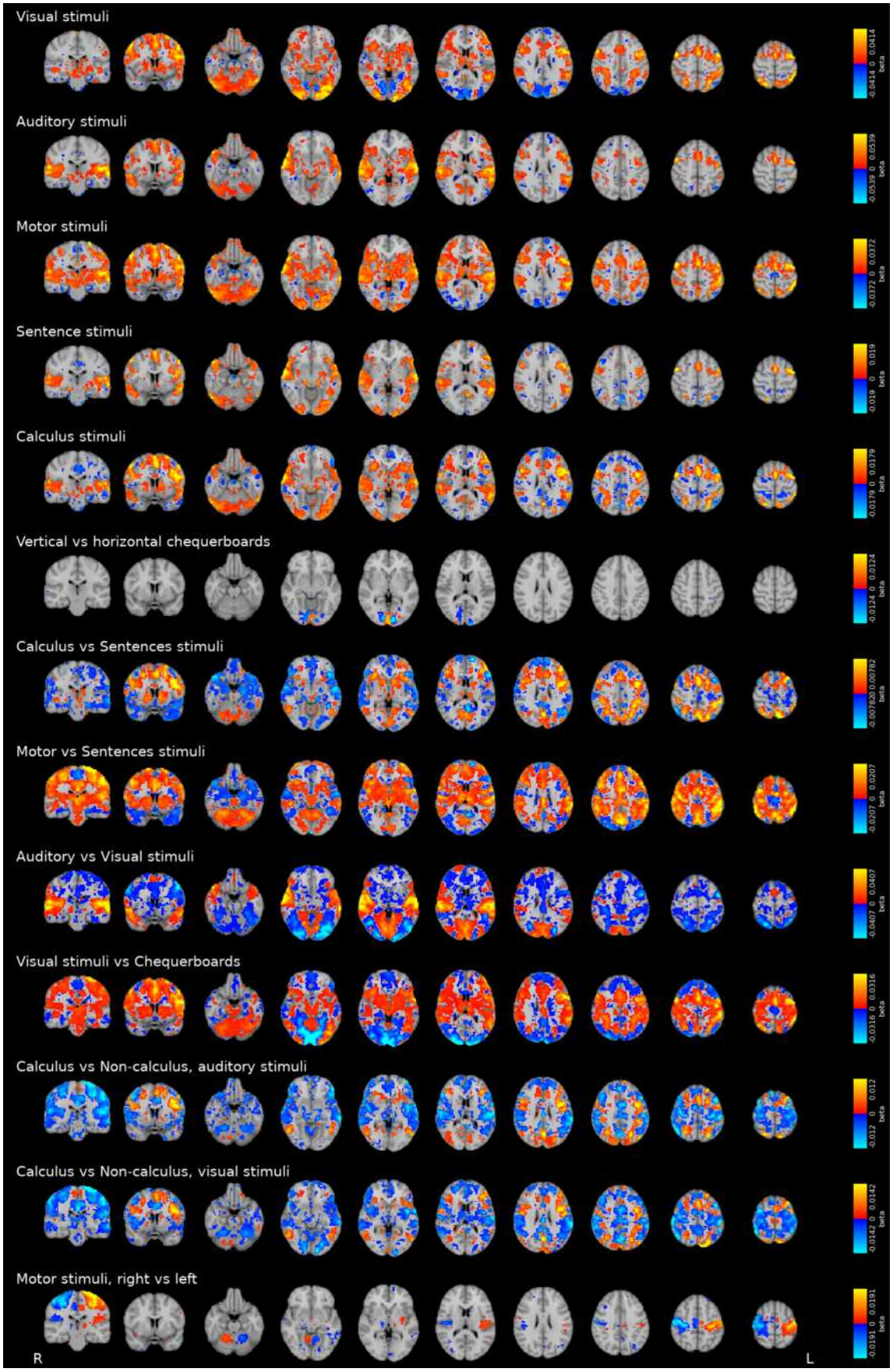

Figure B.16: Results of the one-sample MEMA test at the subject level, for subject 004, for all contrasts of the Pinel task ($p < 0.05$, FDR corrected).

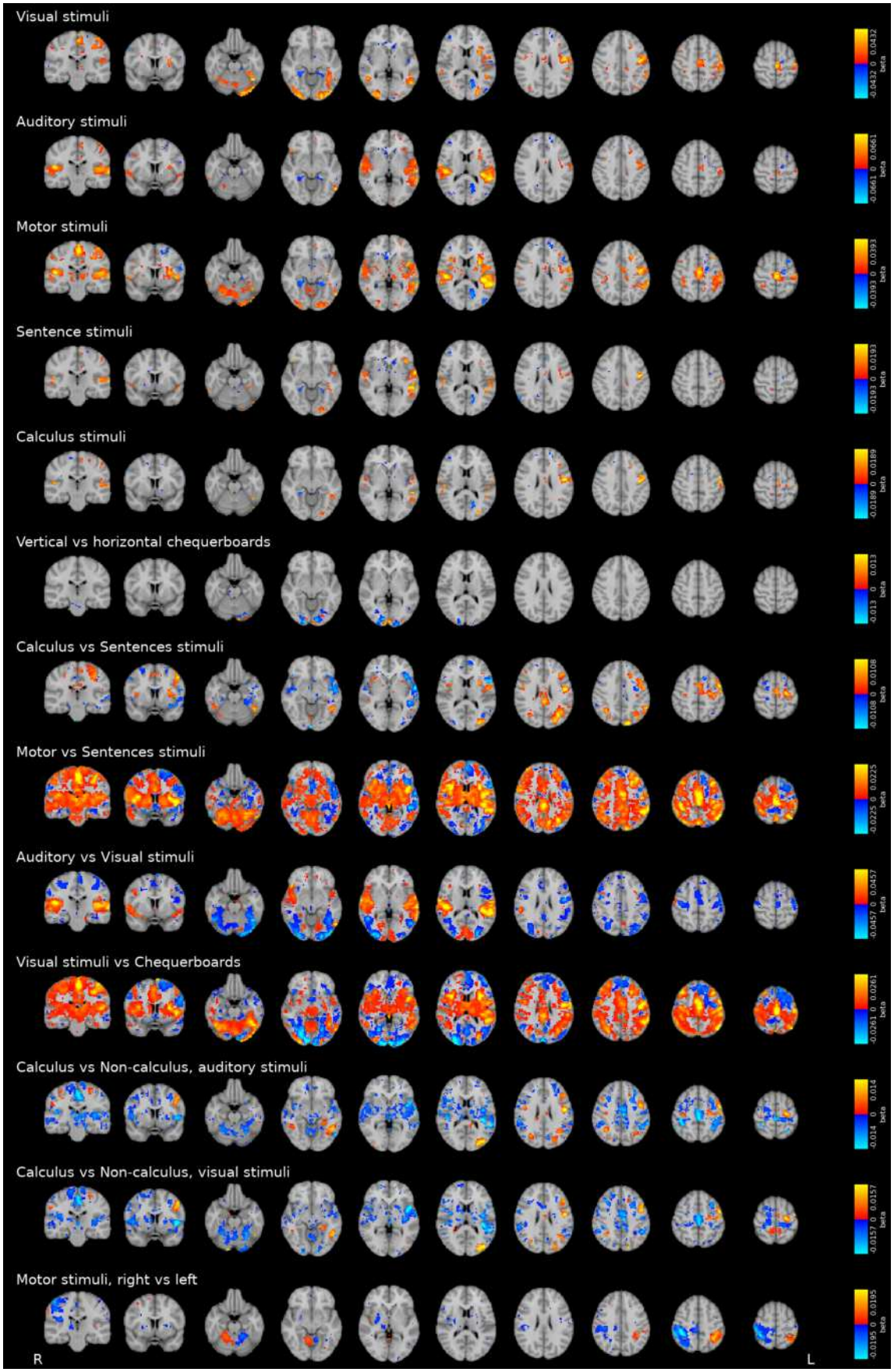

Figure B.17: Results of the one-sample MEMA test at the subject level, for subject 008, for all contrasts of the Pinel task ($p < 0.05$, FDR corrected).

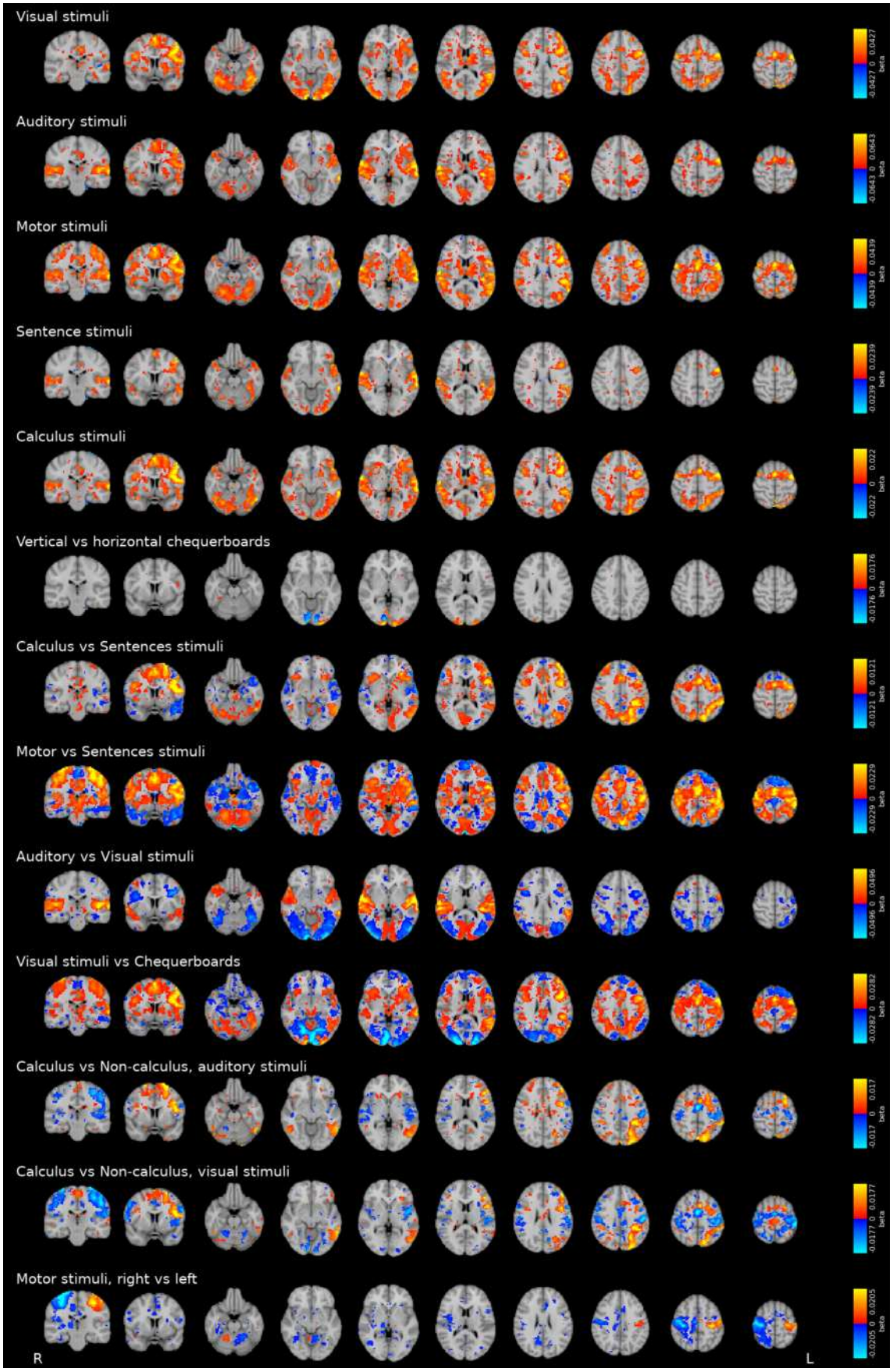

Figure B.18: Results of the one-sample MEMA test at the subject level, for subject 009, for all contrasts of the Pinel task ($p < 0.05$, FDR corrected).

B.2 Tables

B.2.1 Motor task

Size (voxels)	Maxima				Center of Gravity		
	Value (β)	X (mm)	Y (mm)	Z (mm)	X (mm)	Y (mm)	Z (mm)
969	0.00691	30	-6	-2	25.5	-8.62	3.29
909	0.0548	32.5	-18.5	73	40	-27	55.6
734	0.00836	-42.5	-1	3	-28	-5.05	2.7
570	0.0149	-20	-53.5	-19.5	-17.2	-54.2	-19.3
221	0.00916	-55	-28.5	18	-54.8	-30.7	22.7
205	0.00753	25	-58.5	-19.5	27.3	-55.6	-21.4
195	0.0105	5	-6	55.5	1.39	-3.73	48
111	0.0049	20	-66	-59.5	23.7	-58.7	-53
96	0.00889	-17.5	-58.5	-59.5	-18	-55.6	-51.7
48	0.000816	-25	24	28	-20.3	22.4	23.9
22	0.006	-40	-38.5	53	-38.4	-35	53.5
21	0.00763	2.5	-28.5	75.5	2.89	-27.6	73.7
21	0.0057	7.5	-18.5	45.5	8.78	-21	45.1
21	0.00437	60	9	20.5	58.4	6.81	16.9

Table B.1: Clusters of positive contrast between left fingertapping and sham trials of the motor task

Size (voxels)	Minima				Center of Gravity		
	Value (β)	X (mm)	Y (mm)	Z (mm)	X (mm)	Y (mm)	Z (mm)
50	-0.00318	32.5	-16	-37	24.4	-10.6	-38
23	-0.000974	37.5	-63.5	-42	35.6	-64.1	-39.4

Table B.2: Clusters of negative contrast between left fingertapping and sham trials of the motor task

Size (voxels)	Maxima				Center of Gravity		
	Value (β)	X (mm)	Y (mm)	Z (mm)	X (mm)	Y (mm)	Z (mm)
1203	0.00814	-42.5	-1	5.5	-25.4	-9.09	2.59
853	0.0138	17.5	-53.5	-17	17.6	-55.3	-24.9
568	0.0524	-37.5	-23.5	70.5	-36	-31.7	62.3
266	0.00317	27.5	-3.5	0.5	25.2	-2.94	1.78
183	0.00947	-55	-28.5	18	-50.9	-31.2	19.7
103	0.00404	45	1.5	5.5	44.8	2.94	6
80	0.00551	-27.5	-58.5	-19.5	-25.2	-56.4	-20.7
77	0.00475	55	-31	25.5	57.6	-32.6	26.9
55	0.00449	-7.5	-3.5	43	-1.27	1.76	39.1
37	0.00431	2.5	-76	-9.5	6.28	-80.8	-12.2
29	0.00855	35	-13.5	70.5	29.8	-11.1	68.1
20	0.00588	27.5	-53.5	-59.5	31	-57.3	-59.6

Table B.3: Clusters of positive contrast between right fingertapping and sham trials of the motor task

Size (voxels)	Minima				Center of Gravity		
	Value (β)	X (mm)	Y (mm)	Z (mm)	X (mm)	Y (mm)	Z (mm)
46	-0.00162	-5	-51	-47	-5.96	-50	-44.6
44	-0.00136	37.5	-66	-44.5	31.5	-65.9	-43.6
36	-0.00098	22.5	-73.5	-27	20.6	-73.7	-31.4
31	-0.00379	-10	-1	-32	-11.3	-2.29	-33.5
24	-0.00311	-37.5	-26	-29.5	-44.9	-19.8	-32.6

Table B.4: Clusters of negative contrast between right fingertapping and sham trials of the motor task

Size (voxels)	Maxima				Center of Gravity		
	Value (β)	X (mm)	Y (mm)	Z (mm)	X (mm)	Y (mm)	Z (mm)
185	0.00798	32.5	-21	15.5	26	-12.6	7.29
119	0.0217	5	-33.5	78	5.27	-35.5	71.5
83	0.0109	-12.5	-36	-24.5	-14.5	-36.5	-25.5
81	0.00333	-25	1.5	3	-25.4	-8.05	3.54
79	0.00913	55	-31	25.5	50.6	-29.2	23.2
58	0.00832	7.5	-8.5	43	1.61	-6.59	47.2
47	0.00637	45	1.5	5.5	44.4	2.07	5.95
35	0.00923	-42.5	-1	3	-43.8	0.00924	4.32

Table B.5: Clusters of positive contrast between left toe movement and sham trials of the motor task

Size (voxels)	Minima				Center of Gravity		
	Value (β)	X (mm)	Y (mm)	Z (mm)	X (mm)	Y (mm)	Z (mm)
20	-0.00326	30	-63.5	45.5	25.7	-64.9	44.7

Table B.6: Clusters of negative contrast between left toe movement and sham trials of the motor task

Size (voxels)	Maxima				Center of Gravity		
	Value (β)	X (mm)	Y (mm)	Z (mm)	X (mm)	Y (mm)	Z (mm)
141	0.0227	-12.5	-38.5	80.5	-8.58	-36.5	72.3
80	0.00715	-32.5	-23.5	15.5	-29.2	-20.5	8.93
47	0.0106	-55	-28.5	18	-51.3	-32.1	19.5
43	0.0102	12.5	-36	-22	14.6	-35	-23.7
41	0.01	-42.5	-1	3	-42.4	-0.62	5.11
40	0.00558	45	1.5	5.5	43.9	2.8	4.25
35	0.00735	55	-31	25.5	53.7	-29.9	25.1
27	0.0084	-2.5	-8.5	53	-4.41	-6.24	46.1
27	0.00294	-20	-8.5	-4.5	-21.4	-8.38	-2.68

Table B.7: Clusters of positive contrast between right toe movement and sham trials of the motor task

Size (voxels)	Minima				Center of Gravity		
	Value (β)	X (mm)	Y (mm)	Z (mm)	X (mm)	Y (mm)	Z (mm)
35	-0.00216	40	4	28	36.1	4.09	35

Table B.8: Clusters of negative contrast between right toe movement and sham trials of the motor task

Size (voxels)	Maxima				Center of Gravity		
	Value (β)	X (mm)	Y (mm)	Z (mm)	X (mm)	Y (mm)	Z (mm)
13673	0.061	-60	9	33	-2.27	-7.82	-1.51
51	0.00828	0	-33.5	73	-5.66	-34.3	74.7
46	0.012	0	31.5	-29.5	-0.96	29.7	-26.5
31	0.0121	22.5	-28.5	-34.5	21.7	-30.3	-34.2
26	0.00261	-5	-33.5	10.5	-1.69	-35.4	13.3

Table B.9: Clusters of positive contrast between tongue movement and sham trials of the motor task

Size (voxels)	Minima				Center of Gravity		
	Value (β)	X (mm)	Y (mm)	Z (mm)	X (mm)	Y (mm)	Z (mm)
1611	-0.0212	7.5	-56	-64.5	1.39	-72.6	-42.6
1437	-0.0183	-2.5	4	-22	0.0833	15.3	-9.77
655	-0.0219	12.5	69	18	6.32	66.7	4.78
323	-0.0113	15	-104	10.5	32.7	-90.8	0.0305
291	-0.0116	-25	-96	23	-35.3	-90.3	-1.11
76	-0.00317	25	-61	50.5	25.7	-61.7	44.1
72	-0.0136	22.5	-96	23	21	-92.9	25.6
37	-0.0123	-12.5	46.5	-24.5	-17.3	39.9	-21.7
37	-0.0066	65	-41	-19.5	64.2	-44.7	-14.8
35	-0.0156	42.5	59	-4.5	43.2	52.6	-10.7
34	-0.00723	70	-38.5	5.5	66.7	-36.2	0.474
30	-0.0124	-37.5	59	-7	-38.2	52.2	-13.1
20	-0.0086	-7.5	-104	13	-10.3	-103	9.15

Table B.10: Clusters of negative contrast between tongue movement and sham trials of the motor task

B.2.2 Simon task

Size (voxels)	Maxima				Center of Gravity		
	Value (β)	X (mm)	Y (mm)	Z (mm)	X (mm)	Y (mm)	Z (mm)
82128	0.224	-47.5	-81	-17	0.543	-36.3	16.9
29	0.137	-15	41.5	53	-12.1	44.7	50.4

Table B.11: Clusters of positive correlates of all congruent trials of the Simon task

Size (voxels)	Minima				Center of Gravity		
	Value (β)	X (mm)	Y (mm)	Z (mm)	X (mm)	Y (mm)	Z (mm)
67	-0.0123	7.5	-8.5	23	-0.297	-6.64	22.5
61	-0.0484	-42.5	-73.5	48	-47.9	-70.4	41.3
57	-0.0103	0	26.5	-2	-0.859	26.9	-3.1
48	-0.0308	-52.5	39	-9.5	-52.5	30.9	-2.14
29	-0.351	12.5	1.5	-34.5	12.4	1.34	-33.3
23	-0.0907	-52.5	-46	-42	-52.7	-49.6	-39.2
21	-0.00632	-25	-51	10.5	-26.7	-52.1	7.24
21	-0.175	50	-43.5	-44.5	48.9	-44.5	-45.8
20	-0.011	65	-6	-27	65.3	-6.84	-23.8
20	-0.0189	-62.5	-18.5	-32	-59.1	-8.78	-34.4

Table B.12: Clusters of negative correlates of all congruent trials of the Simon task

Size (voxels)	Maxima				Center of Gravity		
	Value (β)	X (mm)	Y (mm)	Z (mm)	X (mm)	Y (mm)	Z (mm)
87430	0.229	-47.5	-81	-17	0.695	-34.7	16

Table B.13: Clusters of positive correlates of all incongruent trials of the Simon task

Size (voxels)	Minima				Center of Gravity		
	Value (β)	X (mm)	Y (mm)	Z (mm)	X (mm)	Y (mm)	Z (mm)
108	-0.0141	0	31.5	-2	-0.761	30.4	-4.17
74	-0.0124	-2.5	-1	20.5	-0.947	-6.01	22.2
60	-0.0564	-42.5	-73.5	48	-47.2	-71.4	41
43	-0.0108	55	4	-37	61.9	-0.441	-26.2
28	-0.0225	-52.5	39	-9.5	-51.5	35.1	-6.24
23	-0.0985	-5	-96	30.5	-0.251	-88.4	37.1
21	-0.173	50	-43.5	-44.5	49.3	-44.6	-45.4
20	-0.0284	0	61.5	35.5	3.28	64	30.3

Table B.14: Clusters of negative correlates of all incongruent trials of the Simon task

Size (voxels)	Maxima				Center of Gravity		
	Value (β)	X (mm)	Y (mm)	Z (mm)	X (mm)	Y (mm)	Z (mm)
86543	0.453	-47.5	-81	-17	0.611	-35.3	16.4

Table B.15: Clusters of positive correlates of all (correct) trials of the Simon task

Size (voxels)	Minima				Center of Gravity		
	Value (β)	X (mm)	Y (mm)	Z (mm)	X (mm)	Y (mm)	Z (mm)
72	-0.0239	0	29	-4.5	-0.738	28.3	-3.49
69	-0.0242	-2.5	-1	20.5	-0.713	-6.24	22.3
65	-0.105	-42.5	-73.5	48	-48.6	-69.6	41.4
50	-0.0242	55	4	-37	61.9	-2.05	-27.4
44	-0.0636	-57.5	26.5	0.5	-54.2	23.8	19
33	-0.0547	-52.5	39	-9.5	-51.4	35.1	-7.66
27	-0.0389	52.5	-61	48	50.2	-59.1	49.5
26	-0.044	-32.5	36.5	48	-23.5	34.2	53.9
26	-0.566	12.5	1.5	-34.5	12.4	1.46	-33.4
24	-0.034	-57.5	-8.5	-39.5	-58.6	-9.09	-35.4
23	-0.203	-52.5	-46	-42	-53	-49.3	-38.6
21	-0.35	50	-43.5	-44.5	49.1	-44.5	-45.6
20	-0.0429	-2.5	69	20.5	2.11	65.9	26
20	-0.0211	5	14	-24.5	2.11	13.3	-20.6

Table B.16: Clusters of negative correlates of all (correct) trials of the Simon task

Size (voxels)	Minima				Center of Gravity		
	Value (β)	X (mm)	Y (mm)	Z (mm)	X (mm)	Y (mm)	Z (mm)
51	-0.0301	-22.5	-8.5	-47	-18.7	-6.25	-42.4
47	-0.0348	22.5	66.5	-12	27.8	62.6	-13
31	-0.0279	22.5	-11	-44.5	29.8	-6.11	-45.1
25	-0.0325	-42.5	54	10.5	-40	58.1	3.78
21	-0.0276	-32.5	64	-9.5	-30	61.7	-12

Table B.17: Clusters of negative contrast between congruent and incongruent trials of the Simon task

B.2.3 Pinel functional localiser task

Size (voxels)	Maxima				Center of Gravity		
	Value (β)	X (mm)	Y (mm)	Z (mm)	X (mm)	Y (mm)	Z (mm)
11446	0.115	-67.5	-16	0.5	-3.24	-21.9	4.02
550	0.0297	0	-1	63	3.45	-0.0249	54.1
379	0.0203	2.5	39	-32	0.451	48.7	-21.5
75	0.0089	-30	41.5	33	-31.1	37	29.9
68	0.0149	32.5	-6	-49.5	35.7	-2.81	-46
48	0.00768	32.5	-46	43	37.5	-44.2	39.8
37	0.0334	40	-28.5	70.5	40.1	-28.6	68.2
32	0.0147	0	-58.5	60.5	-0.383	-61.6	60.4
30	0.00406	5	-36	-24.5	3.36	-35	-26.6
28	0.0116	-40	-11	-44.5	-40.7	-9.57	-42
26	0.0428	-15	61.5	30.5	-7.76	61.1	34.7
26	0.0345	-60	-58.5	-22	-57.7	-57.7	-20.8
24	0.0069	-40	-28.5	-29.5	-44.5	-25.7	-29.6
23	0.0527	52.5	-1	53	49.9	-3.36	56.3
23	0.00641	37.5	36.5	30.5	33.8	37.3	33

Table B.18: Clusters of positive correlates of all auditory trials of the Pinel task

Size (voxels)	Minima				Center of Gravity		
	Value (β)	X (mm)	Y (mm)	Z (mm)	X (mm)	Y (mm)	Z (mm)
572	-0.0161	27.5	-93.5	23	40.1	-69.8	0.644
356	-0.0174	-42.5	-88.5	-9.5	-42.6	-78	-1.6
329	-0.00581	5	46.5	8	2.41	38.7	6.72
65	-0.0145	47.5	-66	50.5	48.2	-64.1	42.7
53	-0.0215	30	66.5	-9.5	19.1	67.3	-8.64
44	-0.0072	-7.5	-51	25.5	-7.27	-54.2	24
41	-0.00603	22.5	34	45.5	21.1	30.2	41.1
41	-0.0288	-35	-88.5	-27	-37.7	-80.8	-34.4
35	-0.0164	-52.5	-63.5	45.5	-42.8	-69.4	40.7
33	-0.0194	-22.5	-76	58	-23.4	-80.2	50.4
32	-0.00931	-15	29	58	-12.5	32.5	54.6
31	-0.0077	47.5	-66	-49.5	49.1	-67.7	-41.3
30	-0.00732	-22.5	29	43	-20.7	26.6	44.3
28	-0.0165	-52.5	-56	-44.5	-48.8	-62.2	-41.9
25	-0.004	-30	-41	-4.5	-29.6	-43.5	-3.57
22	-0.00994	27.5	-81	48	29	-79.7	46.1
21	-0.00312	27.5	-36	-2	25.5	-38.2	0.483

Table B.19: Clusters of negative correlates of all auditory trials of the Pinel task

Size (voxels)	Maxima				Center of Gravity		
	Value (β)	X (mm)	Y (mm)	Z (mm)	X (mm)	Y (mm)	Z (mm)
2596	0.0281	-67.5	-16	0.5	-43.1	-27.3	2.82
1408	0.0138	55	-16	8	49.8	-9.38	5.08
1061	0.011	60	-51	-24.5	27.7	-67.3	-23.9
222	0.00921	-20	34	-24.5	-0.558	49.1	-21.5
103	0.00774	30	-63.5	45.5	30.1	-61.2	39.4
72	0.00988	50	-1	45.5	45.6	1.36	35.1
58	0.0105	-25	-63.5	35.5	-29	-52.6	38.6
36	0.01	2.5	9	48	5.41	9.34	44.5
29	0.00552	32.5	-6	-49.5	31.1	0.15	-46.8
26	0.0298	42.5	6.5	60.5	50.1	1.45	53.5
26	0.00384	0	6.5	25.5	2.98	0.852	25.8
25	0.012	-15	11.5	70.5	-21.7	8.18	69.6
24	0.0017	-15	19	28	-16.1	20.4	27
22	0.00689	-27.5	-76	28	-24.7	-80.1	28.9
20	0.0119	0	-6	63	-3.1	-5.57	61.5

Table B.20: Clusters of positive correlates of all calculus trials of the Pinel task

Size (voxels)	Minima				Center of Gravity		
	Value (β)	X (mm)	Y (mm)	Z (mm)	X (mm)	Y (mm)	Z (mm)
297	-0.00345	0	44	20.5	2.84	41.4	6.81
61	-0.0138	50	-63.5	48	47	-63.4	45.4
55	-0.00455	-7.5	-43.5	33	-0.822	-44.3	31.1
34	-0.00583	12.5	31.5	60.5	11.3	26.3	57.1
27	-0.00503	-37.5	-83.5	-32	-31.8	-83.6	-38
22	-0.00854	10	69	-9.5	8.42	69.4	-7.66
21	-0.00339	20	34	45.5	19.7	32.1	42.3
20	-0.00888	-17.5	-8.5	-42	-13.4	-5.29	-38.5

Table B.21: Clusters of negative correlates of all calculus trials of the Pinel task

Size (voxels)	Maxima				Center of Gravity		
	Value (β)	X (mm)	Y (mm)	Z (mm)	X (mm)	Y (mm)	Z (mm)
18874	0.0128	-42.5	4	23	-5.18	-26.9	17.4
132	0.00388	35	64	-9.5	26.4	52.9	-11.9
67	0.00364	47.5	49	15.5	38.3	56.2	13.4
55	0.00426	25	4	53	25.4	0.415	49
28	0.00284	7.5	-96	25.5	11.8	-91.7	27.5

Table B.22: Clusters of positive contrast between calculus and sentences trials of the Pinel task

Size (voxels)	Minima				Center of Gravity		
	Value (β)	X (mm)	Y (mm)	Z (mm)	X (mm)	Y (mm)	Z (mm)
2611	-0.0098	-55	31.5	10.5	-42.4	0.659	-14.7
2204	-0.00595	-12.5	36.5	58	0.285	38	13.6
1227	-0.00572	57.5	31.5	5.5	50.6	10.2	-7.5
136	-0.00267	25	-33.5	-19.5	26.5	-35.1	-16
54	-0.00327	20	-11	-37	28.9	-10.6	-39.7
53	-0.00359	-7.5	-48.5	30.5	-7	-51.6	26.2
49	-0.00245	-10	-53.5	5.5	-13.3	-52.1	8.16
44	-0.00309	-67.5	-46	3	-64.3	-41.8	3.2
43	-0.00533	45	-61	55.5	47.5	-63.8	44.1
30	-0.00344	67.5	-31	38	64	-32.7	33.6
26	-0.0016	47.5	-78.5	-29.5	40.9	-79.2	-33.8
23	-0.00169	15	-48.5	8	15.8	-47	8.11
22	-0.00435	-47.5	-73.5	40.5	-46.4	-68.6	43.1
21	-0.00124	57.5	-26	25.5	57.3	-25.6	23.5
21	-0.0032	17.5	69	8	12	69.6	15
20	-0.00199	27.5	6.5	-22	25.2	9.36	-20.4

Table B.23: Clusters of negative contrast between calculus and sentences trials of the Pinel task

Size (voxels)	Maxima				Center of Gravity		
	Value (β)	X (mm)	Y (mm)	Z (mm)	X (mm)	Y (mm)	Z (mm)
32329	0.0908	-32.5	1.5	68	-3.67	-27.5	13.3
776	0.0208	2.5	39	-32	2.91	48.8	-18.5
99	0.019	5	1.5	-29.5	31.4	-3	-43
28	0.00964	-40	-11	-44.5	-41.9	-9.31	-42.1
25	0.0515	-15	61.5	30.5	-8.17	61.6	33.8
23	0.0263	-2.5	-33.5	75.5	-1.49	-33.4	74.7

Table B.24: Clusters of positive correlates of all motor trials of the Pinel task

Size (voxels)	Minima				Center of Gravity		
	Value (β)	X (mm)	Y (mm)	Z (mm)	X (mm)	Y (mm)	Z (mm)
230	-0.0146	-50	16.5	-32	-41.7	7.2	-33.2
220	-0.00654	0	34	-2	-0.174	30	0.646
112	-0.00483	-12.5	-13.5	25.5	-5.82	-17.6	22.8
111	-0.00507	-27.5	-41	-7	-27.2	-46	2
94	-0.0122	20	14	-29.5	27.9	13.4	-36
90	-0.00797	-5	-58.5	23	-5.73	-55.8	21.4
83	-0.00952	-15	34	55.5	-13.1	32.9	49.8
81	-0.0069	-20	-16	-19.5	-21.6	-16.3	-19
73	-0.00352	30	-41	-4.5	26.2	-41.9	6.95
67	-0.0457	-15	-106	-4.5	-9.31	-101	14.7
65	-0.00594	20	29	45.5	20.2	28.8	43.2
63	-0.0221	-5	69	-14.5	-6.63	64.9	-5.02
58	-0.0262	-52.5	-73.5	33	-51	-71.8	31.3
49	-0.0191	57.5	-63.5	33	50.6	-68.6	35.5
46	-0.00485	17.5	-11	-22	23.1	-14.6	-18.6
41	-0.00791	50	-71	-37	48.7	-68.8	-40.1
40	-0.00769	-47.5	-71	-37	-40.2	-77.2	-37.2
37	-0.0159	2.5	69	-9.5	8.98	69.3	-5.56
28	-0.0154	-10	-3.5	-39.5	-13	-4.5	-37
27	-0.00983	67.5	-3.5	18	62.8	-5.96	22.4
26	-0.0305	-37.5	-88.5	30.5	-33.9	-83	38.6
25	-0.0272	-52.5	-56	-44.5	-49.4	-63.1	-42.5
24	-0.00749	-2.5	56.5	23	-3.11	55.3	24.7
22	-0.0239	-42.5	54	-12	-43.3	53.3	-6.48
20	-0.0258	0	4	-29.5	-0.309	3.53	-26.7

Table B.25: Clusters of negative correlates of all motor trials of the Pinel task

Size (voxels)	Maxima				Center of Gravity		
	Value (β)	X (mm)	Y (mm)	Z (mm)	X (mm)	Y (mm)	Z (mm)
50139	0.0457	32.5	9	65.5	-0.254	-24.6	21.8
37	0.00554	52.5	-6	-42	50.8	-6.42	-40.6

Table B.26: Clusters of positive contrasts between motor and sentences trials of the Pinel task

Size (voxels)	Minima				Center of Gravity		
	Value (β)	X (mm)	Y (mm)	Z (mm)	X (mm)	Y (mm)	Z (mm)
6588	-0.0222	-55	31.5	10.5	-15.7	2.45	-15.1
293	-0.00992	-20	34	55.5	-9.61	44.7	41.5
70	-0.0185	-52.5	-73.5	25.5	-46.6	-73.5	33.7
67	-0.00615	45	-76	38	41.5	-80.6	22.5
59	-0.0248	-2.5	-96	28	0.208	-88.1	38.1
58	-0.00859	5	49	50.5	8.82	49.8	44.6
38	-0.00453	17.5	-91	-37	15	-87.1	-39.8
34	-0.00816	-47.5	-38.5	3	-47.1	-39.1	2.92
33	-0.00874	-7.5	-33.5	-54.5	-7.46	-37.9	-59.5
32	-0.0062	30	-86	38	28.2	-84.5	39.3
20	-0.00549	67.5	-8.5	28	66.4	-7.38	24.2
20	-0.00429	-35	-93.5	13	-35	-91.5	8.96
20	-0.00781	57.5	29	0.5	56.4	30.4	2.56

Table B.27: Clusters of negative contrasts between motor and sentences trials of the Pinel task

Size (voxels)	Maxima				Center of Gravity		
	Value (β)	X (mm)	Y (mm)	Z (mm)	X (mm)	Y (mm)	Z (mm)
1474	0.0317	-67.5	-16	0.5	-52.7	-16.5	2.11
771	0.0152	57.5	16.5	-9.5	56.6	-12.8	2.93
500	0.00914	-35	-96	-2	-30.5	-74.8	-14.5
245	0.00689	45	-66	-19.5	32.9	-67.2	-18.8
193	0.00854	-12.5	59	-22	-0.447	50	-23.3
102	0.00678	37.5	-93.5	0.5	33.5	-86.6	-4.89
65	0.00663	-32.5	-11	-44.5	-35.2	-8.27	-42.3
65	0.00556	32.5	-6	-49.5	35.1	-3.83	-45.4
57	0.00869	57.5	26.5	-2	54.2	30.1	-1.03
32	0.00216	-7.5	-71	-39.5	-8.17	-69.8	-36.5
26	0.00619	-37.5	1.5	33	-38.1	-0.91	31.7
24	0.0123	-50	-1	48	-46.2	-7.66	46.1

Table B.28: Clusters of positive correlates of all sentences trials of the Pinel task

Size (voxels)	Minima				Center of Gravity		
	Value (β)	X (mm)	Y (mm)	Z (mm)	X (mm)	Y (mm)	Z (mm)
244	-0.00596	-2.5	-73.5	33	1.37	-69.1	34.9
68	-0.0053	52.5	-61	43	50.3	-53.6	42.4
35	-0.00418	5	-38.5	23	6.12	-37.5	26.6
32	-0.0029	7.5	44	15.5	8.43	39.3	11.9
25	-0.003	-27.5	16.5	-9.5	-28.2	15.9	-10.3
25	-0.0049	-37.5	-83.5	-32	-33.1	-83.2	-38.7
22	-0.00306	-22.5	49	25.5	-20.7	50.8	22
20	-0.00576	-32.5	36.5	45.5	-35.4	37.1	41.7

Table B.29: Clusters of negative correlates of all sentences trials of the Pinel task

Size (voxels)	Maxima				Center of Gravity		
	Value (β)	X (mm)	Y (mm)	Z (mm)	X (mm)	Y (mm)	Z (mm)
17978	0.104	-50	1.5	53	-7.88	-40.9	4.61
518	0.0204	2.5	39	-32	0.0427	48.6	-20.2
456	0.0212	25	-61	50.5	31.9	-57.5	41.1
433	0.0237	67.5	-43.5	10.5	56.7	-38.9	19.5
129	0.0202	0	-63.5	60.5	0.00562	-62.2	60
73	0.00879	35	39	40.5	34.5	37.3	33
39	0.00775	-40	-8.5	-47	-39.8	-10.6	-40.6
35	0.00492	12.5	-23.5	38	13.8	-23.2	41.7
33	0.017	20	-8.5	-44.5	28.1	-1.47	-46.4
33	0.0264	-37.5	-41	-54.5	-43.5	-48.3	-52.1
24	0.0197	-25	-76	33	-25.6	-77.3	29.7
21	0.0264	40	-51	65.5	41.6	-54.2	62
21	0.0383	-15	61.5	30.5	-6.39	61.9	33.8

Table B.30: Clusters of positive correlates of all visual trials of the Pinel task

Size (voxels)	Minima				Center of Gravity		
	Value (β)	X (mm)	Y (mm)	Z (mm)	X (mm)	Y (mm)	Z (mm)
150	-0.00972	47.5	-11	8	45.2	-11.7	4.58
110	-0.0107	-42.5	-13.5	0.5	-41.7	-16	1.89
88	-0.0058	-27.5	-58.5	3	-26.8	-49.1	3.11
84	-0.00767	0	-56	30.5	-1.44	-63.2	28
80	-0.031	-15	-106	-4.5	-9.04	-101	14.5
77	-0.00515	2.5	31.5	0.5	0.0134	31.5	2.72
71	-0.02	-42.5	-73.5	-47	-38.9	-79.1	-36.2
68	-0.00537	20	26.5	45.5	19.9	28.5	43.9
56	-0.00664	60	-16	5.5	62.9	-16.2	5.57
44	-0.00387	27.5	-48.5	3	25	-44.3	8.31
42	-0.0206	-42.5	54	-12	-43.7	50.8	-6.64
42	-0.014	-50	16.5	-34.5	-49.1	8.31	-30.3
39	-0.0208	47.5	-68.5	48	47.7	-64.9	46.5
33	-0.00954	20	14	-29.5	22.7	11.4	-34
28	-0.0139	10	69	-9.5	9.62	68.9	-8.8
25	-0.0107	-7.5	-78.5	-4.5	-6.55	-77.4	-4.42
25	-0.00449	-25	9	-29.5	-29.1	7.7	-31.7
24	-0.00611	47.5	-71	-39.5	48.6	-69.1	-40.1
23	-0.0166	-17.5	-8.5	-42	-12.2	-3.63	-37.9

Table B.31: Clusters of negative correlates of all visual trials of the Pinel task

Size (voxels)	Maxima				Center of Gravity		
	Value (β)	X (mm)	Y (mm)	Z (mm)	X (mm)	Y (mm)	Z (mm)
31	0.00561	50	-51	-12	52	-49.8	-13.6
28	0.0036	52.5	16.5	-29.5	43.2	17.2	-37
27	0.0134	-37.5	1.5	30.5	-42	3.16	27.2
27	0.0087	-22.5	-68.5	33	-25.3	-74.4	28.1
26	0.00241	35	-58.5	-37	37	-58.7	-41.8
23	0.00921	-37.5	26.5	20.5	-40.8	25.3	21.8

Table B.32: Clusters of positive contrasts between auditory calculus and non-calculus trials of the Pinel task

Size (voxels)	Minima				Center of Gravity		
	Value (β)	X (mm)	Y (mm)	Z (mm)	X (mm)	Y (mm)	Z (mm)
1022	-0.0113	-67.5	-18.5	5.5	-47.5	-19.3	7.14
850	-0.00856	55	-16	8	51.8	-15.4	5.65
218	-0.00584	25	-53.5	-19.5	19.3	-51.6	-18.8
201	-0.00816	-32.5	-26	53	-38.1	-30.5	59.3
113	-0.0076	-2.5	-13.5	48	-1.76	-6.17	45
72	-0.00406	22.5	-53.5	-59.5	22.5	-53.3	-51.9
68	-0.00531	-22.5	-53.5	-19.5	-24.4	-50.2	-23
61	-0.00539	35	-26	53	41.9	-25.8	53.3
37	-0.00511	0	31.5	48	0.939	30.6	47.4
30	-0.00513	40	-3.5	13	40.8	-1.34	12.4
27	-0.00281	10	-28.5	43	10.5	-24.3	39.1
26	-0.00438	30	-23.5	68	27.8	-16.9	69.3
26	-0.00573	52.5	-46	35.5	52.1	-47.7	36.4
23	-0.0034	12.5	-21	3	13.4	-22.2	0.734
22	-0.00512	-7.5	-26	45.5	-11.7	-28.9	39.3
22	-0.00359	-10	-21	3	-12.2	-24.6	1.68
22	-0.00289	2.5	44	-29.5	2.55	42.6	-27.8

Table B.33: Clusters of negative contrasts between auditory calculus and non-calculus trials of the Pinel task

Size (voxels)	Maxima				Center of Gravity		
	Value (β)	X (mm)	Y (mm)	Z (mm)	X (mm)	Y (mm)	Z (mm)
2365	0.116	67.5	-11	10.5	54.3	-15.7	3.71
2334	0.014	-5	-73.5	-7	0.178	-75.3	7.69
1955	0.108	-67.5	-16	0.5	-52.1	-21.1	4.9
95	0.00532	37.5	-3.5	-49.5	34.9	-3.42	-45.3
71	0.00674	-12.5	-28.5	-7	-10	-30.6	-9.81
37	0.00377	-45	-78.5	-29.5	-40.6	-80.2	-31.4
33	0.00505	12.5	-28.5	-7	13.2	-26.7	-3.53
33	0.00269	-22.5	16.5	-34.5	-21.4	9.94	-36.9
33	0.00607	-7.5	-56	-64.5	-13.3	-59.8	-58.8
27	0.00471	-37.5	29	-2	-40.1	26.6	-2.74

Table B.34: Clusters of positive contrasts between auditory and visual trials of the Pinel task

Size (voxels)	Minima				Center of Gravity		
	Value (β)	X (mm)	Y (mm)	Z (mm)	X (mm)	Y (mm)	Z (mm)
18974	-0.0593	-40	-68.5	-17	-2.86	-60.1	-0.25
389	-0.0532	32.5	9	65.5	33.4	1.03	57.9
45	-0.00595	15	71.5	0.5	18.6	68.7	1.13
41	-0.00445	-7.5	-33.5	-59.5	-3.79	-38.2	-60.2
29	-0.00133	-5	-51	18	-9.23	-50.8	19.6
28	-0.00146	-25	-11	8	-25.4	-9.07	8.57
26	-0.00171	12.5	-51	18	12.2	-48.9	16.6
23	-0.0159	22.5	14	68	19.6	23.6	63.3
23	-0.00407	-45	44	-19.5	-46.8	34.9	-17.1
21	-0.00223	27.5	-23.5	63	27.1	-26.9	60.2
20	-0.00577	-15	69	-4.5	-17.2	65.3	-11.7

Table B.35: Clusters of negative contrasts between auditory and visual trials of the Pinel task

Size (voxels)	Maxima				Center of Gravity		
	Value (β)	X (mm)	Y (mm)	Z (mm)	X (mm)	Y (mm)	Z (mm)
1021	0.0205	-35	-21	70.5	-36.9	-26.4	58.5
436	0.00633	15	-51	-17	15.1	-51.6	-18.7
234	0.00354	-45	-18.5	18	-42.2	-22.1	13.8
194	0.00263	12.5	-58.5	-47	14.8	-58	-46.8
86	0.00348	-5	-13.5	48	-5.86	-20.8	46
61	0.00254	-15	-23.5	0.5	-14.5	-23	2.92
50	0.00291	22.5	56.5	-19.5	21.7	55.2	-16.1
42	0.00137	45	54	-12	41.4	50.1	-12.7
39	0.00292	42.5	-3.5	-7	43.4	-0.843	-9.76
39	0.00211	-22.5	6.5	-47	-20.2	3.64	-41.7
30	0.00173	-42.5	-28.5	-29.5	-49.4	-29	-27.2
23	0.00221	-17.5	-13.5	-37	-19.9	-10.7	-36.7
21	0.00164	25	26.5	-24.5	20.5	28.4	-23.9

Table B.36: Clusters of positive contrasts between right and left motor trials of the Pinel task

Size (voxels)	Minima				Center of Gravity		
	Value (β)	X (mm)	Y (mm)	Z (mm)	X (mm)	Y (mm)	Z (mm)
40715	-0.024	32.5	-23.5	73	9.44	-33	24.7

Table B.37: Clusters of negative contrasts between right and left motor trials of the Pinel task

Size (voxels)	Maxima				Center of Gravity		
	Value (β)	X (mm)	Y (mm)	Z (mm)	X (mm)	Y (mm)	Z (mm)
136	0.0151	-42.5	4	23	-41.6	2.58	27
130	0.00341	27.5	-63.5	-29.5	29.4	-64.7	-38.6
106	0.0097	-25	-63.5	35.5	-25.2	-68.5	32.8
94	0.00904	-55	-48.5	-34.5	-51.4	-52.3	-16.4
92	0.0107	-50	39	15.5	-44.3	29.4	18.8
57	0.00174	27.5	-38.5	13	27.9	-37.5	5.53
45	0.00429	50	-51	-12	50.7	-49.2	-13
41	0.0055	30	-66	45.5	26.3	-63.4	43.6
37	0.00315	27.5	-46	40.5	29.9	-48	37.6
28	0.0124	-17.5	-83.5	50.5	-22.9	-78.9	52
24	0.00382	25	-78.5	-52	27.7	-74.7	-54.4
22	0.00415	-20	11.5	58	-15.7	9.7	54

Table B.38: Clusters of positive contrasts between visual calculus and non-calculus trials of the Pinel task

Size (voxels)	Minima				Center of Gravity		
	Value (β)	X (mm)	Y (mm)	Z (mm)	X (mm)	Y (mm)	Z (mm)
5321	-0.0217	-62.5	1.5	0.5	3.9	-11.2	9.42
2575	-0.0108	-25	-98.5	-17	-2.55	-62.4	-16.5
994	-0.0202	35	-3.5	65.5	32.1	-22.9	62.7
818	-0.0128	0	-3.5	48	-0.298	-10.7	42.4
776	-0.024	-27.5	-21	75.5	-30.6	-30.6	63.6
652	-0.00543	22.5	-53.5	-59.5	7.79	-55.4	-50.7
303	-0.00849	7.5	34	60.5	6.7	34.4	44.3
166	-0.00903	45	26.5	45.5	40.1	25.6	45.6
143	-0.00494	2.5	-51	50.5	5.84	-49.5	40.8
85	-0.00657	65	-53.5	10.5	61.1	-49.4	8.44
74	-0.00693	-57.5	-53.5	45.5	-45.7	-63.2	43.1
54	-0.00529	50	-11	-42	43.3	-3.9	-44.3
45	-0.00257	-27.5	56.5	0.5	-26.9	55.3	-1.21
39	-0.00193	32.5	-83.5	-29.5	30.1	-83.2	-31.1
38	-0.00377	-12.5	59	-22	-7.4	51.3	-22.4
36	-0.0156	-15	61.5	30.5	-18.4	59.4	19.3
30	-0.00459	22.5	66.5	-9.5	16.6	61.3	-16.8
27	-0.00396	-55	-66	13	-53.8	-62.2	11.9
26	-0.0024	0	34	10.5	-3.19	32.7	11.8
22	-0.00275	5	-28.5	-52	6.19	-32	-45.8
21	-0.00197	-65	-13.5	-27	-61.3	-10.4	-30
21	-0.00318	60	-13.5	-34.5	62.9	-17.6	-28.3
20	-0.0019	-7.5	51.5	-2	-7.71	45.4	-5.79

Table B.39: Clusters of negative contrasts between visual calculus and non-calculus trials of the Pinel task

Size (voxels)	Maxima				Center of Gravity		
	Value (β)	X (mm)	Y (mm)	Z (mm)	X (mm)	Y (mm)	Z (mm)
33048	0.116	-50	1.5	53	-6.03	-25.6	20.4
93	0.00406	25	54	-7	25.3	47.4	-11.4
69	0.00552	-37.5	-11	-44.5	-38.7	-6.82	-44.4
54	0.00626	42.5	4	-47	39.4	-5.29	-44.3
21	0.00264	-20	64	-14.5	-19.2	59.3	-15.4

Table B.40: Clusters of positive contrasts between visual stimuli and chequerboards trials of the Pinel task

Size (voxels)	Minima				Center of Gravity		
	Value (β)	X (mm)	Y (mm)	Z (mm)	X (mm)	Y (mm)	Z (mm)
4608	-0.0261	47.5	54	-7	-3.13	38.9	7.45
3832	-0.0413	15	-104	10.5	3.49	-81.7	2.94
127	-0.0109	50	-43.5	-44.5	46.6	-61.3	-41.5
88	-0.014	-45	-71	45.5	-46.9	-67.4	40.8
78	-0.00967	42.5	-68.5	53	49.5	-66.6	38
58	-0.00224	50	-31	-27	59.6	-20.8	-25.4
34	-0.00213	27.5	-88.5	-37	26.7	-86.2	-38.4
30	-0.00713	-52.5	-73.5	23	-51.2	-71	25.2
29	-0.0152	20	-83.5	48	15.6	-83	43.3
22	-0.00405	-47.5	-68.5	-42	-49	-67.1	-38.8

Table B.41: Clusters of negative contrasts between visual stimuli and chequerboards trials of the Pinel task

C. Supplementary material for Chapter 4

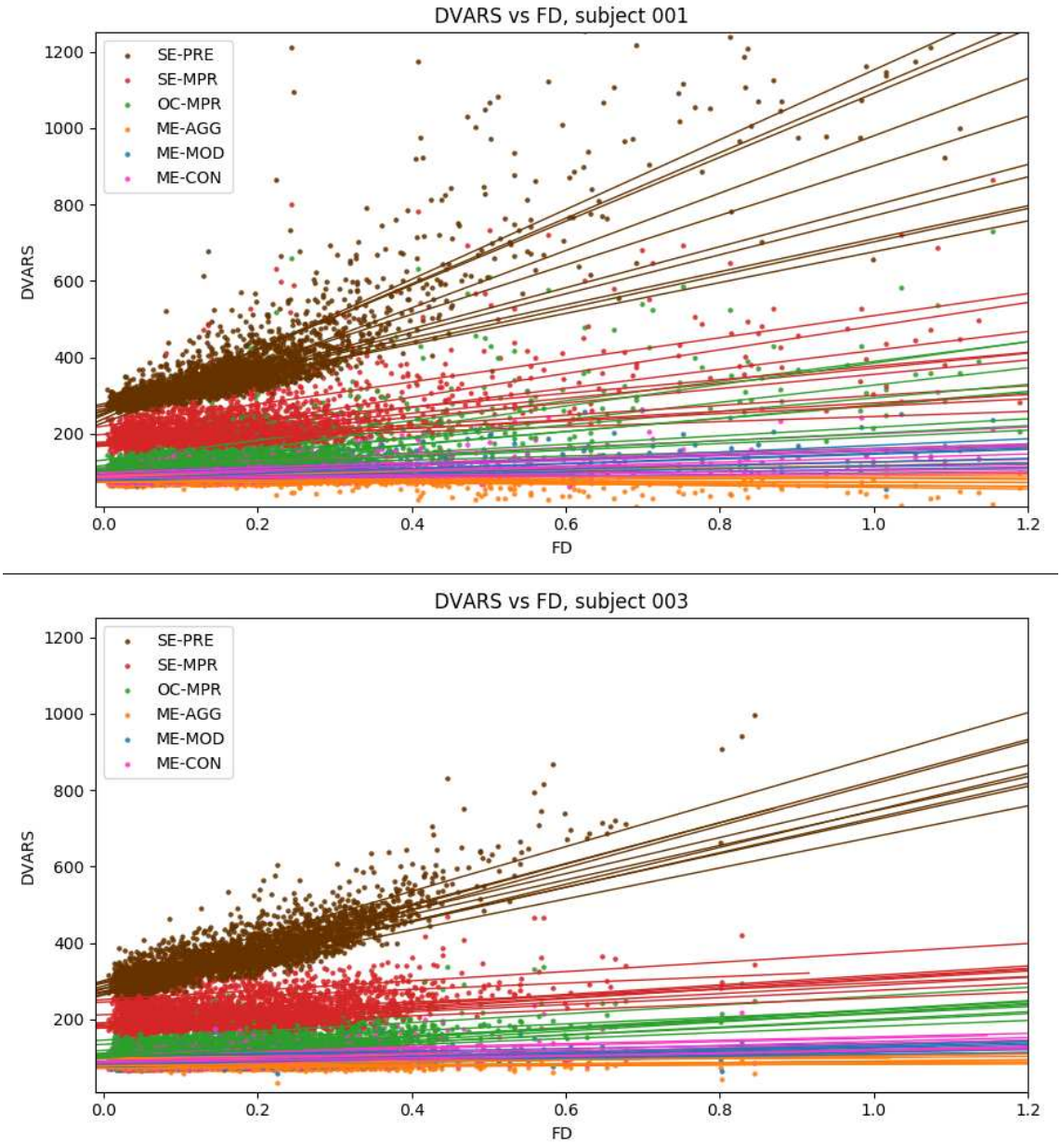

Figure C.1: Relation between the DVARS of the denoised data following different analysis pipelines and FD for subjects 001 and 003. Refer to Figure 4.4 for further explanation.

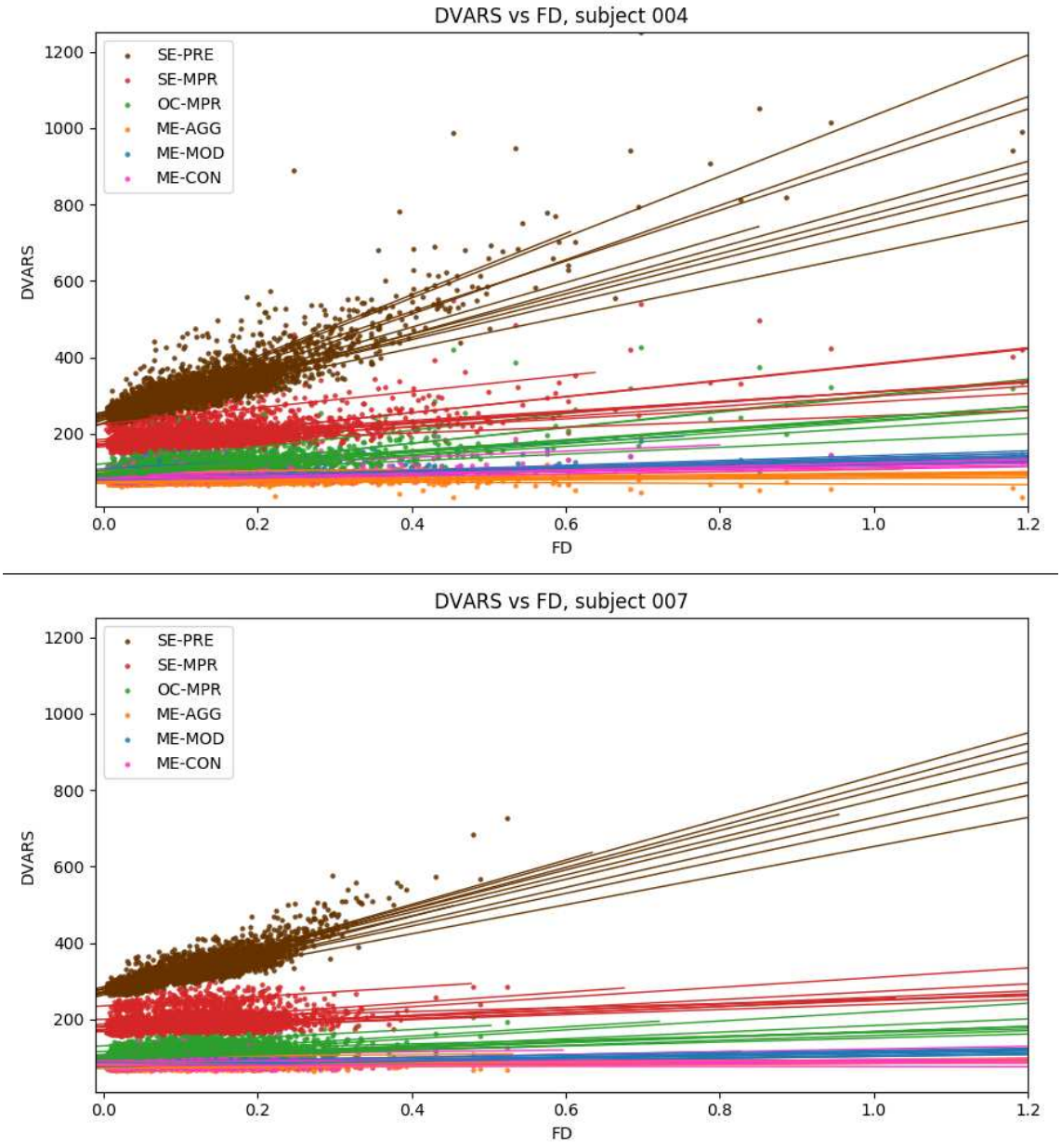

Figure C.2: Relation between the DVARS of the denoised data following different analysis pipelines and FD for subjects 004 and 007. Refer to Figure 4.4 for further explanation.

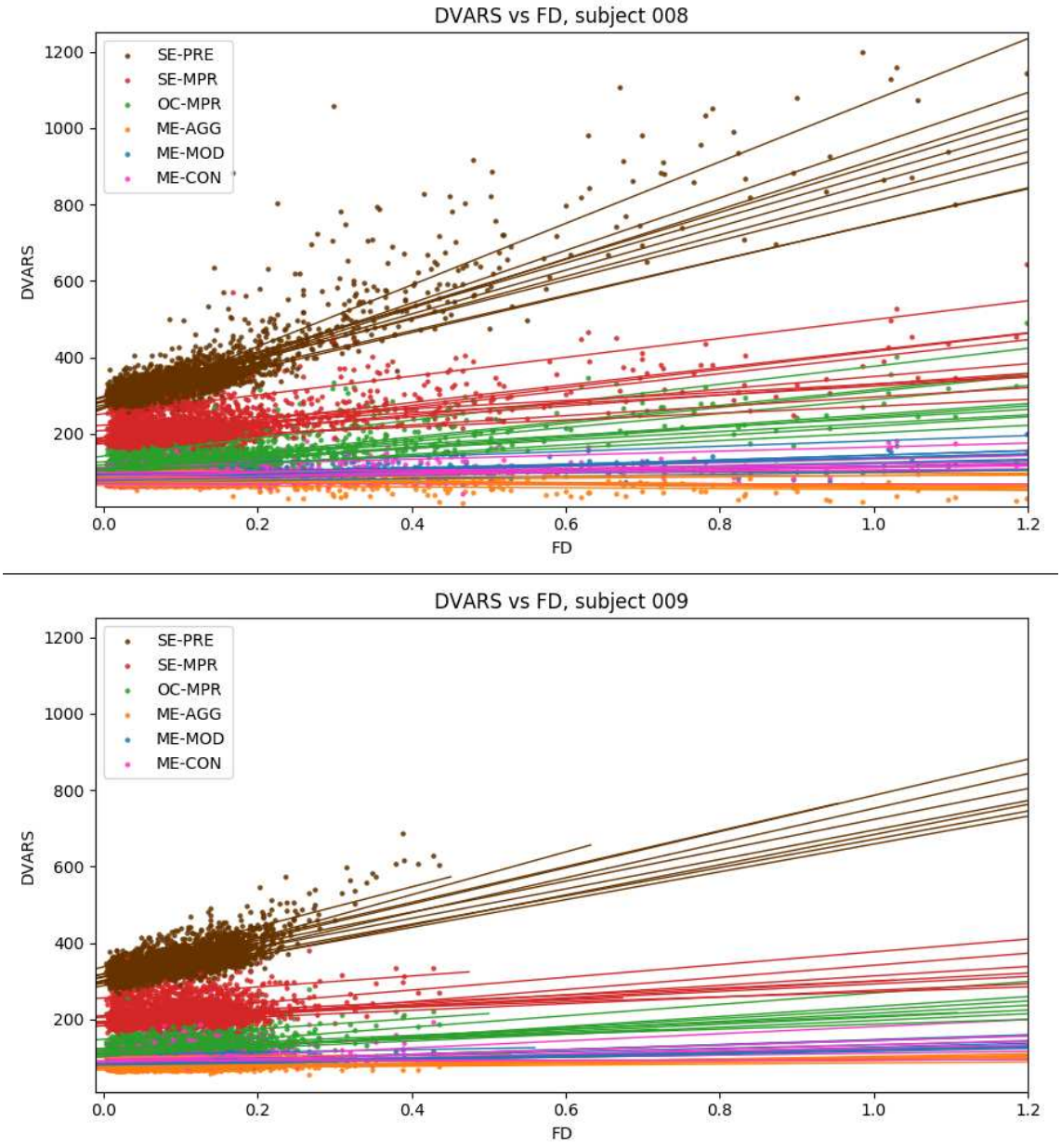

Figure C.3: Relation between the DVARS of the denoised data following different analysis pipelines and FD for subjects 008 and 009. Refer to Figure 4.4 for further explanation.

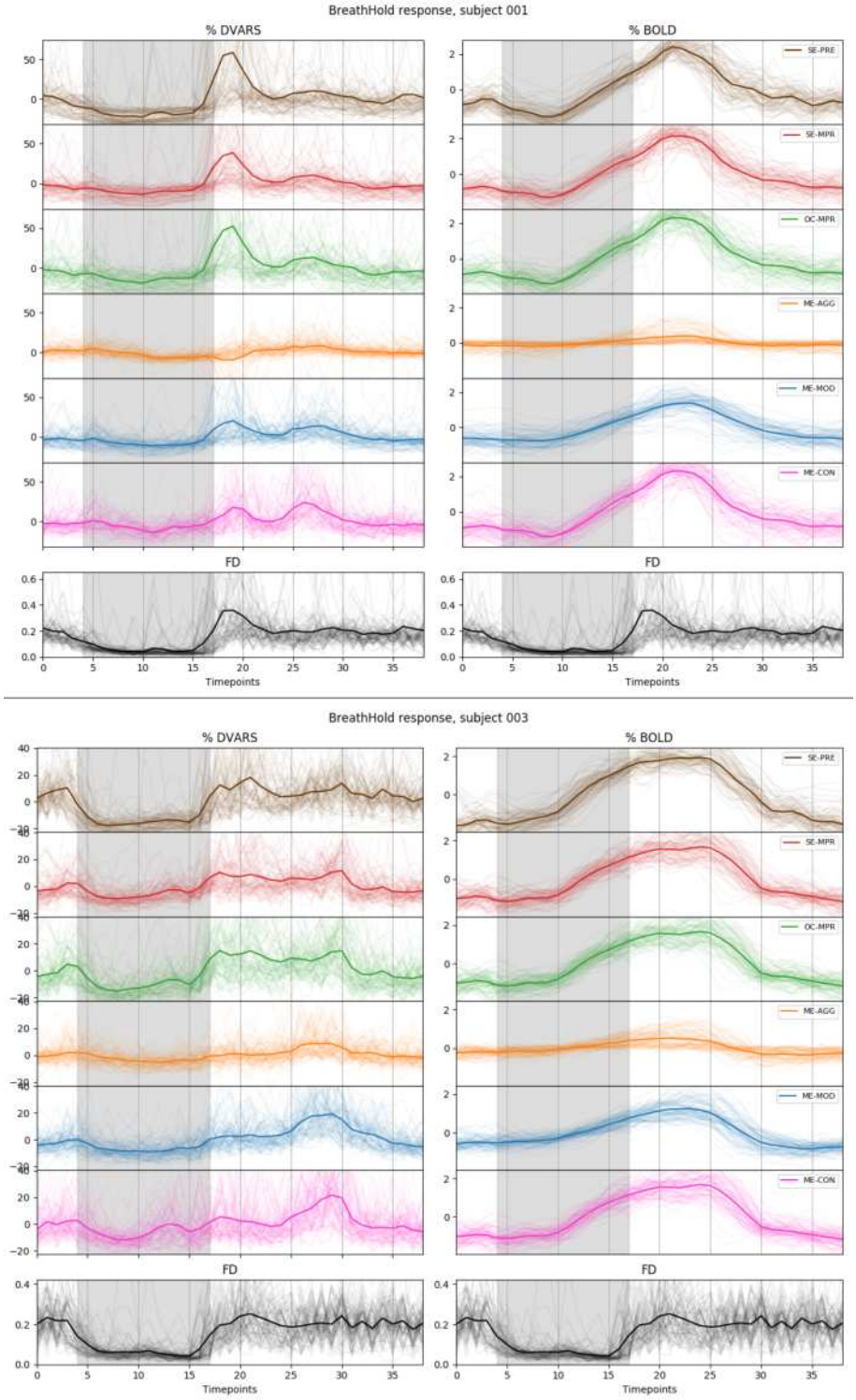

Figure C.4: Average GM %DVARS and %BOLD response of all BH trials across ten sessions for subjects 001 and 003. Refer to Figure 4.5 for further explanation.

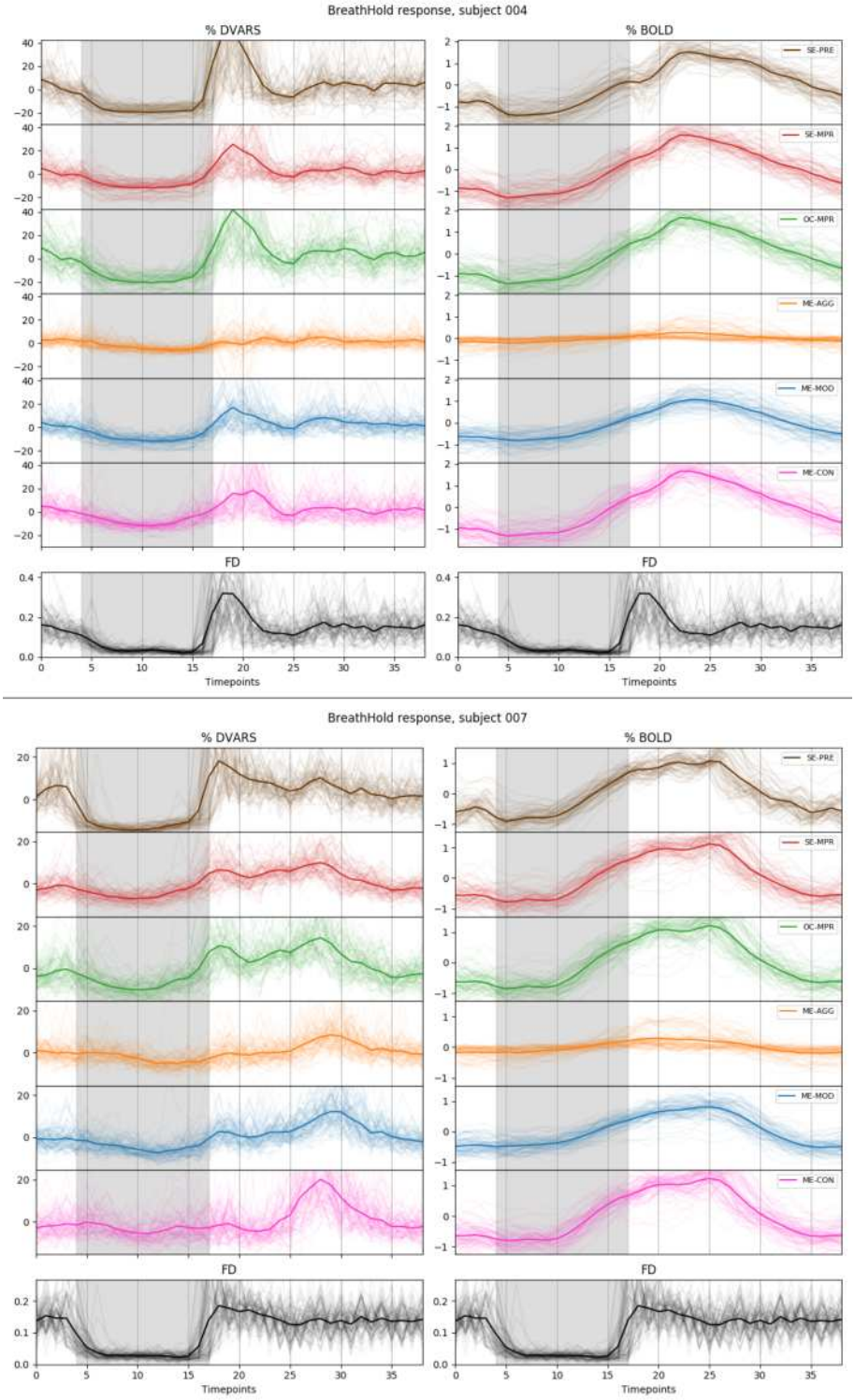

Figure C.5: Average GM %DVARS and %BOLD response of all BH trials across ten sessions for subjects 004 and 007. Refer to Figure 4.5 for further explanation.

C

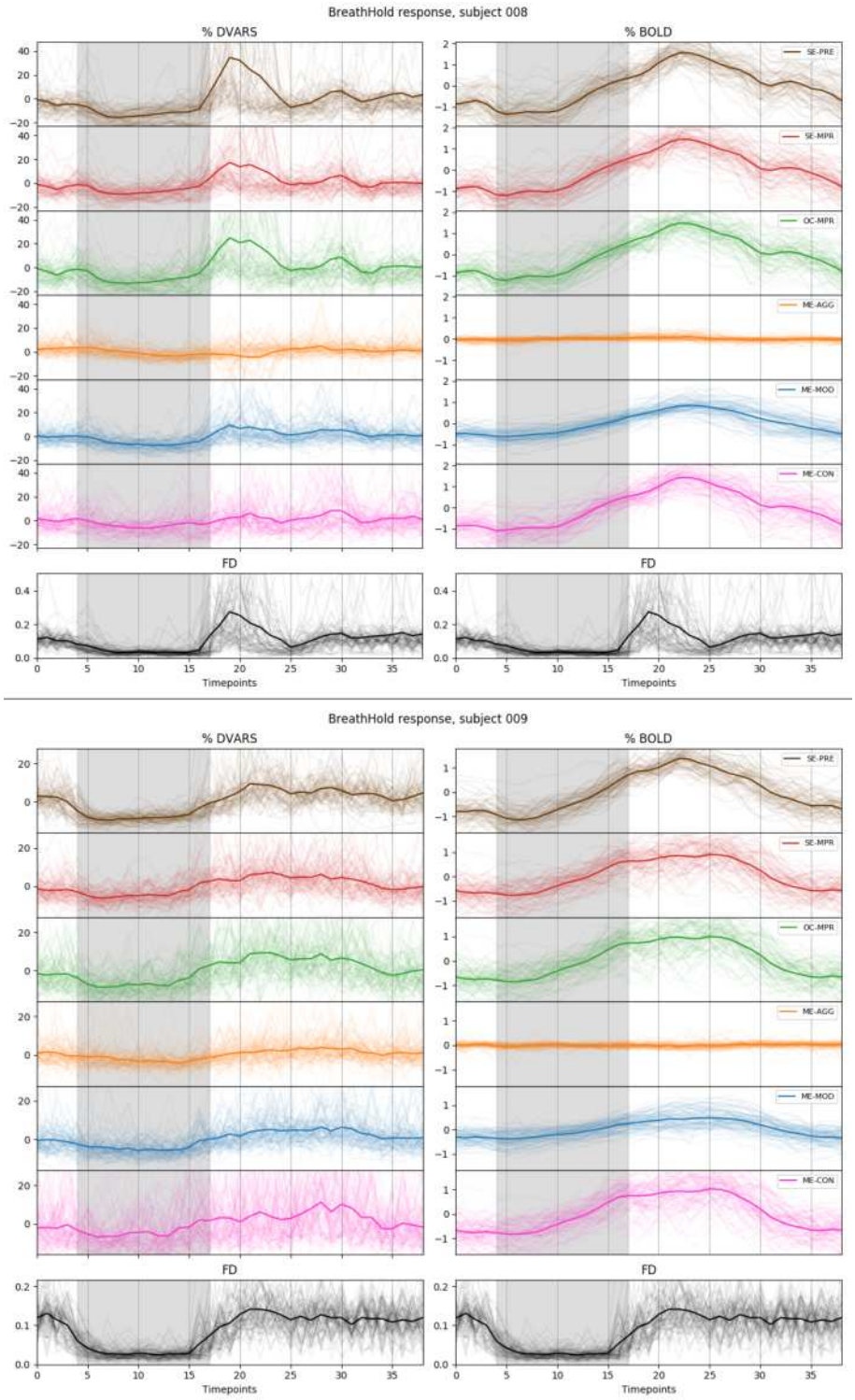

Figure C.6: Average GM %DVARS and %BOLD response of all BH trials across ten sessions for subjects 008 and 009. Refer to Figure 4.5 for further explanation.

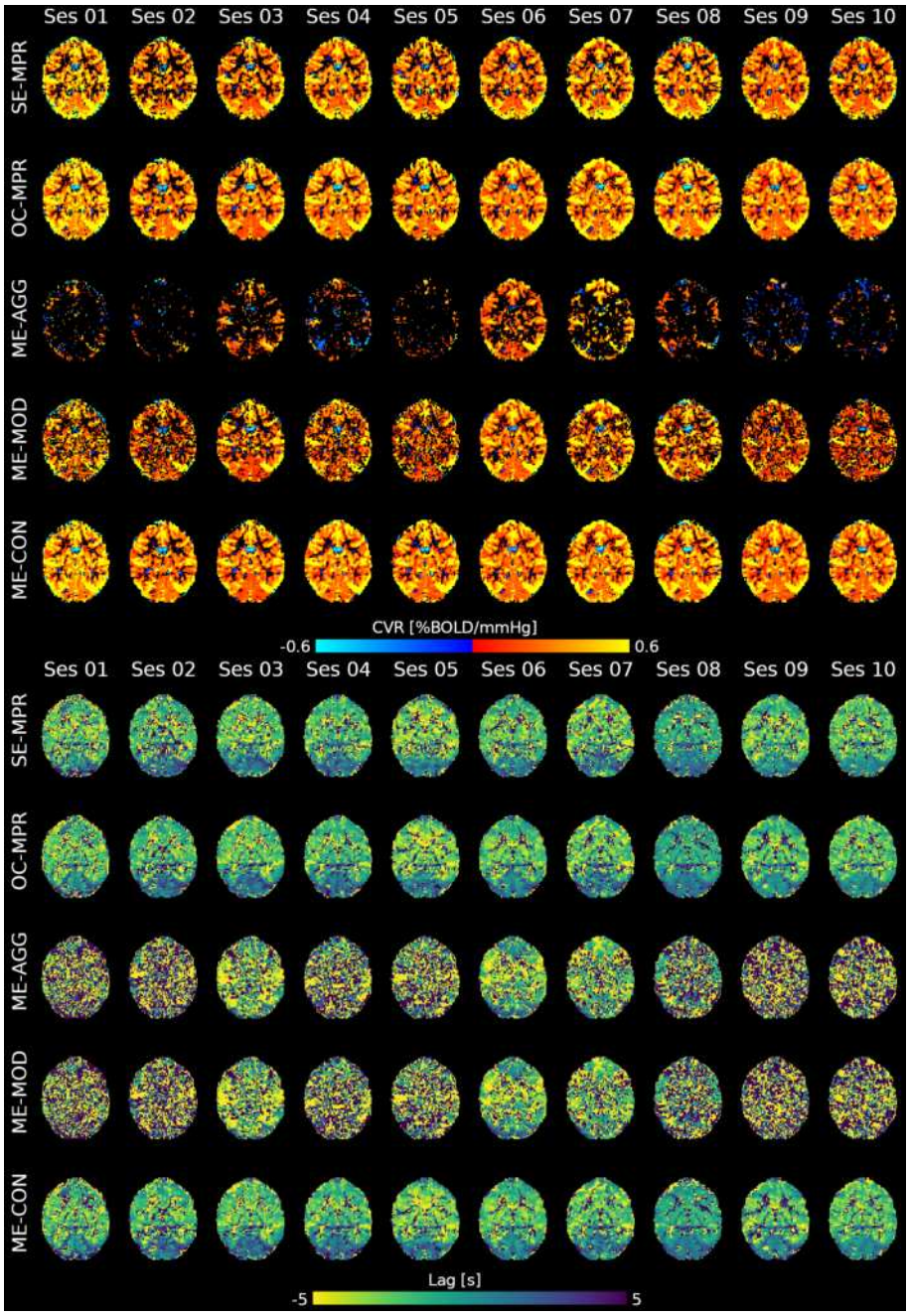

Figure C.7: Top: thresholded CVR map obtained with the different lagged-GLM analysis for all the sessions of subject 001. Bottom: unthresholded lag map obtained with the different lagged-GLM analysis, for all the sessions of the same subject. Refer to Figure 4.6 for further explanation.

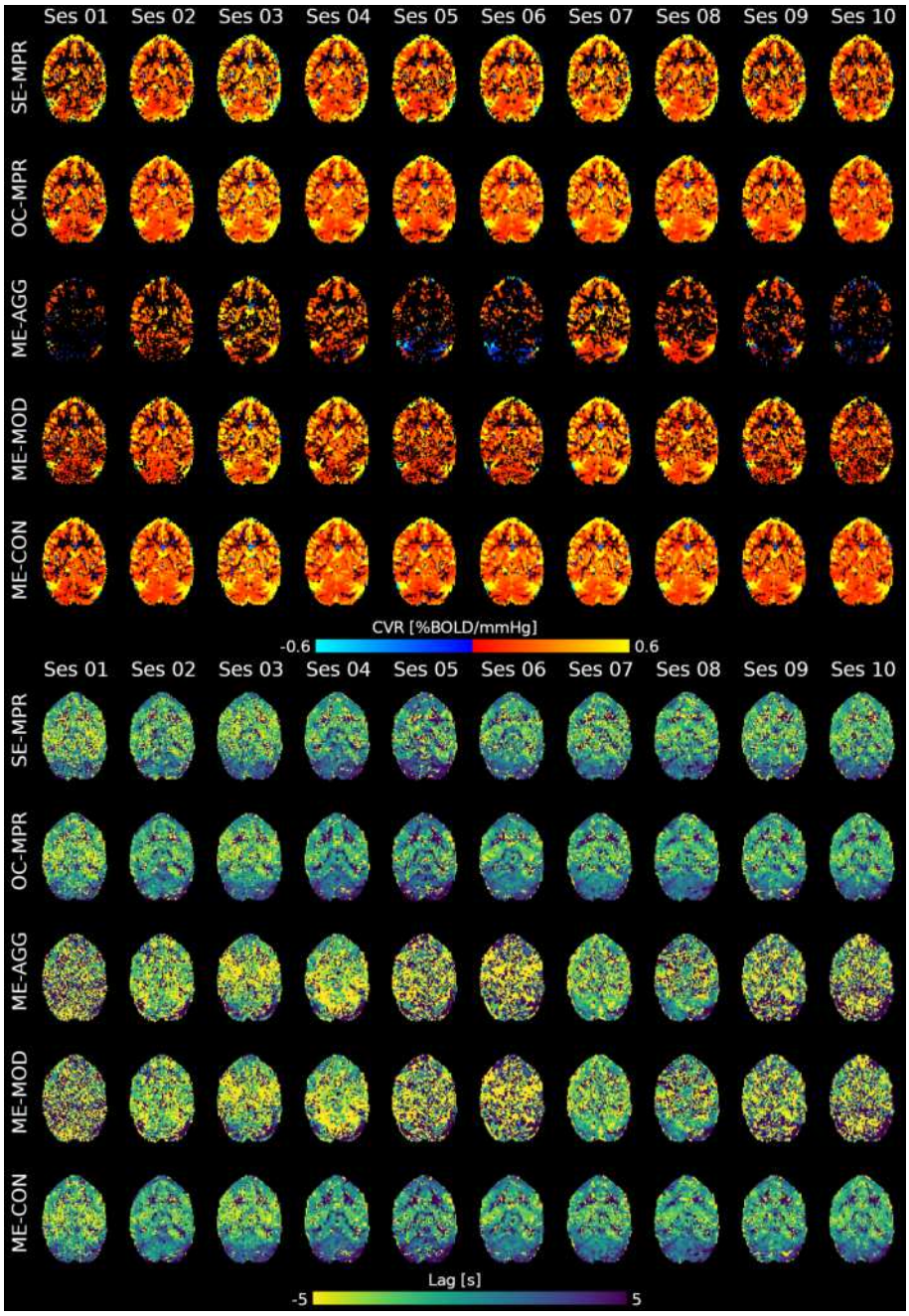

Figure C.8: Top: thresholded CVR map obtained with the different lagged-GLM analysis for all the sessions of subject 003. Bottom: unthresholded lag map obtained with the different lagged-GLM analysis, for all the sessions of the same subject. Refer to Figure 4.6 for further explanation.

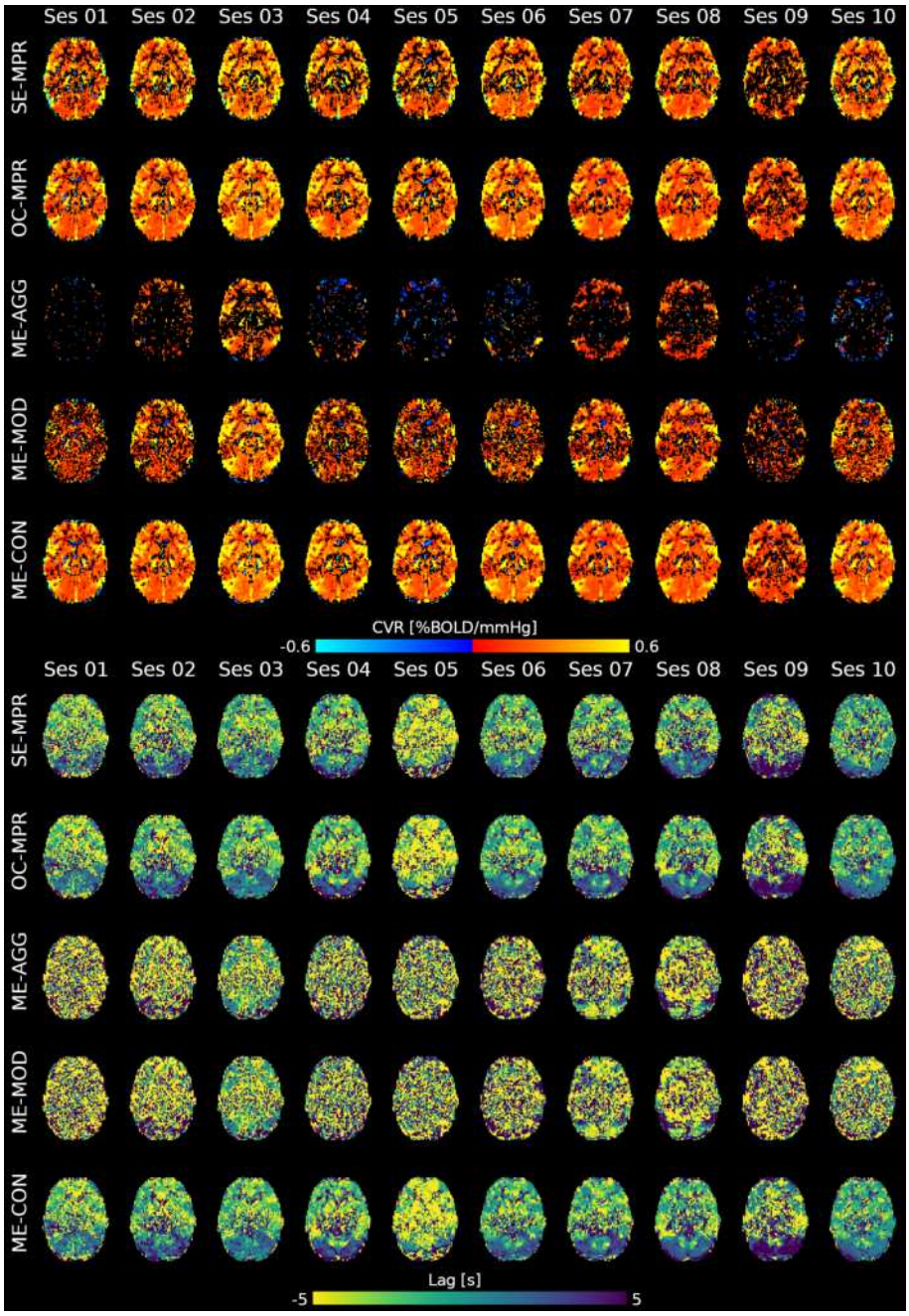

Figure C.9: Top: thresholded CVR map obtained with the different lagged-GLM analysis for all the sessions of subject 004. Bottom: unthresholded lag map obtained with the different lagged-GLM analysis, for all the sessions of the same subject. Refer to Figure 4.6 for further explanation.

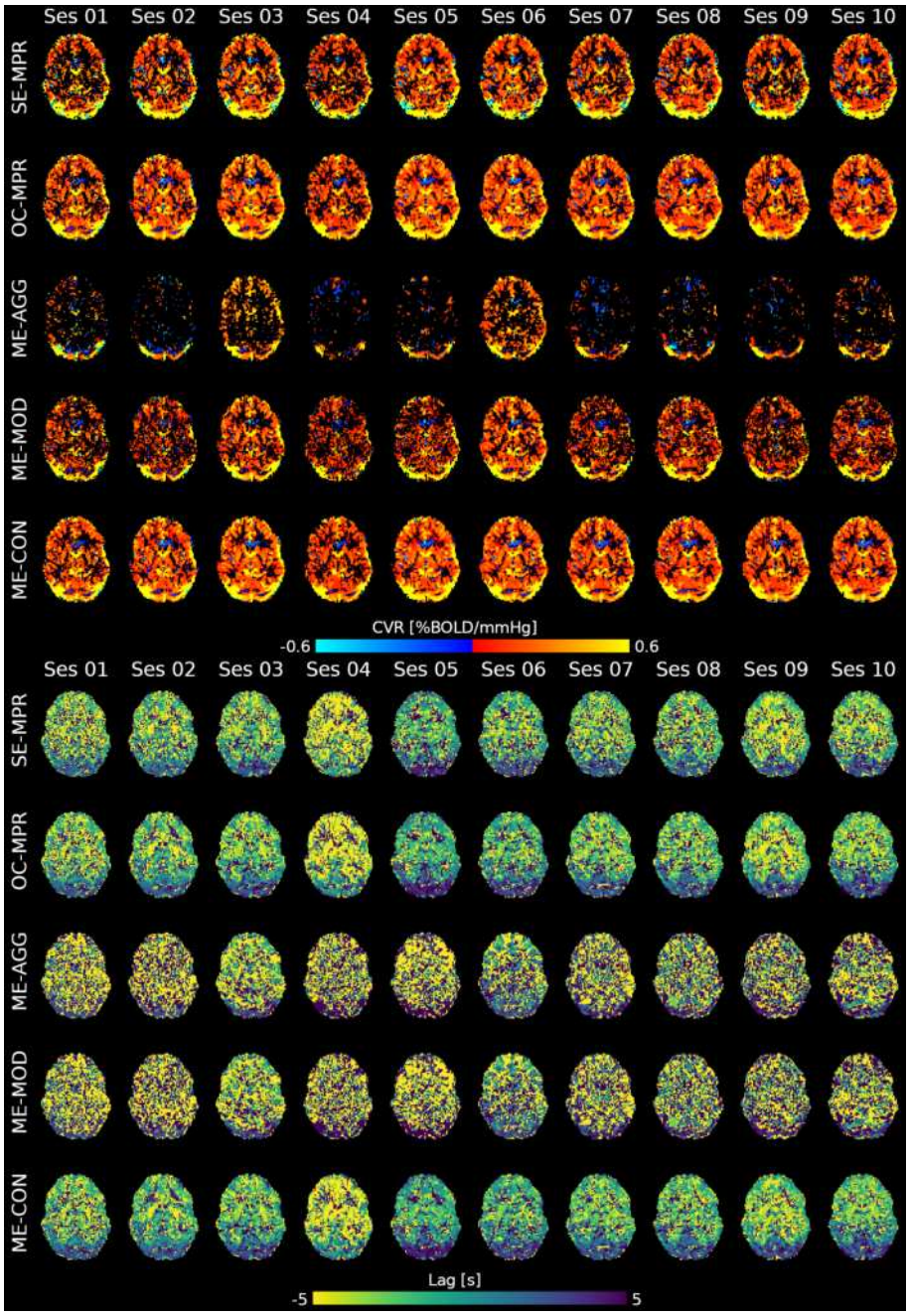

Figure C.10: Top: thresholded CVR map obtained with the different lagged-GLM analysis for all the sessions of subject 007. Bottom: unthresholded lag map obtained with the different lagged-GLM analysis, for all the sessions of the same subject. Refer to Figure 4.6 for further explanation.

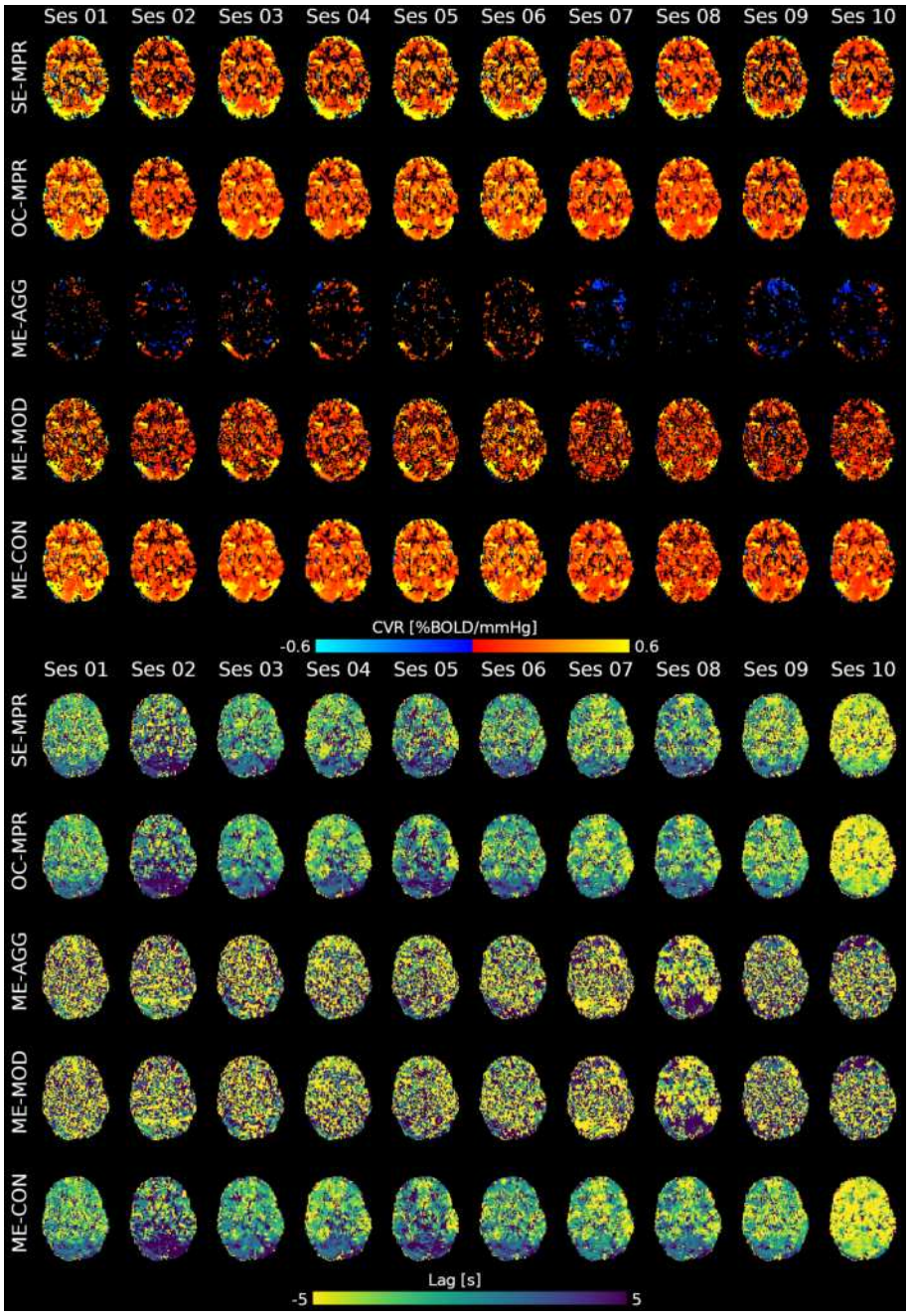

Figure C.11: Top: thresholded CVR map obtained with the different lagged-GLM analysis for all the sessions of subject 008. Bottom: unthresholded lag map obtained with the different lagged-GLM analysis, for all the sessions of the same subject. Refer to Figure 4.6 for further explanation.

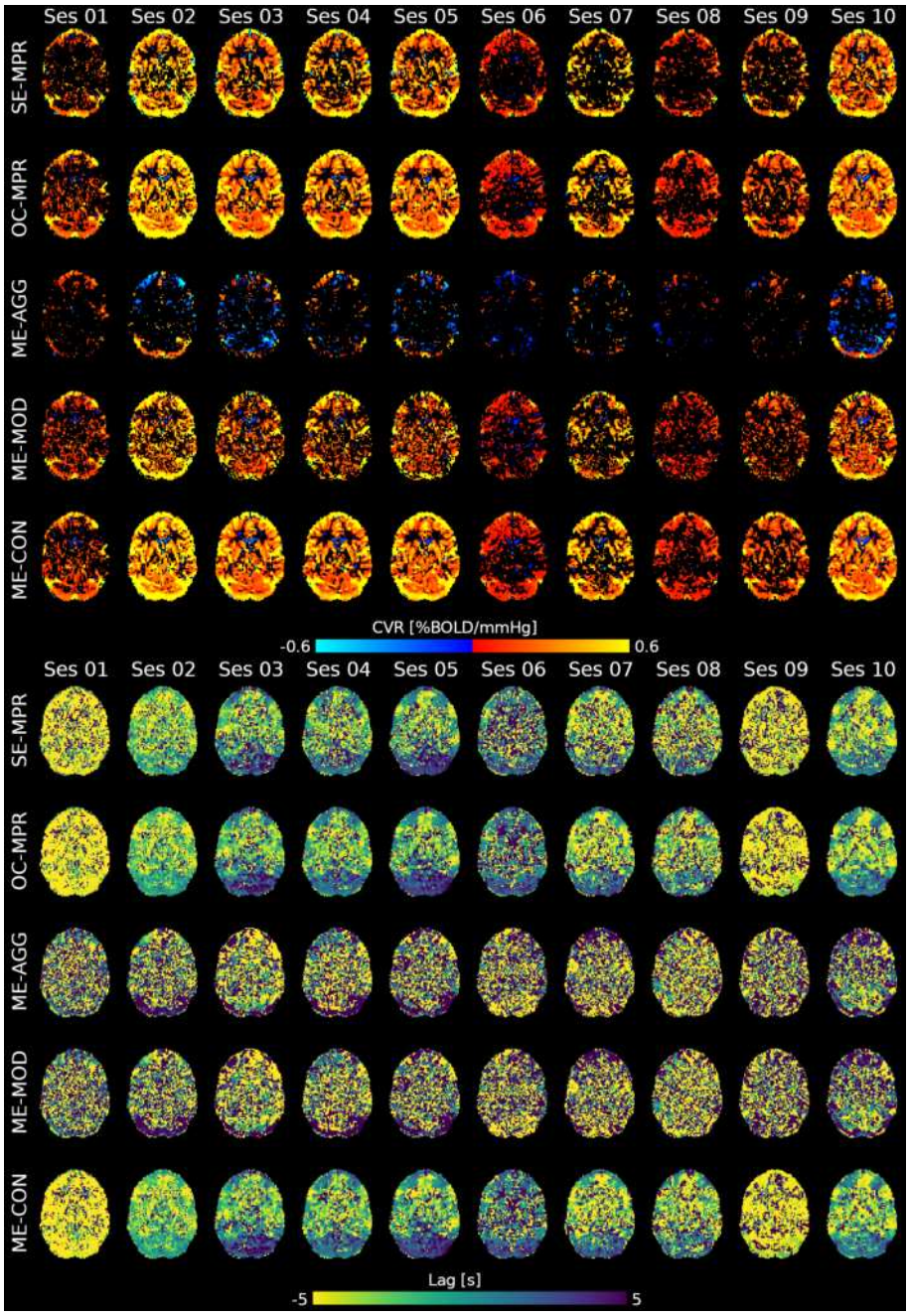

Figure C.12: Top: thresholded CVR map obtained with the different lagged-GLM analysis for all the sessions of subject 009. Bottom: unthresholded lag map obtained with the different lagged-GLM analysis, for all the sessions of the same subject. Refer to Figure 4.6 for further explanation.

D. Tables of impact for the relationships between Cerebrovascular Reactivity, Blood Pressure, and Sex, in Chapter 5

Size (voxels)	Maxima				Center of Gravity		
	Value (β)	X (mm)	Y (mm)	Z (mm)	X (mm)	Y (mm)	Z (mm)
2824	0.102	-52.5	-56	-29.5	-2.73	-61.7	-11.7
1062	0.0958	50	11.5	-7	50.8	-14.4	4.81
1062	0.113	-2.5	-23.5	73	-42.7	-19.9	25.6
636	0.075	0	-1	43	0.563	0.0131	36.4
300	0.0379	-52.5	-56	5.5	-45	-63.6	11.2
109	0.0772	55	-66	-9.5	49.6	-59.7	-2.59
96	0.0767	2.5	-18.5	13	6.78	-18.7	8.94
93	0.0485	20	-33.5	78	18	-32.8	69.8
67	0.106	-12.5	-76	50.5	-15.7	-73.2	48.7
65	0.0623	5	-43.5	58	8.58	-39	49.8
59	0.0447	40	-16	53	35.6	-22.7	53.3
49	0.0513	-10	-11	-14.5	-3.66	3.29	-11.4
48	0.0491	-52.5	-68.5	-2	-51.4	-70.2	-3.18
47	0.0325	22.5	-6	65.5	20.3	-7.53	62.9
47	0.0203	-52.5	-48.5	-17	-52.1	-34	-10.2
42	0.0279	-2.5	44	-7	0.414	42.3	-5.87
40	0.0651	0	24	53	-0.363	24.8	50.7
40	0.061	-27.5	-66	55.5	-28.6	-57.4	50.4
40	0.0833	40	29	40.5	37.9	30.3	37.1
39	0.0336	42.5	44	3	42.2	41.6	2.95
37	0.0444	27.5	61.5	-2	27.4	55.7	-6.61
31	0.0267	37.5	-71	10.5	43	-70.2	12.8
28	0.048	45	1.5	53	40.5	-2.45	51.7
27	0.0415	55	-33.5	50.5	51.4	-31.5	50.5
27	0.0279	-12.5	-46	33	-9.76	-48.9	37
27	0.0335	-22.5	36.5	28	-25.1	36	29.2
27	0.0504	27.5	-86	5.5	28.4	-86.8	6.2
26	0.036	-50	-58.5	38	-49.5	-60.1	34
26	0.0571	-50	34	10.5	-50.3	33.3	8.27
25	0.0311	-42.5	-6	-47	-40.2	-4.19	-46.7
21	0.0358	-15	-8.5	68	-11.3	-10.2	65.1
21	0.0376	42.5	4	33	40.7	3.98	31.7
20	0.019	65	-13.5	-22	63.7	-17	-23.7

Table D.1: Identified clusters of positive relationship of MAP and CVR.

Size (voxels)	Maxima				Center of Gravity		
	Value (β)	X (mm)	Y (mm)	Z (mm)	X (mm)	Y (mm)	Z (mm)
109	0.023	47.5	9	33	41.2	16.3	27.9
92	0.0242	-37.5	-11	-7	-33	7.93	-6.65
71	0.0198	-2.5	29	50.5	-5.57	25.3	40.1
63	0.0207	30	6.5	58	25.7	13	50.8
63	0.0261	5	6.5	35.5	6.1	11.9	41.1
62	0.0293	40	29	-17	41.3	33.9	-11
57	0.0232	60	-46	5.5	59.1	-42.7	1.74
55	0.0176	-25	11.5	58	-23.7	10.7	52.6
43	0.0404	-25	-71	50.5	-21.3	-68.5	45.7
37	0.0307	20	-66	-14.5	15	-67.7	-18.4
36	0.0222	32.5	9	-17	37.7	5.5	-5.37
36	0.0225	35	-36	-27	32.5	-39.4	-25.9
35	0.0129	5	-16	38	8.31	-14.5	37.7
34	0.0294	-47.5	19	8	-48.9	18.3	6.69
33	0.0185	20	-56	20.5	18.7	-54.4	20.3
26	0.0168	22.5	6.5	-4.5	20.5	10.3	-6.46
25	0.0199	-25	51.5	8	-23.7	50.2	6.59
24	0.0113	-7.5	1.5	50.5	-9.57	0.503	48.7
22	0.0152	5	26.5	20.5	5.8	27.8	18.1
22	0.0165	-10	-48.5	-47	-12	-51.3	-47.6
20	0.0133	52.5	1.5	8	49.2	-4.25	11.3

Table D.2: Identified clusters of positive relationship of PP and CVR.

Size (voxels)	Maxima				Center of Gravity		
	Value (β)	X (mm)	Y (mm)	Z (mm)	X (mm)	Y (mm)	Z (mm)
25	1.83	-2.5	69	-2	-4.6	66.7	-7.6

Table D.3: Identified clusters of positive relationship of sex and CVR (i.e. males showed higher CVR than females).

Size (voxels)	Minima				Center of Gravity		
	Value (β)	X (mm)	Y (mm)	Z (mm)	X (mm)	Y (mm)	Z (mm)
25763	-9.99	-2.5	-81	43	-0.267	-35.1	10.4
67	-1.45	17.5	-18.5	73	14.2	-11.4	66.5
43	-1.2	-45	14	-42	-40	15.6	-37.6
39	-0.725	50	-1	-39.5	46.3	-0.339	-36.5
35	-2.11	47.5	-71	-14.5	41.2	-73.9	-12.6
32	-0.603	12.5	44	-2	12.6	46.1	0.461
31	-0.535	-25	36.5	-14.5	-23.3	37.1	-11.6
30	-0.332	-52.5	1.5	-27	-53.1	-0.767	-21.7
29	-1.18	-35	-8.5	43	-36	-7.44	45.6
22	-0.544	-45	-1	38	-43.6	-3.09	37.5
21	-0.563	-5	54	3	-7.37	51.3	-2.65

Table D.4: Identified clusters of negative relationship of sex and CVR (females showed higher CVR than males).

Size (voxels)	Minima				Center of Gravity		
	Value (β)	X (mm)	Y (mm)	Z (mm)	X (mm)	Y (mm)	Z (mm)
6645	-12.9	-22.5	-38.5	-49.5	-6.24	-51	-8.7
423	-11.6	40	-31	15.5	50.1	-41.3	12.3
292	-9.13	37.5	-8.5	20.5	31.3	4.13	2.98
254	-7.08	10	6.5	33	1.51	7.94	34.1
142	-7.55	52.5	-1	-9.5	54.5	-10.6	-11.2
113	-7.05	-7.5	44	25.5	-2.04	48.8	21.1
106	-8.69	-7.5	-41	73	-5.18	-36.2	65.1
77	-6.48	-10	16.5	48	-7.99	14.6	59
66	-5.71	-32.5	-53.5	48	-29.8	-55.8	47.5
65	-7.07	45	-18.5	35.5	50.5	-18.4	36.5
46	-6.34	27.5	-73.5	38	26.4	-72.4	38.7
43	-5.6	32.5	1.5	53	36.8	1.08	52.5
43	-6.83	-35	9	8	-39.7	8.1	6.72
43	-7.49	-7.5	-1	-9.5	-10.5	-8.82	-13.5
40	-7.89	-25	-93.5	10.5	-24.4	-90.7	11.2
40	-5.02	-22.5	-1	8	-25.1	3.59	2.55
38	-4.63	50	16.5	28	49.3	17	31.5
29	-6.98	-27.5	26.5	48	-26.4	21.9	42.3
28	-5.07	-40	-21	58	-39.2	-25.3	54.7
27	-4.99	-62.5	-46	28	-57.9	-48.4	31.2
27	-4.72	-37.5	-3.5	-12	-33.6	-6.85	-8.41
26	-7.96	-7.5	-3.5	53	-8.58	-5.51	50
26	-6.68	-65	-16	-19.5	-64.2	-15.9	-20.3
25	-6.35	-32.5	36.5	30.5	-30.5	33.8	31.3
24	-5.35	22.5	34	38	20.9	35.8	36.4
24	-7.46	15	-93.5	20.5	16	-90.3	22.3
24	-5.94	-55	-11	13	-54.8	-9.43	13.6
23	-8.79	-50	-28.5	35.5	-47.5	-28.7	36.5
23	-4.84	42.5	54	20.5	42.2	45.2	22
21	-4.98	-30	46.5	18	-28.5	45	23.1
20	-6.29	-52.5	-68.5	-9.5	-53.1	-65.3	-6.54

Table D.5: Identified clusters of negative impact of sex on CVR (females showed higher CVR than males), for FDR corrected results at $p < 0.005$.

E.1 Relationship between CVR and RS fluctuations

Size (voxels)	Maxima				Center of Gravity		
	Value (β)	X (mm)	Y (mm)	Z (mm)	X (mm)	Y (mm)	Z (mm)
171	3.59	-25	-71	-34.5	-35.5	-64.1	-34.8
144	6.33	32.5	-88.5	-24.5	8.54	-76.8	-23.2
65	3.71	52.5	-36	-14.5	53.4	-30.9	-11.4
44	3.92	10	-46	23	7.46	-44.3	30.6
37	5.56	62.5	-18.5	5.5	62.6	-18.7	6.61
37	4.24	-7.5	49	-7	-7.14	50.6	-10.2
34	3.44	17.5	31.5	53	22	30.8	45
34	7.34	15	4	-37	25.2	6.99	-39.7
31	4.17	-42.5	19	3	-41	17.1	3.31
30	3.78	7.5	39	0.5	-0.636	39.5	0.386
27	3.76	-67.5	-36	35.5	-56.4	-38.9	41.4
25	3.97	-37.5	-43.5	30.5	-38.4	-43.2	31.1
21	3.75	22.5	-1	65.5	25.3	-1.19	62.6
21	4	47.5	14	0.5	49.1	10.9	-0.357

Table E.1: Identified clusters of positive impact of CVR on ALFF.

Size (voxels)	Maxima				Center of Gravity		
	Value (β)	X (mm)	Y (mm)	Z (mm)	X (mm)	Y (mm)	Z (mm)
169	3.75	-45	-58.5	-47	-35.2	-63.4	-35.7
80	3.41	7.5	-78.5	-22	2.58	-76.4	-23.6
38	3.69	55	-33.5	-14.5	56.8	-31.9	-13.4
36	3.55	5	-41	30.5	7.35	-43.8	28.5
35	5.35	62.5	-18.5	5.5	62.9	-19.2	7.33
34	3.7	22.5	-83.5	-24.5	27.3	-81.3	-22.8
29	3.89	-55	-43.5	43	-56.4	-38.5	40.9
28	3.76	32.5	4	-37	30.6	7.18	-40
27	4.24	-7.5	49	-7	-8.23	50.7	-10.6
25	4.19	5	61.5	-9.5	5.61	57.9	-14.1
21	3.58	27.5	-1	60.5	25.2	-1.32	63.1
21	3.13	27.5	26.5	43	23.2	31.2	43.2
20	3.55	-40	-43.5	33	-38.6	-42.8	32.7

Table E.2: Identified clusters of positive impact of CVR on RSFA.

Size (voxels)	Maxima				Center of Gravity		
	Value (β)	X (mm)	Y (mm)	Z (mm)	X (mm)	Y (mm)	Z (mm)
63	6	5	14	70.5	3.06	22.9	61.8
35	4.9	27.5	-88.5	-27	25.9	-88.2	-24.9
34	3.92	-50	-46	-29.5	-45	-50.7	-29.6
23	4.43	47.5	-71	-19.5	50.2	-62.5	-23
20	4.12	-47.5	-26	25.5	-48.3	-25.4	27.1

Table E.3: Identified clusters of positive impact of CVR on fALFF.

E.2 Relationship between RS fluctuations, CVR, and the motor task

Size (voxels)	Maxima				Center of Gravity		
	Value (β)	X (mm)	Y (mm)	Z (mm)	X (mm)	Y (mm)	Z (mm)
82	5.15	-25	-58.5	58	-17.4	-62.8	59.8
36	3.77	-32.5	-43.5	-47	-24.6	-44.8	-46.4
35	3.6	40	-18.5	10.5	47.5	-21.5	14.2
34	10.2	47.5	-83.5	3	42.6	-70.8	4.47
32	4.5	25	-66	-57	28.9	-67.5	-54.5
31	3.77	42.5	-78.5	-7	45.2	-74.9	-10.6
30	3.84	-47.5	11.5	25.5	-40.2	9.4	25.9
29	4.02	30	-58.5	48	33.2	-59.2	50.9
26	4.32	20	-58.5	50.5	15.9	-64.9	54.4
25	4.67	15	-76	-19.5	14	-73	-22.6
23	4.49	-45	-41	50.5	-43.6	-43	46
20	3.99	-20	-51	45.5	-21.4	-55.5	41.8
20	5.25	-60	-61	-17	-55.3	-58.3	-15
20	3.9	55	-51	-19.5	53.7	-55.8	-16.2

Table E.4: Identified clusters of positive impact of CVR on the motor vs sham contrast.

Size (voxels)	Minima				Center of Gravity		
	Value (β)	X (mm)	Y (mm)	Z (mm)	X (mm)	Y (mm)	Z (mm)
81	-4.46	5	49	20.5	4.34	52.1	21
29	-3.85	-50	-23.5	-14.5	-51.9	-23.2	-14.5
23	-3.45	47.5	-38.5	-4.5	49.5	-32.6	-6.42

Table E.5: Identified clusters of negative impact of CVR on the motor vs sham contrast.

Size (voxels)	Maxima				Center of Gravity		
	Value (β)	X (mm)	Y (mm)	Z (mm)	X (mm)	Y (mm)	Z (mm)
26	4.62	2.5	14	13	1.83	13.2	13.8

Table E.6: Identified clusters of positive impact of ALFF on the motor vs sham contrast.

Size (voxels)	Minima				Center of Gravity		
	Value (β)	X (mm)	Y (mm)	Z (mm)	X (mm)	Y (mm)	Z (mm)
476	-5.67	-17.5	-63.5	40.5	-16.4	-52	27.4
204	-4.85	37.5	-13.5	60.5	31	-28.8	58.6
174	-4.71	-12.5	-23.5	43	-6.92	-13.7	43
157	-9.45	-40	-88.5	-17	-26	-87.9	-12
152	-5.02	37.5	-31	23	37.6	-24.7	16.3
110	-6.09	27.5	-53.5	8	17.4	-52.2	-0.202
97	-4.05	12.5	-86	18	6.75	-82.2	14.7
88	-4.4	25	-76	-2	22	-74.9	-3.27
77	-5.08	-52.5	-11	3	-50.4	-11.1	-0.0374
63	-6.13	-60	-8.5	-14.5	-58.3	-8.68	-14.8
55	-4.24	-15	-83.5	13	-10.2	-89.9	8.92
55	-4.43	45	-16	-2	47.9	-13.5	1.11
49	-4.63	47.5	-33.5	-2	54.3	-30.7	-4.8
40	-4.13	5	-26	-4.5	3.06	-28	-3.9
31	-4.01	-25	-83.5	3	-28.3	-84.6	2.9
29	-3.91	-30	-28.5	18	-34.2	-26	15.6
26	-3.84	-37.5	-21	-2	-34.9	-24.4	0.478
25	-4.88	37.5	-56	23	40.4	-55.3	26.3
24	-3.89	15	-38.5	50.5	11.3	-41.8	49.3
24	-3.85	-32.5	29	8	-34.9	32.7	8.75
23	-3.89	-5	-11	-7	-5.58	-11.8	-6.19
23	-5.19	-22.5	-18.5	-32	-25	-14.9	-29.2
22	-3.41	12.5	-58.5	63	19.6	-54.8	59.4

Table E.7: Identified clusters of negative impact of ALFF on the motor vs sham contrast.

Size (voxels)	Maxima				Center of Gravity		
	Value (β)	X (mm)	Y (mm)	Z (mm)	X (mm)	Y (mm)	Z (mm)
26	5.22	5	6.5	20.5	2.15	12.7	14.3

Table E.8: Identified clusters of positive impact of RSFA on the motor vs sham contrast.

Size (voxels)	Minima				Center of Gravity		
	Value (β)	X (mm)	Y (mm)	Z (mm)	X (mm)	Y (mm)	Z (mm)
221	-5.37	-15	-68.5	18	-13.6	-69.6	18.9
211	-4.98	45	-16	-2	40.6	-22	10.7
197	-5.32	37.5	-33.5	70.5	30.9	-28.8	58.6
182	-12.5	-60	6.5	-7	-54.5	-10.9	-4.51
149	-4.51	-12.5	-23.5	43	-7.57	-13.6	43.6
141	-10.8	-35	-93.5	-14.5	-27.9	-87.5	-9.56
107	-5.16	-12.5	-43.5	63	-18	-37.9	62.4
88	-4.4	25	-76	-2	22.6	-75	-3.51
78	-5.36	30	-53.5	5.5	21.7	-53.5	2.16
69	-4	12.5	-86	18	10.5	-86.6	16.6
64	-4.06	-7.5	-93.5	5.5	-8.9	-90.3	9.73
61	-5.23	-12.5	-41	-2	-14	-44	-6.28
48	-4.4	-57.5	26.5	10.5	-42.2	30.7	10.8
41	-4.06	-12.5	14	38	-8.73	14.1	33.2
38	-4.56	5	-26	-4.5	1.6	-28.3	-4.05
38	-4.51	57.5	-31	-4.5	55	-30.9	-4.51
33	-5.65	-10	-43.5	50.5	-9.07	-46.7	49.5
32	-4.39	37.5	-56	23	42.4	-57.8	25.7
32	-4.6	-27.5	-28.5	-17	-25.9	-26	-19.2
30	-3.35	-47.5	-21	-17	-52.4	-23.6	-12.5
29	-3.87	-37.5	-21	-2	-35	-24	-0.0648
28	-7.95	-27.5	-21	-32	-25	-15.5	-29.2
23	-4.35	27.5	-36	-19.5	27.3	-35.1	-21.3
22	-5.03	-15	-81	53	-16	-76.3	52
21	-13.6	-22.5	16.5	68	-26.6	15.9	62.7
21	-3.58	-12.5	-26	13	-9.74	-20.4	12.8
21	-3.78	-2.5	-11	-4.5	-4.86	-12.3	-6.11
20	-4.19	20	-71	18	18	-65.7	16.6

Table E.9: Identified clusters of negative impact of RSFA on the motor vs sham contrast.

Size (voxels)	Minima				Center of Gravity		
	Value (β)	X (mm)	Y (mm)	Z (mm)	X (mm)	Y (mm)	Z (mm)
149	-4.49	7.5	-63.5	15.5	-6.03	-68.6	31
134	-4.77	-12.5	-16	38	-9.62	-5.74	41.4
72	-3.59	15	-86	20.5	10.6	-83.5	16.7
55	-4.62	37.5	-21	18	37.9	-25	18.4
53	-4.57	-15	-38.5	-4.5	-8.84	-46.6	-6.59
40	-5.15	-25	-41	-19.5	-27.8	-41.5	-19.4
39	-3.94	22.5	-43.5	3	21.6	-49.8	-2.44
38	-4.11	-52.5	-11	0.5	-49.8	-11.8	1.13
37	-4.5	-25	-36	58	-22.6	-36.8	58.2
34	-3.73	-5	-96	5.5	-8.31	-92.8	8.28
31	-3.68	5	-6	43	6.84	-8.2	44.3
28	-3.95	30	-68.5	-2	27.8	-71.2	-3.45
20	-4.46	12.5	-41	53	13.4	-41	53.1

Table E.10: Identified clusters of negative impact of fALFF on the motor vs sham contrast.

E.3 Relationship between RS fluctuations, CVR, and the Simon task

Size (voxels)	Maxima				Center of Gravity		
	Value (β)	X (mm)	Y (mm)	Z (mm)	X (mm)	Y (mm)	Z (mm)
57	4.73	-17.5	34	58	-17.9	23.4	51.2
45	5.58	-40	6.5	43	-38	3.33	46.2
43	3.66	40	-71	-22	36.8	-66	-22.5
40	5.16	-2.5	-63.5	35.5	-0.806	-66	32.1
34	3.85	-32.5	-68.5	40.5	-30.9	-65.9	37.6
27	4.25	-45	-43.5	-24.5	-40.1	-45.6	-24.6
22	3.54	30	4	-2	32.1	4.53	-4.72
20	4.58	-5	11.5	60.5	-8.11	11.1	58.5

Table E.11: Identified clusters of positive impact of CVR on all congruent responses contrast.

Size (voxels)	Maxima				Center of Gravity		
	Value (β)	X (mm)	Y (mm)	Z (mm)	X (mm)	Y (mm)	Z (mm)
54	4.02	5	1.5	53	1.16	-2.39	55.7
44	3.88	35	-43.5	40.5	30.2	-46.4	39.4
39	4.2	-27.5	-73.5	20.5	-26.6	-76.4	22.7
33	6.02	40	-73.5	-52	37.6	-68.3	-47.1

Table E.12: Identified clusters of positive impact of ALFF on all congruent responses contrast.

Size (voxels)	Maxima				Center of Gravity		
	Value (β)	X (mm)	Y (mm)	Z (mm)	X (mm)	Y (mm)	Z (mm)
57	4.01	2.5	-1	55.5	2.3	-2.57	56.7
34	3.73	32.5	-46	38	30.8	-46.7	38.6
30	4.74	-30	-46	33	-32.7	-46.6	34.9
27	5.28	40	-73.5	-52	37.4	-68.1	-47
23	3.93	-27.5	-73.5	20.5	-26.9	-76.2	22.8

Table E.13: Identified clusters of positive impact of RSFA on all congruent responses contrast.

Size (voxels)	Minima				Center of Gravity		
	Value (β)	X (mm)	Y (mm)	Z (mm)	X (mm)	Y (mm)	Z (mm)
26	-3.85	-2.5	44	13	-2.24	44.4	13.8

Table E.14: Identified clusters of negative impact of fALFF on all congruent responses contrast.

Size (voxels)	Maxima				Center of Gravity		
	Value (β)	X (mm)	Y (mm)	Z (mm)	X (mm)	Y (mm)	Z (mm)
28	4.1	42.5	-13.5	30.5	44.4	-10.1	32.4
27	3.95	-40	6.5	43	-40.3	5.11	45.6
25	4.43	-42.5	-56	33	-41.3	-58.3	38.6
20	4.28	-37.5	-51	20.5	-41.4	-50.9	21.6

Table E.15: Identified clusters of positive impact of CVR on all incongruent responses contrast.

Size (voxels)	Minima				Center of Gravity		
	Value (β)	X (mm)	Y (mm)	Z (mm)	X (mm)	Y (mm)	Z (mm)
27	-3.84	12.5	-61	-49.5	9.41	-65.2	-43.1

Table E.16: Identified clusters of negative impact of fALFF on all incongruent responses contrast.

Size (voxels)	Maxima				Center of Gravity		
	Value (β)	X (mm)	Y (mm)	Z (mm)	X (mm)	Y (mm)	Z (mm)
65	4.88	-37.5	-51	20.5	-40.7	-55.3	31.3
39	5.44	-40	6.5	43	-40.3	4.38	45.7
26	4.71	-2.5	-66	35.5	-0.995	-67.7	30.9
24	3.81	45	-73.5	-22	43.4	-70.8	-20.5
23	3.14	-25	21.5	48	-28.6	19.8	46.6
20	3.53	-27.5	-61	43	-28.4	-63	48.8
20	3.76	42.5	-13.5	30.5	45.9	-10.2	33.2

Table E.17: Identified clusters of positive impact of CVR on all congruent and incongruent responses contrast.

Size (voxels)	Maxima				Center of Gravity		
	Value (β)	X (mm)	Y (mm)	Z (mm)	X (mm)	Y (mm)	Z (mm)
33	3.57	27.5	-46	38	28.5	-47	41.5
27	4.18	5	-1	55.5	2.29	-1.37	54.8
25	4.32	42.5	-68.5	-47	38.5	-67.7	-46.4
24	4.29	-25	-73.5	20.5	-26.4	-76.1	22.9

Table E.18: Identified clusters of positive impact of ALFF on all congruent and incongruent responses contrast.

Size (voxels)	Maxima				Center of Gravity		
	Value (β)	X (mm)	Y (mm)	Z (mm)	X (mm)	Y (mm)	Z (mm)
25	4.59	-30	-46	33	-32.5	-46.9	35

Table E.19: Identified clusters of positive impact of RSFA on all congruent and incongruent responses contrast.